

In silico and in vitro estimation of the displacement of an implanted electrode in rat brain

Brecht Lenaerts
Jeroen Samoeys

Promotor: prof. dr. ir. Kathleen Denis

Copromotor: prof. dr. Dimitar Prodanov

Masterproef ingediend tot het behalen van de
graad van Master of Science in de Industriële
Wetenschappen: Elektromechanica

Academiejaar 2020-2021

© Copyright KU Leuven

Zonder voorafgaande schriftelijke toestemming van zowel de promotor(en) als de auteur(s) is overnemen, kopiëren, gebruiken of realiseren van deze uitgave of gedeelten ervan verboden. Voor aanvragen i.v.m. het overnemen en/of gebruik en/of realisatie van gedeelten uit deze publicatie, kan u zich richten tot KU Leuven Campus Groep T Leuven, Andreas Vesaliusstraat 13, B-3000 Leuven, +32 16 30 10 30 of via e-mail iiw.groept@kuleuven.be.

Voorafgaande schriftelijke toestemming van de promotor(en) is eveneens vereist voor het aanwenden van de in deze masterproef beschreven (originele) methoden, producten, schakelingen en programma's voor industrieel of commercieel nut en voor de inzending van deze publicatie ter deelname aan wetenschappelijke prijzen of wedstrijden.

Preface

First of all, we would like to thank our copromotor prof. dr. Dimitar Prodanov for giving us the opportunity to conduct this thesis. During our weekly meetings he always challenged us to take this thesis and ourselves to a higher level. We were able to rely on his insights and experience while he gave us the opportunity to determine the direction of the thesis ourselves.

Special thanks to our promotor prof. dr. ir. Kathleen Denis. She consistently provided relevant insights during our meetings. It is absolutely clear that she always encouraged us to continue working at a fast pace, without losing sight of our personal well-being. Furthermore, we would like to thank her for thoroughly proofreading the thesis and giving very valuable feedback.

Furthermore, we want to thank the Interuniversity Microelectronics Centre (IMEC) and Kloosterman Lab of NeuroElectronics Research Flanders (NERF) for welcoming us as thesis students and for sharing their knowledge and facilities. Special thanks go out to dr. Jyh-Jang Sun, member of Kloosterman Lab, for sharing his opinion on the experiment set-up. We could always count on him to solve our practical issues.

Thanks to Horacio Londoño Ramirez, who advised us on the electronic circuit and the use of the anti-vibration table. Ing. Frank Gijbels also deserves a word of appreciation for sharing his experience in the realisation of electronic circuits.

We would also like to thank Gunther Penninckx and Eddy Smets for sawing the profile parts of the frame of the set-up.

Many thanks to ing. Luc Janssens, who advised us on the sensor selection. His confidence in our self-designed micromotion sensor was enormously motivating and his enthusiasm was definitely contagious.

Appreciation to Henrik Szabo and Materialise for their guidance in the 3D-printing of the micromotion sensor. Our gratitude also goes to Jurgen Mangelschots, founder of Strain 2 Data, for the application of the strain gauges on the micromotion sensor. The experiment would not have been possible without his work under time pressure.

Thanks to Marijke Lenaerts for proofreading the thesis in detail. Furthermore, thanks to ir. Rudi Lenaerts, who also proofread the thesis and gave advice from his perspective as an engineer.

Last but not least, we would like to thank our fellow students and family. The interest and support of our grandparents, parents and sisters motivated us again and again to go all out for our studies and thesis, also during harder times. Our parents' contribution to our development as young engineers is beyond words.

Sincere thanks to all.

Brecht Lenaerts and Jeroen Samoeys

Samenvatting

De levensduur van hersenelektroden is afhankelijk van de mechanische stabiliteit van de elektroden in het hersenweefsel. De mechanische mismatch tussen het implantaat en het hersenweefsel kan leiden tot spanningsopbouw. Daarom verbetert de schatting van de implantaatverplaatsing in het hersenweefsel de huidige kennis van interne mechanische interacties. De hoofddoelstelling van deze thesis was de ontwikkeling en validatie van een techniek om de verplaatsing van een implantaat in het hersenweefsel van een rat te bepalen tijdens normaal diergedrag.

Eerst werd een reeks vereenvoudigde eindige elementen methode (EEM) modellen van de hersenen ontwikkeld. De EEM-modellen werden in meerdere iteraties gewijzigd om de weefseigenschappen en fysiologische processen zoals ademhaling en bloedcirculatie beter na te bootsen. Ter vereenvoudiging werd de hersenvorm voorgesteld als balkvormig, waarbij de afmetingen gebaseerd waren op de anatomie van echte rattenhersenen. Het hersenweefsel werd gemodelleerd als visco-elastisch materiaal, gebaseerd op een tweede orde Kelvin-Voigt-model. Zowel de fysiologische activiteit als het normaal diergedrag beïnvloedden de mechanische interacties. Statische intracraniele druk, ademhaling en hartslag werden beschouwd als relevante fysiologische factoren die de mechanische interacties beïnvloedden. Normaal dierlijk gedrag omvat zowel lineaire beweging als rotatie van het hoofd.

De resultaten toonden aan dat de grootste implantaatverplaatsing veroorzaakt wordt door ademhaling. Deze verplaatsing wordt geschat op $70,6\text{ }\mu\text{m}$ aan de punt van het implantaat en op $11,4\text{ }\mu\text{m}$ aan het bovenoppervlak van het hersenweefsel. De resultaten van de EEM-modellen komen bovendien overeen met reeds bestaande onderzoeksgegevens over de implantaatverplaatsing loodrecht op het hersenoppervlak als gevolg van ademhaling, die varieert tussen $5\text{ }\mu\text{m}$ en $30\text{ }\mu\text{m}$.

Daarna werd een experimentopstelling ontworpen en gebouwd om een ademhalings-EEM-model te valideren. Voor deze experimentopstelling werd een schaafactor van 10:1 gebruikt vanwege de geometrische beperkingen van het implantaat. Het visco-elastische hersenweefsel werd voorgesteld door een weefselfantoom bestaande uit een agarosegel met een elasticiteitsmodulus van 50 kPa . Om de microbeweging van het implantaat te meten, is een op maat gemaakte sensor met bijhorende signaalconditionering ontworpen. Een lineaire actuator brengt de ademhalingsdruk op het hersenweefsel aan. Een cyclische beweging met een translatie van 2 mm en frequenties van 2 Hz , 1 Hz , $0,5\text{ Hz}$ en $0,25\text{ Hz}$ werd uitgeoefend op het caudale oppervlak van de hydrogel. Dit veroorzaakt een druk van 1130 Pa .

Ten slotte werd de rostrale implantaatverplaatsing tijdens een proof of concept experiment gemeten. De resultaten toonden een implantaatverplaatsing in de opgeschaalde opstelling die varieert tussen $300\text{ }\mu\text{m}$ en $400\text{ }\mu\text{m}$ aan het bovenoppervlak van het weefselfantoom. Het EEM-model werd aangepast rekening houdend met de beperkingen van de experimentele opstelling en toonde een resultaat van ongeveer $400\text{ }\mu\text{m}$ voor de verplaatsing van het implantaat aan het bovenoppervlak van het fantoomweefsel. In effectieve hersendimensies resulteert dit in een rostrale verplaatsing aan het hersenoppervlak van $40\text{ }\mu\text{m}$. Deze waarde is in overeenstemming met de metingen. Verder onderzoek moet evenwel aandacht besteden aan de ontwikkeling van een betere hydrogel-malverbinding en de toepassing van een gelijkmatig verdeelde druk op het caudale oppervlak.

Abstract

The longevity of brain recoding electrodes depends on the mechanical stability of the electrode-brain tissue interface. The mechanical mismatch between the implant and the brain tissue could lead to stresses. Hence, the estimation of the displacement of an implant in the brain tissue improves the current knowledge on internal mechanical interactions. The main goal of this thesis was the development and validation of a technique to estimate the displacement of an implant in rat brain tissue during normal animal behaviour.

First, a series of simplified finite element method (FEM) models of the brain was developed. The FEM models were modified in multiple iterations to better match tissue properties and physiological processes such as respiration and blood circulation. For reasons of simplification, the geometries consisted of cuboids with dimensions based on the anatomy of the real rat brain. The brain tissue was modelled as a viscoelastic material, using a second order Kelvin-Voigt model with material constants from literature sources. Both the normal physiological activity and behaviour influence the mechanical interactions. Static intracranial pressure, respiration and heartbeat were considered the relevant physiological factors that influence the mechanical interactions. Normal animal activity includes both linear movement and rotation of the head.

Results showed that the largest rostral implant displacement is caused by respiration and is estimated at 70,6 μm at the tip of the implant and at 11,4 μm at the top surface of the brain tissue. The results of the FEM models also corresponded with existing literature data on the implant displacement perpendicular to the brain surface due to respiration, ranging from 5 μm to 30 μm .

Next, in order to validate a respiration FEM model, an experiment set-up was designed and built using a scale factor of 10:1. This scale factor was used due to the geometrical constraints of the implant. A tissue phantom consisting of an agarose hydrogel with an elastic modulus of 50 kPa represented the viscoelastic brain tissue. To measure the micromotion of the implant, a customised sensor with corresponding signal conditioning was designed. A linear actuator applied the respiration pressure wave acting on the brain tissue. A cyclic motion with a translation of 2 mm and frequencies of 2 Hz, 1 Hz, 0,5 Hz and 0,25 Hz was imposed on the caudal surface of the hydrogel, causing a pressure of 1130 Pa.

Finally, the rostral displacement of the implant was measured during a proof of concept experiment. The results of the implant displacement in the upscaled set-up showed a displacement ranging from 300 μm to 400 μm at the top surface of the tissue phantom. The FEM model was adapted according to the experiment boundary conditions showing a displacement of the implant of approximately 400 μm at the top surface of the tissue phantom. Converting this value to real brain tissue dimensions resulted in a rostral displacement at the brain surface of 40 μm . This value is in agreement with the measurements. However, further research should pay attention to both the development of a more efficient hydrogel-mould connection and the application of an equally distributed pressure on the caudal surface.

Keywords: implanted electrode, FEM modelling, tissue phantom, micromotion sensor, viscoelasticity, rat brain

TABLE OF CONTENTS

Preface	i
Samenvatting.....	ii
Abstract	iii
List of figures and tables	viii
List of symbols.....	xv
List of abbreviations	xix
1 Introduction	1
1.1 Background.....	1
1.2 Goal of the thesis	3
1.3 Methodology	3
2 Literature study	5
2.1 Physiology and behaviour of rats	5
2.1.1 Anatomical planes and directions.....	5
2.1.2 The rat brain.....	6
2.1.3 Intracranial pressure	10
2.1.4 Heart rate and blood pressure.....	11
2.1.5 Respiration.....	12
2.1.6 Linear acceleration.....	13
2.1.7 Head rotation	14
2.2 Implanted electrodes.....	14
2.2.1 Probes	15
2.2.2 Hyperdrive	16
2.3 Rat brain finite element models	17
2.4 Conclusion	19
3 Description of finite element models	20
3.1 ONELAB software package.....	20
3.2 Mathematical model of FEM analysis	20
3.2.1 Elastic displacement calculation.....	21
3.2.2 Viscoelastic displacement calculation.....	22
3.2.3 Different mathematical steps.....	24
3.3 Multiple loads model	25

3.3.1	Geometry	25
3.3.2	Material properties	26
3.3.3	Mesh	27
3.3.4	Boundary conditions.....	29
3.3.5	Solver.....	34
3.4	<i>Heartbeat model</i>	34
3.4.1	Geometry	34
3.4.2	Material properties	35
3.4.3	Mesh	36
3.4.4	Boundary conditions.....	37
3.4.5	Solver.....	38
3.5	<i>Respiration model</i>	38
3.5.1	Geometry	38
3.5.2	Material properties	38
3.5.3	Mesh	39
3.5.4	Boundary conditions.....	40
3.5.5	Solver.....	40
3.6	<i>Conclusion</i>	41
4	Results and verification of finite element models.....	42
4.1	<i>Convergence analysis</i>	42
4.1.1	Multiple loads model	42
4.1.2	Heartbeat model	43
4.1.3	Respiration model	44
4.2	<i>Viscoelastic analysis</i>	44
4.3	<i>Results discussion</i>	45
4.3.1	Multiple loads model	45
4.3.2	Heartbeat model	51
4.3.3	Respiration model	52
4.4	<i>Verification</i>	54
4.5	<i>Choice of model to be validated</i>	57
4.6	<i>Conclusion</i>	57
5	Experiment set-up	59
5.1	<i>Micromotion sensor</i>	59
5.1.1	Selection	60

5.1.2 Mechanical design	62
5.1.3 Electronic design.....	68
5.2 <i>Structural components</i>	76
5.2.1 Anti-vibration table	76
5.2.2 Frame	77
5.2.3 Mould.....	79
5.3 <i>Actuator</i>	81
5.3.1 Selection	81
5.3.2 Control	83
5.3.3 Pressure sensors	84
5.4 <i>Tissue phantom</i>	88
5.5 <i>Conclusion</i>	89
6 Experiment.....	90
6.1 <i>Protocol</i>	90
6.2 <i>Gel preparation</i>	90
6.3 <i>Sensor calibration</i>	92
6.3.1 Micromotion sensor.....	92
6.3.2 Pressure sensors	94
6.4 <i>Assembly and implant insertion</i>	97
6.5 <i>Electrical connections and motor control</i>	99
6.6 <i>Measurements</i>	100
6.7 <i>Conclusion</i>	102
7 Validation of finite element model.....	103
7.1 <i>Data analysis</i>	103
7.2 <i>Differences between respiration model and experiment</i>	112
7.3 <i>Experiment model</i>	115
7.4 <i>Discussion and conclusion</i>	118
8 Conclusion.....	120
References.....	121
Appendices.....	125
Appendix A Elastic modulus calculation	A.1
Appendix B Creep function calculation	B.1
Appendix C Convergence graphs	C.1
Appendix D Motor selection calculation	D.1

Appendix E	Preparation protocol and experiment protocol.....	E.1
Appendix F	Preparation of hydrogel.....	F.1
Appendix G	Micromotion sensor calibration curves.....	G.1
Appendix H	FSR calibration curves	H.1
Appendix I	Electronic components.....	I.1
Appendix J	Technical drawings.....	J.1

Provided on an electronic medium

Appendix K	NanoJ script for motor control
Appendix L	FEM models
Appendix M	Calibration data
Appendix N	Measurement data
Appendix O	Movie experiment

List of figures and tables

Figure 1-1 Rat with attached hyperdrive (van Daal, et al., 2020)	1
Figure 1-2 Coronal section of a rat brain with visible probe track and electrolytic lesion (van Daal, et al., 2020)	2
Figure 1-3 Schematic drawing with mechanical interactions of the implant and brain tissue (Delbeke, Haesler, & Prodanov, 2020)	2
Figure 2-1 Anatomical planes and directions (Andersen & Tufik, 2016)	5
Figure 2-2 Electrode insertion in a brain slice of a rat, electrode penetrates several layers with different mechanical properties: scalp, bone of skull, dura mater, subarachnoid space and brain tissue (Nowak, et al., 2011)	6
Figure 2-3 Merged image of real skull and its corresponding brain to introduce the craniometric data including distance 1 to 5 in dorsal and sagittal views (Yang, et al., 2018)	7
Figure 2-4 Correlation of body weight with different phases of postnatal days (Sengupta, 2013)	8
Figure 2-5 Ponto-medullary junction (PmJ) and pyramidal decussation (PDx) of the rat brain (Shafieian, Darvish, & Stone, 2009)	10
Figure 2-6 Intracranial pressure during 50 days after surgery, mean \pm standard deviation (Eftekhari, Westgate, Johansen, Bruun, & Jensen, 2012)	10
Figure 2-7 LVP in function of time (Kobayashi, et al., 1996)	11
Figure 2-8 Jugular venous pressure measured for six male Sprague-Dawley rats (Cops, et al., 2018)	12
Figure 2-9 Deflation pressure-volume curve of the lungs of anesthetized Sprague-Dawley rats (Schulz & Muhle, 2000)	12
Figure 2-10 Timeline of an experimental protocol to determine effects of recruitment manoeuvres and PEEP (Camilo, et al., 2018)	13
Figure 2-11 Schematic of an acoustic startle experiment and the startle responses (Pasquet, et al., 2016)	13
Figure 2-12 The angular head velocity for a low-velocity turn (Sharp, Tinkelman, & Cho, 2001)	14
Figure 2-13 Probe configurations: A: 1x16 B: 2x8 C: 3x15+1 D: 4x4 (van Daal, et al., 2020)	15
Figure 2-14 Microdrive designs (van Daal, et al., 2020)	16
Figure 2-15 Hyperdrive cross-section at the left and bottom view of exit tip at the right (van Daal, et al., 2020)	17
Figure 3-1 Kelvin-Voigt model of the first order (Fung, 1981)	22
Figure 3-2 Stepped and continuous stress history (Betten, 2008)	24
Figure 3-3 Geometry of multiple loads model	26
Figure 3-4 Hexahedral element (De Roeck, 2020)	27

Figure 3-5 Meshing tissue multiple loads model: front view, side view, top view and orthogonal view.....	28
Figure 3-6 Meshing implant multiple loads model: top view and side view.....	29
Figure 3-7 Conceptual drawing of the different implant fixation configurations (Prodanov & Delbeke, 2016).....	30
Figure 3-8 Sketch displacement boundary conditions.....	31
Figure 3-9 Diagram of a rat head rotation.....	32
Figure 3-10 Top view free body diagram	34
Figure 3-11 Geometry heartbeat model.....	35
Figure 3-12 Top view heartbeat model	35
Figure 3-13 Meshing tissue heartbeat model: front view, side view, top view and orthogonal view.....	36
Figure 3-14 Pressures in tubes.....	37
Figure 3-15 Top view respiration model.....	38
Figure 3-16 Meshing respiration model: close-up top view	39
Figure 3-17 Meshing tissue respiration model: front view, side view, top view and orthogonal view.....	40
Figure 4-1 Convergence graph multiple loads model, all loads.....	43
Figure 4-2 Convergence graph heartbeat model	43
Figure 4-3 Convergence graph respiration model.....	44
Figure 4-4 Creep and relaxation	44
Figure 4-5 Force versus implant tip displacement.....	45
Figure 4-6 Colour plot displacement due to linear acceleration (section in sagittal plane).....	46
Figure 4-7 Viscoelastic and elastic implant tip displacement in rostral direction due to linear acceleration.....	47
Figure 4-8 Colour plot displacement due to rotation (top view)	47
Figure 4-9 Colour plot displacement due to rotation (section in sagittal plane)	48
Figure 4-10 Colour plot displacement due to static intracranial pressure (section in sagittal plane)	48
Figure 4-11 Colour plot displacement due to respiration (section in sagittal plane).....	49
Figure 4-12 Viscoelastic and elastic implant tip displacement in rostral direction due to respiration	49
Figure 4-13 Colour plot displacement due to multiple loads (section in sagittal plane).....	50
Figure 4-14 Viscoelastic and elastic implant tip displacement in rostral direction due to multiple loads	50
Figure 4-15 Colour plot displacement due to heartbeat (section in sagittal plane)	51

Figure 4-16 Colour plot displacement due to heartbeat (section in transverse plane)	52
Figure 4-17 Viscoelastic and elastic implant tip displacement in rostral direction due to heartbeat	52
Figure 4-18 Colour plot displacement due to respiration acceleration (section in sagittal plane)	53
Figure 4-19 Colour plot displacement due to respiration (section)	53
Figure 4-20 Viscoelastic and elastic implant tip displacement in rostral direction due to respiration	54
Figure 4-21 Approximate locations of displacement measurements in a small craniotomy (Gilletti & Muthuswamy, 2006)	54
Figure 4-22 Displacement for large craniotomy, mean \pm standard deviation (Gilletti & Muthuswamy, 2006)	55
Figure 4-23 Displacement data summary for small craniotomy, mean \pm standard deviation (Gilletti & Muthuswamy, 2006)	55
Figure 4-24 Rat with the brain, windpipe, heart and lungs, respiratory pressure direction towards the brain indicated by arrow	56
Figure 4-25 Implant displacement in the multiple loads model, heartbeat model and respiration model (section in sagittal plane)	56
Figure 4-26 Concept sketches inputs	57
Figure 5-1 CAD drawing of the experiment set-up	59
Figure 5-2 CAD drawing of the first iteration of the implant module	61
Figure 5-3 Microdisplacement sensor (Wu, et al., 2014)	61
Figure 5-4 CAD drawing of the implant module	64
Figure 5-5 FEM model modifications	65
Figure 5-6 Implant displacement in the rostral direction due to respiration for toggle point and with sensitive beams (section in sagittal plane)	66
Figure 5-7 Implant tip displacement in rostral direction due to respiration for toggle point and sensitive beams model	66
Figure 5-8 Implant displacement in the rostral direction due to heartbeat for toggle point and with sensitive beams (section in sagittal plane)	67
Figure 5-9 Implant tip displacement in rostral direction due to heartbeat for toggle point and sensitive beams model	67
Figure 5-10 Sensitive beams displacement due to heartbeat and respiration	68
Figure 5-11 Implant tip displacement in dorsal direction due to respiration and heartbeat for sensitive beams model	68
Figure 5-12 Sketch of the section view of the implant module	69
Figure 5-13 Detailed sketch of the deformed implant module in section view	69
Figure 5-14 Wheatstone bridge configurations	71

Figure 5-15 Analog signal conditioning circuit for the strain gauges.....	73
Figure 5-16 Response of the SPICE simulation of the analog circuit	74
Figure 5-17: Displacement of the sensitive beams in the FEM model.....	75
Figure 5-18 Close-up of an attached strain gauge	75
Figure 5-19 Enclosure of the implant module	76
Figure 5-20 Close-up of the implant module in the enclosure, the frame has outer dimensions equal to 70 mm on 45 mm.....	76
Figure 5-21 CAD drawing of the frame for the implant module	78
Figure 5-22 Frame with the implant module attached to the anti-vibration table	79
Figure 5-23 CAD drawing of the mould.....	80
Figure 5-24 Mould	80
Figure 5-25 CAD drawing motor	82
Figure 5-26 Linear actuator on base frame.....	82
Figure 5-27 GUI of Plug & Drive studio (Nanotec, 2021)	83
Figure 5-28 Motor circuit diagram (Nanotec, 2021).....	83
Figure 5-29 Motor circuit.....	84
Figure 5-30 FSR and piezo attached to the caudal plate	85
Figure 5-31 Arduino circuit diagram.....	86
Figure 5-32 Resistance versus force graph (Interlink Electronics, 2021)	86
Figure 5-33 Burned rostral FSR.....	87
Figure 5-34 Case with electric circuits	87
Figure 6-1 Stirring of the gel solution and measuring of the temperature.....	91
Figure 6-2 The pouring of the gel solution at the left and the gel solution in the mould at the right.....	91
Figure 6-3 Calibration set-up of the implant module	92
Figure 6-4 Calibration of the implant module with a displacement of 75 μm	93
Figure 6-5 Calibration curve of the implant module.....	94
Figure 6-6 Calibration set-up of the caudal FSR.....	94
Figure 6-7 Calibration of the caudal FSR with mass 1	95
Figure 6-8 Calibration curve of the caudal FSR	96
Figure 6-9 Calibration of the caudal FSR at stroke 1	97
Figure 6-10 Implant positioned in the centre, above the hole.....	97
Figure 6-11 Top view of inserted implant module	98
Figure 6-12 Close-up of sensitive beams when gel is not solidified at the left and when the gel has solidified at the right.....	98

Figure 6-13 Connection of mould and motor to the anti-vibration table	99
Figure 6-14 Connected pressure sensor data cables	99
Figure 6-15 Experiment set-up	100
Figure 6-16 Built-in oscilloscope of Plug & Drive Studio (Nanotec, 2021)	101
Figure 7-1 Measurement data of the strain gauges, FSR sensor and piezo sensors for a frequency of 2 Hz	104
Figure 7-2 Measurement data of the strain gauges, FSR sensor and piezo sensors for a frequency of 1 Hz	105
Figure 7-3 Measurement data of the strain gauges, FSR sensor and piezo sensors for a frequency of 0,5 Hz	106
Figure 7-4 Measurement data of the strain gauges, FSR sensor and piezo sensors for a frequency of 0,25 Hz	107
Figure 7-5 Measurement data of the strain gauges for different frequencies	108
Figure 7-6 Scaled power spectrum of the strain gauges, FSR sensor and piezo sensors for a frequency of 2 Hz	109
Figure 7-7 Scaled power spectrum of the strain gauges, FSR sensor and piezo sensors for a frequency of 1 Hz	110
Figure 7-8 Scaled power spectrum of the strain gauges, FSR sensor and piezo sensors for a frequency of 0,5 Hz	111
Figure 7-9 Scaled power spectrum of the strain gauges, FSR sensor and piezo sensors for a frequency of 0,25 Hz	112
Figure 7-10 Air gap between tissue and top plate, indicated by the arrow	113
Figure 7-11 Start and end position inclination difference	113
Figure 7-12 Pressure diagram caudal plate with FSR connected to the linear actuator	114
Figure 7-13 Colour plot displacement experiment model (intersection in sagittal plane)	115
Figure 7-14 Implant displacement in the rostral direction in respiration model at the left and in experiment model at the right (section in sagittal plane)	116
Figure 7-15 Implant rostral displacement vs time at the gel surface level in the experiment FEM model	117
Figure 7-16 Implant rostral displacement vs time at the gel surface level according to the measurement data	117
Figure 7-17 Qualitative hysteresis curve.....	118
Figure B-1 Reduced relaxation function.....	B.2
Figure C-1 Convergence graph multiple loads model, linear acceleration	C.1
Figure C-2 Convergence graph multiple loads model, rotation	C.1
Figure C-3 Convergence graph multiple loads model, static intracranial pressure	C.2
Figure C-4 Convergence graph multiple loads model, respiration.....	C.2

Figure D-1 Position of surface at caudal side	D.1
Figure D-2 Velocity of surface at caudal side.....	D.2
Figure D-3 Acceleration of surface at caudal side.....	D.2
Figure G-1 Measurement of the micromotion sensor calibration with a displacement of 25 μm	G.1
Figure G-2 Measurement of the micromotion sensor calibration with a displacement of 50 μm	G.1
Figure G-3 Measurement of the micromotion sensor calibration with a displacement of 75 μm	G.2
Figure G-4 Measurement of the micromotion sensor calibration with a displacement of 100 μm	G.2
Figure G-5 Measurement of the micromotion sensor calibration with a displacement of 125 μm	G.3
Figure G-6 Measurement of the micromotion sensor calibration with a displacement of 150 μm	G.3
Figure G-7 Measurement of the micromotion sensor calibration with a displacement of 175 μm	G.4
Figure G-8 Measurement of the micromotion sensor calibration with a displacement of 200 μm	G.4
Figure G-9 Measurement of the micromotion sensor calibration with a displacement of 225 μm	G.5
Figure G-10 Measurement of the micromotion sensor calibration with a displacement of 250 μm	G.5
Figure H-1 Calibration of the caudal FSR with mass 2	H.1
Figure H-2 Calibration of the caudal FSR with mass 3	H.2
Figure H-3 Calibration of the caudal FSR with mass 4	H.2
Figure H-4 Calibration of the caudal FSR with mass 5	H.3
Figure H-5 Calibration of the caudal FSR at stroke 2.....	H.3
Figure H-6 Calibration of the caudal FSR at stroke 3.....	H.4
Figure H-7 Calibration of the caudal FSR at stroke 4.....	H.4

Table 2-1 Craniometric measurements of rats aged ten weeks, mean \pm standard deviation (Yang, et al., 2018).....	7
Table 2-2 Brain dimensions, mean \pm standard deviation (Gefen, Gefen, Zhu, Raghupathi, & Margulies, 2003).....	8
Table 2-3 Apparent elastic moduli E_0 , E_1 and E_2 , of brain tissue at each strain rate, mean \pm standard deviation (Rashid, Destrade, & Gilchrist, 2012).....	9
Table 2-4 Material parameters for reduced relaxation function at PmJ and PDx, mean \pm 95 % confidence interval (Shafieian, Darvish, & Stone, 2009)	10
Table 2-5 Weight and pressures measured for six male Sprague-Dawley rats median [minimum; maximum] (Cops, et al., 2018)	11
Table 3-1 Material parameters reduced creep function (Shafieian, Darvish, & Stone, 2009)	27
Table 5-1 Selection of the implant displacement sensor	60
Table 5-2 Criteria material selection implant.....	63
Table 5-3 Demands/wishes and technical data actuator.....	81
Table 5-4 Property table piezo and FSR.....	85
Table E-1 Preparation protocol on the day before the measurements	E.1
Table E-2 Experiment protocol on the day of the measurements.....	E.1
Table F-1 Overview of the measured masses before mixing and heating	F.1
Table F-2 Overview of the measured masses after mixing and heating.....	F.1
Table F-3 Heating process of the solutions during the five stages	F.2
Table I-1 Parts list of the electronic components	I.1

List of symbols

a_n	Normal acceleration	[m/s ²]
a_t	Tangential acceleration	[m/s ²]
$a(t)$	Acceleration function	[m/s ²]
c	Concentration	[%]
dV	Volume differential	[mm ³]
f_{app}	Applied frequency	[Hz]
f_c	Cut-off frequency	[Hz]
g_k	Reduced shear moduli	[-]
g_∞	Long-term reduced shear modulus	[-]
$g(t)$	Reduced relaxation function	[-]
$k_{i,j}$	Stiffness between node i and node j	[N/m]
$k(t)$	Reduced creep function	[-]
$[k]$	Stiffness matrix	[N/m]
l	Length of element	[mm]
l_{beam}	Length of sensitive beam	[mm]
Δl_{beam}	Difference in length of the sensitive beam	[mm]
$l_{implant}$	Implant length	[mm]
l_t	Tissue length	[mm]
$m_{agarose}$	Agarose mass	[g]
m_b	Rat brain mass	[g]
$m_{solution}$	Solution mass	[g]
r_1	Distance between COR and caudal side	[mm]
r_2	Distance between caudal side and rostral side	[mm]
t_m	Meninges thickness	[mm]
t_t	Tissue thickness	[mm]
t_h	Hydrogel thickness	[mm]
\tilde{u}_i	Displacement of node i	[mm]
$u_e(t)$	Elastic displacement	[mm]
$u_v(t)$	Viscoelastic displacement	[mm]
$\{\mathbf{u}\}$	Displacement vector of the nodes	[mm]
$\Delta u_{e,i}$	Displacement difference between time i and time i-1	[mm]

$v(t)$	Velocity function	[m/s]
w_t	Tissue width	[mm]
w_h	Hydrogel width	[mm]
x_{caud}	Maximal displacement of the caudal surface	[mm]
$x(t)$	Position function	[m]
Δx	Displacement	[mm]
Δz	Difference in height	[μ m]
$[B]$	Strain-displacement matrix	[-]
C	Capacitance	[F]
D_{FSR}	Distance between the bottom of the caudal plate and the FSR	[mm]
E	Elastic modulus	[N/mm ²]
E_0	Instant elastic modulus	[N/mm ²]
E_1	Elastic modulus in intermediate stage	[N/mm ²]
E_2	Elastic modulus in late stage	[N/mm ²]
E_b	Elastic modulus of brain	[N/mm ²]
E_m	Elastic modulus of meninges	[N/mm ²]
$[E]$	Material property matrix	[N/mm ²]
F_n	Normal force	[N]
F_t	Tangential force	[N]
F_{mot}	Motor force	[N]
\tilde{F}_i	Load at node i	[N]
$\{\mathbf{F}\}$	Load vector of the nodes	[N]
GF	Gauge factor	[-]
$G(s)$	Reduced relaxation function in Laplace domain	[-]
H	Height of caudal plate	[mm]
$K(s)$	Reduced creep function in the Laplace domain	[-]
L_1	Distance between interaural line and Lambda	[mm]
L_2	Distance between interaural line and Bregma	[mm]
L_3	Distance between rear-end of orbital plane and sagittal suture	[mm]
L_4	Height from interaural line to Lambda	[mm]
L_5	Height from interaural line to incisors	[mm]
L_{FSR}	FSR side length	[mm]

$[N]$	Shape function matrix	[-]
P_{app}	Applied pressure	[Pa]
$P_{c,HB}$	Blood pressure in caudal tube	[mmHg]
$P_{c,lin}$	Pressure at caudal side due to linear acceleration	[Pa]
$P_{c,resp}$	Pressure at caudal side due to respiration	[Pa]
P_{meas}	Measured pressure	[Pa]
$P_{r,HB}$	Blood pressure in rostral tube	[mmHg]
P_{Tot}	Total applied pressure	[Pa]
Q	Distributed pressure	[Pa/mm]
R	Resistance	[Ω]
R_1	Resistance of resistor 1	[Ω]
R_2	Resistance of resistor 2	[Ω]
R_3	Resistance of resistor 3	[Ω]
R_4	Resistance of resistor 4	[Ω]
ΔR	Difference in resistance	[Ω]
V_b	Brain volume	[mm ³]
V_{ex}	Excitation voltage	[V]
V_{in}	Input voltage	[V]
V_m	Meninges volume	[mm ³]
V_o	Output voltage	[V]
α	Angular acceleration	[rad/s ²]
β_k	Decay rate	[s ⁻¹]
$[\delta]$	Derivative matrix	[-]
ε	Strain	[μ s]
ε_0	Constant strain	[-]
$\varepsilon(t)$	Strain function	[-]
$\varepsilon_e(t)$	Elastic strain function	[-]
$\varepsilon_v(t)$	Viscoelastic strain function	[-]
θ_1	Angle 1	[°]
θ_2	Angle 2	[°]
θ_i	Time at step i	[s]
ν	Poisson's ratio	[-]

σ_0	Constant stress	[N/mm ²]
σ_e	Elastic response	[N/mm ²]
$\sigma(t)$	Stress function	[N/mm ²]
$\Delta\sigma_{e,i}$	Stress difference between time i and time i-1	[N/mm ²]
ω	Angular velocity	[rad/s]

List of abbreviations

COR	Centre of rotation
CSF	Cerebrospinal fluid
EP	Experimental period
FEM	Finite element method
FSR	Force sensitive resistor
GUI	Graphic user interface
ICP	Intracranial pressure
IMEC	Interuniversity Microelectronics Centre
IDE	Integrated development environment
JVP	Jugular venous pressure
LVEDP	Left ventricular end-diastolic pressure
LVP	Left ventricular pressure
MAP	Mean arterial pressure
NERF	NeuroElectronics Research Flanders
ONELAB	Open Numerical Engineering LABoratory
PDx	Pyramidal decussation
PEEP	Positive end-expiratory pressure
Piezo	Piezo electric pressure sensor
PmJ	Ponto-medullary junction
PP	Physiological period
PV	Deflation pressure-volume
RP	Recovery period
RV	Residual volume
TLC	Total lung capacity
VC	Vital capacity
VIB	Vlaams Instituut voor Biotechnologie

1 INTRODUCTION

This thesis starts with a short background on the use of implants in research and the consequences of implant insertion in rat brain. In this context, a general problem definition of the implant insertion, with possible adverse consequences, is provided. Next, the goal of this thesis is determined and all research questions are explained. Finally, the different steps taken are described in the methodology.

1.1 Background

Brain diseases count for approximately 35% of all diseases (NERF, 2021). NeuroElectronics Research Flanders (NERF) is an academic research initiative, empowered by Interuniversity Microelectronics Centre (IMEC), KU Leuven and the Flemish Institute of Biotechnology (VIB). It is among other active in the development of neurobiological technologies. Diagnostic equipment is a substantial requirement to monitor brain activity in studies on for instance Parkinson's disease or Alzheimer's disease. Animal models are irreplaceable in these studies. Figure 1-1 shows a rat with a hyperdrive attached to its skull, containing neural probes to monitor brain activity.



Figure 1-1 Rat with attached hyperdrive (van Daal, et al., 2020)

The investigation of fundamental mechanisms on the operation of the brain, including the representation, storing and processing of information, requires reliable monitoring of neural activity, for instance by implanted neural electrodes. However, up to now long term performances of implanted neural electrodes have limited success. Microhaemorrhages, also known as microbleedings, inflammations and vascular damages are some of the possible consequences of the implantation. Figure 1-2 shows a section from a rat brain where the track of an implanted probe and corresponding electrolytic lesion, or tissue damage, is visible. Although the rat is not adversely affected by the implantation, tissue damage is detrimental to the measurements.

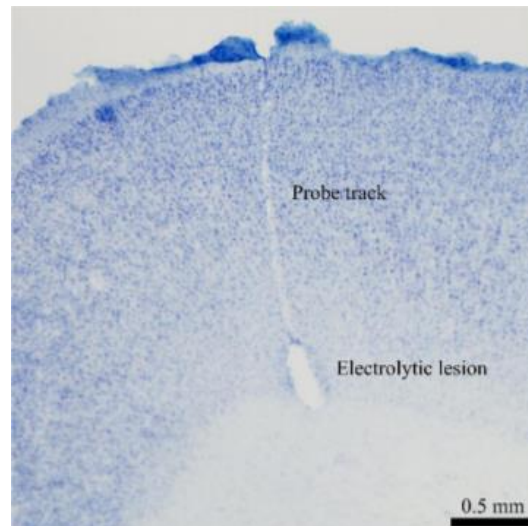


Figure 1-2 Coronal section of a rat brain with visible probe track and electrolytic lesion (van Daal, et al., 2020)

A significant group in the classification of failure modes occurring in inserted implants consists of design errors, leading to mechanical mismatches and lack of biocompatibility. The mechanical mismatches are related to pressure interactions, stretch and strain phenomena, whereas the biocompatibility is influenced by surface material properties, electrochemical reactions, photochemical reactions and thermal effects (Delbeke, Haesler, & Prodanov, 2020).

Hence, the biocompatibility of neural implants is a limiting factor in the long-term viability of implants in brain tissue. A good understanding of implant failures is required to ultimately obtain a long-term monitoring electrode. Up to now, there is only limited knowledge about the mechanical behaviour of neural implants in brain tissue. Figure 1-3 shows a schematic drawing of an implant in brain tissue with some mechanical interactions like compression and shear. The validation of computer simulations is one of the most significant limitations in the search for mechanical interactions of implants because of a lack of knowledge regarding the mechanical properties (Antona-Makoshi, Eliasson, Davidsson, Ejima, & Ono, 2015). Hence, a good knowledge of the interactions between brain tissue and implants is substantial for further research.

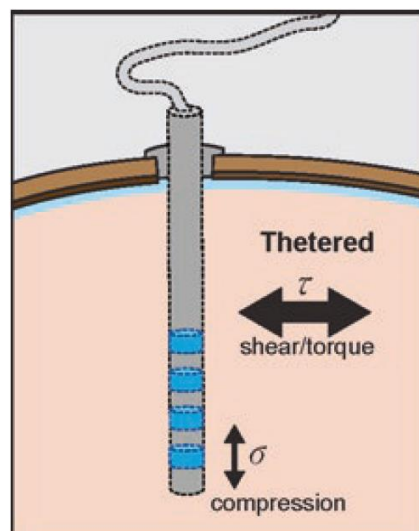


Figure 1-3 Schematic drawing with mechanical interactions of the implant and brain tissue (Delbeke, Haesler, & Prodanov, 2020)

1.2 Goal of the thesis

The main goal of this thesis is the development and validation of an estimation technique to determine the micromotion of an implanted electrode in rat brain tissue during normal animal behaviour. As a result, a flexible and simplified, yet accurate, finite element method (FEM) model of a rat brain tissue with an implanted electrode must be obtained. Additionally, this model is preferably verified using existing literature data. As a proof of concept, an appropriate set-up is designed in accordance with the boundary and mechanical load conditions of the FEM model. The FEM model should be validated by conducting an experiment in which the displacement of the implant is measured. The acquired data have to be analysed and the experiment observations are to be discussed.

Hence, the goal of this thesis is to answer the following research questions:

- How can a FEM model be developed, mimicking the viscoelastic brain tissue and the implant?
- How do the results of the FEM model relate to existing data of implant displacements? Which physiological or normal animal behaviour factors influence the implant-tissue interface?
- How can an implant be emulated in an experiment set-up? How can its displacement be measured?
- How do the experiment measurements relate to the results of the FEM analysis?
- How does the experiment differ from the FEM model? Which adaptations have to be made to model the experiment?
- Which improvements are necessary in further research based on this proof of concept?

1.3 Methodology

First, a literature study is carried out in Chapter 2. This research aims at collecting information regarding the physiology and the behaviour of rats. The most attention is paid to the properties of rat brains and the forces acting on it. Additionally, a brief summary of the state of the art of implants is given. The literature study ends with a discussion of existing rat brain FEM models.

A description of the developed FEM models is given in Chapter 3. It includes a discussion on the mathematical model used to calculate implant and tissue displacements. In addition, three different models are presented. The first model is the multiple loads model, which includes loads due to linear acceleration, head rotation, static intracranial pressure and respiration. The second model is the heartbeat model, mimicking the influence of the heartbeat by the blood pressure in mimicked blood vessels. The last model is the respiration model, which mimics the respiration pressure on tissue inside the skull.

In Chapter 4, the models are tested on accuracy and viscoelasticity by conducting a convergence and viscoelastic analysis. Furthermore, the results of the three models are presented and the simulated implant displacements are verified based on available research data. Finally, the most interesting model is chosen to validate.

Before conducting experiments, an experiment set-up has to be defined and prepared. All details of this set-up are described in Chapter 5. All different mechanical and electrical components are introduced including a custom micromotion sensor. The behaviour of this sensor and its impact on the tissue and implant displacements are investigated by adapting the previously obtained FEM models by adding the sensor. In this way, two new models are obtained: one model mimicking the heartbeat and one model mimicking the respiration. The selection of a tissue mimicking the gel is also discussed in this chapter.

A discussion of the experiment follows in Chapter 6 in which the experiment protocol is described as well as the tissue mimicking gel preparation and calibration of used sensors. Furthermore, the electrical and mechanical connections are discussed, followed by an explanation of the implant insertion process. Finally, the measurements themselves deserve to be discussed.

The measurement data are analysed in Chapter 7, followed by a description of the differences between the respiration FEM model and the experiment. Based on the observations during the experiment, other constraints are defined in the previous respiration FEM model. Hence, a sixth model is defined as the experiment FEM model. This model does not mimic the influence of respiration on the implant displacement but mimics the physical interactions during the experiment. Some proposals are made for further experiment set-up iterations based on the observations and the values obtained by the FEM models, the measurements and the available data.

Finally, a general conclusion of this thesis is presented in Chapter 8, in which all research questions are answered and the final result is discussed.

2 LITERATURE STUDY

To fully grasp what happens on a mechanical level between the implant and the rat brain tissue, it is necessary to know the basics of the physiology of rats. A basic understanding of normal rat behaviour with regard to movement is also important to estimate forces. As far as the implant is concerned, a short introduction is given into the topic as well as on the attachment of the implant to the skull using a hyperdrive. Finally, a literature review on earlier FEM models of the interaction between implant and brain tissue is discussed.

2.1 Physiology and behaviour of rats

Physiology determines a number of boundary conditions or properties that must be taken into account during the development of the estimation technique. More specifically, the anatomy and the viscoelastic properties of rat brain tissue are determining factors. The different pressures in the body that influence the movement of the implant, also deserve to be discussed. Static intracranial pressure, heart rate and respiration all result in pressures applied onto the rat brain tissue. Not only the physiology, but also the behaviour of the rat determines which forces and pressures are applied to the brain. In normal rodent movement, two different motions can be distinguished: linear acceleration and head rotation.

2.1.1 Anatomical planes and directions

The anatomy of the body is described with reference to three orthogonal planes along three principal directions. Figure 2-1 shows the different anatomical planes of the rat body: the *transverse plane*, the *frontal* or *coronal plane* and the *sagittal plane*. The anatomical directions are also indicated. *Proximal-distal* refers to respectively closer to and further away from the heart, *dorsal-ventral* are the respective directions to the back and the abdomen, *rostral-caudal* are the directions towards the nose and towards the tail. *Anterior-posterior* are respectively the directions towards the front and the back, *lateral* is the direction towards the sides and *superior-inferior* are the directions up and down.

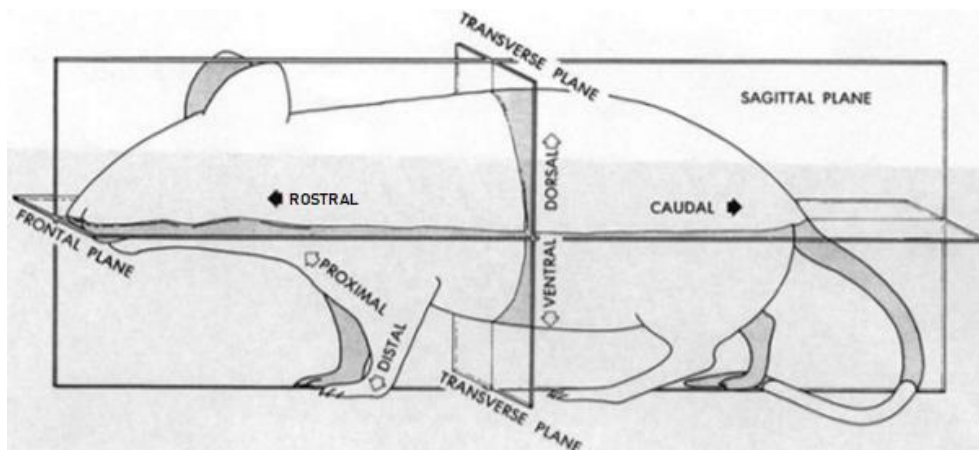


Figure 2-1 Anatomical planes and directions (Andersen & Tufik, 2016)

2.1.2 The rat brain

Like the human brain, the rat brain is a complex heterogeneous organ. Basic knowledge of the anatomy of the brain and its different structures and dimensions is essential to create a performant FEM model. A literature research on the elastic and viscoelastic properties of the brain is also necessary because these properties are used in the mathematical model in the FEM analysis.

2.1.2.1 Anatomy

The head of a rat consists of different layers: the scalp, the bone of the skull, the dura mater, the subarachnoid space and the brain tissue. Figure 2-2 shows an electrode insertion in a brain slice of a rat. The brain slice consists of the aforementioned different layers and their respective thickness (Hamilton, 1982):

- *Scalp*, outer soft skin that covers the skull.
- *Periosteum*, fibrous membrane that covers the bone of the skull, inside are periosteal arteries, which supply the bone with rich blood.
- *Bone of skull*, flat bone that protects the brain.
- *Dura mater*, thick membrane, which is the outer layer of the meninges and is responsible for supplying blood, draining blood and cerebrospinal fluid, etc.
- *Arachnoid mater*, middle layer of the meninges, which keeps the cerebrospinal fluid in the subarachnoid space.
- *Subarachnoid space*, space filled with cerebrospinal fluid, which protects the brain from shocks and vibrations.
- *Pia mater*, thin inner layer of the meninges through which vessels run, which supply the brain with blood.
- *Brain*, consists of three large parts: the cerebrum, the cerebellum and the truncus cerebri, also known as the brain stem.

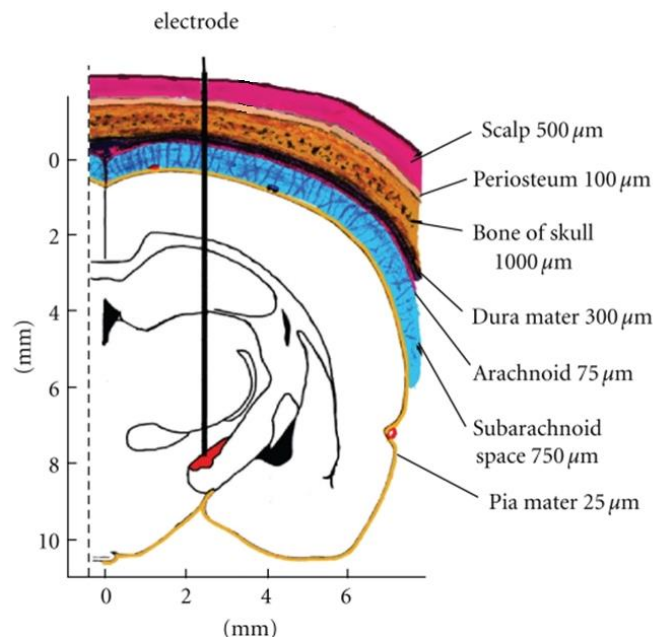


Figure 2-2 Electrode insertion in a brain slice of a rat, electrode penetrates several layers with different mechanical properties: scalp, bone of skull, dura mater, subarachnoid space and brain tissue (Nowak, et al., 2011)

The skull contains and protects the brain, which fits very well in the cranial cavity. Therefore, a direct link between the geometry of the skull and the geometry of the brain can be made. Based on craniometric measurements, the geometry of the brain can be estimated. Figure 2-3 shows a merged image of a dorsal and a sagittal view of a Wistar rat skull and brain (Yang, et al., 2018). Bregma and Lambda are two points where the sagittal suture, indicated by '2', meets with respectively the coronal suture and the lambdoid suture. Sutures are fibrous tissue joints that connect the different bones of the skull with each other. The interaural line is the line between the midpoints of the external auditory meatus of the ears of the rat (University of Washington, 2021).

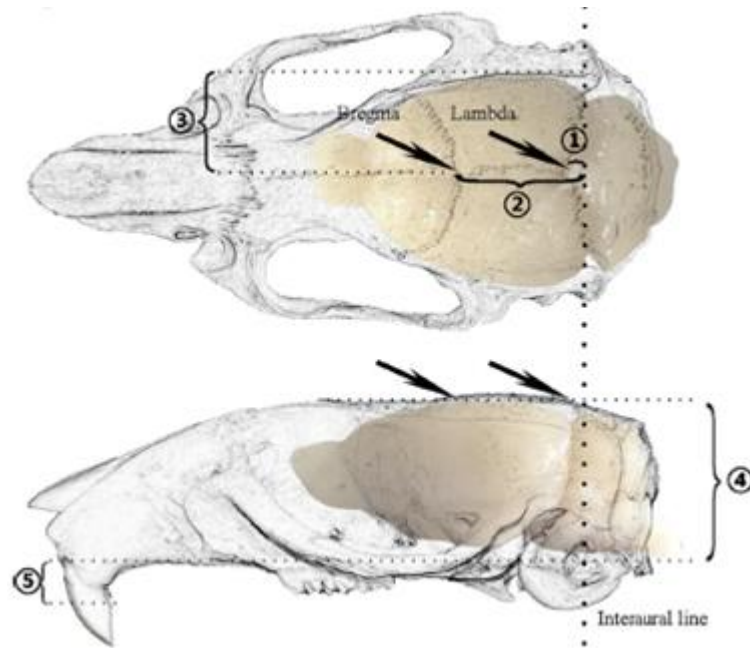


Figure 2-3 Merged image of real skull and its corresponding brain to introduce the craniometric data including distance 1 to 5 in dorsal and sagittal views (Yang, et al., 2018)

Table 2-1 lists the different distances indicated in Figure 2-3 based on measurements on four male Wistar and four male Sprague-Dawley rats aged ten weeks. Figure 2-4 shows that a rat reaches the adult age at ten weeks (Sengupta, 2013). L_1 and L_2 are the distances between the interaural line and respectively Lambda and Bregma. L_3 is the distance between the rear-end of the orbital plane and the sagittal suture. L_4 is the height from the interaural line to Lambda. L_5 is the height from the interaural line to the incisors.

Table 2-1 Craniometric measurements of rats aged ten weeks, mean \pm standard deviation (Yang, et al., 2018)

Strain	Body weight (grams)	L_1 (mm)	L_2 (mm)	L_3 (mm)	L_4 (mm)	L_5 (mm)
Wistar	358,75 \pm 5,06	0,860 \pm 0,416	10,315 \pm 0,767	8,370 \pm 0,163	10,285 \pm 0,019	-4,445 \pm 0,140
Sprague-Dawley	409,50 \pm 11,09	1,050 \pm 0,513	9,475 \pm 0,465	8,4125 \pm 0,115	10,605 \pm 1,001	-3,430 \pm 0,465

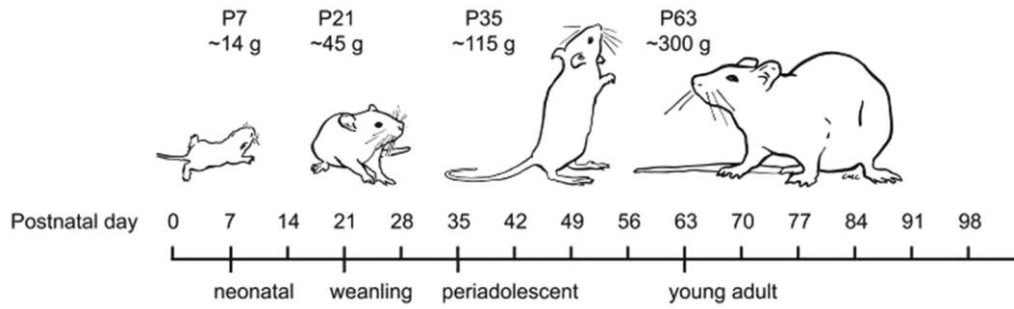


Figure 2-4 Correlation of body weight with different phases of postnatal days (Sengupta, 2013)

Aside from craniometry, a direct measurement of the brain dimensions is also possible. In Table 2-2 the length, width and thickness are listed based on measurements of eleven rats aged 90 days. The lateral brain width corresponds with approximately two times L_3 . The superior-inferior brain thickness corresponds with approximately L_4 .

Table 2-2 Brain dimensions, mean \pm standard deviation (Gefen, Gefen, Zhu, Raghupathi, & Margulies, 2003)

Anterior-posterior brain length (mm)	Lateral brain width (mm)	Superior-inferior brain thickness (mm)
20,70 \pm 0,61	15,50 \pm 1,17	9,34 \pm 0,93

2.1.2.2 Elastic properties

Because the rat brain tissue is heterogeneous and viscoelastic, it is difficult to find apparent elastic properties. On one hand, the tissue consists of multiple complex structures with different material properties. On the other hand, the tissue is viscoelastic, which means that it exhibits both viscous and elastic behaviour. Although these two limitations are valid, the rat brain tissue can be modelled as an elastic homogeneous material. Therefore, elastic material properties need to be available.

The apparent elastic modulus can be calculated by an indentation test in which living rat brain is indented. An indenter is attached to a motorised platform, which puts force on the dorsal surface of the cerebrum. Stepwise force can thus be applied, while the indentation depth can be measured. In 14 male Sprague-Dawley rats, weighing 350-370 grams, an indentation test resulted in $E = 31 \pm 2$ kPa, mean \pm standard deviation (Shulyakov, Fernando, Cenkowski, & Bigio, 2009).

The apparent elastic modulus can also be estimated by conducting a compression test. This kind of test procedure is done more often on the human brain than on the rat brain. Cylindrical samples of human cerebrum are compressed at different strain rates while also measuring the force. The applied strains and measured forces can be used to calculate the apparent elastic moduli. Table 2-3 shows three different apparent elastic moduli based on ten samples for each strain rate. E_0 is the instant elastic modulus, E_1 and E_2 are the elastic moduli in the intermediate and later stages of testing (Rashid, Destrade, & Gilchrist, 2012).

Table 2-3 Apparent elastic moduli E_0 , E_1 and E_2 , of brain tissue at each strain rate, mean \pm standard deviation (Rashid, Destrade, & Gilchrist, 2012)

Strain rate (1/s)	E_0 (kPa)	E_1 (kPa)	E_2 (kPa)
30	$19,0 \pm 0,4$	$28,6 \pm 1,3$	$40,5 \pm 1,9$
60	$28,2 \pm 0,8$	$48,5 \pm 1,9$	$52,0 \pm 3,1$
90	$37,9 \pm 0,8$	$56,9 \pm 1,2$	$65,2 \pm 1,4$

The aforementioned values of the elastic moduli are determined for the cerebrum. As indicated in 2.1.2.1, the brain is surrounded by different layers. Previous traumatic brain injury studies discussing FEM models used elastic moduli for a combination of layers. In a first model the elastic modulus and the Poisson's ratio are mentioned for the meninges: 20 MPa and 0,45 (Mao, Zhang, Yang, & King, 2006). In a second model the elastic modulus and Poisson's ratio are mentioned for respectively the dura mater (31,5 MPa and 0,45) and the pia-arachnoid mater (12,5 MPa and 0,45) (Baumgartner, Lamy, & Willinger, 2009).

2.1.2.3 Viscoelastic properties

As mentioned in 2.1.2.2, brain tissue is viscoelastic. A viscoelastic material's deformation under load and recovery from deformation are both time dependent. Therefore, viscoelastic materials are characterised by creep and relaxation, respectively changes in strain over time under constant stress and changes in stress over time under constant strain (Holzapfel & Ogden, 2006). During a stress relaxation test, the relaxation modulus $g(t)$ can be defined as the responding stress $\sigma(t)$ divided by the constant strain ε_0 :

$$g(t) = \frac{\sigma(t)}{\varepsilon_0} \quad (2-1)$$

Similarly, the creep compliance $k(t)$ can be derived during a creep test dividing the responding strain $\varepsilon(t)$ by the constant stress σ_0 :

$$k(t) = \frac{\varepsilon(t)}{\sigma_0} \quad (2-2)$$

The reduced relaxation function consists of a Prony series:

$$g(t) = g_\infty + \sum_{k=0}^N g_k e^{-\beta_k t} \quad g(0) = 1 \quad (2-3)$$

with:

- g_∞ , long-term reduced shear modulus
- g_k , reduced shear moduli
- β_k , decay rate (s^{-1})

This function allows experimental parameter estimation. Indentation experiments can be set up to test the mechanical behaviour of the brain tissue. Afterwards, the parameters of the relaxation function are estimated by comparing the measurement data with a curve fit based on the relaxation function. A first research used eleven Sprague-Dawley rats weighing 300-400 grams. Their brain was removed from the body and indented at two places: the pyramidal decussation (PDx) and the ponto-medullary junction (PmJ), both indicated on Figure 2-5. A flat indenter with 1,56 mm diameter was used 1 hour post-mortem to press down the tissue with approximately 1-2 mm. The displacement of the indenter and the force were both measured. Based on these measurements the reduced shear moduli and decay rates could be estimated.

Table 2-4 shows the resulting values for these material properties. The Poisson's ratio is estimated to be 0,49 (Shafieian, Darvish, & Stone, 2009).

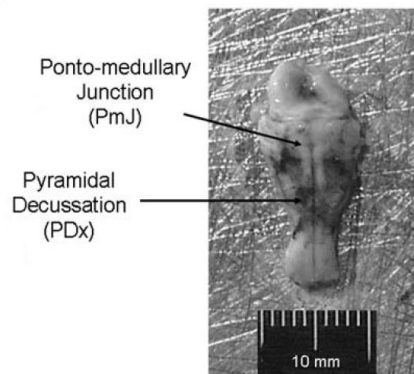


Figure 2-5 Ponto-medullary junction (PmJ) and pyramidal decussation (PDx) of the rat brain (Shafieian, Darvish, & Stone, 2009)

Table 2-4 Material parameters for reduced relaxation function at PmJ and PDx, mean \pm 95 % confidence interval (Shafieian, Darvish, & Stone, 2009)

Material parameter	PmJ	PDx
g_{∞}	0,000 \pm 0,236	0,141 \pm 0,117
g_1	0,324 \pm 0,303	0,145 \pm 0,160
g_2	0,167 \pm 0,112	0,243 \pm 0,063
g_3	0,506 \pm 0,062	0,471 \pm 0,029
β_1 (s ⁻¹)	0,352 \pm 0,139	0,386 \pm 0,155
β_2 (s ⁻¹)	6,060 \pm 2,966	4,483 \pm 1,553
β_3 (s ⁻¹)	65,461 \pm 29,676	57,875 \pm 27,569
R^2	0,933	0,991

2.1.3 Intracranial pressure

The intracranial pressure (ICP) is the pressure exerted on the rat brain tissue in the subarachnoid space by the cerebrospinal fluid (CSF). In order to measure the intracranial pressure, a telemetric device can be implanted in a rat. This was executed on fourteen female Sprague-Dawley rats weighing 240-310 grams. Figure 2-6 shows the ICP over different periods after surgery: the recovery period (RP), the physiological period (PP) and the experimental period (EP). The total measuring time was 50 days. The mean values are indicated for all three periods (Eftekari, Westgate, Johansen, Bruun, & Jensen, 2012).

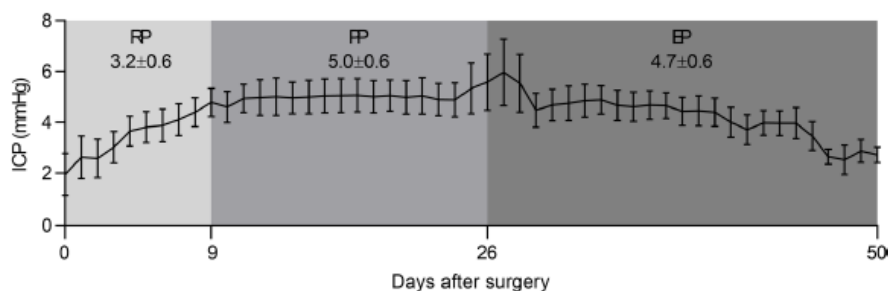


Figure 2-6 Intracranial pressure during 50 days after surgery, mean \pm standard deviation (Eftekari, Westgate, Johansen, Bruun, & Jensen, 2012)

Another indentation test based on the same principle proves that the ICP is different for six male Sprague-Dawley rats weighing 350-370 grams. A telemetric pressure transmitter was placed in the cisterna magna of three rats and in the lumbar subarachnoid space of three other rats. Both the cisterna magna and the lumbar subarachnoid space are in the subarachnoid space and therefore the pressure exerted by the CSF is measured. The pressures measured at these two locations were respectively 10 ± 3 mmHg and 9 ± 3 mmHg, mean \pm standard deviation (Shulyakov, Fernando, Cenkowski, & Bigio, 2009).

2.1.4 Heart rate and blood pressure

A first factor related to the heartbeat is its frequency represented by the heart rate in beats/min. The heart rate reported for ten male Wistar rats is $386,1 \pm 8,6$ beats/min, mean \pm standard deviation (Naessens, Vos, VanBavel, & Bakker, 2018). These rats, aged 42 weeks, are pre-adolescent. For the *rattus norvegicus*, the heart rate is reported 260-400 beats/min (Sengupta, 2013).

A second factor related to the heartbeat is the blood pressure. While the heart is pumping the blood through the body, the pressure also varies in time. The pressure in the arteries and the left ventricle, pumping the rich blood from the heart to the body, can be described as the mean arterial pressure (MAP), the left ventricular pressure (LVP) and the left ventricular end-diastolic pressure (LVEDP). The LVP and the LVEDP are respectively the systolic and diastolic pressure in the left ventricle of the heart. The MAP is the average blood pressure in the arteries.

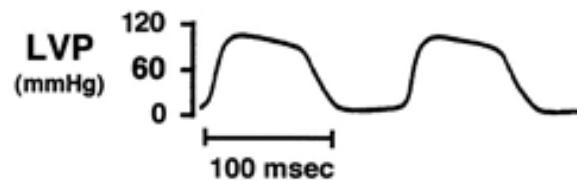


Figure 2-7 LVP in function of time (Kobayashi, et al., 1996)

Figure 2-7 shows a time-varying pressure signal, the peak value corresponding with LVP and the lowest value corresponding with LVEDP. The arterial pressure is similar to the left ventricular pressure, with the same peak value but the diastolic pressure is higher than the LVEDP. When MAP and LVP are established, the diastolic arterial pressure can be calculated. Table 2-5 shows the median, minimum and maximum weight and pressures for six adult male Sprague-Dawley rats.

Table 2-5 Weight and pressures measured for six male Sprague-Dawley rats median [minimum; maximum] (Cops, et al., 2018)

Weight (grams)	524 [455;790]
MAP (mmHg)	68,3 [65,4;71,1]
LVP (mmHg)	99,4 [93,9;111,9]
LVEDP (mmHg)	16,5 [8,4;27,4]

In addition to the pressure in the artery and the left ventricle, the pressure in the jugular veins is also important. The jugular veins are the veins through which deoxygenated blood flows back to the heart. The jugular venous pressure (JVP) is measured for the same six Sprague-Dawley rats. Figure 2-8 indicates the JVP for each individual rat.

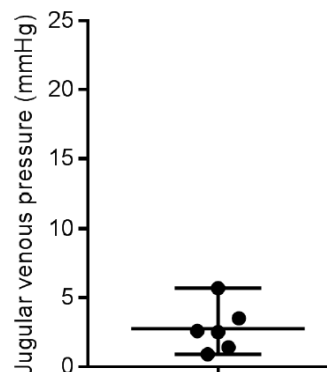


Figure 2-8 Jugular venous pressure measured for six male Sprague-Dawley rats (Cops, et al., 2018)

2.1.5 Respiration

The respirational rate of *rattus norvegicus* varies from 75 to 115 breaths/min (Sengupta, 2013). The respirational rate of anesthetized Wistar rats of 250-350 grams is 90 breaths/min (Camilo, et al., 2018). Seven week old Sprague-Dawley rats breathe at a rate varying from 132 ± 7 breaths/min to 152 ± 6 breaths/min (Mautz & Bufalino, 1989).

The total lung capacity (TLC) of a rat varies according to strain, age and condition and is usually determined between 8 and 18 cm³ (Schulz & Muhle, 2000). The difference between the TLC and the residual volume (RV) represents the gas volume expelled from the lungs and is called the vital capacity (VC). The VC achieves values of around 75-90 % of the TLC (Schulz & Muhle, 2000).

Figure 2-9 shows a deflation pressure-volume (PV) curve of the lungs from anesthetized Sprague-Dawley rats. P_L indicates the PV curve of the lungs, P_{es} the PV curve of the chest wall and P_{ao} the PV curve of the total respiratory system. The volume of 75-90 % TLC corresponds roughly with a lung pressure of 8 cm H₂O to 15 cmH₂O, the equivalent of 6 mmHg to 11 mmHg or a pressure of approximately 780 Pa to 1470 Pa.

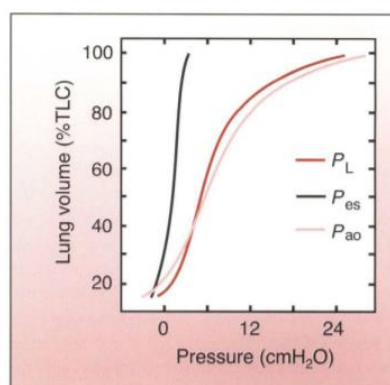


Figure 2-9 Deflation pressure-volume curve of the lungs of anesthetized Sprague-Dawley rats (Schulz & Muhle, 2000)

Figure 2-10 displays the timeline of an experimental protocol determining effects of recruitment manoeuvres and positive end-expiratory pressure (PEEP) throughout surgery on anesthetized Wistar rats (250-350 grams). The recruitment manoeuvre is a manoeuvre of increasing the transpulmonary pressure to open up collapsed alveoli (Nickson, 2020). The obtained respiratory airway pressure throughout the protocol reaches values of 10 cmH₂O or 980 Pa.

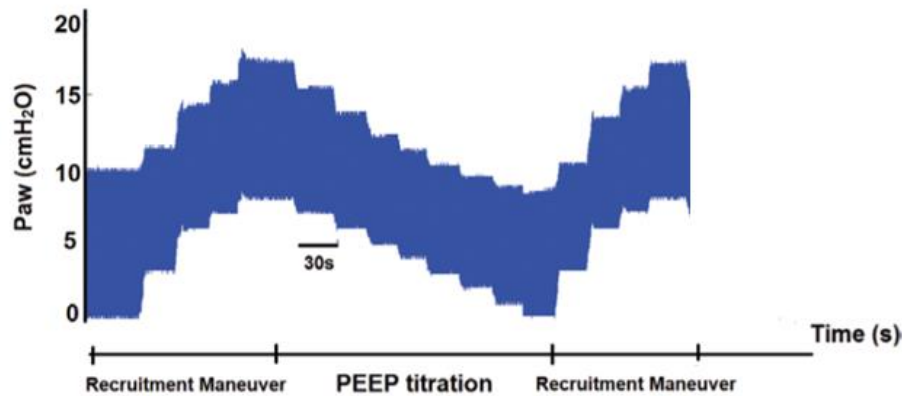


Figure 2-10 Timeline of an experimental protocol to determine effects of recruitment manoeuvres and PEEP (Camilo, et al., 2018)

2.1.6 Linear acceleration

When a rat runs with a velocity between 50 and 100 cm/s, its head oscillates vertically with a frequency of 6-12 Hz. Moreover, the head oscillations are an increasing function of the running velocity (Ledberg & Robbe, 2011).

Inertial forces cause the brain to move relatively to the skull. The brain mass of a Sprague-Dawley rat weighting 400 grams is estimated to be 2,3 grams (Zhou, Li, Cavanaugh, & Zhang, 2020). Acceleration and deceleration of this mass at normal behaviour are resulting from inertial forces and thus a pressure is exerted on the contact area of the brain. An acoustic startle experiment, as shown in Figure 2-11, with an accelerometer attached to the skull of a rat, shows that the rat reaches a linear acceleration in the rostral direction of $3,33 \pm 1,37$ g, or $32,67 \pm 13,44$ m/s² due to the startle reaction (Pasquet, et al., 2016). Hence, the force needed to accelerate the rat and its brain is calculated as the product of the brain mass and the linear acceleration and equals approximately 0,075 N.

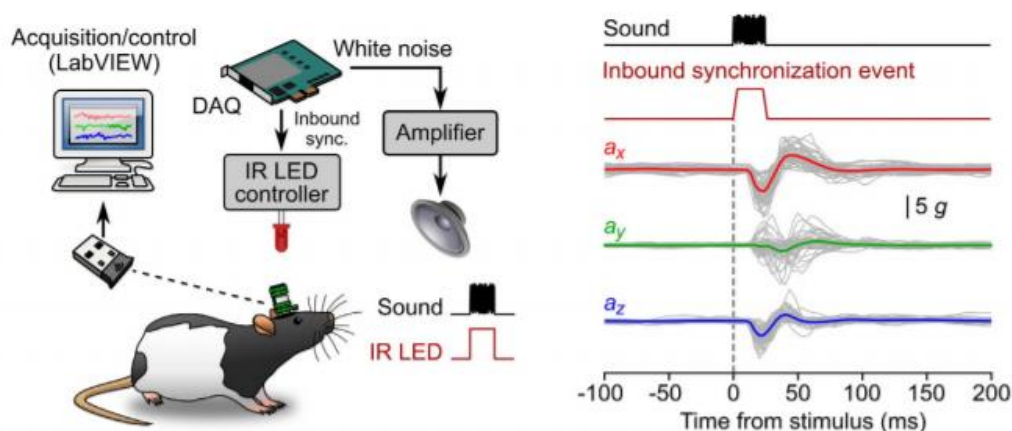


Figure 2-11 Schematic of an acoustic startle experiment and the startle responses (Pasquet, et al., 2016)

The assumption that the force is equally distributed on the caudal surface area of the brain indicates a pressure at the caudal side of the rat brain. The geometrical values of the brain of a 409,50 gram Sprague-Dawley rat from Table 2-1 are used to estimate the contact surface area, which is simplified as a rectangle, in order to calculate the pressure:

$$P_{c,lin} = \frac{F_{inertia,lin}}{A_c} = \frac{0,075 \text{ N}}{2 \cdot L_3 \cdot L_4} = \frac{0,075 \text{ N}}{2 \cdot 8,41 \text{ mm} \cdot 10,61 \text{ mm}} = 420,3 \text{ Pa} \quad (2-4)$$

with:

- $P_{c,lin}$, the pressure at the caudal side due to linear motion
- $F_{inertia,lin}$, the inertial force due to head shake in case of linear motion
- A_c , the area of the surface at the caudal side
- L_3 , the distance according to Table 2-1
- L_4 , the distance according to Table 2-1

2.1.7 Head rotation

The angular velocity and the time span indicate an average angular acceleration at which a rat turns its head. Figure 2-12 shows an angular head velocity curve in function of the elapsed time. A simplified estimation of a constant angular acceleration α leads to a value of approximately 500 °/s² or 8,7 rad/s². This value follows from the derivation of the angular velocity ω that ranges from 0 °/s to 150 °/s between -300 ms and 0 ms.

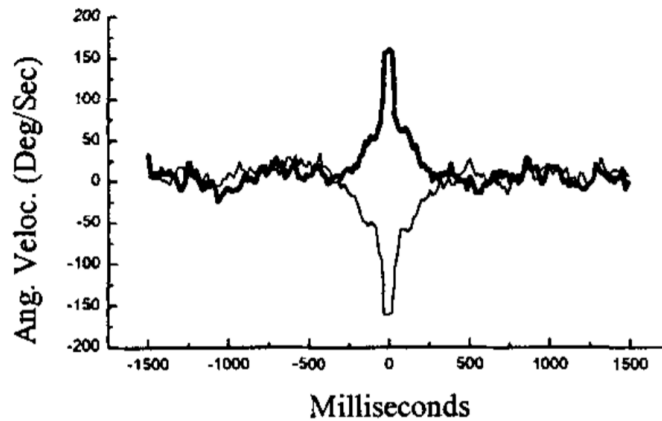


Figure 2-12 The angular head velocity for a low-velocity turn (Sharp, Tinkelman, & Cho, 2001)

2.2 Implanted electrodes

A basic knowledge of the implanted electrodes attached on probes, is necessary for the development of the model. The probes are often custom made for a specific application. Therefore, it is not possible to give a total overview of different probes used in neuroengineering. However, a short discussion of different trends offers the necessary insights. Furthermore, the probes are often attached to a hyperdrive, which in turn is attached to the skull, as shown in Figure 1-1.

2.2.1 Probes

Probes are designed to measure electrical signals in different parts of the brain tissue. Therefore, they are made out of conducting materials like silicon, tungsten and platinum (Delbeke, Haesler, & Prodanov, 2020). A first composition of electrodes consists of four electrodes turned around each other, the so-called tetrode. The diameter of such a tetrode depends on the diameters of the single silicon wires. The total diameter of such a tetrode ranges between approximately 30 μm to 80 μm . This range is however not fixed, moreover it is also possible to produce the wires out of a different material, like tungsten for example (Battaglia, et al., 2009).

A second composition consists of electrodes attached to polymer probes. These probes are often made of parylene-C or polyimide, both polymers with lower elastic moduli than silicon and tungsten. Polymers are used to reduce the mismatch between the elastic moduli of the brain tissue and the implant. Platinum is sputtered on the probe to form the electrodes and connections. This can be done in different possible configurations. Figure 2-13 shows four different probe configurations: 1x16, 2x8, 3x5+1 and 4x4 with their respective dimensions. The total thickness of the probes is 15,6 μm (van Daal, et al., 2020).

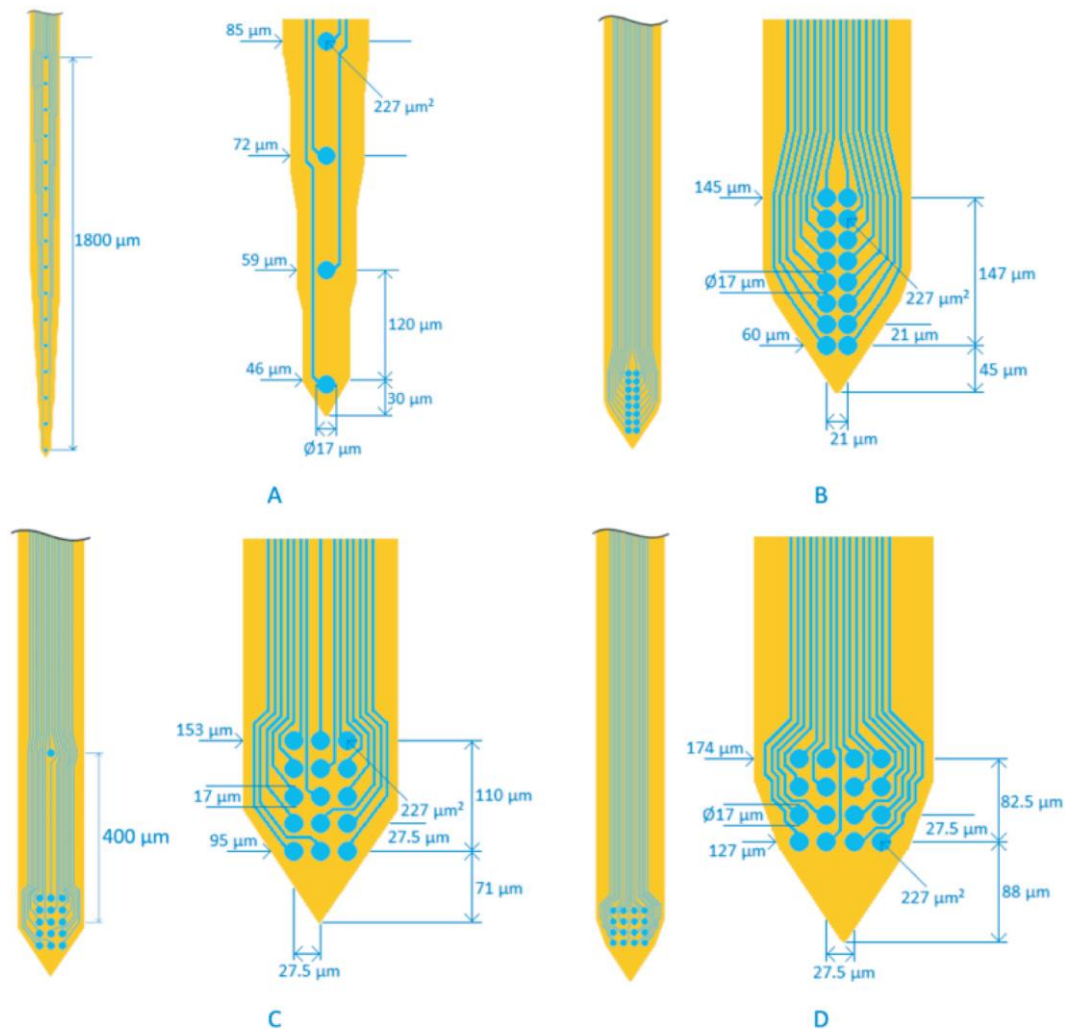


Figure 2-13 Probe configurations: A: 1x16 B: 2x8 C: 3x5+1 D: 4x4 (van Daal, et al., 2020)

2.2.2 Hyperdrive

Both tetrodes and polymer probes can be lowered into the tissue using a microdrive (Battaglia, et al., 2009) (van Daal, et al., 2020). Figure 2-14 shows two microdrive designs based on the same principle. By rotating the screw it is possible to lower the guiding tube in which the probe is attached. In the left side design the drive screw moves also linearly, whereas in the right-hand side design, where a shuttle moves the probe, it remains stationary (van Daal, et al., 2020). One turn of such a drive screw can result in a linear motion of the probe equal to 250 μm (Battaglia, et al., 2009). The probes are not immediately lowered at one moment but this can be done by rotating the screw drive at several consecutive days.

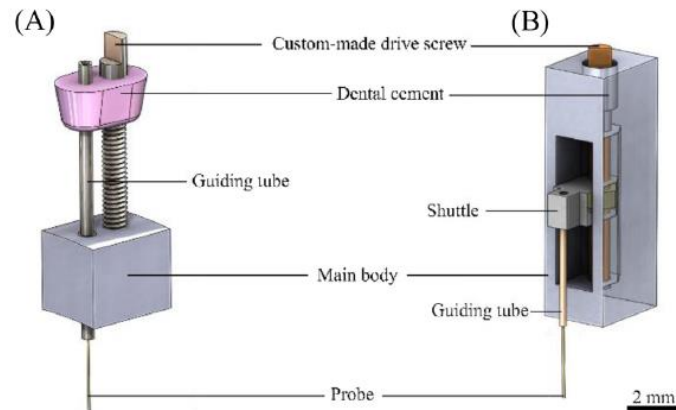


Figure 2-14 Microdrive designs (van Daal, et al., 2020)

The main body of the microdrive needs to be attached to the rat's skull. Therefore, hyperdrives are designed in which the microdrives can be arranged. These conical hyperdrives, often 3D-printed, are attached to the skull with special skull attachment flanges, dental cement and screws. Figure 2-15 shows such a hyperdrive indicating all different elements of the hyperdrive at the top of the figure. An electronic interface is also embedded in the conical design, which is protected by a removable cap. Typical of this design is the arrangement of 16 different shuttle based microdrives. Note that the drive screw heads are reachable from the outside of the cone. Finally, the probes exit the hyperdrive via an exit tip. To ensure passage through the skull, a hole of approximately 1 mm is drilled in the skull (van Daal, et al., 2020).

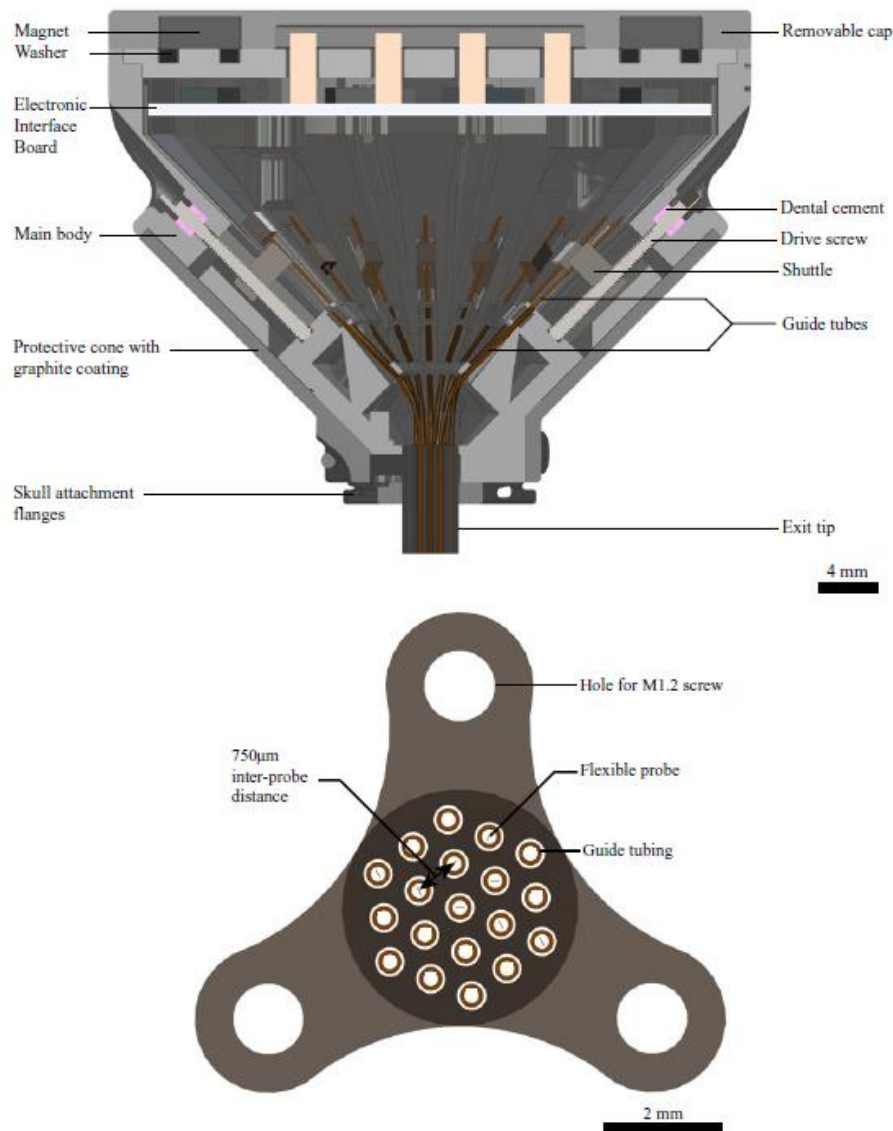


Figure 2-15 Hyperdrive cross-section at the left and bottom view of exit tip at the right (van Daal, et al., 2020)

2.3 Rat brain finite element models

State-of-the-art research (Antona-Makoshi, Eliasson, Davidsson, Ejima, & Ono, 2015) indicates that the lack of knowledge about mechanical properties is a significant limitation in the use of FEM modelling. Antona-Makoshi et al. have studied possible effects of age-related intracranial changes under rotational head traumas of rats with the aim of investigating head traumas due to traffic-related injuries. In their research, a lack of rotational trauma experimental data of old rats limited the validation of the developed FEM model. However, the validation of FEM models is important in order to develop reliable models that can then be modified and parametrised. The parametrisation of FEM models and the scaling of animal experimental data allows researchers to estimate similar effects in both animal brain tissue and human brain tissue (Antona-Makoshi, Eliasson, Davidsson, Ejima, & Ono, 2015). For this reason FEM models are only valuable when the results can be validated with relevant experimental data.

Baumgartner et al. also investigated traumatic brain injury mechanisms in rat brain resulting in the same conclusions. The combination of numerical modelling and animal experimental testing is viable to understand traumatic brain injuries. Accurate FEM models are thus a powerful tool in accident reconstructions (Baumgartner, Lamy, & Willinger, 2009). Baumgartner et al. obtained an accurate FEM model by including the cerebrum, the cerebellum, the brainstem, the brain-skull interface and the skull. In addition, they assumed the skull and the brain-skull interface to be linear elastic, isotropic and homogeneous. The other anatomical parts were assumed to behave viscoelastic, isotropic and homogeneous. One of their results emphasises the importance of the brain-skull interface in the FEM model since the dynamic response of the brain is significantly influenced by this (Baumgartner, Lamy, & Willinger, 2009).

Other studies investigate the interface between brain tissue and neural probes. One of the most important concerns regarding the recording and the stimulation of neural electrodes relates to the interfacial strain around the implant site. Subbaroyan et al. developed a quarter-symmetry FEM model of the brain tissue along with an implanted electrode in order to investigate the tethering forces. This model was assumed to be elastic. Time-dependent viscous properties were neglected because the strain rates from the simulations fell into the instantaneous elastic region (Subbaroyan, Martin, & Kipke, 2005). Three implant material candidates were formulated: silicon, polyimide and a hypothetical soft material. Results showed that a probe made of softer materials than silicon, such as polyimide, can reduce interfacial strains by 65% to 94%, thus indicating the relevance of adequate probing materials (Subbaroyan, Martin, & Kipke, 2005).

Polanco et al. also assessed the interface between the brain tissue and neural probes. Their study focuses on the transient behaviour of neural probes in viscoelastic brain tissue. Transient motions with a frequency varying from 1 Hz to 40 Hz were applied on the model in order to mimic the behaviour of a rat brain responding to vascular pulsation, respiration and walking. Results showed that a soft probe exhibits high stresses levels at low frequencies compared to high frequencies as a result of converting kinetic energy of the head to strain energy in the probe (Polanco, Bawab, & Yoon, 2016).

As a conclusion from the findings of the abovementioned studies, further research in the investigation of mechanical interactions of the brain tissue should emphasise the following:

- The validation of FEM models with experimental data is crucial in the search of reliable techniques for FEM modelling.
- The assessment of mechanical and material properties is important in the development of FEM models within a certain field of application.
- The effects at implant-brain tissue interfaces are significant in the search of suitable candidates for neural probing.
- Furthermore, a good knowledge on mechanical interactions exerted on the brain tissue is a key element in the success of the operation of a neural electrode.

2.4 Conclusion

An overview of the physiological factors is given and the anatomical planes and directions are introduced. Relevant physiological properties include the anatomy of the rat brain as well as its geometrical dimensions. In addition, rat brain tissue is characterised by elastic and viscoelastic material properties. Subsequently, an overview of mechanical interactions is given, including static intracranial pressure, heart rate and blood pressure, respiration, linear acceleration and head rotation.

Afterwards, state-of-the-art tetrodes and polymer probes are introduced. Different electrode materials and probe configurations are summarized. Furthermore, the attachment of the probing equipment to the skull is discussed by an explanation on the hyperdrive enclosing microdrives, which are used to lower the implants in the brain tissue.

Based on rat brain finite element models in earlier studies, it can be concluded that a validation of these models can only be achieved when sufficient data on mechanical properties is available. Furthermore, rat brain modelling studies emphasise the importance of the interface between the brain tissue and neural probes in order to ultimately select implant materials that improve the implant biocompatibility.

3 DESCRIPTION OF FINITE ELEMENT MODELS

The main goal of this thesis is the development of a FEM-based model, which consists of the implanted electrode and the rat brain. Forces and pressures are applied to the model. In this way the displacement of the implant can be estimated. FEM is a numerical method to solve partial differential equations. The volumes of the implant and the rat brain are subdivided in smaller finite elements, which are defined by space discretisation of the volumes. In practice this is done by generating a mesh with a certain number of nodes. All calculations are done for these particular nodes by using a FEM software package. A description of the mathematical model follows after a short discussion on the FEM software package, after which, a multiple loads model is presented, taking into account linear acceleration, rotation, static intracranial pressure and respiration. Then, a heartbeat model is discussed, which describes the influence of the heartbeat onto the brain. Finally, a respiration model is presented in which the influence of respiration is examined.

3.1 ONELAB software package

The mathematical model behind FEM software is often hidden behind the graphic user interface (GUI). Although this is the case for most software, an interesting software package is available, which enables the creation of a custom FEM model and run it in the GUI. This is the first reason why Open Numerical Engineering LABoratory (ONELAB) is used. A second reason is the fact that this package is open-source. The third reason is the flexibility of the software, allowing different branches of physics to be modelled.

ONELAB is a software package consisting of a mesh generator Gmsh and the finite element solver GetDP. Gmsh itself has a GUI in which the geometry and the mesh can be completely specified. All information about the geometry and mesh is kept by automatically generating a code-based file. For the geometry and the mesh the software will respectively generate a .geo file and a .msh file. Both files can be accessed by a text editor, for example Notepad++. In this way, the geometry and the mesh can also be generated by writing code.

The FEM solver code itself is written in a .pro file, also accessible by a text editor, and can be run by the finite element solver. In this way GetDP can generate three file types. The first file is the .pre file, which contains the preprocessing information. The second file is the .res file, which contains the solution of the mathematical problem. The last files are the .pos files, which include certain desired printed values (ONELAB, 2021).

3.2 Mathematical model of FEM analysis

A complete introduction into FEM modelling would be too elaborate for the scope of this master's thesis. The basis of FEM is the determination of the elastic displacement under a certain load. This displacement is needed to calculate the viscoelastic displacement of the tissue. Therefore, it is worthwhile to start with an explanation of the way the elastic displacement is

calculated. Afterwards, the link with the viscoelastic displacement will become clear. Finally, the different steps that must be undertaken to follow the mathematical model are listed.

3.2.1 Elastic displacement calculation

As mentioned before, it is possible to calculate displacements for all nodes in the mesh. In FEM this is done by solving the following matrix equation:

$$[k]\{\mathbf{u}\} = \{\mathbf{F}\} \quad (3-1)$$

with:

- $[k]$, the stiffness matrix
- $\{\mathbf{u}\}$, the displacement vector of the nodes
- $\{\mathbf{F}\}$, the load vector of the nodes

For n nodes the FEM formulation (3-1) can also be written as:

$$\begin{bmatrix} k_{1,1} & k_{1,2} & \dots & k_{1,n-1} & k_{1,n} \\ k_{2,1} & k_{2,2} & \dots & k_{2,n-1} & k_{2,n} \\ \vdots & \vdots & \ddots & \vdots & \vdots \\ k_{n-1,1} & k_{n-1,2} & \dots & k_{n-1,n-1} & k_{n-1,n} \\ k_{n,1} & k_{n,2} & \dots & k_{n,n-1} & k_{n,n} \end{bmatrix} \begin{Bmatrix} \tilde{u}_1 \\ \tilde{u}_2 \\ \vdots \\ \tilde{u}_{n-1} \\ \tilde{u}_n \end{Bmatrix} = \begin{Bmatrix} \tilde{F}_1 \\ \tilde{F}_2 \\ \vdots \\ \tilde{F}_{n-1} \\ \tilde{F}_n \end{Bmatrix} \quad (3-2)$$

with:

- $k_{i,j}$, the stiffness between node i and node j
- \tilde{u}_i , the displacement of node i
- \tilde{F}_i , the force or moment exerted on node i

The nodes in formulation (3-2) have only one degree of freedom. If more degrees of freedom are necessary, such as in the following 3D models, the equations for a specific node will be inserted below the already existing equation of that node. When a constraint in terms of displacement is given, \tilde{u}_i is known for node i and can be filled out in the equation. The same is true for the force or moment, if it is known for node i , \tilde{F}_i can be filled out in the load vector. This indicates why it is important to set the right kind of constraints and to apply the correct number of forces and moments. If too little boundary conditions and/or loads are known, the FEM equation cannot be calculated.

The stiffness matrix is calculated in a specific way:

$$[k] = \int [B]^T [E] [B] dV \quad (3-3)$$

with:

- $[B]$, the strain-displacement matrix, which relates the nodal displacements to the element strains
- $[E]$, the material property matrix
- dV , the volume differential

$[B]$ is calculated as:

$$[B] = [\delta][N] \quad (3-4)$$

with:

- $[\delta]$, the derivative matrix, which relates the element displacements to the element strains
- $[N]$, the shape function matrix, which relates the nodal displacements to the element displacements

$[E]$ is calculated for a linear elastic isotropic 3D solid as:

$$[E] = \begin{bmatrix} \frac{(1-\nu)E}{(1+\nu)(1-2\nu)} & \frac{\nu E}{(1+\nu)(1-2\nu)} & \frac{\nu E}{(1+\nu)(1-2\nu)} & 0 & 0 & 0 \\ \frac{\nu E}{(1+\nu)(1-2\nu)} & \frac{(1-\nu)E}{(1+\nu)(1-2\nu)} & \frac{\nu E}{(1+\nu)(1-2\nu)} & 0 & 0 & 0 \\ \frac{\nu E}{(1+\nu)(1-2\nu)} & \frac{\nu E}{(1+\nu)(1-2\nu)} & \frac{(1-\nu)E}{(1+\nu)(1-2\nu)} & 0 & 0 & 0 \\ \frac{E}{2(1+\nu)} & 0 & 0 & \frac{E}{2(1+\nu)} & 0 & 0 \\ 0 & \frac{E}{2(1+\nu)} & 0 & 0 & \frac{E}{2(1+\nu)} & 0 \\ 0 & 0 & 0 & 0 & 0 & \frac{E}{2(1+\nu)} \end{bmatrix} \quad (3-5)$$

with:

- E , the elastic modulus of the material
- ν , the Poisson's ratio

As mentioned before, it is possible to calculate displacements and internal loads when sufficient constraints and loads are given. However, it is important to note that the above equations are only valid for linear elastic isotropic materials. Furthermore, rat brain is neither elastic nor isotropic. It is therefore not possible to directly use these equations in order to calculate the displacements in the tissue. Brain implants on the other hand are for example often produced of silicon, platinum or tungsten. These materials are linear elastic isotropic materials, which means that the above equations are valid for the implant material.

The equations are valid for static loads. When a time-varying sinusoidal load is applied, it is possible to calculate the displacement of the tissue and the implant at certain moments in time. It is more efficient to calculate the displacement of the tissue and the implant under a static load equal to the amplitude of the load. The displacements for a static force or pressure can indeed be calculated by the software. Afterwards the displacements need to be multiplied with the time-varying sine function.

3.2.2 Viscoelastic displacement calculation

To fully grasp the theory behind the viscoelastic displacement of the tissue, it is worthwhile to take a look at biomechanical tissue models. It is important to mention that mechanical models are often used to discuss the viscoelastic behaviour of materials including tissues. These mechanical models consist of springs and dashpots (Martin, Burr, Sharkey, & Fyhrie, 2015). A spring is supposed to produce instant deformation in proportion to the load whereas a dashpot causes a velocity of the model in proportion to the load at the model at any instant (Fung, 1981).

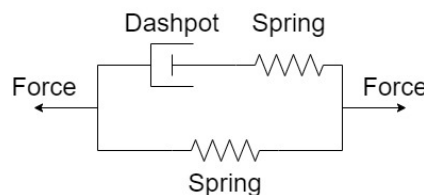


Figure 3-1 Kelvin-Voigt model of the first order (Fung, 1981)

The Kelvin-Voigt model, a quasilinear model, consists of a spring in parallel with a dashpot and spring in series. Figure 3-1 shows a Kelvin-Voigt model of the first order. This is a basic Kelvin-Voigt model. More general models can be built by adding more springs and dashpots to this model. It is for example possible to model viscoelastic materials with a Kelvin-Voigt model of a higher order. Extra springs are thus added in parallel with the Kelvin-Voigt model of the first order. This is merely done to better model nonlinear materials.

Brain tissue is indeed nonlinear viscoelastic. Although many researchers tried to develop mathematical models, there is no single widely used mathematical model. However, based on Fung's quasilinear viscoelastic theory, the relationship between stress and strain can be formulated (Delbeke, Haesler, & Prodanov, 2020). The stress relaxation can be formulated as a product of independent functions of time and strain (Fung, 1981):

$$\sigma(t) = \int_{-\infty}^t g(t - \tau) \frac{d\sigma_e}{d\tau} d\tau \quad (3-6)$$

with:

- $\sigma(t)$, stress relaxation
- $g(t)$, reduced relaxation function

Equation (3-6) indicates the relationship between the stress relaxation of a viscoelastic material and the elastic response of the same material. It would however be useful to find a direct relationship between the elastic displacement and the viscoelastic displacement. A starting point to find that relationship is the reduced relaxation function.

The reduced relaxation function is related to the reduced creep function in the Laplace domain (Betten, 2008):

$$K(s) = \frac{1}{G(s) \cdot s^2} \quad (3-7)$$

with:

- $K(s)$, the reduced creep function in the Laplace domain
- $G(s)$, the reduced relaxation function in the Laplace domain

The reduced relaxation function is determined after the experiments, after which the reduced creep function can be calculated. When a linear viscoelastic body is considered while loaded by different equal stress steps in the past, as illustrated on the left side of Figure 3-2, the creep response of the model can be calculated. It is based on both the creep function and the superposition principle and consists of a Prony series (Betten, 2008):

$$E\varepsilon_v(t) = \sum_{i=0}^n \Delta\sigma_{e,i} \cdot k(t - \theta_i) \quad (3-8)$$

with:

- $\varepsilon_v(t)$, the viscoelastic strain in function of time
- $\Delta\sigma_{e,i}$, the difference between the stress at time i and the stress at time $i-1$
- θ_i , the time in the past when a new stress step begins

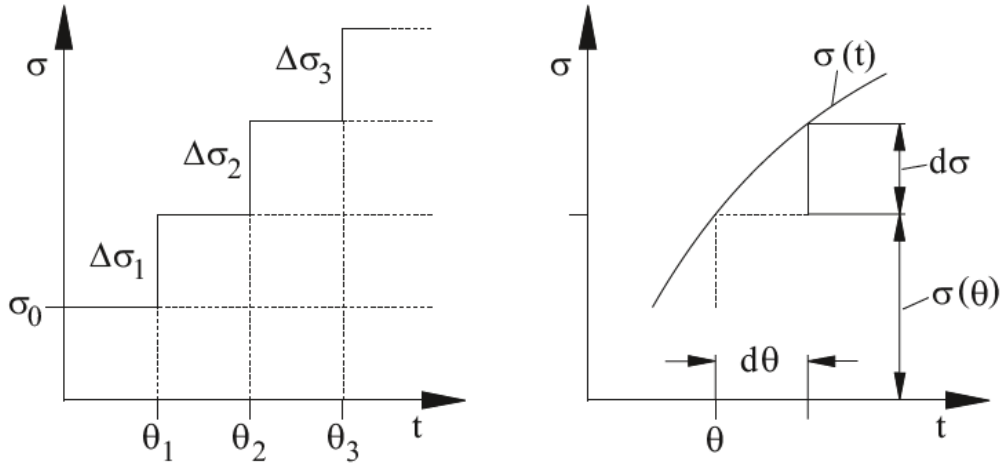


Figure 3-2 Stepped and continuous stress history (Betten, 2008)

The loads that are applied on the tissue however do not consist of stress steps. Heartbeat and respiration behave as a continuous function, similar to a sinusoidal function, as shown at the right side of Figure 3-2. To finally calculate the viscoelastic displacement some simplifications are made. First, the continuous function is simplified as a stepwise function, like shown at the left side of Figure 3-2. Second, the viscoelastic and elastic strain of an element are simplified as:

$$\varepsilon_v(t) \sim \frac{u_v(t)}{l} \quad (3-9)$$

$$\varepsilon_e(t) \sim \frac{u_e(t)}{l} \quad (3-10)$$

with:

- $u_v(t)$, the viscoelastic displacement over time of a node
- l , the length of an element
- $\varepsilon_e(t)$, elastic strain in function of time
- $u_e(t)$, the elastic displacement over time of a node

These simplifications are valid under small strain conditions, typically under 3-4% strain (Karimi & Navidbakhsh, 2014), which is definitely the case because the implant-brain model is dealing with microstrains. (3-11) is obtained by dividing (3-8) at both sides by E , and afterwards filling in (3-9) and (3-10) in (3-8):

$$u_v(t) = \sum_{i=0}^n \Delta u_{e,i} \cdot k(t - \theta_i) \quad (3-11)$$

with:

- $\Delta u_{e,i}$, the difference between the displacements at time i and time $i-1$

3.2.3 Different mathematical steps

Based on the mathematical formulas in 3.2.1 and 3.2.2, the following steps need to be taken in order to calculate the viscoelastic displacement of the implant and the tissue at time j :

1. Calculation of the elastic displacement vector $\{\mathbf{u}\}$ for a load equal to the magnitude of the time-varying input.

2. Calculation of the different elastic displacement vectors for the different points of time θ_i , by multiplying the calculated elastic displacement vector $\{\mathbf{u}\}$ with the value of the sine wave at the different points of time θ_i .
3. Calculation of the j-th creep functions, using the difference in time of the current time θ_j and respectively all the different points of time θ_i as input.
4. Calculation of the viscoelastic displacement vector $\{\mathbf{u}_v\}$ by summation of all multiplications of the difference of the elastic displacement vectors at time θ_i and time θ_{i-1} with the creep function of the time difference of time θ_j and time θ_i .

3.3 Multiple loads model

When numerically calculating the displacement of the implanted electrode and the tissue, certain factors such as the geometry and material properties of the implant and the rat brain need to be taken into account. The mesh is also important because the division into smaller elements needs to be done in a correct way. Finally, constraints are set and loads are applied. Note, the flexible model allows that all different parameters can be varied, including the geometry and the material properties.

3.3.1 Geometry

Two different volumes are present in the model, i.e. the brain tissue and the implant. First, some simplifications are made concerning the geometry of the brain tissue:

- a single homogeneous material is used for the brain and the meninges without adding any layers,
- the brain is modelled as a tissue cuboid,
- the dimensions are based on the craniometric dimensions in Table 2-1 and on the outer dimensions of real cerebrum in Table 2-2.

The length of the tissue cuboid is 20 mm, the width and the thickness are both 15 mm. These values mainly correspond with the outer dimensions of the cerebrum. However, a real cerebrum has a thickness of approximately 10 mm. A thicker tissue has been chosen because this ensures that the movement of the implant is less influenced by a fully fixed bottom surface of the tissue.

Second, also simplifications are done regarding the geometry of the implant:

- the implant is modelled as a beam,
- which means that it has a flat tip instead of a sharp tip,
- the dimensions are based on the dimensions of a silicon tetrode, as noted in 2.2.1, the diameter approximately ranging from 30 μm to 80 μm .

The thickness and width of the implant are 60 μm . The length of the implant is 9 mm and it has an insertion depth of 7 mm, which corresponds with a deep brain measurement, also indicated in Figure 2-2. The difference in total length and insertion depth is 2 mm. This is the length between the upper surface of the brain tissue and the exit tip of the hyperdrive, indicated in Figure 2-15. Figure 3-3 shows the geometry of the tissue and the implant, which is inserted right in the middle of the upper surface of the tissue cuboid. The x-axis is pointing in the rostral

direction, the y-axis in the left direction and the z-axis is pointing in the dorsal direction. This is the case for all following figures.

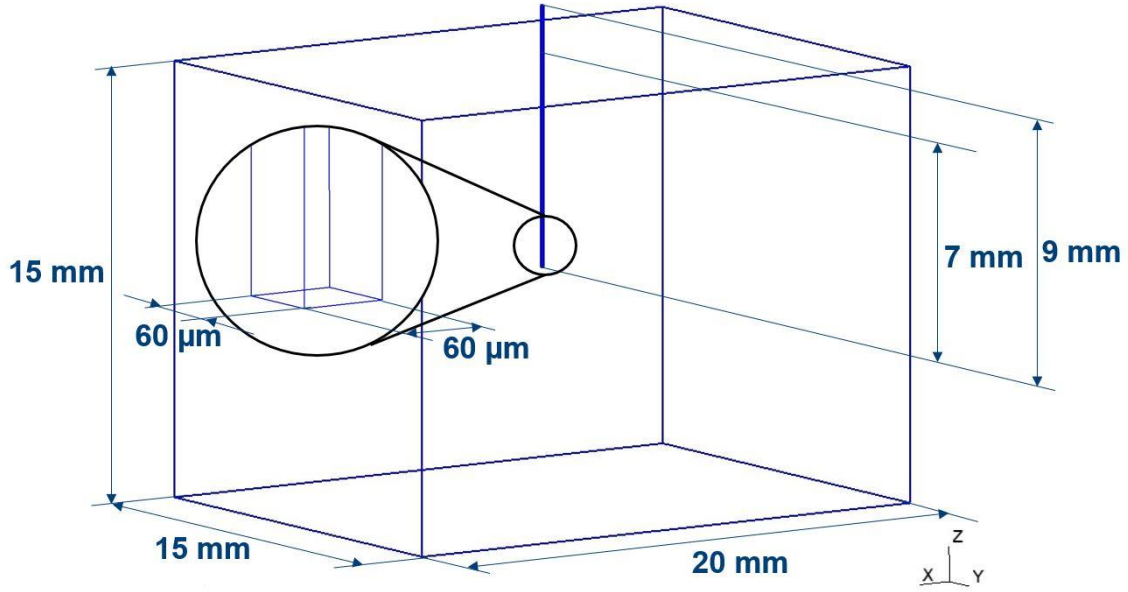


Figure 3-3 Geometry of multiple loads model

3.3.2 Material properties

As described in 3.2, both elastic and viscoelastic properties are needed in order to calculate the apparent elastic and viscoelastic displacements of the tissue. One elastic modulus is calculated for the homogeneous material, which represents both the brain tissue and the meninges. This is done based on the values for elastic moduli in 2.1.2.2: 50 kPa is used as elastic modulus for the brain tissue, whereas 20 MPa is used as elastic modulus for the meninges. An overall elastic modulus of 3 MPa is calculated. A further derivation of the calculations can be found in Appendix A.

Beside the elastic modulus, the reduced creep function is calculated for PDx. A second order reduced creep function is defined based on the third order reduced relaxation function composed by the parameters in Table 2-4. The full derivation is attached in Appendix B. The second order reduced relaxation function and the second order reduced creep function are respectively (3-12) and (3-13), material parameters for (3-13) are listed in Table 3-1. Because of the fact that the functions are defined for a Poisson's ratio of 0,49, this value is also used in the FEM model.

$$g(t) = 0,1649 + 0,5509e^{-57,875t} + 0,2842e^{-4,483t}, \quad g(0) = 1 \quad (3-12)$$

$$k(t) = \exp\left(\frac{\left(\frac{(g_1+g_2)((\beta_1+\beta_2)g_\infty+\beta_1g_2+\beta_2g_1)}{g_\infty} - \frac{2(\beta_1g_2+\beta_2g_1)}{g_\infty}\right)\sinh\left(\frac{At}{2}\right)}{A} - \frac{(g_2+g_1)\cosh\left(\frac{At}{2}\right)}{g_\infty}\right) + \frac{1}{g_\infty} \quad (3-13)$$

with A:

$$A = \sqrt{(\beta_2^2 - 2\beta_1\beta_2 + \beta_1^2)g_\infty^2 + ((2\beta_1^2 - 2\beta_1\beta_2)g_2 + (2\beta_2^2 - 2\beta_1\beta_2)g_1)g_\infty + \beta_1^2g_2^2 + 2\beta_1\beta_2g_1g_2 + \beta_2^2g_1^2}$$

Table 3-1 Material parameters reduced creep function (Shafieian, Darvish, & Stone, 2009)

Material parameter	PDx
g_{∞}	0,1649
g_1	0,5509
g_2	0,2842
β_1 (s ⁻¹)	57,875
β_2 (s ⁻¹)	4,483

In addition to the material properties of the brain tissue, the material properties of the implant are also defined. These are based on the material properties of silicon. The elastic modulus equals 165 MPa and the Poisson's ratio is 0,3 (Hopcroft, Nix, & Kenny, 2010). Because of the fact that the implant-tissue volume ratio is equal to $5,6 \cdot 10^{-6}$ it is assumed that the implant moves simultaneously with the tissue. Therefore, the implant displacement depends on the reduced creep function of the tissue. Consequently, the displacement of the implant is calculated as the viscoelastic displacement of the tissue.

3.3.3 Mesh

The meshes of the tissue and the implant are generated by dividing both volumes in smaller sub volumes, which in their turn are subdivided in quadratic hexahedral 3D elements. Note the following:

- Hexahedral elements are chosen because they are the most accurate compared to the same number of other 3D elements (Cook, 1995).
- Figure 3-4 shows a quadratic hexahedral element. It is defined by eight nodes, which serve as corners (indicated in black), twelve mid nodes on the ribs of the hexahedron (indicated in white), six mid nodes on the surfaces and one mid node of the entire volume (both indicated in grey) (De Roeck, 2020). Quadratic elements are chosen because they offer the opportunity to better approximate bends in the tissue and especially the implant.

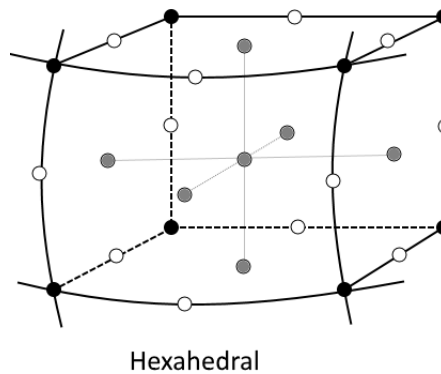


Figure 3-4 Hexahedral element (De Roeck, 2020)

- To obtain a full symmetry the mesh is structured. A nonsymmetrical geometry of the mesh would probably result in slightly divergent behaviour of the implant when a linear force at one side would be applied.

As a result the tissue is divided in eight large sub volumes, four sub volumes above the tip surface of the implant and four sub volumes below that surface. Notice that the mesh gradually has smaller elements around the implant with a factor 0,75. More nodes are consequently placed around the implant, which enhances the accuracy of the calculations. At all lines of the sub volumes, five corner nodes are placed, twenty in terms of the insertion depth. The thickness of the elements ranges from 0,37 mm to 2,92 mm, the width from 1,16 mm to 2,74 mm and the length from 1,54 mm to 3,66 mm. Figure 3-5 shows this mesh of the tissue, with a total of 4160 nodes and 3040 elements.

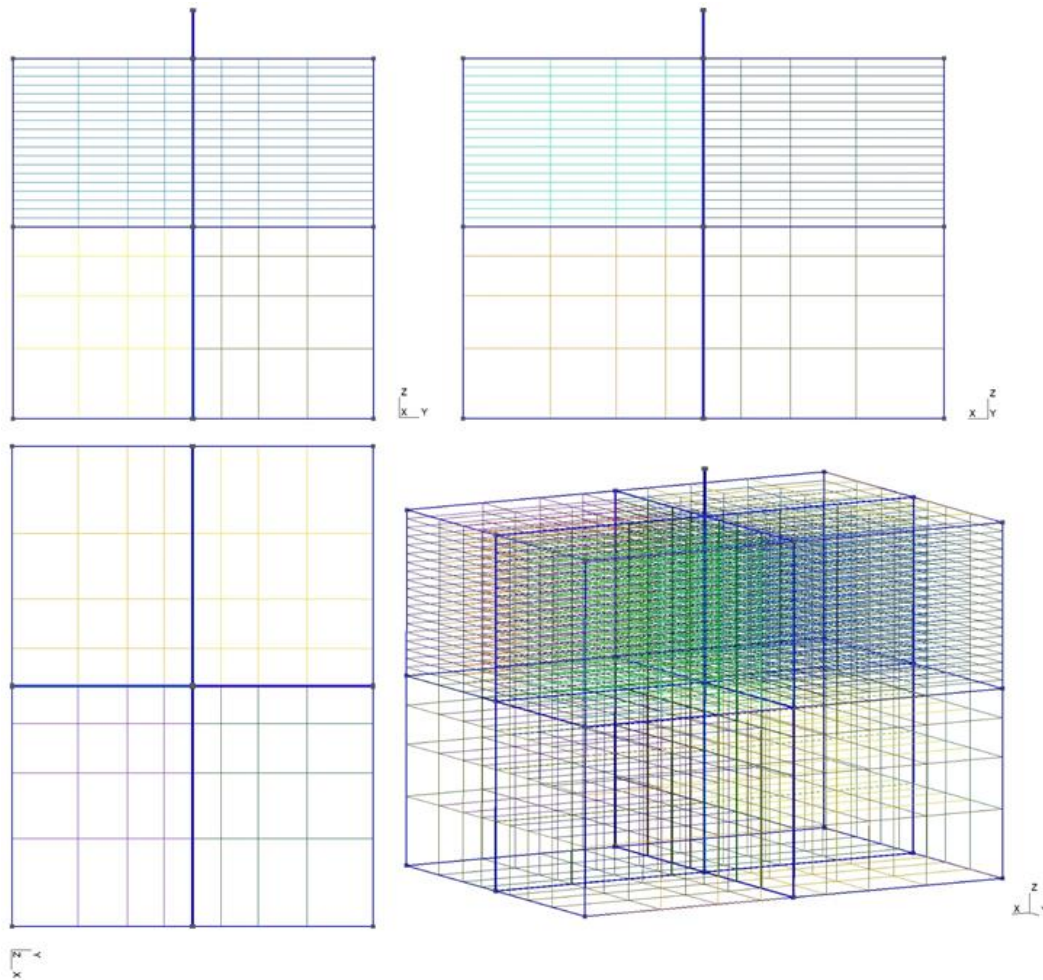


Figure 3-5 Meshing tissue multiple loads model: front view, side view, top view and orthogonal view

The elements of the implant on the outside are also hexahedrons, but their top surfaces are not rectangular but trapezoidal as shown on Figure 3-6. The large square is the top surface of the implant. The size of these elements decreases towards the inner part of the implant whereas the upper surfaces are rectangular. The outer part is divided in four sub volumes in the tissue and four sub volumes above the tissue. The inner part is divided in one sub volume in the tissue and one sub volume above the tissue. At all lines five corner nodes are placed except for the insertion depth and the length between the upper surface of the tissue and the top of the implant where twenty corner nodes are placed.

Figure 3-6 also shows a side view of the upper part of the implant, with elements of 0,10 mm long. In this way the thickness of the elements ranges from 1,5 μm to 6,75 μm , the width from 1,5 μm to 15 μm and the length from 0,10 mm to 0,37 mm. To structure the mesh in a correct

way, extra sub volumes are added to the tissue in line with all surfaces of the implant. The left part of Figure 3-6 shows these extra sub volumes at all sides of the implant. The length and thickness of the elements correspond with the length and thickness of the elements in the large sub volumes of the tissue. The width equals 15 μm . A critical point of the meshing is the aspect ratio. The aspect ratio is the ratio of the length of an element on the thickness or the width, which should be less than ten. By gradually decreasing the size towards the middle of the implant, the aspect ratio is optimised. However, due to the fact that the dimensions of the implant and the tissue are of a completely other order, it is not possible to guarantee the optimisation of the aspect ratio throughout the mesh. This would result in too many elements. The implant mesh has 3471 nodes and 3040 elements.

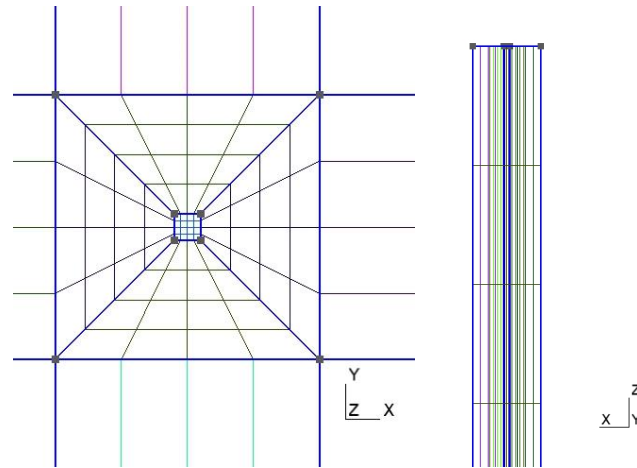


Figure 3-6 Meshing implant multiple loads model: top view and side view

3.3.4 Boundary conditions

First, two different types of displacement boundary conditions are defined, i.e. contact constraints and boundary constraints. The first type describes the contact between implant and tissue, while the second type defines how the tissue and the implant are connected with the environment. Second, different load boundary conditions are applied on the tissue based on the physiology and normal behaviour of a rat, described in 2.1.

3.3.4.1 Displacement boundary conditions

To enhance biocompatibility, implants are coated with hydrogel coatings, often made of collagen. In general, the biocompatibility of some implant materials like silicon, inserted in brain tissue is not good. Not only can inflammatory effects be expected, also different mechanical failures can be encountered, such as gap forming or encapsulation (Prodanov & Delbeke, 2016). For reasons of simplification, it is however assumed that the implant and tissue do not move with respect to each other. Or in other words, the tissue and implant are glued.

This assumption has also been made for the description of different implant fixation configurations presented by Figure 3-7. Three configurations are defined in 2D, which are idealised cases of the real fixation. The implant is represented as a bar with length L , the cap corresponds with the hyperdrive and finally the skull is presented as the ground. Configuration A is semiflexible, which means that the hyperdrive is not rigidly attached to the skull. Forward and upward forces F_x and F_y applied on the hyperdrive result in a displacement of the implant in those directions as well as a rotation about the angle θ . A maximal displacement is expected around the entry point of the implant in the brain. Configuration B models the attachment of

the hyperdrive to the skull as rigid. This causes the force F_w to be dominantly exerted on the lower part of the implant, resulting in both larger displacement in that part of the implant and a rotation around the top of the implant. Finally, configuration C displays free radial displacements of the implant and restricted upward displacements due to the fact that the attachment to the hyperdrive is modelled as a spring with force F_y (Prodanov & Delbeke, 2016).

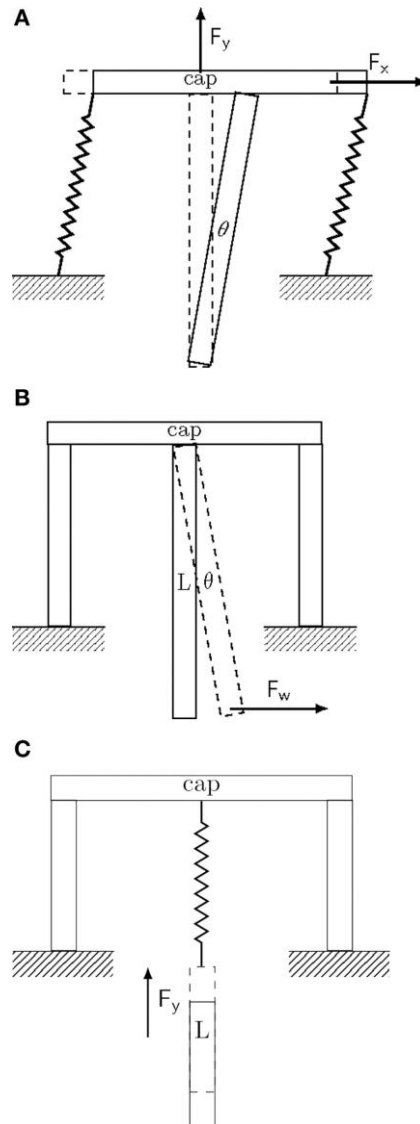


Figure 3-7 Conceptual drawing of the different implant fixation configurations (Prodanov & Delbeke, 2016)

One of these three configurations is chosen to be modelled: configuration B. In comparison with A the rigid attachment of the hyperdrive to the skull is more realistic. In reality the flanges of the hyperdrive are attached with dental cement and screws, which counteract flexibility. On top of that, it is assumed that the implant is attached to the tissue and cannot move neither up nor down, which eliminates configuration C. Therefore, the implant is modelled as a bar, which can toggle around the connection point with the hyperdrive in all directions. This toggle point is located 2 mm above the upper surface of the brain tissue. The small square in Figure 3-6 is entirely clamped in and models the toggle point. Its dimensions are $6 \mu\text{m} \times 6 \mu\text{m}$ and is symbolically represented in Figure 3-8 at the implant top.

Finally, the bottom surface of the brain tissue is totally fixed, also symbolically indicated in Figure 3-8. All other surfaces of the tissue in the model are not constrained. In reality, the brain tissue is surrounded with CSF in the subarachnoid space and is therefore not attached at the bottom surface to the skull. However, because the displacement of the implant is of high interest, this simplification can be made. This means that the displacement of the tissue at the surfaces cannot be compared with real tissue displacements. It is assumed that this simplification allows the determination of the implant displacement with respect to the brain.

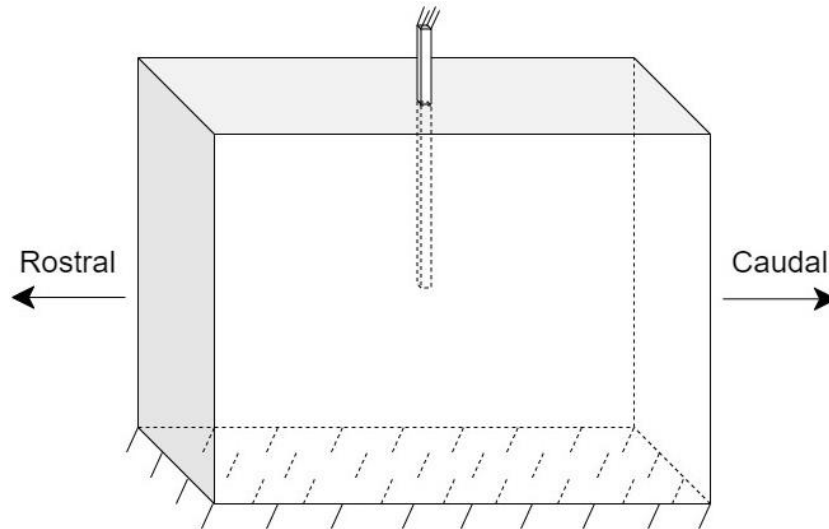


Figure 3-8 Sketch displacement boundary conditions

3.3.4.2 Linear acceleration

The linear acceleration acts as a pressure of 420,3 Pa at the contact surface between the brain tissue and the skull throughout the intermediate layers, according to 2.1.6. Hence, an equal distributed pressure is applied at the caudal surface of the brain tissue. The pressure is multiplied with a sinusoidal function with a frequency of 10 Hz. This frequency indicates the head oscillations in a linear movement. Although these oscillations are in reality vertical oscillations, for simplification reasons they are assumed to be horizontal within the context of this applied load. This simplification follows the assumption of Ledberg A. and Robbe D. in the study on locomotion-related oscillatory body movements, where vertical head oscillations were used as an approximation for all rhythmical locomotion behaviours (Ledberg & Robbe, 2011).

3.3.4.3 Head rotation

A discretised FEM model of a rat brain is composed of multiple small elements. Each of these elements has its own mass and mechanical interactions, meaning that rotational accelerations are acting on every element. However, the FEM model as described in 3.3 is constructed as one simplified cuboid. Therefore mechanical loads can only be applied at the side surfaces of this simplified cuboid. This implies that the rotational accelerations cannot be applied at every element separately and as a consequence that simplifications are introduced in the FEM model.

Figure 3-9 shows a diagram of a rat rotating its head with an angular velocity ω of 2,6 rad/s and an angular acceleration α of 8,7 rad/s² around the centre of rotation (COR), according to 2.1.7. The normal acceleration a_n and the tangential acceleration a_t are calculated based on

the angular velocity and the angular acceleration. A rough estimation of the distance r_1 indicates a value of 10 mm at the caudal side of the brain with respect to the COR. The value of r_2 is the anterior-posterior brain length of approximately 20 mm according to Table 2-2.

$$a_n = \omega^2 \cdot \left(r_1 + \frac{r_2}{2}\right) = \left(2,6 \frac{rad}{s}\right)^2 \cdot \left(10 \text{ mm} + \frac{20 \text{ mm}}{2}\right) = 0,135 \frac{m}{s^2} \quad (3-14)$$

with:

- a_n , the normal acceleration
- ω , the angular velocity
- r_1 , the distance according to Figure 3-9
- r_2 , the distance according to Figure 3-9

$$a_t = \alpha \cdot \left(r_1 + \frac{r_2}{2}\right) = 8,7 \frac{rad}{s^2} \cdot \left(10 \text{ mm} + \frac{20 \text{ mm}}{2}\right) = 0,174 \frac{m}{s^2} \quad (3-15)$$

with:

- a_t , the tangential acceleration
- α , the angular acceleration
- r_1 , the distance according to Figure 3-9
- r_2 , the distance according to Figure 3-9

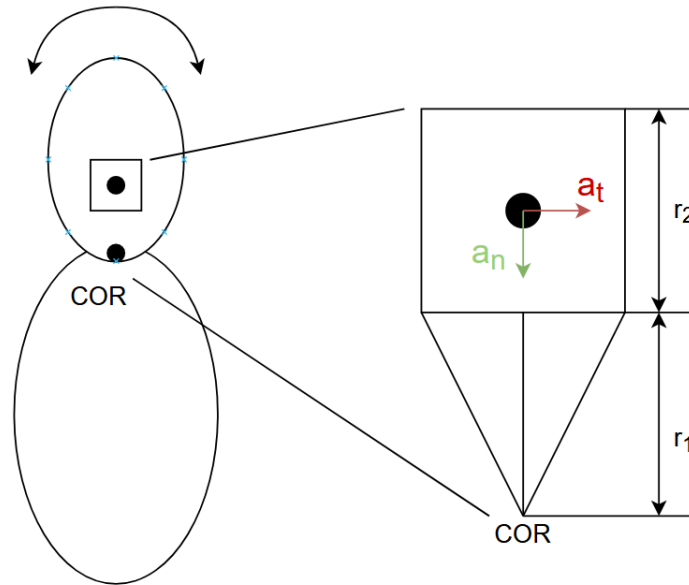


Figure 3-9 Diagram of a rat head rotation

The cuboid in Figure 3-9 is rigid and it does not consist of elements, as explained above. Moreover, only interactions can be applied at the side surfaces of the cuboid and not on the centre of gravity of the rigid body. The normal force F_n and tangential force F_t , causing the normal acceleration a_n and tangential acceleration a_t respectively, are calculated by representing the cuboid as a point mass situated at its centre of gravity. Nevertheless, they are applied in the FEM model at respectively the rostral surface and the left surface for simplification purposes.

$$F_n = m_b \cdot a_n = 2,3 \text{ grams} \cdot 0,135 \frac{m}{s^2} = 0,311 \text{ mN} \quad (3-16)$$

with:

- F_n , the normal force
- m_b , the mass of the brain
- a_n , the normal acceleration

$$F_t = m_b \cdot a_t = 2,3 \text{ grams} \cdot 0,174 \frac{m}{s^2} = 0,400 \text{ mN} \quad (3-17)$$

with:

- F_t , the tangential force
- m_b , the mass of the brain
- a_t , the tangential acceleration

3.3.4.4 Static intracranial pressure

Based on Figure 2-6 in 2.1.3 the maximum intracranial pressure is defined as 6 mmHg, which equals 800 Pa. This pressure is exerted on the outer surface of the brain tissue by the CSF in the subarachnoid space. It can be modelled by a static pressure at all outer surfaces of the brain tissue, except the clamped in bottom surface. Because this pressure is applied at all surfaces with the same size, toggling is not expected. It is however possible to observe a downforce exerted on the implant.

3.3.4.5 Respiration

Respirational responses interacting with the brain tissue are represented by a sinusoidal wave with an amplitude of 980 Pa according to Figure 2-10, indicating the pressure in the airways and lungs when a rat breathes in. The transpulmonary pressure is in this assumption directly applied to the caudal side of the brain tissue without a pressure drop in the intermediate tissue. The frequency of the sinusoidal wave is 2 Hz, representing the breathing frequency of a rat in normal behaviour.

3.3.4.6 Multiple loads

All loads resulting from linear acceleration, rotation, static intracranial pressure and respiration, can be combined in a multiple loads model. Because superposition is valid, all displacements resulting from different loads can be summed, which results in total displacement. Figure 3-10 is the top view of a free body diagram, including the different loads. The black arrows and crosses represent the distributed static intracranial pressure, the blue arrows represent forces related to linear acceleration. Rotation is represented as the red distributed forces and finally the green distributed pressure is the respiration pressure.

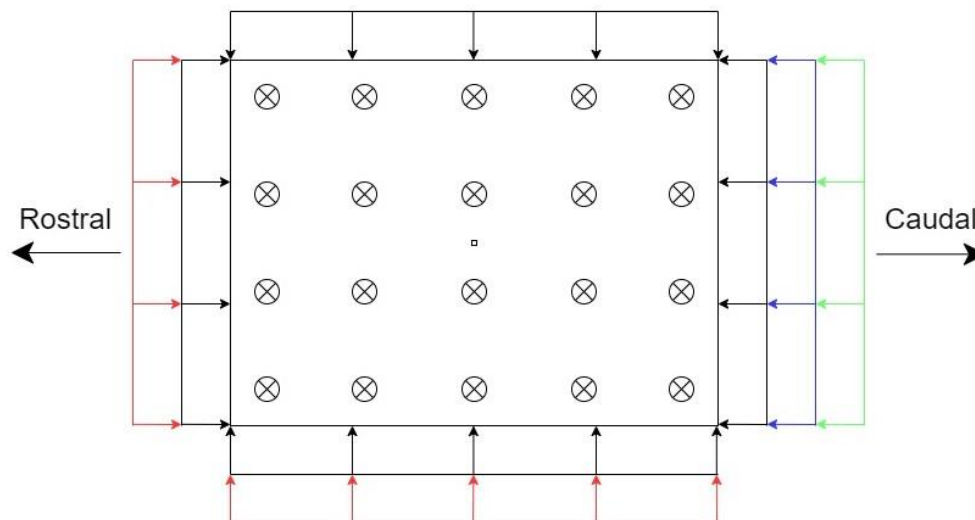


Figure 3-10 Top view free body diagram

3.3.5 Solver

Two time-varying loads are applied on the brain tissue: the force causing linear acceleration at a frequency of 10 Hz and respiration at a frequency of 2 Hz. To simulate a full period of respiration the simulation is done during a time span of 0,5 seconds, including five periods of the forces causing linear acceleration. In FEM it is recommended to represent a sine wave by six to ten points of time per period. When six points of time per rotation period are simulated a total of 30 points of time is needed to simulate a time span of 0,5 seconds. The viscoelastic displacements are calculated for each single load as indicated in 3.2. Finally, all displacements are superposed to derive the total displacement.

The total processing CPU-times that ONELAB requires to do the calculations on the linear acceleration, rotation, static intracranial pressure and respiration are respectively 320, 333, 340 and 329 seconds. The ONELAB files are attached in Appendix L, provided on an electronic medium.

3.4 Heartbeat model

In the multiple loads model, the heartbeat is not modelled. This can be done by modelling the arteries and veins in the brain tissue and by applying blood pressure in them. However, there are many similarities between the multiple loads model and the heartbeat model in terms of geometry, material properties and mesh. The main difference is the application of one single load, i.e. blood pressure, instead of multiple loads. Finally, a few more refined assumptions are made and indicated. Completely similar to the previous model, this flexible model allows that all different parameters can be varied, including the geometry and the material properties.

3.4.1 Geometry

The geometries of the tissue and the implant are exactly the same in the heartbeat model as in the multiple loads model. The only difference is the simplification of arteries and veins in the

head. Figure 3-11 shows these blood vessels, which are modelled by tubes of 12 mm long with a diameter of 1 mm. A top view of the model is shown in Figure 3-12. Notice real blood vessels are part of a complex blood vessel structure in terms of geometry. However, different kinds of blood pressures are known: LVP, LVEDP and JVP. These pressures are applied in the tubes mimicking the real pressure in the arteries and the veins. Smaller blood vessels are not modelled because the pressure in these vessels is much smaller than the pressure inside the arteries and veins.

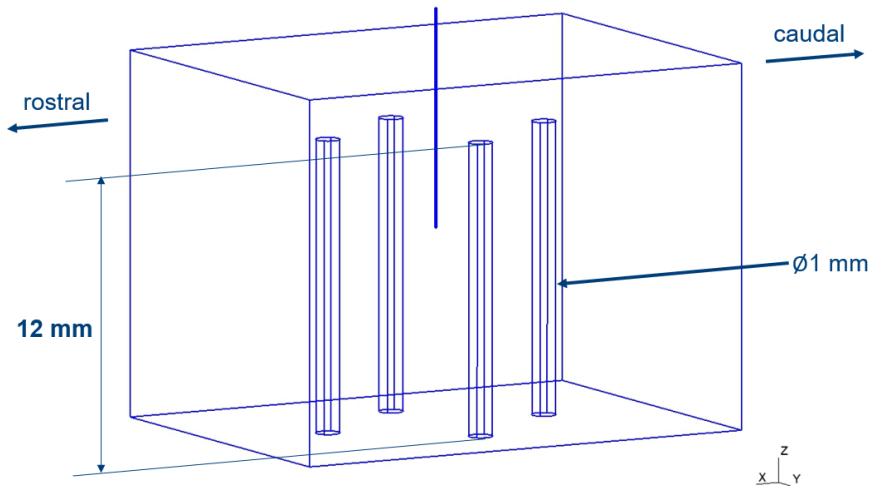


Figure 3-11 Geometry heartbeat model

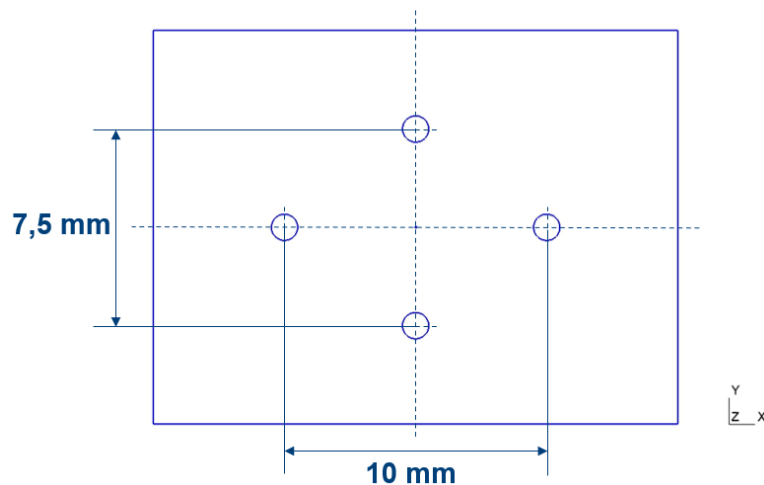


Figure 3-12 Top view heartbeat model

3.4.2 Material properties

In the multiple loads model the elastic modulus is a calculated overall elastic modulus for the composition of brain tissue and meninges. This simplification can be refined due to the fact that blood vessels are situated inside the brain tissue or on the outer surface of the brain tissue. Indeed, the blood pressure is mainly applied on the brain tissue and not on the meninges. Therefore, the simplification of one homogeneous material for brain tissue and meninges is not valid and only the brain tissue is mimicked. As in the multiple loads model, 50 kPa is used as elastic modulus for the brain tissue. The reduced creep function and the Poisson's ratio remain unchanged. This also applies to the elastic modulus and Poisson's ratio of silicon, the implant material.

3.4.3 Mesh

Meshing is done by dividing the tissue and implant volumes in sub volumes, which consist of quadratic hexahedral 3D elements. In addition, in this model the tissue volume is divided in different sub volumes in three levels. The lowest level reaches the tip of the implant, the middle level is situated between the tip of the implant and the top of the tubes, the highest level is the level between the top of the tubes and the upper surface. These levels are clearly visible in the front and side view in Figure 3-13. In the lower two levels 16 sub volumes are determined, all located around the tubes. In the highest level the same 16 sub volumes exist with an extra of 20 sub volumes on top of the tube tops. The boundaries of these sub volumes are visible in the top view in Figure 3-13.

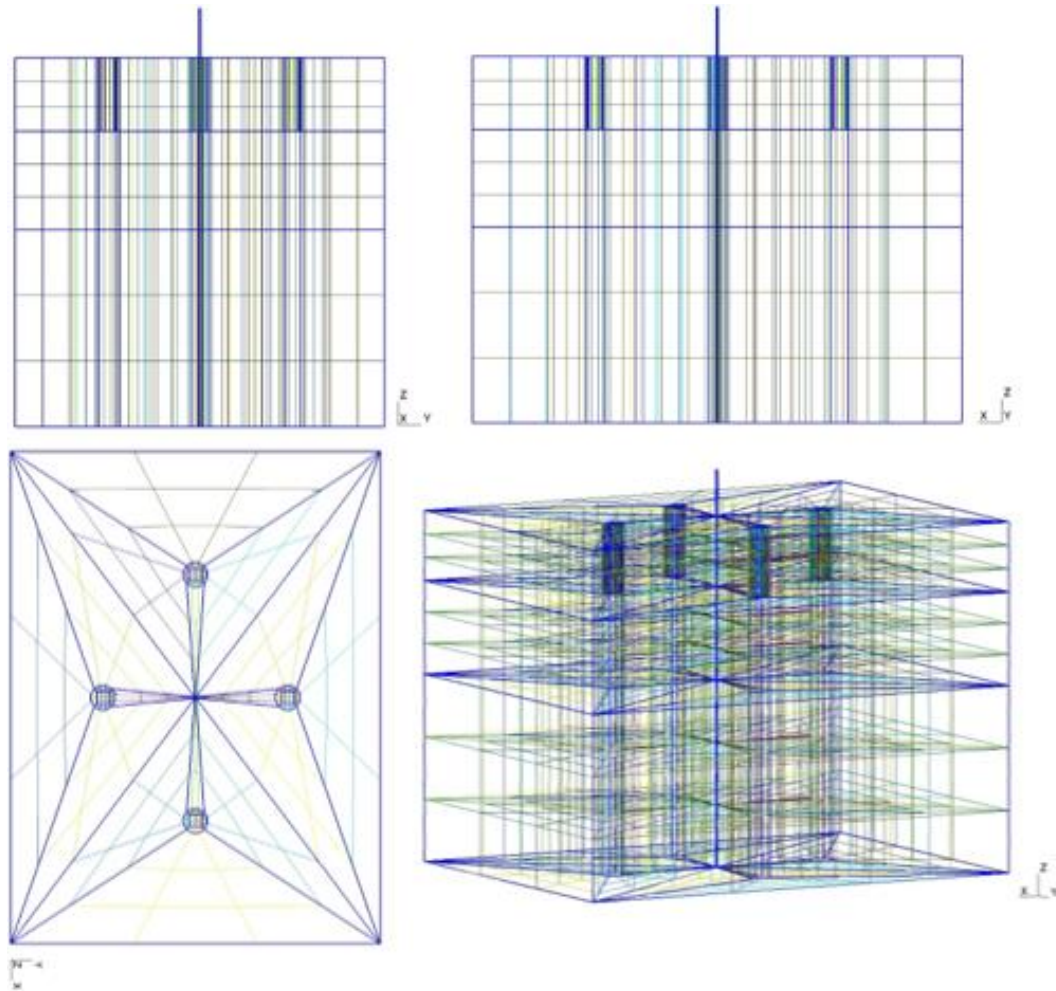


Figure 3-13 Meshing tissue heartbeat model: front view, side view, top view and orthogonal view

Four corner nodes are placed at an equal distance at all the lines of the sub volumes. Note that the elements around the implant and the tubes are smaller than the elements further away. The thickness of the elements ranges from 0,67 mm to 2,67 mm, the width from 1,08 mm to 1,50 mm and the length from 1,10 mm to 6,67 mm. Figure 3-13 shows this meshing of the tissue, it has a total of 2560 nodes and 1971 elements. The elements of the implant are equivalent with the elements of the implant in the multiple loads model, although the lengths are different. The length of the elements ranges from 0,67 mm to 1,67 mm. The implant mesh has 520 nodes and 405 elements.

3.4.4 Boundary conditions

As in the multiple loads model the implant cannot move with respect to the tissue. In addition, in this model the bottom surface of the tissue is also totally constrained in all degrees of freedom. Adding the tubes, mimicking the blood vessels, results in four holes in the bottom surface. Pressure is applied in these tubes, mimicking the blood pressure. Based on Table 2-5 and Figure 2-7 the pressures in the tubes are determined. In the caudal tube the following pressure sine wave is applied, based on the maximal LVP and the minimal LVEDP:

$$P_{c,HB} = 60,15 + 51,75 \sin(2\pi \cdot 6 \text{ Hz} \cdot t) \text{ mmHg} \quad (3-18)$$

The pressure in the caudal tube mimics the pressure in the arteries. Note that the time-varying pressure in the left ventricle is applied. This simplification is done based on the fact that the maximal pressures in the left ventricle and arteries often almost equal each other. Also note that the time-varying pressure in reality, as shown in Figure 2-7, does not behave like a sine wave. The frequency of 6 beats/second corresponds with real measurements in rats, mentioned in 2.1.4. Presenting the pressure as a sine wave is an extra simplification.

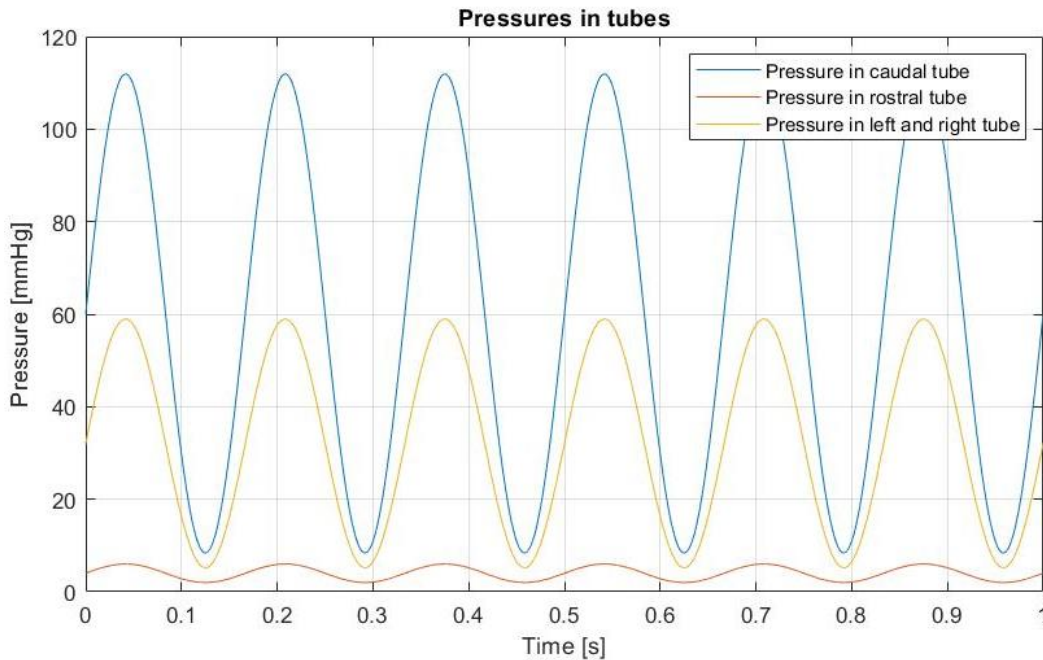


Figure 3-14 Pressures in tubes

In the rostral tube the following pressure sine wave is applied, based on the mean JVP and an assumed magnitude of 2 mmHg:

$$P_{r,HB} = 4 + 2 \sin(2\pi \cdot 6 \text{ Hz} \cdot t) \text{ mmHg} \quad (3-19)$$

This pressure mimics the pressure in the veins. The jugular venous pressure is applied in this rostral tube. In the left and the right tubes the average of $P_{c,HB}$ and $P_{r,HB}$ is applied. These tubes therefore represent all blood vessels with pressures varying from low venous pressures to high artery pressures. Figure 3-14 shows all the time-varying pressures.

3.4.5 Solver

Only one time-varying load is applied on the brain tissue, i.e. the blood pressure at a frequency of 6 Hz. To simulate one full period, the simulation is done for a time span of 0,167 seconds. Twelve time steps of 0,0139 seconds are simulated to get a more accurate simulation. The total processing CPU-time that ONELAB requires to do the calculations is 166 seconds. The ONELAB files are attached in Appendix L, provided on an electronic medium.

3.5 Respiration model

In the multiple loads model the brain tissue and the meninges are considered as one homogeneous material. An extra refined assumption can be made such as in the heartbeat model: only the brain tissue is mimicked without meninges. To constraint the brain tissue, a skull is added to the model. Note, this model also allows that all different parameters can be varied, including the geometry and the material properties.

3.5.1 Geometry

The geometry is exactly the same as the geometry of the multiple loads model except for one aspect. In this model, the bottom, top, front, left and right surfaces represent the skull. To ensure passage of the implant to the brain, a hole is drilled in the skull. This hole is represented in the model as a circle with a diameter equal to 1 mm and located right in the middle of the top surface. Figure 3-15 shows a top view of the respiration model, with the hole and implant in the middle.

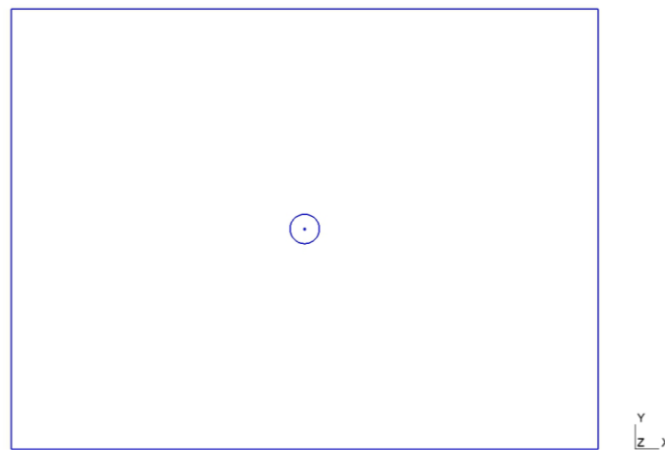


Figure 3-15 Top view respiration model

3.5.2 Material properties

The material properties of both the brain and the implant are exactly the same as the material properties proposed for the heartbeat model, described in 3.4.2.

3.5.3 Mesh

The mesh is very similar to the mesh of the multiple loads model. On a number of factors, this mesh performs better than the meshes of the two previous models:

- As for the multiple loads model, the element size decreases towards the implant, which is done to increase the accuracy of the model. Figure 3-17 shows that the elements are smaller around the implant. Furthermore, this mesh is altered in such a way that the aspect ratio is lowered. In other words there are less slender elements.
- Extra sub volumes are added around the implant by adding a hole in the geometry. In Figure 3-16 a top view of four sub volumes is visible, the sub volumes are a quarter of a cylinder. Like in the multiple loads model a cross is formed in the tissue with other sub volumes, also visible in Figure 3-16. The elements of the cross are larger this time, whereas dimensions are not ten times larger than dimensions of neighbouring elements. FEM requires that elements should not be ten times larger than neighbouring elements.
- In comparison with the elements of the heartbeat model, the elements in this model are less skewed. The angles between the surfaces are less sharp in this model.

These improvements are done to avoid ill-conditioned stiffness matrices, which are detrimental to the FEM calculations. At all lines of the sub volumes, five corner nodes are placed, twenty in terms of the insertion depth. The order of dimensions corresponds with the order of dimensions of the multiple loads model. The mesh of the implant is exactly the same as the mesh of the multiple loads model. 5741 nodes and 4736 elements are required for the tissue mesh and 3243 nodes and 2736 elements for the implant mesh.

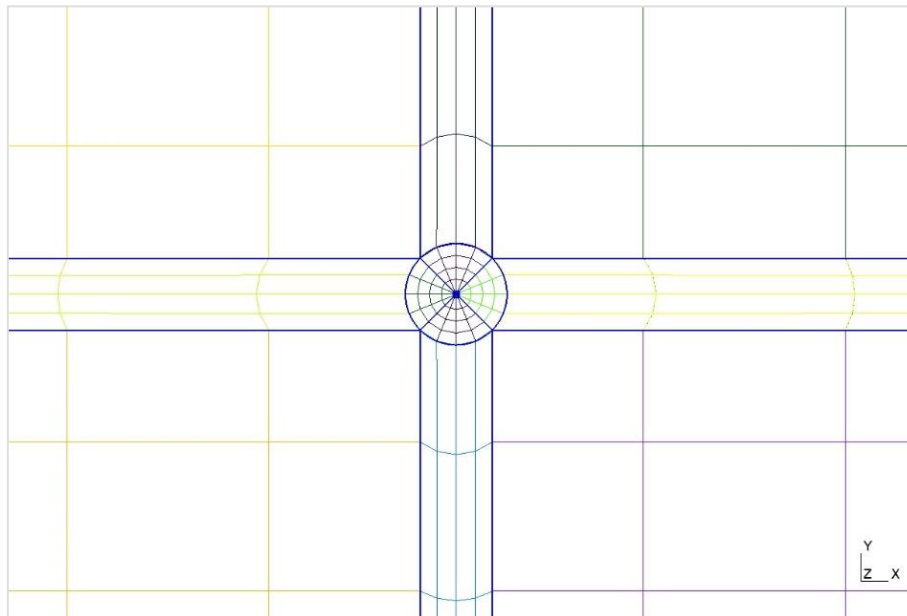


Figure 3-16 Meshing respiration model: close-up top view

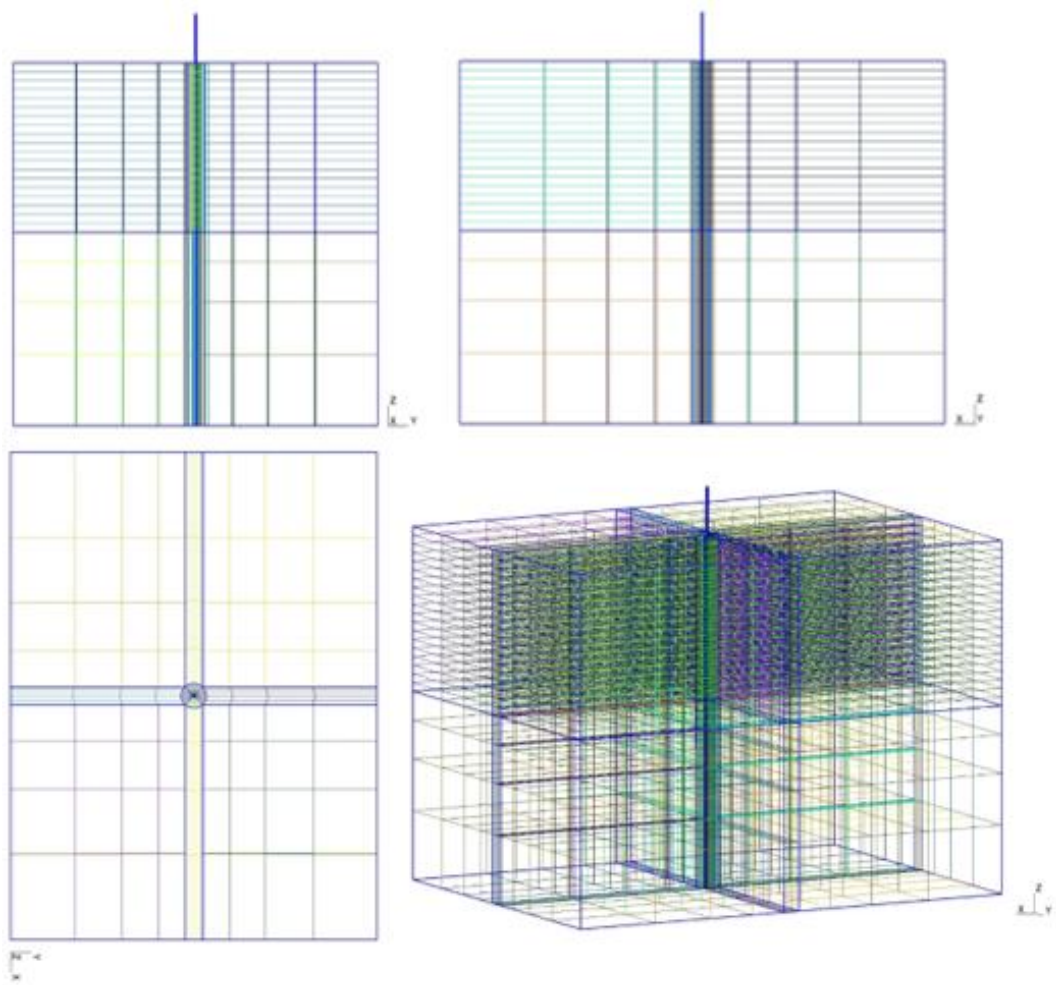


Figure 3-17 Meshing tissue respiration model: front view, side view, top view and orthogonal view

3.5.4 Boundary conditions

The boundary conditions are the same as in the multiple loads model. However, in addition to the bottom surface, the left, right and front surfaces are also constrained in all degrees of freedom to mimic the skull. In addition, the top surface is clamped in except for the hole in the middle of the skull. The back surface of the tissue can move freely because the load is applied at this side. The applied pressure of 980 Pa stays the same, as in the multiple loads model. It is equally distributed at the caudal side. In addition, the frequency of 2 Hz corresponding with the breathing rate remains the same.

3.5.5 Solver

Only one time-varying load is applied to the brain tissue, the respiration at a frequency of 2 Hz. To simulate one full period, the simulation is done for a time span of 0,5 seconds. Twelve time steps of 0,0417 seconds are simulated to get an accurate simulation. The total processing CPU-time that ONELAB requires to do the calculations is 149 seconds. This is the quickest model by so far in terms of processing CPU-time. The ONELAB files are attached in Appendix L, provided on an electronic medium.

3.6 Conclusion

The FEM software package ONELAB is used to generate meshes and solve the FEM models. First, the elastic displacement of the tissue and the implant is calculated. Second, the viscoelastic displacement can be determined as the sum of elastic displacement differences multiplied by the reduced creep function. This is done for three different models, the multiple loads model, the heartbeat model and the respiration model. Linear acceleration, rotation, static intracranial pressure and respiration are incorporated in the multiple loads model whereas in the heartbeat and the respiration model respectively, the heartbeat and the respiration are used as inputs.

The tissue is modelled as viscoelastic in all three models. In the multiple loads model an elastic modulus of 3 MPa is used as an overall elastic modulus for the brain and meninges. In the heartbeat and respiration model, 50 kPa is used as an elastic modulus, while only modelling the brain tissue and not the meninges. Furthermore, the geometries consist of cuboids and the bottom surface and toggle point of the implant are clamped. The blood vessels are modelled as tubes in the heartbeat model. In the respiration model a skull is modelled by clamping all surfaces of the brain tissue except the caudal surface. The aspect ratio for the respiration model is better than the aspect ratios of the multiple loads model and the heartbeat model. This results from the fact that the respiration model has less slender elements than the multiple loads model and is less skewed than the heartbeat model.

4 RESULTS AND VERIFICATION OF FINITE ELEMENT MODELS

Now that the mathematical models have been drawn up and three different finite element models have been described, the models can be verified and the results can be interpreted. First, a convergence analysis is performed in order to investigate whether the number of nodes is high enough to achieve a desired accuracy. Second, a viscoelastic analysis is conducted to qualitatively test the viscoelasticity incorporated in the mathematical model. Next, the results of the simulation of each model are presented, after which they are verified by using already obtained values for the implant displacement in real rat brain tissue according to existing data. Finally, one model is chosen as the best model to validate. Based on this model an experiment set-up is built.

4.1 Convergence analysis

The convergence analysis is performed by varying the number of nodes in the mesh. A higher number of nodes means a higher level of accuracy of the calculations. Note that this does not imply that the model describes reality better. By increasing the number of nodes, the calculated displacement converges to a certain value. However, an infinite number of nodes results in an infinite calculation time. Because of that, a trade-off must be made between accuracy and calculation time.

4.1.1 Multiple loads model

As mentioned in 3.3.3, five corner nodes are placed on all lines of the sub volumes of the tissue and the implant. Twenty corner nodes are placed on the lines corresponding to the insertion depth and the length between the upper surface of the tissue and the top of the implant. This results in a total of 7631 nodes and an average CPU-time for all loads of 341 seconds. The number of corner nodes placed on the lines is varied in order to conduct the convergence analysis. First, only three and twelve corner nodes are placed instead of the earlier mentioned five and twenty corner nodes. This results in 1295 nodes and a CPU-time of 20 seconds. Second, four and sixteen nodes are placed resulting in 3580 nodes and a CPU-time of 89 seconds. The third simulation uses 7631 nodes, as mentioned above. Finally, six and 24 nodes are placed resulting in a total of 13952 nodes and a CPU-time of 1009 seconds.

The maximal implant tip displacement in rostral direction and over time serves as the analysed converging factor. Figure 4-1 shows that the calculated values converge as the number of nodes increases. It ranges from 13,63 to 14,70 μm , with a difference of 1,07 μm between the smallest number of nodes and the largest number of nodes. The third calculated value is 14,55 μm and thus is more accurate than the first two calculated displacements. Its CPU-time is almost three times shorter than the CPU-time of the fourth simulation, which is on the other

hand more accurate. However, the third simulation is sufficiently accurate as well as fast enough. The convergence graphs of the separate loads are added in Appendix C.

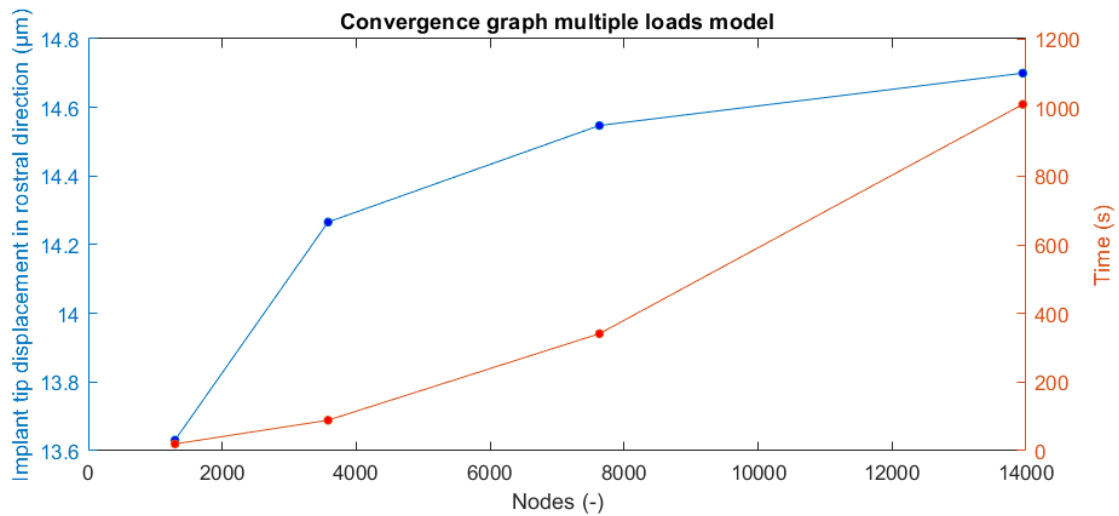


Figure 4-1 Convergence graph multiple loads model, all loads

4.1.2 Heartbeat model

A totally similar convergence analysis is performed for the heartbeat model. Four corner nodes are placed on all lines of the sub volumes, as described in 3.4.3. This results in a total of 3080 nodes and a CPU-time of 147 seconds. Four simulations are performed with respectively two, three, four and five corner nodes placed on the lines. This results in respectively 168, 1018, 3080 and 6882 nodes and CPU-times of 2, 29, 147, 517 seconds. Figure 4-2 shows the convergence graph for the heartbeat model. The displacement ranges from 2,34 to 4,45 µm, the third simulation reaches a value of 4,20 µm. The second simulation results in an unexpected high value. Probably this can be explained by the skewness of the elements resulting in calculation deviations. Indeed, skewness has to be limited. However, from the third to the fourth simulation the value converges again. Hence, the third simulation is better in terms of accuracy than the first and second simulation and in terms of speed better than the fourth calculation.

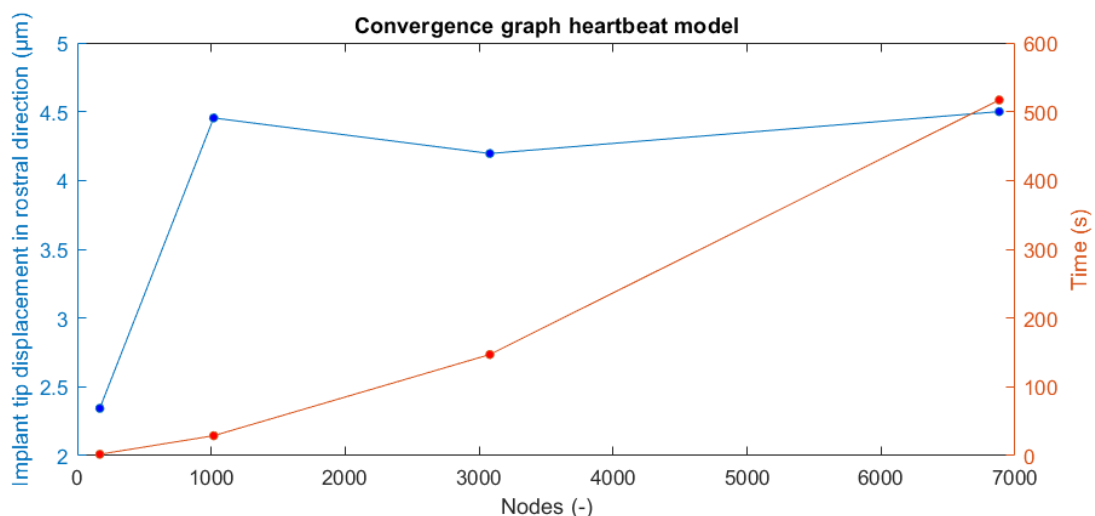


Figure 4-2 Convergence graph heartbeat model

4.1.3 Respiration model

A final convergence analysis is performed for the respiration model. As mentioned in 3.5.3, five corner nodes are placed on all lines of the sub volumes, twenty in terms of the insertion depth. Four simulations are performed with respectively three, four, five and six corner nodes and twelve, sixteen, twenty and 24 corner nodes placed on the lines. This results in respectively 1500, 4190, 8984 and 16488 nodes and CPU-times of 8, 41, 155, 479 seconds. Figure 4-3 shows the convergence graph for the respiration model. The displacement ranges from 64,6 to 71,6 μm , the third simulation reaches a value of 70,6 μm . The result of the fourth simulation is the most accurate. The first, second and third simulation deviate by respectively 7 μm , 3 μm and 1 μm . Hence, this third simulation again proofs to be more accurate compared to the first and second simulation. It is also faster than the fourth simulation.

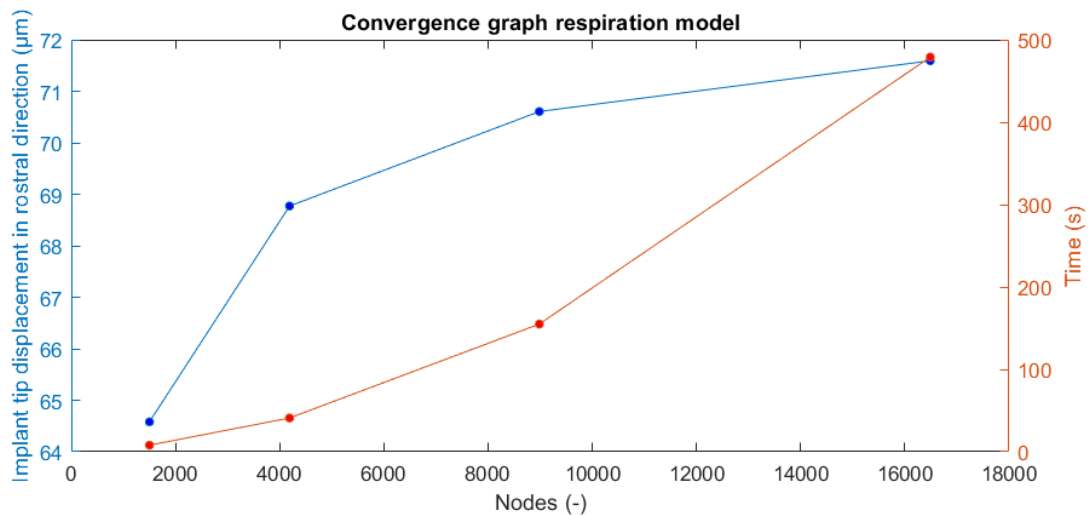


Figure 4-3 Convergence graph respiration model

4.2 Viscoelastic analysis

The strain increases linearly in elastic materials by increasing the load. This is however not the case for viscoelastic materials. Figure 4-4 shows that when a constant load is applied there is instant strain but also creep over time. Retracting the constant load results in an instant strain drop but also relaxation over time. Hence, linearly increasing the load does not result in a linear increase of the strain. When additional loads are added, there is an increase of creep in the material.

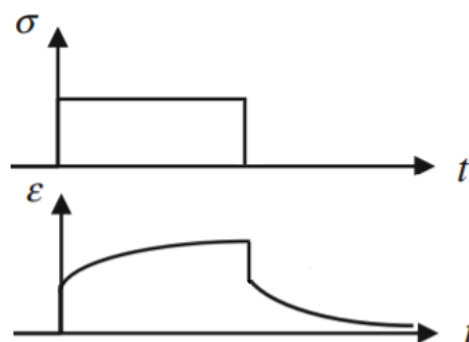


Figure 4-4 Creep and relaxation

The viscoelasticity incorporated in the model is tested by applying a force at the right surface of the tissue in the multiple loads model. More specifically, this is a stepwise force of 0,025 N. Each step, 0,025 N is added to the load until the load reaches 0,125 N, after which the load is reduced during five steps by 0,025 N. During the two last steps, no load is applied. The time length of one step is 42 ms, the total time is 0,5 s. The implant tip displacement towards the left direction is plotted in Figure 4-5. The displacement difference between the start and the end of a time step increases due to creep while the load increases. In addition, the reverse is true due to relaxation. The displacement difference between the start and end of a time step increases while the load decreases. Hence, a hysteresis curve is determined, the area inside is the energy lost during the loading and unloading cycle. This is in contrast with an elastic material in which energy is stored during strain as strain energy. After unloading, the displacement is not zero, whereas during the last two time steps it decreases towards zero. All foregoing findings lead to the conclusion that the model exhibits viscoelastic behaviour.

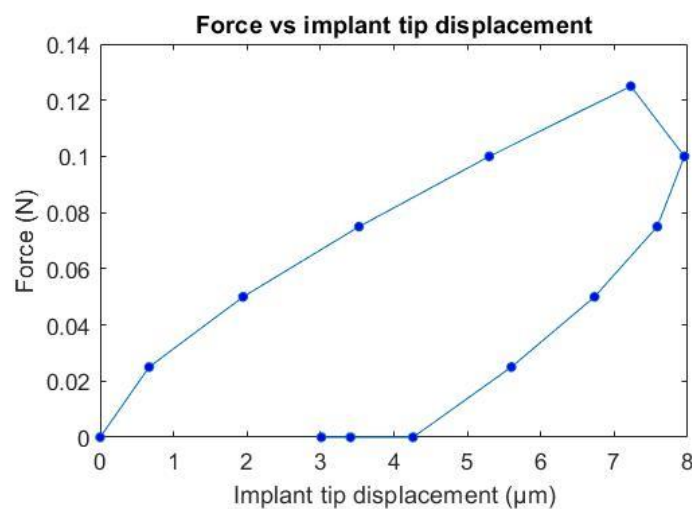


Figure 4-5 Force versus implant tip displacement

4.3 Results discussion

Since the FEM model was set up to estimate the implant displacement, a discussion on resulting qualitative and quantitative behaviour of the implant is necessary. Configuration B is modelled in Figure 3-7. The implant is estimated to toggle around its toggle point while bending is not expected. The largest implant displacement is estimated to be at the tip. Therefore, the tip displacement is the most important displacement. In addition, colour plots of the entire implant displacement are discussed. This is done for the multiple loads model, the heartbeat model and the respiration model. Note all displacements are enlarged on all figures.

4.3.1 Multiple loads model

Linear acceleration, rotation, intracranial static pressure and respiration are the loads applied in the multiple loads model. A simulation is performed for each single load. These simulations are then used to compose the total displacement vector. A colour plot of the implant and tissue displacement is given for each load. These colour plots are all sections in the sagittal plane. The x-, y- and z-axis point respectively towards the rostral, left and dorsal direction.

4.3.1.1 Linear acceleration

Figure 4-6 is a colour plot of the displacement field at the step where most displacement is observed. It is a section in the sagittal plane. Note that the displacement field is averaged for a better visualisation. The maximal displacement of the implant is $7,32\text{ }\mu\text{m}$, which is situated close to the upper surface of the tissue. It is clear that the implant toggles towards the rostral side but bends towards the caudal side. This bending is most probably a result of the stiff tissue and the totally clamped bottom surface of the tissue. The displacement magnitude depends on the distance to that bottom surface. The toggling towards the rostral side is expected as the linear acceleration points towards that direction. There is no lateral displacement.

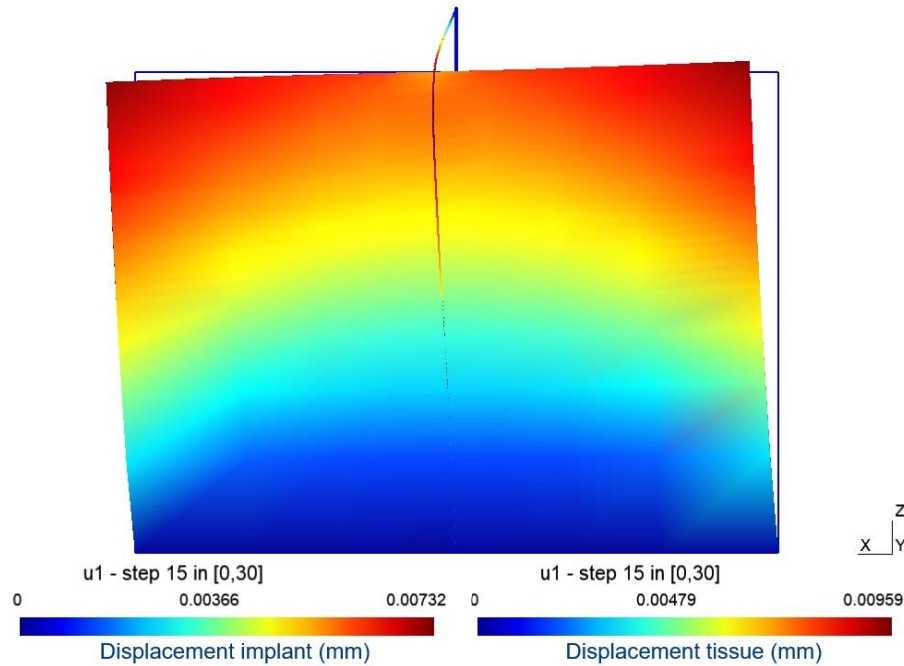


Figure 4-6 Colour plot displacement due to linear acceleration (section in sagittal plane)

As mentioned in 3.2, the viscoelastic displacement is calculated based on the elastic displacement. It is worthwhile to plot both the elastic and the viscoelastic displacement as depicted in Figure 4-7 to discuss differences between both displacements. The implant tip displacement in the rostral direction is plotted for 30 points of time. Two major differences can be clearly observed. The first difference is the magnitude difference as a result of creep. The second difference is a phase shift due to the viscous and elastic behaviour of the material. The strain of an elastic material is in phase with the stress. The sinusoidal stress is applied from time 0 and a phase shift is not visible as far as the elastic displacement is concerned. However, viscous strain lags the stress with a phase shift of 90° because the strain rate is the highest at the highest stress rate (Vincent, 2012). Hence, the phase shift of a viscoelastic material equals a value between 0° and 90° . The larger the phase shift, the higher the viscosity. Note that the time discretisation is not that accurate for only six points of time in one period. However, the sinusoidal signal is clearly observable.

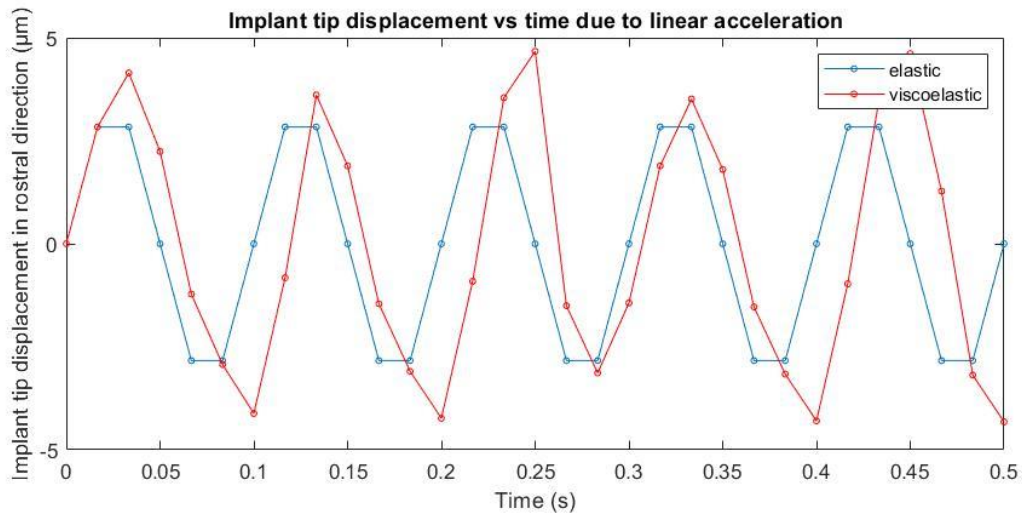


Figure 4-7 Viscoelastic and elastic implant tip displacement in rostral direction due to linear acceleration

4.3.1.2 Rotation

A constant load applied to the tissue during rotation is assumed. Figure 4-8 shows the top view of the simulation. The tissue clearly rotates around the COR towards the right side and translates towards the rostral side. The maximal displacement of the implant is $0,0764 \mu\text{m}$, which is very small compared to the displacements resulting from other loads. Figure 4-9 shows a section in the sagittal plane. There is a larger displacement towards the rostral side because the normal force is applied at that side.

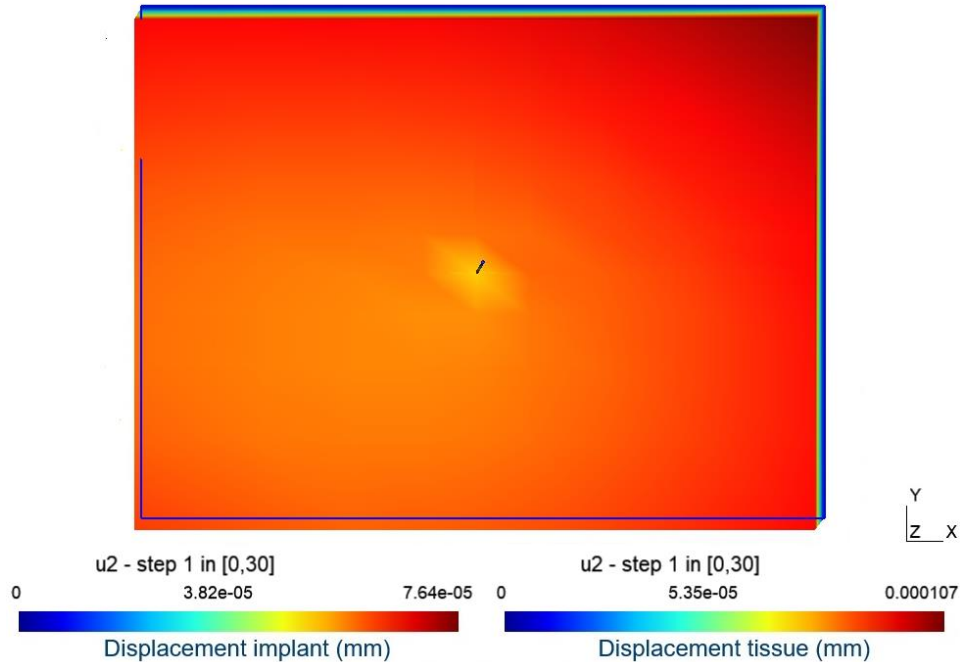


Figure 4-8 Colour plot displacement due to rotation (top view)

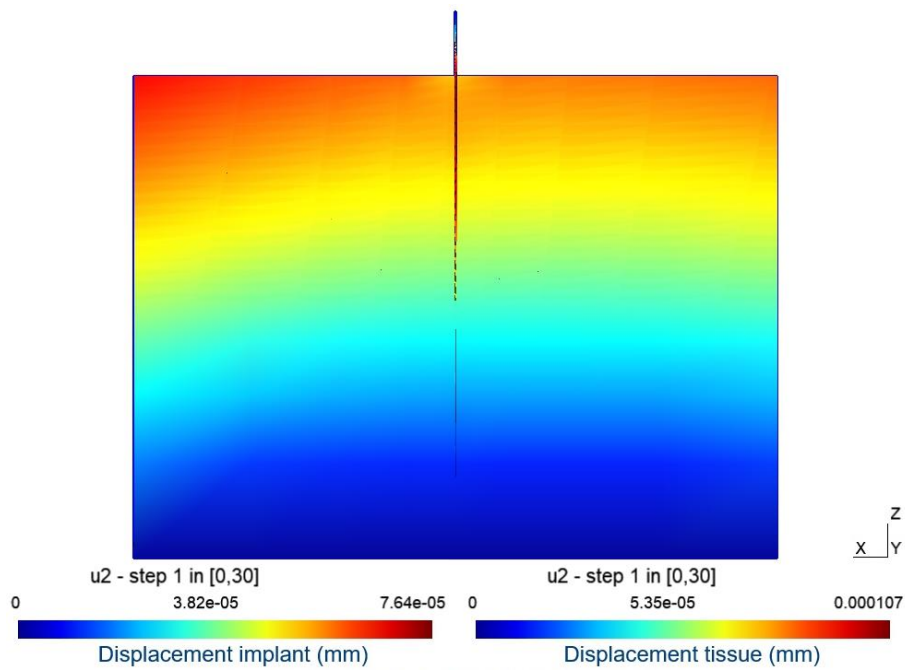


Figure 4-9 Colour plot displacement due to rotation (section in sagittal plane)

4.3.1.3 Static intracranial pressure

The static intracranial pressure results in static load applied to all sides of the tissue, except at the bottom. Figure 4-10 shows a section in the sagittal plane of the displacement field. The tissue displacement is clearly more constrained towards the clamped bottom surface and towards the glued connection with the implant. The maximal implant displacement is 0,187 μm .

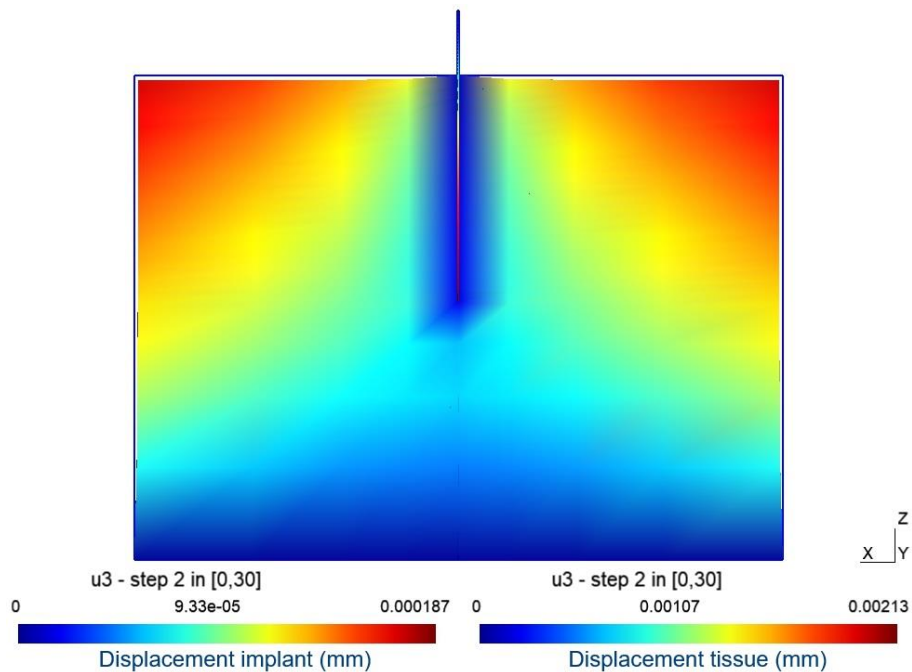


Figure 4-10 Colour plot displacement due to static intracranial pressure (section in sagittal plane)

4.3.1.4 Respiration

As mentioned earlier, respiration is modelled as a sinusoidal wave with an amplitude of 980 Pa and with a frequency of 2 Hz applied at the caudal side of the tissue. The largest displacement is visible at the top of the caudal surface in Figure 4-11. Similar to the simulation of the linear acceleration, both toggling and bending are observed. The largest displacement of 18 μm is situated close to the upper surface.

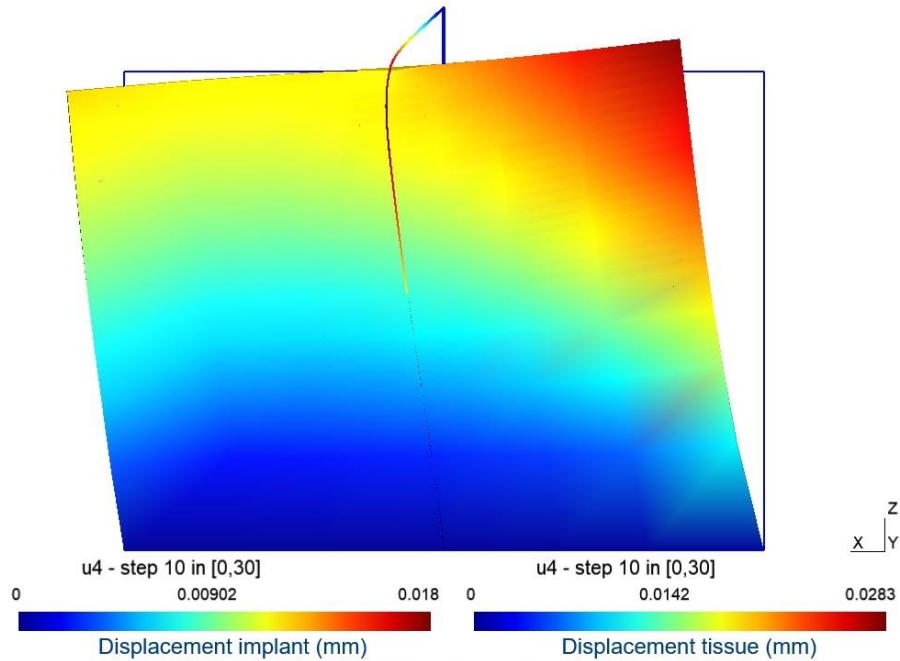


Figure 4-11 Colour plot displacement due to respiration (section in sagittal plane)

Figure 4-12 shows the plot of the elastic and viscoelastic implant tip displacement for 30 points of time. The phase shift between both is clearly visible and is estimated at approximately 35° . The viscoelastic displacement is definitely larger than the elastic displacement. Again, this is a result of the creep in the material. The maximal tip displacement is 11,63 μm .

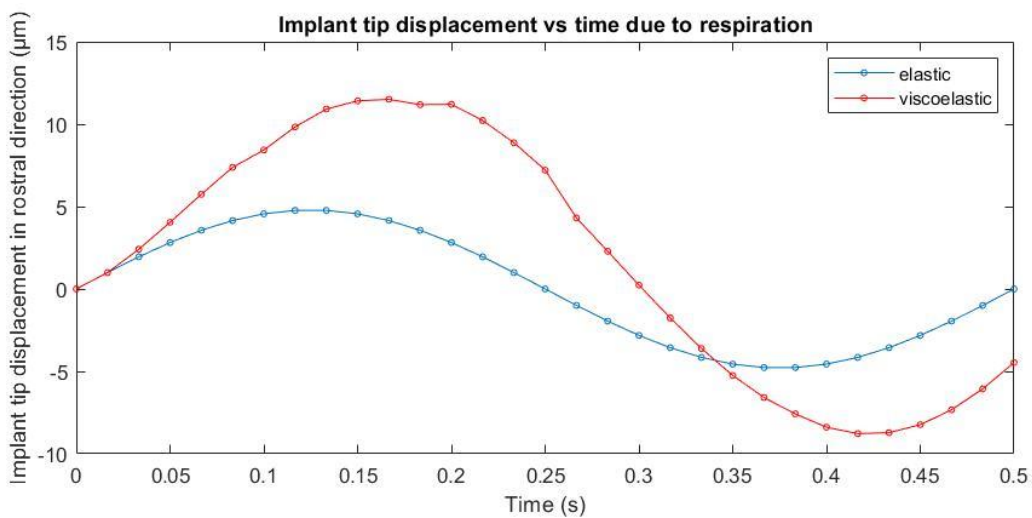


Figure 4-12 Viscoelastic and elastic implant tip displacement in rostral direction due to respiration

4.3.1.5 Multiple loads

All loads can be combined in one colour plot in Figure 4-13. Similar to the other colour plots, this is a section in the sagittal plane. The displacements due to rotation and static intracranial pressure can be neglected in comparison with the displacements of the linear acceleration and the respiration. Therefore, the linear acceleration and respiration contribute the most to the total displacement. Again, a maximal implant displacement is observed near the upper surface, equal to 22,8 μm .

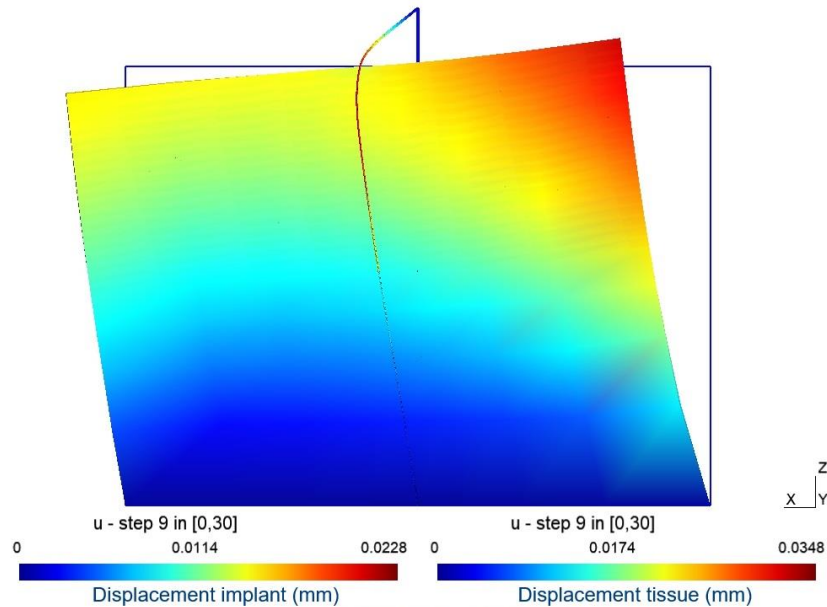


Figure 4-13 Colour plot displacement due to multiple loads (section in sagittal plane)

Finally, Figure 4-14 shows a plot of the implant tip displacement due to all loads. The maximal viscoelastic implant tip displacement is 14,55 μm , which is again larger than the calculated elastic displacement. Note that the two frequencies are clearly observable, more specifically 2 Hz and 10 Hz. 2 Hz corresponds with the respiration and 10 Hz with the linear acceleration. In the mathematical model all previous points of time are taken into account. However, there are no points of time before the start time. Hence, no full viscoelastic period is simulated.

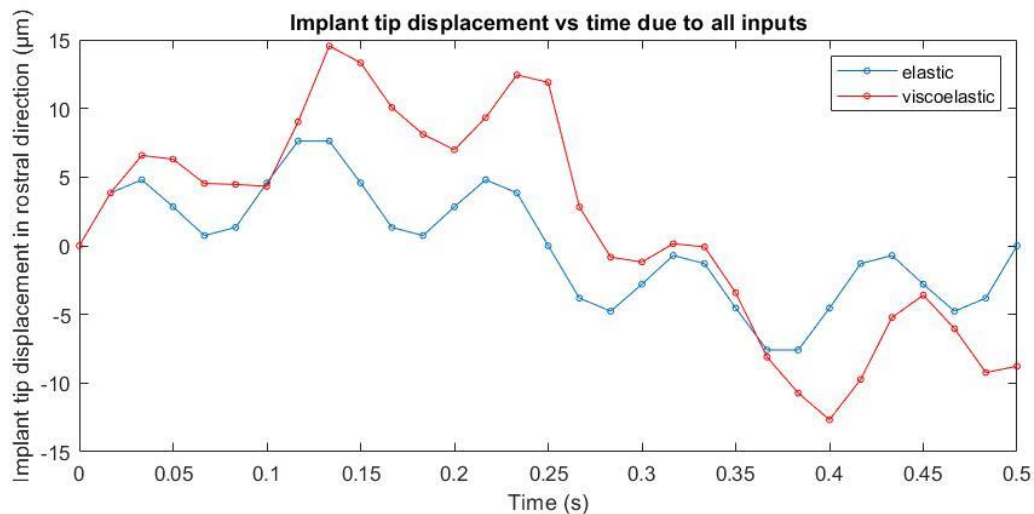


Figure 4-14 Viscoelastic and elastic implant tip displacement in rostral direction due to multiple loads

4.3.2 Heartbeat model

The displacement field of the heartbeat model looks totally different, compared to the multiple loads model. Loads are applied in tubes, mimicking blood vessels. The applied pressures are determined in 3.4.4, with the pressure applied in the caudal tube much bigger than the one applied in the rostral tube. Therefore, a displacement towards the rostral side is expected, which is visible in a section of the sagittal plane in Figure 4-15. In this model the implant does not bend but only toggles around its toggle point, which is better visible in Figure 4-25. Hence, the maximal displacement of the implant is situated at the tip and equals $4,25\text{ }\mu\text{m}$. This tissue has an elastic modulus of 50 kPa, which is much smaller than the elastic modulus of 3 MPa in the previous model. This is why the implant experiences less resistance and consequently does not bend in the heartbeat model. For a complete view on the inputs, a section of the transverse plane is added in Figure 4-16. The pressures in the left and the right tube are equal, resulting in an absence of displacement in the lateral direction.

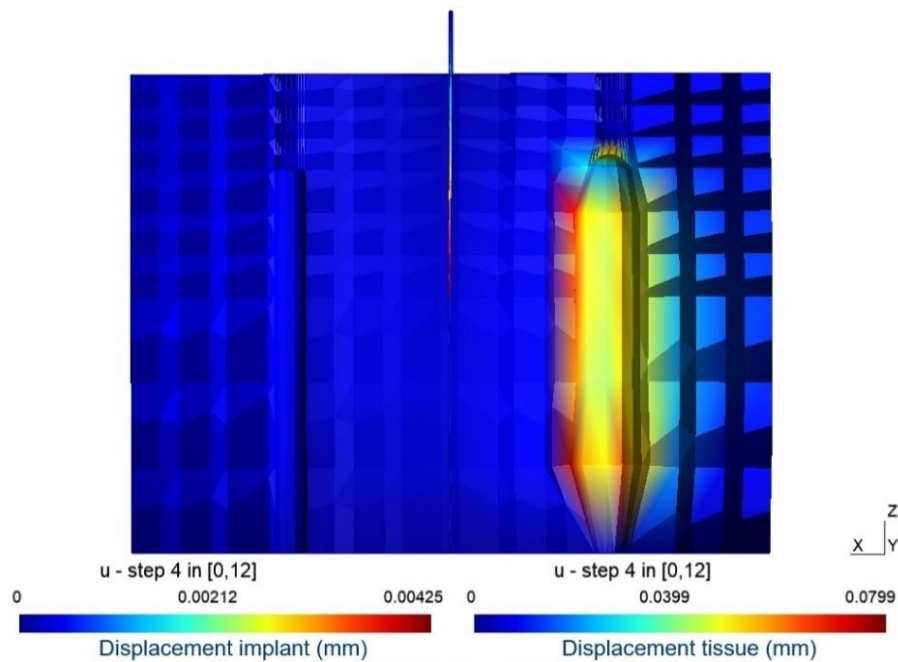


Figure 4-15 Colour plot displacement due to heartbeat (section in sagittal plane)

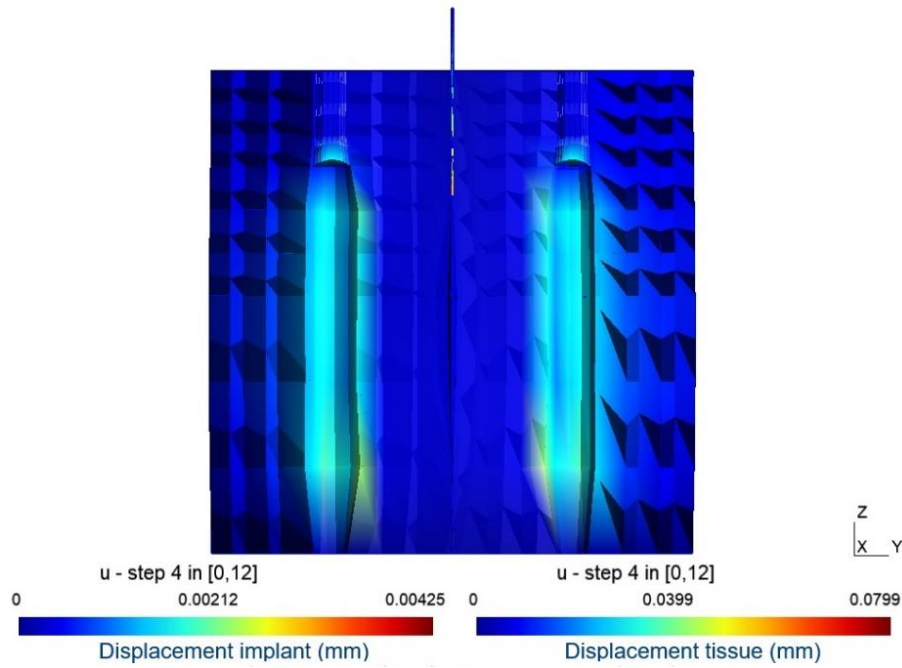


Figure 4-16 Colour plot displacement due to heartbeat (section in transverse plane)

Figure 4-17 shows the elastic and viscoelastic displacement in rostral direction at the implant tip due to the heartbeat. Similar to previous comparisons there is a phase shift between the elastic and the viscoelastic displacement. Furthermore, the viscoelastic displacement is larger due to creep.

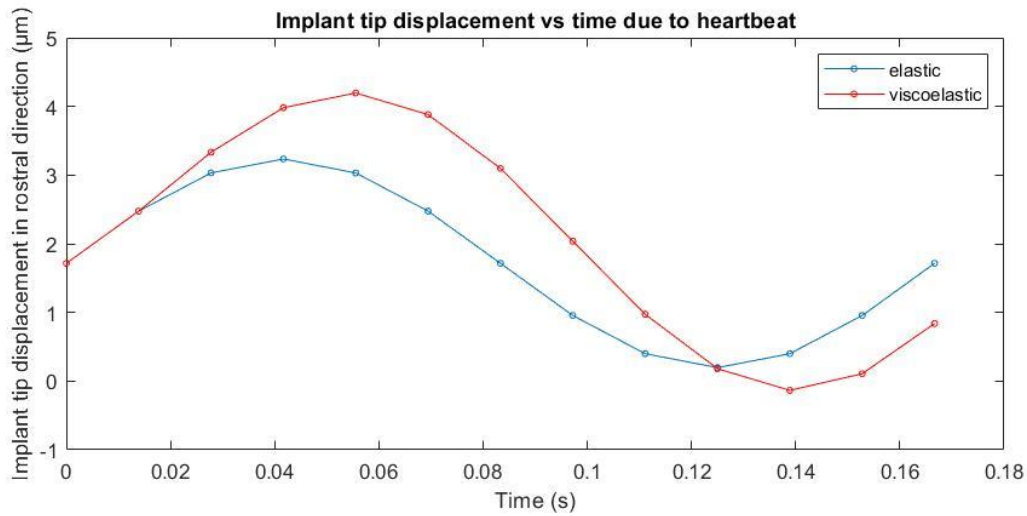


Figure 4-17 Viscoelastic and elastic implant tip displacement in rostral direction due to heartbeat

4.3.3 Respiration model

Unlike the other models, the front, left, right and top surface in this model are completely clamped. As a consequence, no large displacements are observable in a section of the sagittal plane as shown in Figure 4-18. As expected, the implant toggles around its toggle point towards the rostral side. In addition, the implant does not bend as a result of the low elastic modulus of the tissue. Hence, the maximal displacement of the implant is situated at the tip and equals 70,6 µm. Figure 4-19 also shows a section of the sagittal plane but from a different

angle. The caudal surface bends towards the midpoint of the surface. This is a result of clamping the surrounding surfaces.

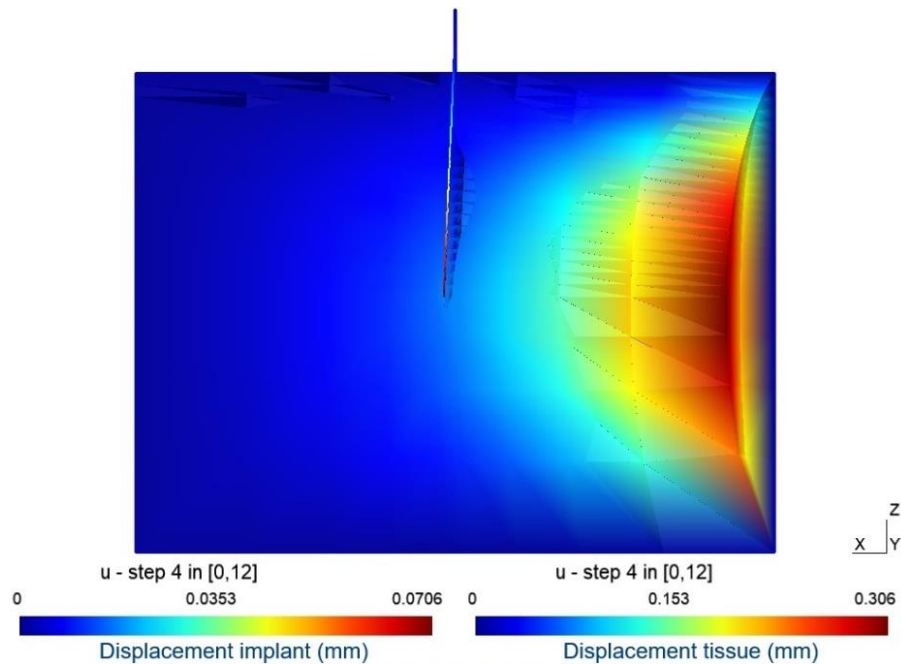


Figure 4-18 Colour plot displacement due to respiration acceleration (section in sagittal plane)

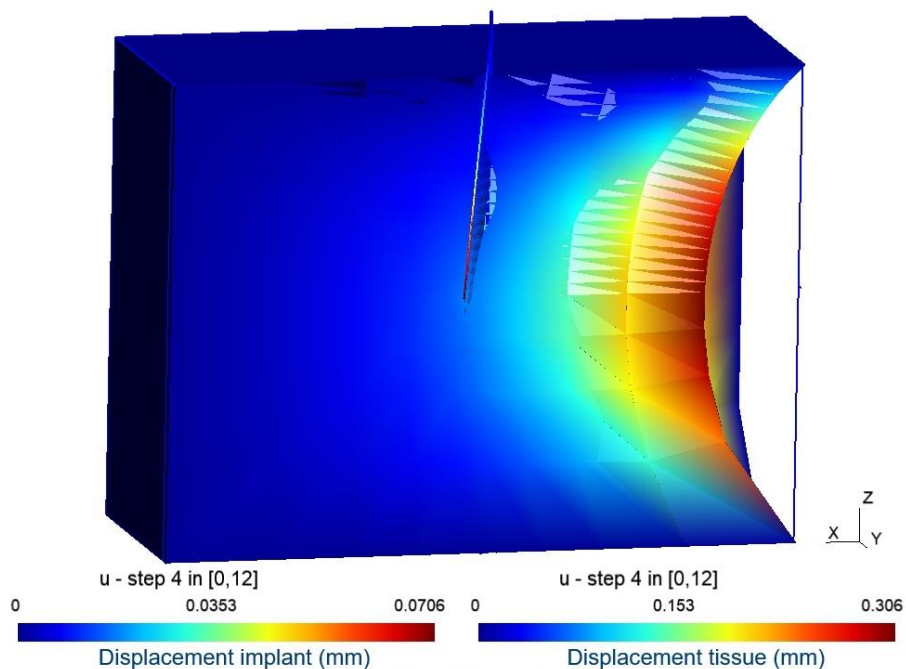


Figure 4-19 Colour plot displacement due to respiration (section)

Finally, Figure 4-20 shows the elastic and viscoelastic displacement due to respiration. The curves are very similar to the previously described curves. The creep again results in a phase shift and larger viscoelastic displacement. The displacement is more than six times larger than the displacement due to respiration in the multiple loads model plotted in Figure 4-12. This can be explained by the fact that the elastic modulus is smaller in this model, which is stated to be a better assumption.

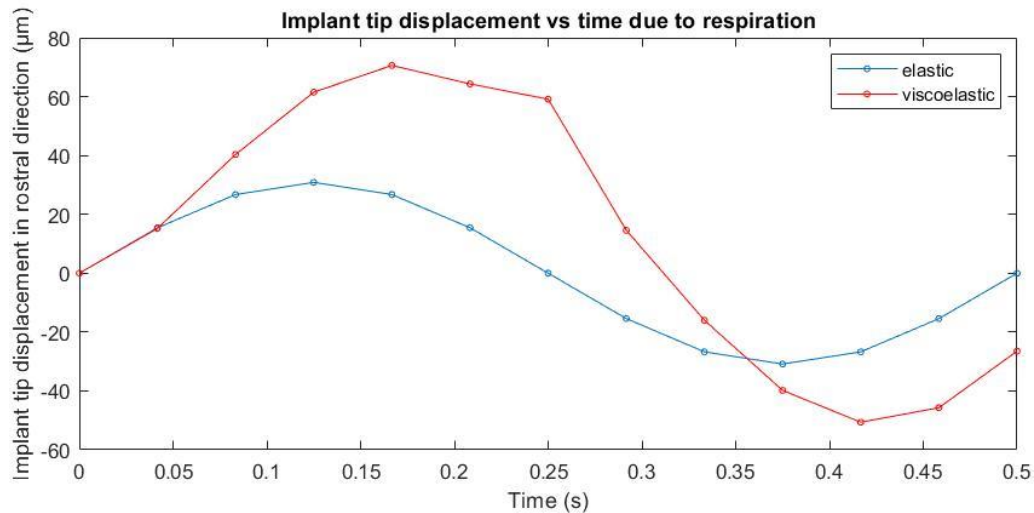


Figure 4-20 Viscoelastic and elastic implant tip displacement in rostral direction due to respiration

4.4 Verification

A verification of the results described above can be done based on available measurement data in existing research articles. However, not many studies have been done on implant displacements in rat brain. Hence, the verification is based on the research of Gilletti and Muthuswamy. The purpose of that research was to measure the surface micromotion in the somatosensory cortex, a part of the cerebrum, against implants, which are assumed to be stationary. Six adult male Sprague-Dawley rats, weighing 200 to 300 grams, were used in this study (Gilletti & Muthuswamy, 2006).

First, the rats were anesthetised and intubated, the tube was connected to a capnograph, which monitored the respiratory rate. The heart rate was sampled by placing electrodes into the right front and both rear limbs. Afterwards, a craniotomy, this is the removal of bone parts of the skull, was conducted 1 mm posterior of the bregma and 3 mm from the midline. In three rats, a small craniotomy was performed, whereas in the other three rats a large craniotomy was executed, with respective diameters of 2,35 mm and 4,7 mm. Figure 4-21 shows the three locations at which differential variable reluctance transducer is placed against the brain surface (Gilletti & Muthuswamy, 2006).

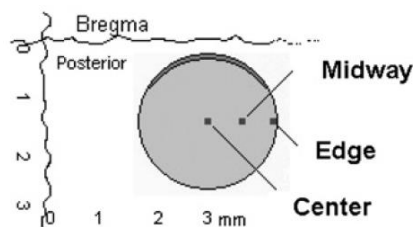


Figure 4-21 Approximate locations of displacement measurements in a small craniotomy (Gilletti & Muthuswamy, 2006)

The differential variable reluctance transducer measured the displacement perpendicular to the surface. In first instance, this was done with an intact dura mater, in second instance, after a removal of the dura mater. The displacement signal consisted of two periodic signals with different frequencies. Hence, the heart rate and respiratory rate were measured. Fundamental

frequencies between 4 Hz and 6 Hz and just below 2 Hz were determined. These signals were related to the displacement signal. Figure 4-22 and Figure 4-23 show the displacements of the surface. The first column of plots are the displacements for the first rodent, the second for the second, etc. The first rows are the respiration displacements and the second rows the cardiac displacements. The colours indicate the location and whether the dura is intact or not (Gilletti & Muthuswamy, 2006).

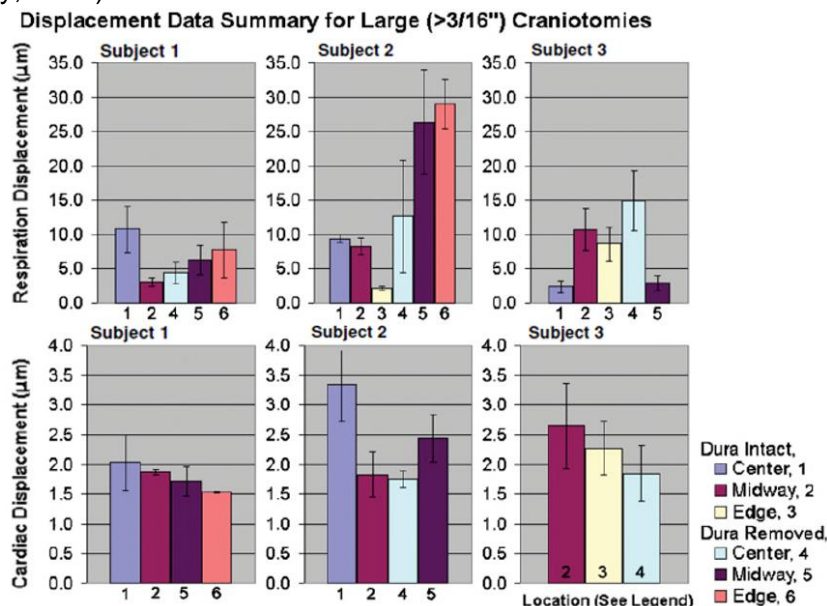


Figure 4-22 Displacement for large craniotomy, mean \pm standard deviation (Gilletti & Muthuswamy, 2006)

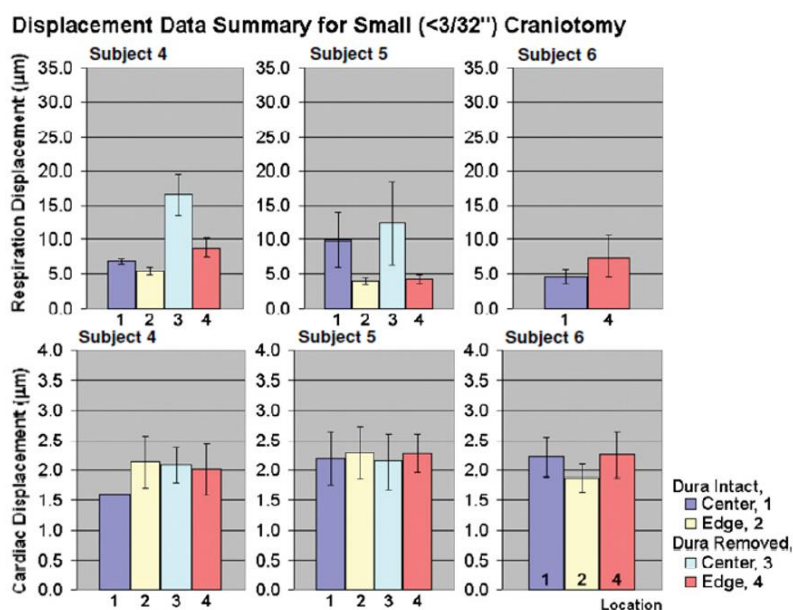


Figure 4-23 Displacement data summary for small craniotomy, mean \pm standard deviation (Gilletti & Muthuswamy, 2006)

In general, one can conclude that the removal of the dura has no influence on the cardiac displacement. This is not the case for respiration displacement, which is larger when the dura is removed. For large craniometries it reaches 30 μm . In addition, respiration displacements are larger for large craniotomies, while cardiac displacements are situated in the same range from 2 μm to 4 μm for both large and small craniotomies (Gilletti & Muthuswamy, 2006). Although these are displacements perpendicular to the brain surface, it is assumed that these

displacements also give an indication of the order of magnitude of the rostral displacements of the brain surface. When the brain surface moves up due to respiration or blood pressure, it also moves forward. Regarding respiration, this can be explained by considering the anatomy of the rat shown in Figure 4-24. The black arrow indicates the respiratory pressure direction towards the rat brain. The pressure waves propagate in the intermediate tissue. Due to the position of the brain with respect to the lungs, the pressure pushes the brain not only forward but also upward. Furthermore, when the blood pressure increases in the brain, the brain expands in all directions, while it contracts again in all directions when the blood pressure decreases.

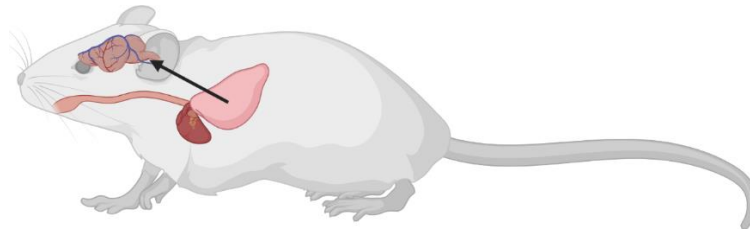


Figure 4-24 Rat with the brain, windpipe, heart and lungs, respiratory pressure direction towards the brain indicated by arrow

Figure 4-25 shows the implant displacement for the different models described. Note that the displacements are enlarged and only the respiration is applied in the multiple loads model. For that model, a section of the implant in the sagittal plane is placed at the right side. The rostral displacement of the implant at the level of the brain surface is $16,9 \mu\text{m}$. At the left side, a section of the respiration model is placed. The rostral displacement near the brain surface equals $11,4 \mu\text{m}$. It must also be noted that the craniotomy in the model has a diameter of 1 mm. Both rostral displacement values correspond with the normal displacement data due to respiration at the centre of a small craniotomy when the dura is removed. Finally, the rostral displacement field due to the heartbeat is placed in the middle of the figure. Near the brain surface it equals $1,4 \mu\text{m}$, which is a little less than the perpendicular displacement data range from $2 \mu\text{m}$ to $4 \mu\text{m}$. It can be concluded that the rostral displacements near the brain surface in the models correspond almost exactly with the perpendicular displacement data obtained by Gilletti and Muthuswamy.

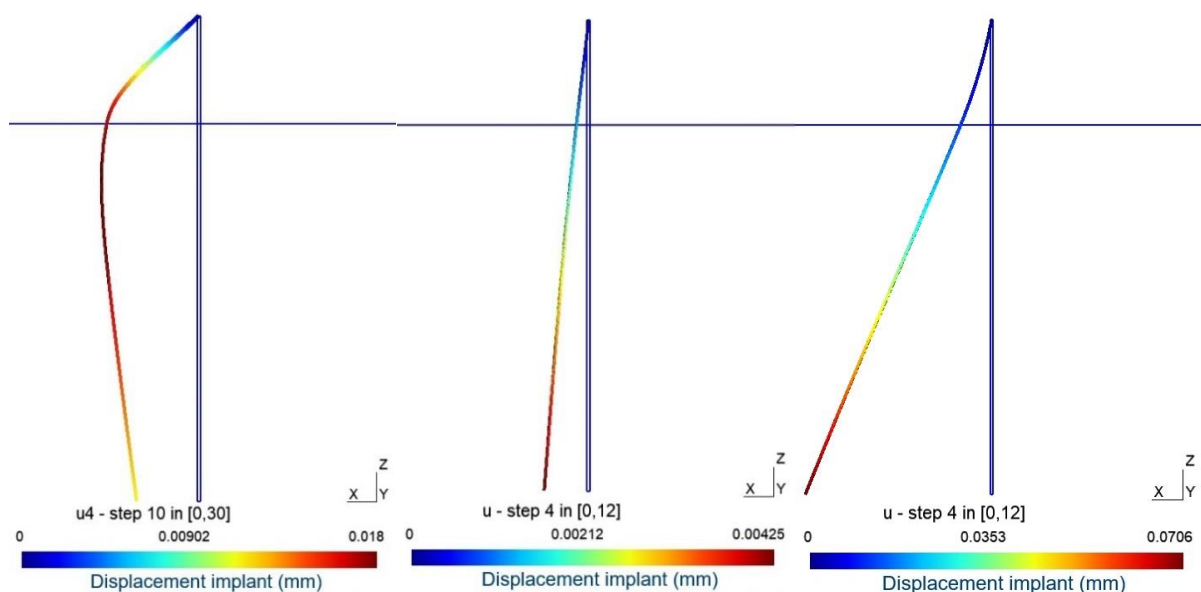


Figure 4-25 Implant displacement in the multiple loads model, heartbeat model and respiration model (section in sagittal plane)

4.5 Choice of model to be validated

A first observation is the different deformation of the implant in the multiple loads model compared to the heartbeat and respiration model. As mentioned before, the elastic modulus of the tissue in the last two models is 50 kPa, which is smaller than the modulus in the first model, which equals 3 MPa. An overall elastic modulus for both the brain and meninges tissue is assumed to be less valid than using only one elastic modulus for the brain tissue. When 50 kPa is used, only toggling can be observed, which is to be expected. Bending occurs unexpectedly due to an overall stiffer elastic modulus assumed in the multiple loads model. Hence, the heartbeat and the respiration model represent the brain tissue properties more accurately.

Second, adding the skull boundary constraints better mimics reality. This is only done in the respiration model. However, adding a skull to the heartbeat model would not decrease the implant displacement that much. That is because the displacement is related to the pressures in the tubes, which are applied through the already clamped bottom surface. Figure 4-15 and Figure 4-16 show that the surfaces barely displace without adding skull constraints.

Finally, the models show that respiration has the largest influence on the displacement, followed by linear acceleration, heartbeat, static intracranial pressure and rotation. The calculated values are verified by real displacement values due to heartbeat and respiration. Hence, the respiration model is advised to validate because it has the largest impact. In addition, a set-up for the respiration model is probably easier to develop and to use compared to a set-up for the heartbeat model. Figure 4-26 shows a concept sketch of the inputs for the heartbeat model on the left. Pumps are used to apply the pressure in the tubes. On the right, a concept sketch for the respiration model is shown. The use of a linear actuator is less complicated than the use of synchronised pumps.

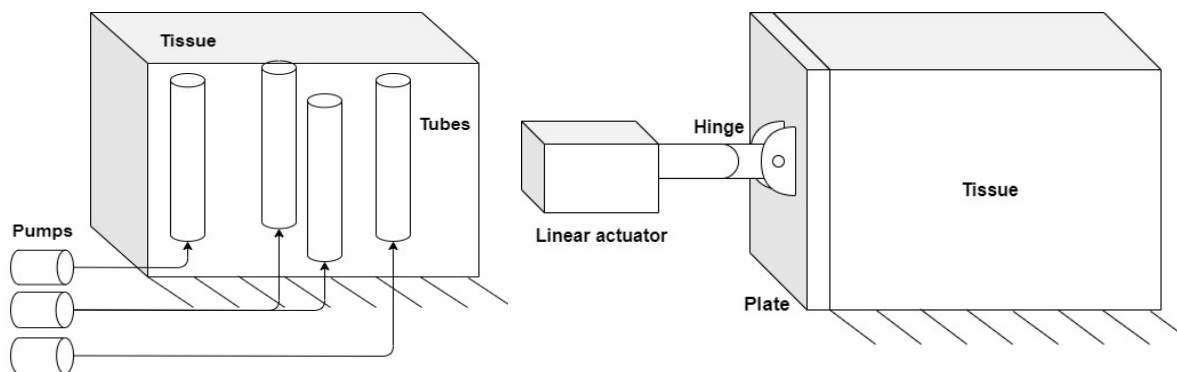


Figure 4-26 Concept sketches inputs

4.6 Conclusion

The convergence analyses show that the third simulation of each model is the best trade-off between accuracy and speed. In addition, based on the viscoelastic analysis, it appears that the tissue behaves viscoelastic in the models as desired. When the resulting rostral implant tip displacements are considered in the multiple loads model, it can be concluded that the respiration causes the largest displacement followed by linear acceleration, static intracranial pressure and rotation. Furthermore, the viscoelastic displacements due to respiration and linear

acceleration are larger than the calculated elastic displacements and are lagging these displacements. A similar effect is observed for the displacement in the heartbeat and the respiration model.

The maximal rostral implant displacement at the level of the brain surface equals 1,4 μm and 11,4 μm for respectively the heartbeat and the respiration model. The results of the FEM analyses are verified with research data on implant displacements perpendicular to the brain surface. The results are in the same order of magnitude as the research data results since the research data show an implant displacement ranging from 2 μm to 4 μm due to heartbeat and from 5 μm to 30 μm due to respiration. Finally, the respiration model is chosen to be validated because of the fact it causes the largest displacement based on the research data and the results of the FEM analyses.

5 EXPERIMENT SET-UP

It is the aim of the experiment set-up to validate the results obtained from the FEM model. Hence, a tissue phantom with implant represents the FEM model in a physical environment. A micromotion sensor measures the displacement of the implant in the tissue, established by an actuator. Therefore, some components are defined, i.e. a micromotion sensor, a frame to connect the micromotion sensor to the environment, an actuator and a hydrogel representing the tissue phantom. Figure 5-1 shows a CAD drawing of the experiment set-up. A mould, which contains the hydrogel, is placed in the middle underneath a frame onto an anti-vibration table. The actuator is attached to the mould at the caudal side while the micromotion sensor is attached to the frame. Note that all technical drawings are attached in Appendix J.

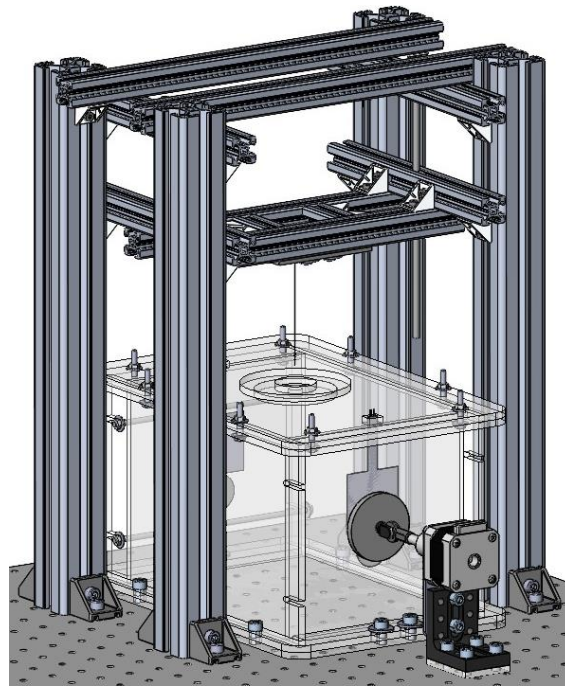


Figure 5-1 CAD drawing of the experiment set-up

5.1 Micromotion sensor

The implant micromotion in the tissue phantom has to be measured along the axial direction of the actuation. Therefore, some important constraints and practical trade-offs need to be taken into account. First, it is not feasible to have a micromotion sensor at the inserted section of the implant. Moreover, a limited space is available above the inserted section, taking into account the insertion depth with respect to the entire length of the implant.

Second, if the sensor is not directly embedded into the tissue or onto the implant and the sensor measures the micromotion for instance remotely, then the visual appearance is of importance. The opacity of the tissue can cause a restricted view of the inserted part of the implant. Also other physical properties, like the refractive index or vibration damping, obstruct mechanical and electromagnetic waves towards the implant.

5.1.1 Selection

The sensor selection is generally split up into three parts, a remote displacement measurement device, a proximity measurement external device and a measurement device directly placed on the implant measuring a certain deformation of the implant module.

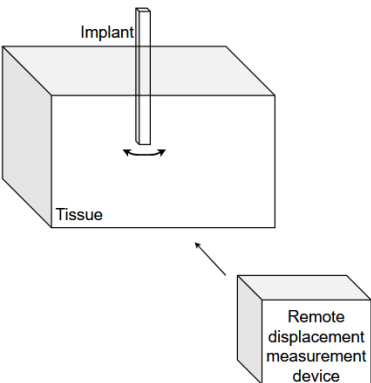
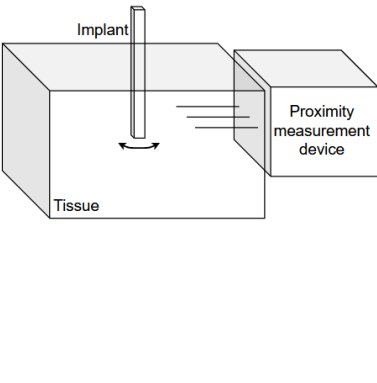
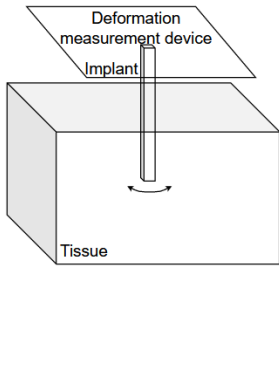
Remote measurement devices based on a vision technique, like a recording system with a camera for instance, are useful when the implant is visible. However, if the implant is not visible, advanced illumination techniques can provide a visible image of the implant in the opaque tissue. Still, a good image processing system is required in order to have an accurate image of the implant at a certain distance from the camera.

A proximity sensor expresses the change in distance of the implant with respect to the sensor itself in electrical quantities. However, the sensitivity decreases with an increasing distance and this distance is imposed because of geometry constraints. Furthermore, the material of the tissue can block rays coming from the sensor. Moreover, a laser-based technique, for instance, has some drawbacks regarding the misalignments of the laser and it requires substantial equipment, which is usually expensive.

Measuring the deformation in the implant module ensures a direct measurement without taking into account the surroundings of the tissue. The deformation is measurable in electrical quantities, although it is required to condition these quantities. In addition, the deformation has to be converted into a displacement of the implant tip.

Table 5-1 shows an overview of the considered measurement principles. Within these categories, some examples are given as well as clarifying drawings.

Table 5-1 Selection of the implant displacement sensor

Remote measurement	Proximity measurement	Deformation measurement
		
Example: <ul style="list-style-type: none"> • Vision sensor 	Examples: <ul style="list-style-type: none"> • Capacitive sensor • Inductive sensor • Hall-effect sensor • Ultrasonic sensor • Laser sensor 	Examples: <ul style="list-style-type: none"> • Strain gauge sensor • Piezoresistive sensor

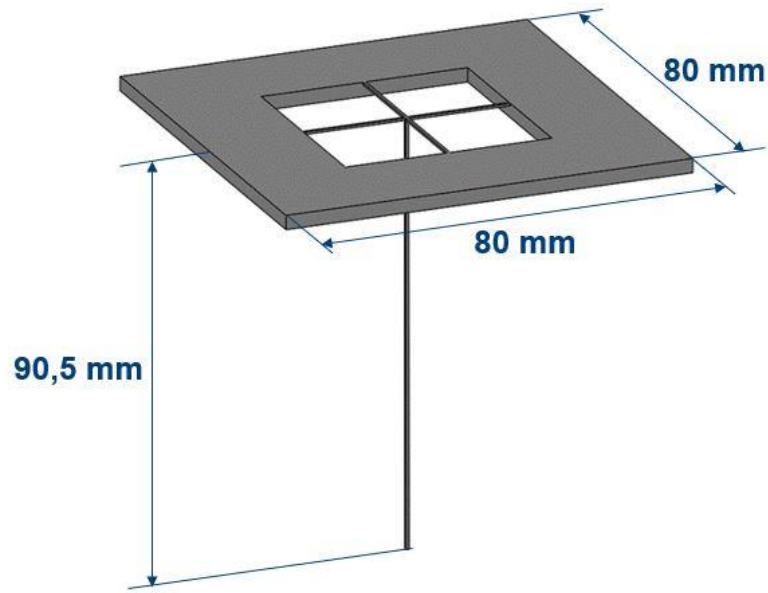


Figure 5-2 CAD drawing of the first iteration of the implant module

The measurement of electrical quantities in the design of a deformation sensor with strain gauges or piezo resistive sensors can be interpreted immediately during the experiment. The design shown in Figure 5-2 is inspired by a sensor measuring microdisplacements (Wu, et al., 2014). Figure 5-3 shows the sensor, which is originally designed with piezoresistive sensitive parts. The principle remains the same when the sensor is modified and the piezo electric parts are replaced by strain gauges. The strain gauges will measure a strain in the sensitive area in order to measure a displacement of the shank of the implant structure. This implies that the sensitive beams need to be as thin as possible.

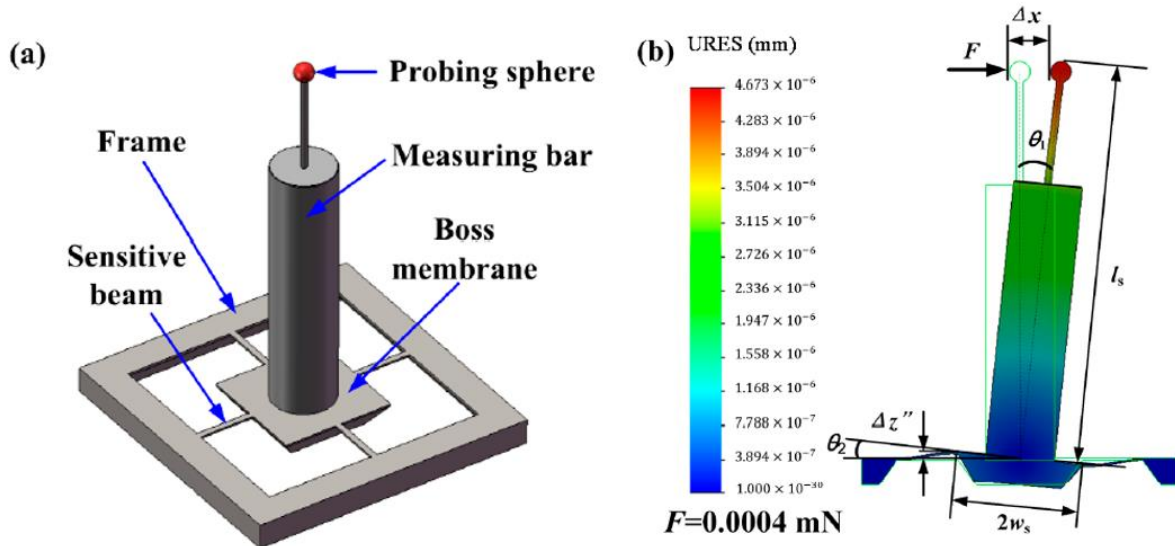


Figure 5-3 Microdisplacement sensor (Wu, et al., 2014)

Because of the above mentioned considerations and the advantages of a simple data acquisition, the strain gauges are the most suitable candidate. The technical camera does not suffice because of the required illumination infrastructure, nor does the laser due to the complicated infrastructure settings. Furthermore, the proximity sensor requires another geometry in order

to measure with high resolving power. The choice between piezoresistive sensitive parts and strain gauges is determined by the fabrication process. The piezoresistive sensing unit uses a MEMS bulk silicon process and thus requires silicon wafers. Strain gauges, on the other hand, are available of the shelf in a large variety of sizes, geometries, materials and applications.

5.1.2 Mechanical design

The mechanical design of the implant module with attached strain gauges entails a material selection in order to obtain a suitable elastic modulus according to the FEM model. The material selection interacts with the selection of a suitable production process, meaning that the number of materials is limited.

5.1.2.1 Production process selection

A major limitation of the implant module is the manufacturability constraint of the implant. The real-scale implant has an area of $60\text{ }\mu\text{m}$ by $60\text{ }\mu\text{m}$. Only a few production processes are suitable to ensure the manufacturability of the implant. Most of them are either too expensive for this experiment set-up or not suitable with regard to the required mechanical properties of the implant. Machining processes on a microscale are expensive and require high precision cutting. Likewise, casting processes require an expensive mould and are complicated for three-dimensional geometries with concave and convex shapes with perpendicular adjacent surfaces. In short, this means that these production processes are not feasible. Additive production processes, on the other hand, are achievable. Metal 3D printing techniques can perform high precisions and show an added value in terms of production time and cost in a prototyping phase. Provided that some design constraints are taken into account, it is fairly easy to go from the CAD design to the production of a finished product. However, there are again geometrical and dimensional constraints. The minimal wall thickness as well as the maximum build dimensions and the minimum layer thickness are significant limitations to take into account.

Materialise is a specialist in the area of additive manufacturing and one of its services is the 3D printing of metal parts. According to its design guidelines and technical specifications, a minimal wall thickness of $0,5\text{ mm}$ is required. The maximum achievable building volume is limited to $500\text{ mm} \times 280\text{ mm} \times 315\text{ mm}$ and the layer thickness varies from $0,03\text{ mm}$ to $0,1\text{ mm}$ depending on the material used (Materialise, 2020).

Because of the limitations in minimal wall thickness and due to the limitation of size of the strain gauges, a dimensional scale factor of 10:1 applies when building and testing the experiment set-up. This means that the dimensions of the tissue and the dimensions of the implant scale up ten times so that the implant width and thickness equal $600\text{ }\mu\text{m}$. This complies with the design guidelines and the technical specifications of the 3D printing process. Consequently, the same scale factor also applies to the dimensions of the tissue. This entails a scaled height of 150 mm , a width of 150 mm and a length of 200 mm .

5.1.2.2 Material selection

The selection of the material depends on the desired mechanical properties and the adhesiveness of the implant structure and the strain gauges. Only a limited number of materials is available at Materialise for the 3D printing of the metal implant, all with different elastic moduli, yield strengths, roughness etc. A selection procedure and feasibility analysis reveal which material is the best option for the implant application. The following materials are analysed:

- Titanium alloy (Ti₆Al₄V)
- Stainless Steel (SS316L)
- Aluminium alloy (AlSi₁₀Mg)

First, multiple criteria are defined to select the material:

1. 3D printing performance: 3D printing processes differ depending on the metal used. Furthermore, the long implant cannot be printed straight in every material.
2. Elastic modulus: the elastic modulus preferably corresponds with the elastic modulus of silicon.
3. Maximum thickness of arms: the finite element models result in a certain strain. When the same strain for each material is assumed, the thickness of the arms can be calculated. The product of elastic modulus and moment of inertia is held constant in this calculation.
4. Minimum printing thickness: this is the minimum thickness, which the 3D printer can produce.
5. Cost: the cost of one piece.
6. Lead time: total process time.

Second, these materials are listed in Table 5-2. For each material a qualitative or quantitative indication is given. Finally, some conclusions can be made based on this table. The first material eliminated is aluminium because 0,7 mm cannot be printed and the performance does not suffice. A second conclusion is that the risk of buckling (of the arms) is the same for titanium and stainless steel, because of the equal products of elastic moduli E and moments of inertia I (EI). Despite the fact that titanium has the best performance, stainless steel is chosen because of the following reasons: the best approximation of the elastic modulus of silicon 165 GPa, low cost, short lead time and the same thickness of arms as in the model.

Table 5-2 Criteria material selection implant

Material Criterium	Titanium alloy (Ti ₆ Al ₄ V)	Stainless Steel (SS316L)	Aluminium alloy (AlSi ₁₀ Mg)
3D printing performance	Best	Good	Bad
Elastic modulus (GPa)	110	180	70
Maximum thickness of arms (mm)	0,6	0,5	0,7
Minimum printing thickness (mm)	0,5	0,5	1,5
Cost (€)	360	280	200
Lead time (days)	12	10	7

5.1.2.3 Design guidelines and constraints

Taken into consideration the material properties and limitations of performance graded SS316L, the implant module is designed as shown in Figure 5-4. The top surface is flat and provides a solid base to print on. The design thus indicates that this part will be printed upside down. This limits the amount of supports because every layer will be on top of a previous layer without supporting studs. The strain gauges are attached on the beams at the top, therefore these beams need to be as thin as possible in order to have a sensitive module. Thus, the

thickness of the beams is limited to 0,5 mm according to the minimum achievable wall thickness (Materialise, 2020). The width equals the width of the upscaled implant of 0,6 mm (= 600 μm). The length of one beam is 20 mm. The four holes at the two opposed sides are the holes for the fixation of the implant to the environment. The cross section of the implant is a square and consequently, the tip has a square surface. This shape does not resemble to a real implant or the tip of a real implant. In a real scale implant, the shape of the cross section is a more rectangular shape and the tip is pointy to facilitate the penetration of the implant in the brain tissue. However, the square cross section and flat tip are defined as such because of the manufacturability constraints of the metal 3D printing process in correspondence with the FEM model.

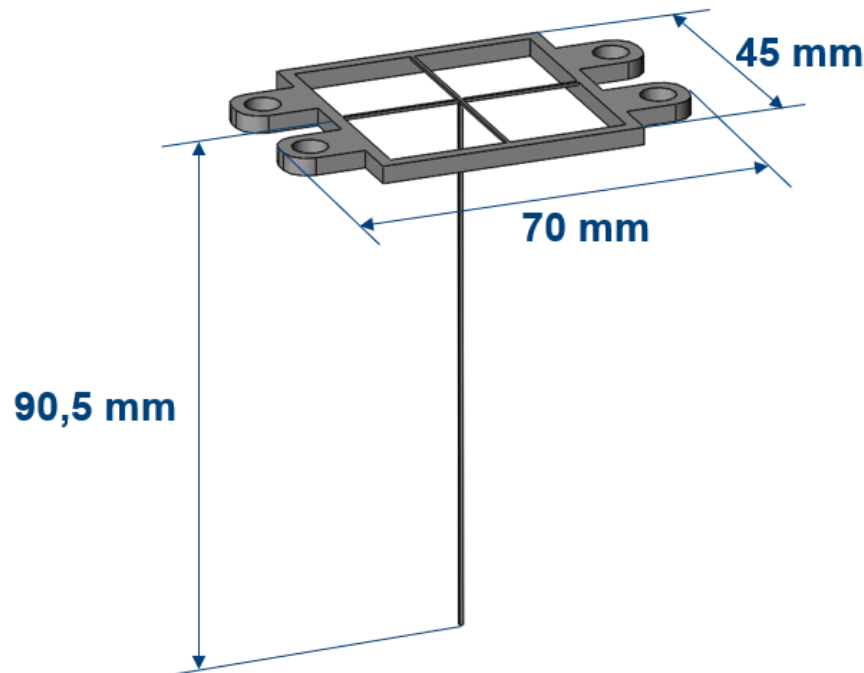


Figure 5-4 CAD drawing of the implant module

5.1.2.4 FEM model modifications

The FEM models are modified to verify whether an implant with sensitive beams behaves identical to an implant with a toggle point. This is done for both the respiration model and the heartbeat model in order to investigate whether the sensor could also be used in future research, which simulate the heartbeat. In the left top corner Figure 5-5 shows the geometry of the respiration model whereas at the right the geometry of the modified respiration model is shown. The sensitive beams are added to the implant. The beam ends are attached to the stiffer frame of the implant module and are therefore totally clamped at the outer surfaces. The toggle point of the first respiration model is removed. The geometry of the heartbeat model is shown on the bottom left of the figure, the right geometry is the modified heartbeat model. Both modified models are scaled by a factor 10:1. Note that this cannot be observed in the figure in which it looks as if the geometries are the same size. The applied pressures however are not scaled. Combined with the scaling of the geometry by a factor 10:1, this results in forces that are 100 times larger than the forces in the initial models. The ONELAB files are attached in Appendix L, provided on an electronic medium.

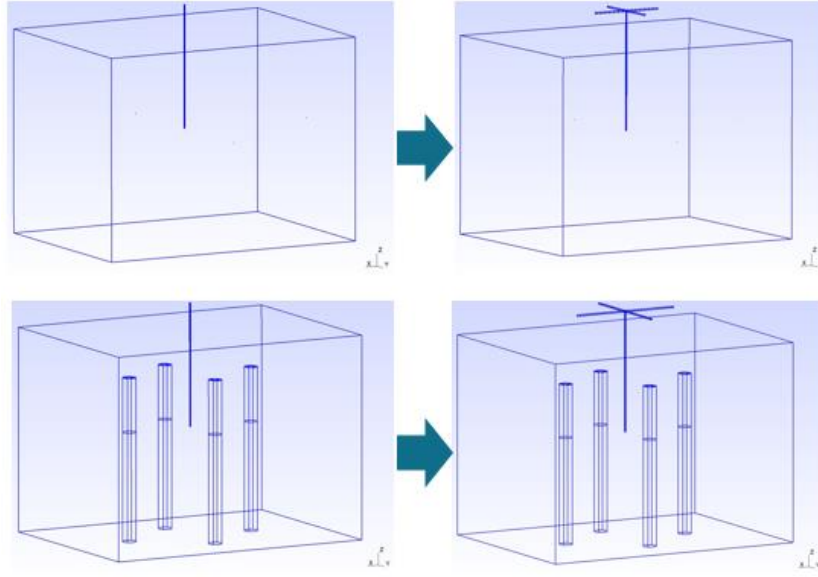


Figure 5-5 FEM model modifications

A colour plot of the implant displacement in the rostral direction due to respiration is plotted in Figure 5-6. The first colour plot shows the model with toggle point, the second represents the model with the sensitive beams. The top of the implant bends slightly more when a toggle point is added in comparison to when attached to sensitive beams. However, the implant displacement in the tissue is almost completely identical for both models. In real scale the maximal rostral displacements in the toggle point model and the sensitive beams model respectively equal 70,6 μm and 71,1 μm . The difference is 5 μm in terms of the upscaled model with sensitive beams. Note that the scale of the toggle point model is not upscaled and that the displacements are enlarged. The displacement in the toggle point model can be compared with the displacement of the sensitive beams model by multiplying it by a factor 10. An explanation for this can be found in the theory on bending in cantilever beams. Based on this theory, the maximal rostral displacement Δx due to the distributed pressure P_{implant} , applied on the caudal side of the implant, is proportional to this pressure (Krenk & Høgsberg, 2013):

$$\Delta x \sim \frac{P_{\text{implant}} \cdot t_{\text{implant}} \cdot l_{\text{implant}}^4}{E \cdot t_{\text{implant}}^4} \quad (5-1)$$

with:

- t_{implant} , the implant thickness and width
- l_{implant} , the implant length
- E , the elastic modulus

As mentioned earlier, only the linear dimensions including t_{implant} and l_{implant} are scaled by factor 10. Therefore, the displacement Δx also increases by factor 10. Although the implant is not completely clamped in the toggle point model and in the sensitive beams model, it is valid to scale the displacement in the toggle point model by a factor 10 to compare it with the displacement in the sensitive beams model. (5-1) shows that the displacement scale factor only depends on the scale factor of the geometry.

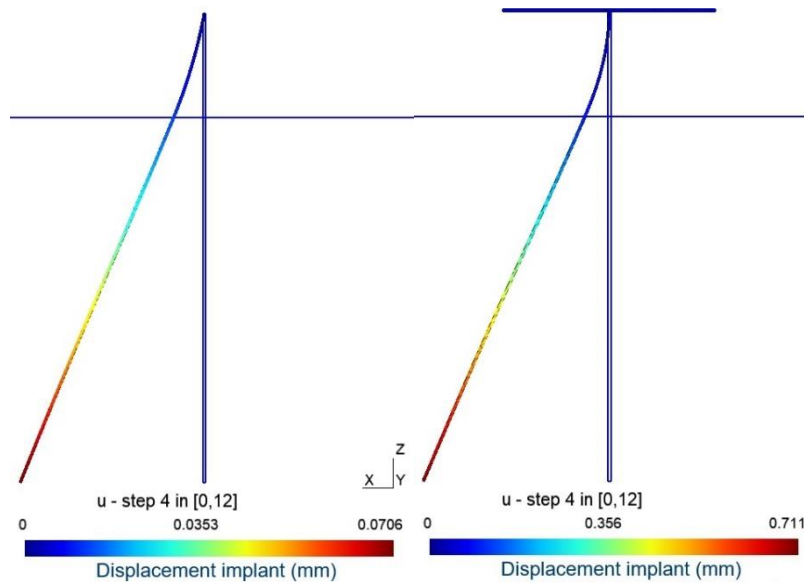


Figure 5-6 Implant displacement in the rostral direction due to respiration for toggle point and with sensitive beams (section in sagittal plane)

Figure 5-7 shows the implant tip displacement in rostral direction due to respiration, both for the toggle point model and the sensitive beams model. The displacements in the upscaled model are downscaled by dividing them by a factor 10. It is clear that both sine waves are almost completely identical. This can be explained because of the fact that the rostral displacement is constrained at its top by both the toggle point and the sensitive beams. Hence, the sensitive beams mimic the connection between the implant and the hyperdrive in a similar way as the toggle point. It can be concluded that the sensitive beams can be used as a replacement of the toggle point.

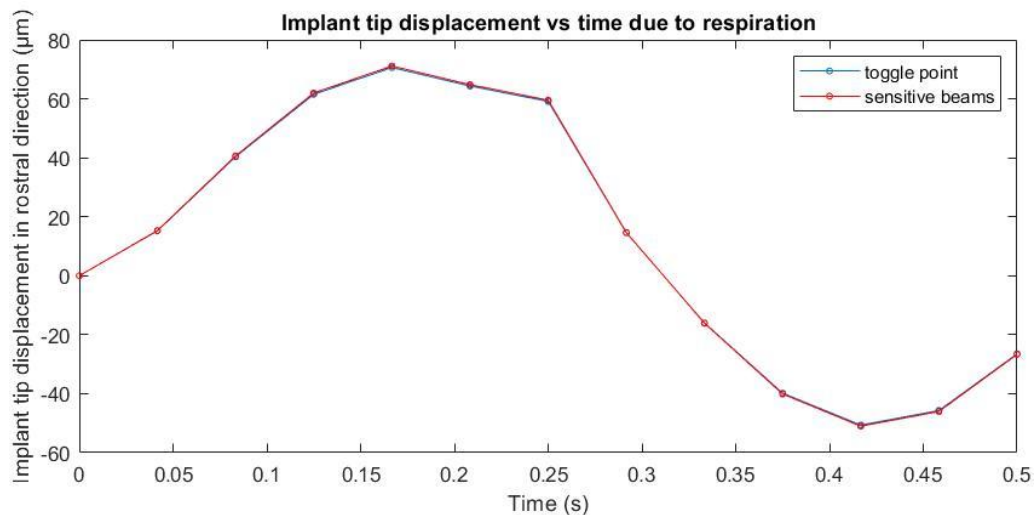


Figure 5-7 Implant tip displacement in rostral direction due to respiration for toggle point and sensitive beams model

Figure 5-8 shows the colour plots of the implant displacement in the rostral direction due to the heartbeat. Equivalent to the previous colour plots, the first model is the model with toggle point and the second one is the model with the sensitive beams. It is clear that the implant attached to the sensitive beams is pushed upwards due to the pressure from below. In the heartbeat model upward pressures are also applied in the tubes, which is not the case in the respiration model. The two models correspond very well with regard to rostral displacement. Based on the

colour plots, the toggling is identical in both models. The maximal displacement difference is $4,4\text{ }\mu\text{m}$ in terms of the upscaled model with sensitive beams. Note that the scale of the toggle point model is real scale and the displacements are enlarged.

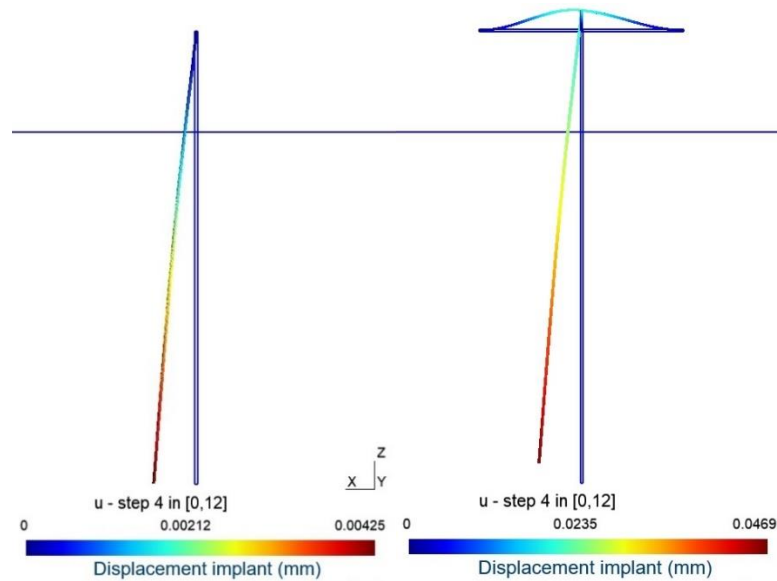


Figure 5-8 Implant displacement in the rostral direction due to heartbeat for toggle point and with sensitive beams (section in sagittal plane)

Stating that the rostral displacement is almost completely identical in both models is supported by Figure 5-9. This is the implant tip displacement in rostral direction due to heartbeat both in the toggle point model and the sensitive beams model. The displacements in the upscaled model are downscaled by dividing them by a factor 10. It is clear that both sine waves are almost completely identical. Hence, the sensitive beams mimic the connection between the implant and the hyperdrive in a similar way as the toggle point if only the rostral displacement is considered.

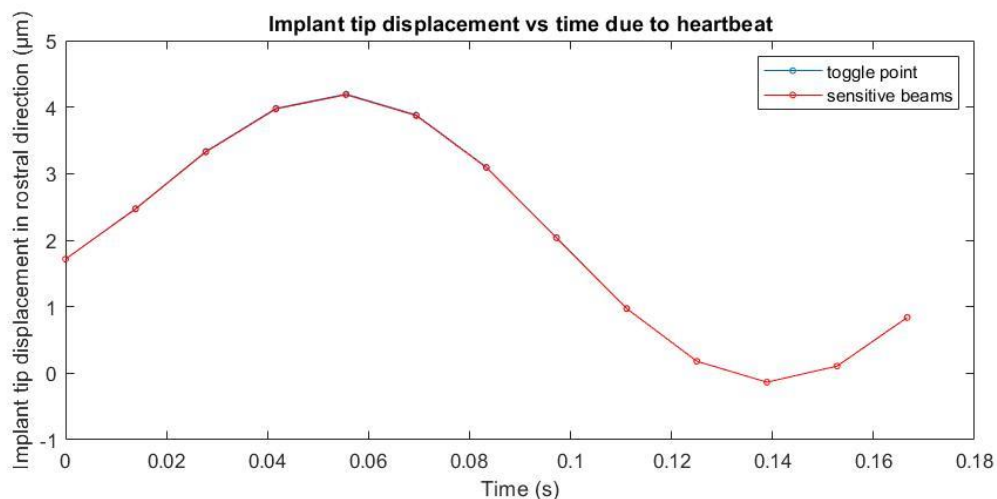


Figure 5-9 Implant tip displacement in rostral direction due to heartbeat for toggle point and sensitive beams model

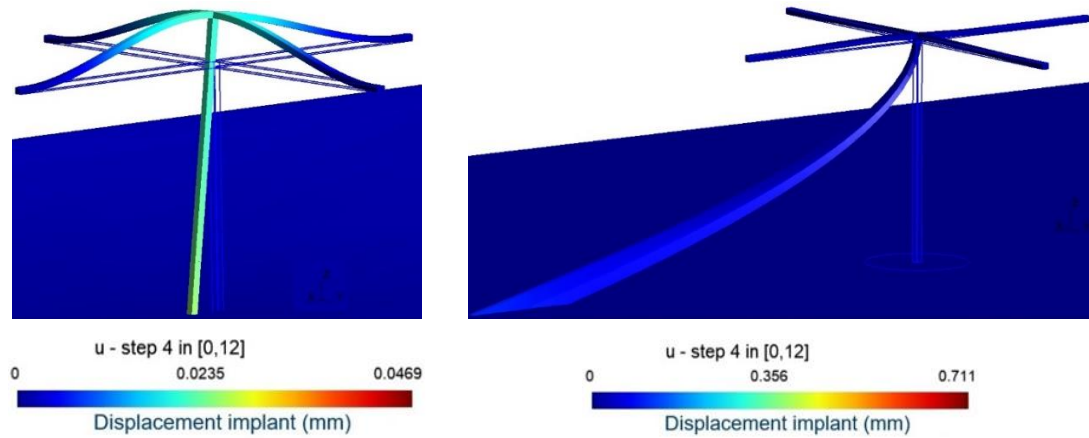


Figure 5-10 Sensitive beams displacement due to heartbeat and respiration

Figure 5-10 shows two close-ups of the sensitive beams in both the heartbeat and the respiration model. The upward dorsal displacement is clearly larger in the heartbeat model. Figure 5-11 represents the implant top displacement quantitatively. The implant top is the same point as the clamped toggle point in the first heartbeat and respiration models. In these models this point is fixed. The dorsal displacements are sine waves, as are the rostral displacements. The most significant difference is that the displacement due to the heartbeat is large and has a maximum of almost 20 μm in the upscaled model. The displacement due to heartbeat is indicated in blue in Figure 5-11. The dorsal displacement due to the respiration has a maximum of only 0,55 μm . The displacement due to the respiration is indicated in orange in Figure 5-11. Note that these displacements are plotted for the upscaled model. It can be concluded that the dorsal displacement is very small in comparison with the rostral displacement, which has a maximum of 711 μm . Hence, the sensitive beams mimic the toggle point in a correct way based on the modified FEM models.

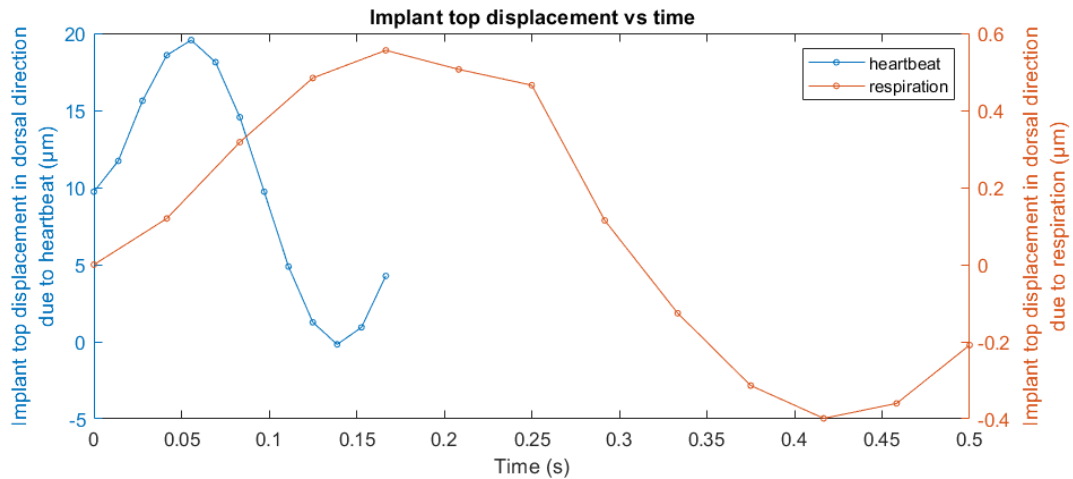


Figure 5-11 Implant tip displacement in dorsal direction due to respiration and heartbeat for sensitive beams model

5.1.3 Electronic design

The strain gauges measure the strain in the sensitive beams. As such, the measured strain needs to be converted into a displacement of the implant shank. Furthermore, the configuration of the strain gauges influences the sensitivity of the sensor, meaning that a comparison and

feasibility analysis of different configurations are required. After the strain gauge design is selected, the signal coming from the strain gauges needs to be processed by a data acquisition.

5.1.3.1 Strain calculation

Following the design of a microdisplacement sensor of Figure 5-3, the strain in the sensitive beams is calculated according to the geometry in Figure 5-12. The calculation is only possible for a linear shape of the implant. Bending of the implant will therefore not be taken into account and the strain is only calculated for a linear displacement of the implant shank above the tissue. Hence, only a rough estimation of the microdisplacement is obtained.

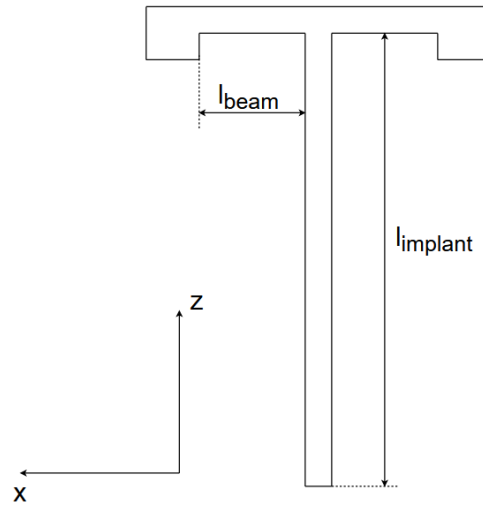


Figure 5-12 Sketch of the section view of the implant module

Figure 5-13 displays a detailed yet simplified representation of the deformation of the implant module when an input is applied at the side of the shank. The displacement Δx represents the displacement of the shank at the level of the top surface of the tissue, as indicated in the assumption above. For an initial estimation of the strain, the deformation of the sensitive beams at the top is assumed to be linear as well. The followed mathematical method is similar to the method of Wu et al. (Wu, et al., 2014).

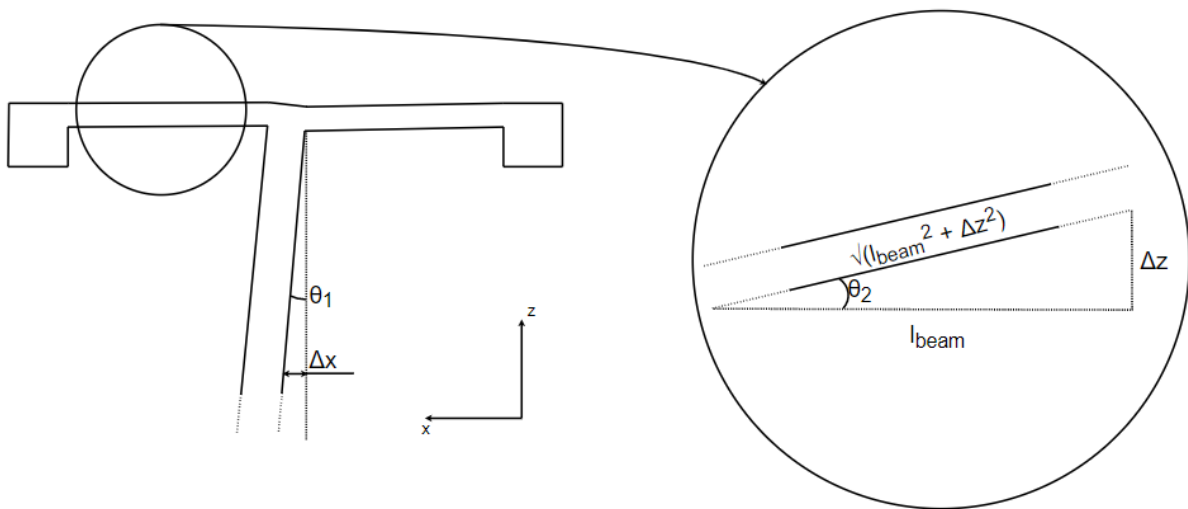


Figure 5-13 Detailed sketch of the deformed implant module in section view

The displacement Δx of the implant at the top surface of the tissue of the FEM model equals $108 \mu m$. This value, together with the length l of $20 mm$ of the non-inserted section, gives an approximate angle θ_1 at which the implant is bent with respect to the initial line:

$$\theta_1 = \frac{\Delta x}{l_{implant}} = \frac{108 \mu m}{20 mm} = 0,0054^\circ \quad (5-2)$$

with:

- θ_1 , the angle as shown in Figure 5-13
- Δx , the displacement
- $l_{implant}$, the length of the implant

This angle is an indication of the angle at which the sensitive beams are stretched or compressed according to the position in rest. The beams are presumptive linear elements with length l_{beam} and the angle estimates the change in height Δz . Note that θ_1 and θ_2 are different angles, according to Figure 5-13. However, these angles are assumed to be equal as in the assumptions in the study of Wu et al (Wu, et al., 2014).

$$\Delta z = l_{beam} \cdot \theta_2 = l_{beam} \cdot \theta_1 = 20 mm \cdot 0,0054^\circ = 108 \mu m \quad (5-3)$$

with:

- Δz , the change in height as shown in Figure 5-13
- l_{beam} , the length of the beam
- θ_2 , the angle as shown in Figure 5-13

The change in length of the sensitive beam can be estimated by the Pythagorean theorem. Based on this estimation, the strain in the sensitive beam is calculated.

$$\varepsilon = \frac{\Delta l_{beam}}{l_{beam}} = \frac{\sqrt{l_{beam}^2 + \Delta z^2} - l_{beam}}{l_{beam}} = \frac{\sqrt{(20 mm)^2 + (108 \mu m)^2} - 20 mm}{20 mm} = 14,6 \mu s \quad (5-4)$$

with:

- ε , the strain
- Δl_{beam} , the change in length of the beam
- l_{beam} , the length of the beam
- Δz , the change in height as shown in Figure 5-13

5.1.3.2 Strain gauges selection

The width of $600 \mu m$ of the implant and thus the width of the sensitive beams at the top is now constrained. The maximum possible width for the selection of the attached strain gauges depends on this constraint. Vishay Precision Group provides an extensive range of Micro-Measurements strain gauges regarding the geometry of the strain gauge, the resistive material, the resistance and applicable working conditions for several applications (Vishay Precision Group, Inc., 2021).

The small dimensions impose that the attachment of the strain gauges to the implant module is executed by a professional with a good expertise in the attachment of tiny strain gauges (Mangelschots, 2021). A layman cannot ensure a solid attachment or an accurate balancing of the strain gauges when put into a Wheatstone bridge. With the design of the implant module as shown in Figure 5-4, a quarter, half and full Wheatstone bridge can be selected. The added value of a half bridge compared to a quarter bridge and a full bridge compared to a half bridge is the sensitivity. When the number of strain gauges in the bridge with opposing excitation is

doubled, also the sensitivity doubles. Figure 5-14 shows an overview of the possible Wheatstone bridge configurations.

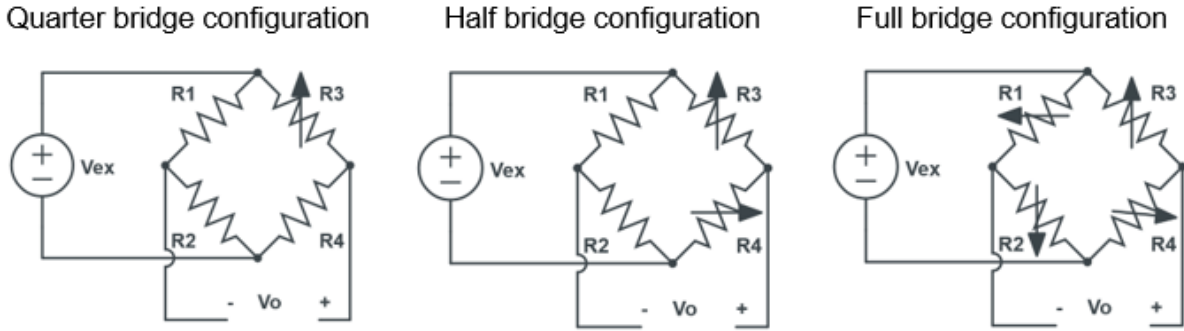


Figure 5-14 Wheatstone bridge configurations

A quarter Wheatstone bridge with only one strain gauge at one of the sensitive beams in the direction of the motion has considerable limitations compared to a half bridge. The behaviour of the sensitive beams according to the FEM model, enables the measurement of opposing signals. When one sensitive beam stretches in the direction of the motion, the other sensitive beam contracts. Thus, the use of at least two strain gauges in the opposite beams is advisable. A half Wheatstone bridge complies with this layout since the two varying resistances of the strain gauges are presumptive to be equal in value and opposite in sign. This does not entirely match the reality because the implant has also a small vertical movement. To compensate this, a full bridge is required since it balances the upright motion in all the varying resistances and is thus not included into the imbalance of the bridge. In this design, the two additional strain gauges are placed at the sensitive beams perpendicular to the direction of the motion. These additional strain gauges do not measure an opposing value but they only compensate the upright motion.

An important remark on the use of a full Wheatstone bridge is the fact that the strain gauges perpendicular to the motion will measure a torsion in the sensitive beams as they are twisted when the implant module moves forward and backward. This effect can hardly be compensated and compensation would require even more strain gauges for which there is only a limited space available on the sensitive beams. In addition, the signal conditioning will become overcomplicated within the specifications of the resolution and precision of the measurements.

Taking into consideration these limitations, a half Wheatstone bridge is the most favourable option. It can measure the forward and backward motion with double sensitivity compared to a quarter bridge. Furthermore, cross-linked torsion will not be measured. The limitation of this choice relates to the upward movement of the implant. However, the upward movement according to the FEM model is approximately 0,5 μm . Furthermore, this configuration is the most practicable option.

Figure 5-14 displays the configuration of the strain gauges in the half Wheatstone bridge. In this configuration, one of the sensitive beams is in tension and the other in compression. The ratio between the output voltage with respect to the excitation voltage indicates the sensitivity of the bridge circuit. Applying Ohm's law and Kirchhoff's voltage law for the voltage divider in the legs of the bridge, the output voltage has a relation to the excitation voltage according to:

$$V_o = \left(\frac{R_2}{R_1 + R_2} - \frac{R_4}{R_3 + R_4} \right) \cdot V_{ex} \quad (5-5)$$

with:

- V_o , the output voltage
- R_1 , resistor 1 as shown in Figure 5-14
- R_2 , resistor 2 as shown in Figure 5-14
- R_4 , resistor 4 as shown in Figure 5-14
- R_3 , resistor 3 as shown in Figure 5-14
- V_{ex} , the excitation voltage

The strain gauges can only withstand a determined voltage of around 2,5 V, which thus limits the voltage to this value. Resistance R_3 and resistance R_4 represent the strain gauges. Their resistance value equals the resistance value of the balancing resistors R_1 and R_2 . The resistance value in the balanced bridge is indicated as R . When the strain gauges stretch and compress, a difference in resistance adds up to the resistance value on one side and subtracts from the resistance on the other side:

$$V_o = \left(\frac{R}{R+R} - \frac{R+\Delta R}{R+\Delta R + R-\Delta R} \right) \cdot V_{ex} \quad (5-6)$$

$$\Leftrightarrow V_o = \frac{\Delta R}{2 \cdot R} \cdot V_{ex} \quad (5-7)$$

with:

- V_o , the output voltage
- R , the resistance value
- ΔR , the change in resistance
- V_{ex} , the excitation voltage

The sensitivity thus equals $\frac{\Delta R}{2 \cdot R}$. The relation between the strain and difference in resistance follows from:

$$\varepsilon = \frac{\Delta R}{GF \cdot R} \quad (5-8)$$

$$\Leftrightarrow \Delta R = GF \cdot R \cdot \varepsilon \quad (5-9)$$

with:

- ε , the strain
- ΔR , the change in resistance
- GF , the gauge factor
- R , the resistance value

GF represents the gauge factor. This value is indicated in the datasheet of the strain gauges and equals 2,1. An estimation of the strain follows from (5-4) and equals 14,6 μs . The gauge factor and the strain together with the balanced resistance value of 350 Ω , give an estimate of the difference in resistance according to

$$\Delta R = 2,1 \cdot 350 \Omega \cdot 14,6 \mu s = 0,011 \Omega. \quad (5-10)$$

The expected output voltage and consequently the expected sensitivity equal

$$V_o = \frac{\Delta R}{2 \cdot R} \cdot V_{ex} = \frac{0,011 \Omega}{2 \cdot 120 \Omega} \cdot 2,50 V = 0,112 mV, \quad (5-11)$$

$$\frac{V_o}{V_{ex}} = \frac{\Delta R}{2 \cdot R} = \frac{0,011 \Omega}{2 \cdot 120 \Omega} = 0,045 \frac{mV}{V}. \quad (5-12)$$

The output voltage has to be conditioned in order to amplify. The signal is thus measurable with the oscilloscope and the data acquisition. Furthermore, an appropriate signal conditioning

reduces noise coming from the Wheatstone bridge or coming from external factors. Hence, the design of an analog circuit is required.

5.1.3.3 Amplifier circuit

The amplifier circuit consists of four main sections: a buffer circuit to produce a stable positive and negative voltage, a first amplification stage, a passive low-pass filter and a second amplification stage. An oscilloscope reads the output voltage of the circuit and a data acquisition based on an Arduino Uno saves the data in a CSV file in order to process later. The oscilloscope is merely to keep visual track on the behaviour of the implant. The processing of the data, together with data of other sensors, is achievable through a script in Python or Matlab.

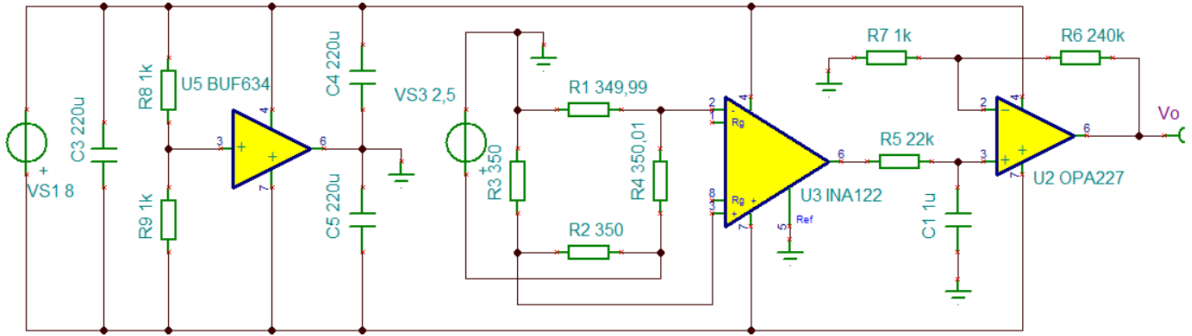


Figure 5-15 Analog signal conditioning circuit for the strain gauges

Figure 5-15 shows the analog circuit. The first stage divides the input rail voltage in half to create a positive voltage and a negative voltage, with respect to an artificial ground. This is necessary because the amplifiers operate between a positive and negative voltage since the signal of the strain gauges also varies between a positive and negative value. Otherwise, the amplifier will cut off the signal. The voltages are fed into the instrumentation amplifier in the next stage. The Wheatstone bridge is connected to this instrumentation amplifier. The next stage is a passive filter to reduce the noise in order to have a clean signal. The last stage is a second amplifier, which amplifies the clean signal to a readable value to feed into the oscilloscope and the data acquisition. A parts list on required components is added in Appendix I.

On the left, a variable power battery of 8 V ensures the input voltage of the circuit, a capacitor is added to stabilise the voltage ripple. The voltage is divided by the two equal resistors in front of the first IC in order to have an equal division of the voltage. The branch point of the voltage divider is connected with a buffer BUF634 to limit the current. The voltage will thus be more stable and will not be affected by the load, which is applied to the input voltage. Furthermore, some capacitors are added for a stabilised voltage.

The Wheatstone bridge with the strain gauges is fed into an instrumentation amplifier AD627. This ensures a first amplification stage with a small amplification factor of 5. Note that the instrumentation amplifier used in the SPICE software is an instrumentation amplifier INA 122, which is a different amplifier than the one used in the experiment set-up. This is because the SPICE software and the instrumentation amplifier are supplied by different companies. The operating principle is, however, similar for both.

Afterwards, a passive low-pass filter with resistor R and capacitor C reduces the high frequency noise. The cut-off frequency equals

$$f_c = \frac{1}{2 \cdot \pi \cdot R \cdot C} = \frac{1}{2 \cdot \pi \cdot 22 \text{ k}\Omega \cdot 1 \text{ }\mu\text{F}} = 7,23 \text{ Hz.} \quad (5-13)$$

with:

- f_c , the cut-off frequency
- R , the resistance value
- C , the capacitance value

A second amplification stage amplifies the noise reduced signal. An operational amplifier OPA227, together with two resistors in a negative feedback loop, creates an amplification of the clean signal with a large gain.

$$\frac{V_o - V_{in}}{240 \text{ k}\Omega} = \frac{V_{in} - 0 \text{ V}}{1 \text{ k}\Omega} \quad (5-14)$$

$$\Leftrightarrow \frac{V_o}{V_{in}} = 240 \text{ k}\Omega \cdot \left(\frac{1}{240 \text{ k}\Omega} + \frac{1}{1 \text{ k}\Omega} \right) = 241 \quad (5-15)$$

with:

- V_o , the output voltage
- V_{in} , the input voltage coming from the passive filter

Simulations in a SPICE software package indicate the performance of the circuit. In this case, the Tina-TI software package from Texas Instruments is used. With this software, the signal is analysed. Figure 5-16 displays the response and indicates that the output voltage is approximately 1000 times the input voltage. This corresponds with the total gain of the first and the second amplification stage combined:

$$GAIN = GAIN_1 \cdot GAIN_2 = 5 \cdot 241 = 1205 \quad (5-16)$$

The rail voltages from the buffer circuit behave as expected and ensure a stable voltage divider of -4 V and +4 V.

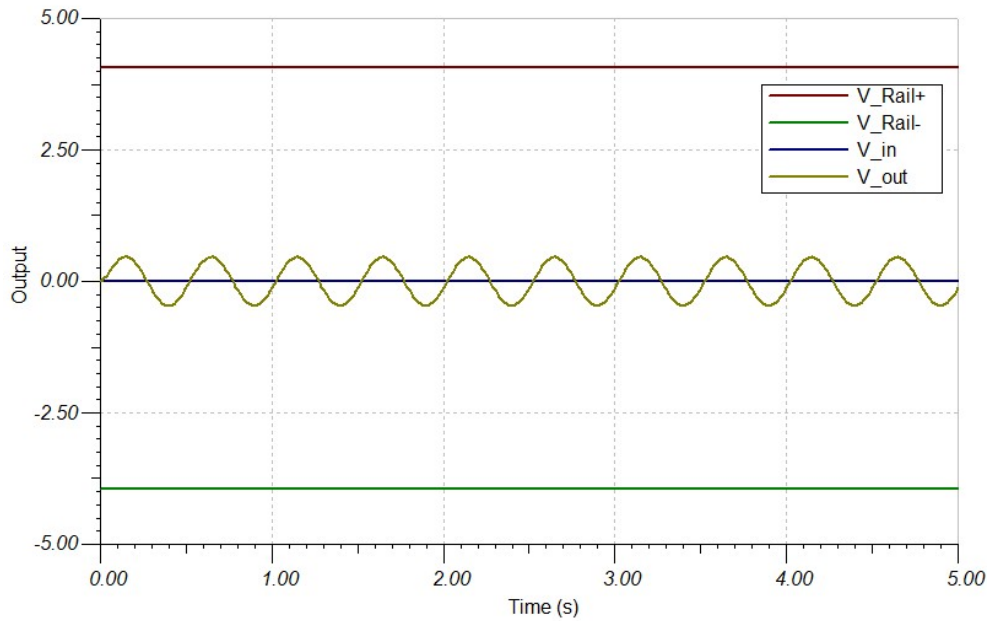


Figure 5-16 Response of the SPICE simulation of the analog circuit

5.1.3.4 Attachment of the strain gauges

The position where the strain gauges are to be attached is based on the result of the FEM model. The displacement of the sensitive beams in the FEM model represents the deformation

of the actual beams. Figure 5-17 displays the displacement of the sensitive beams in the FEM model. The lineal shows the location of the largest displacement, at a distance of 15 mm from the side. Hence, the strain gauges need to be attached at this position by an expert in the field (Mangelschots, 2021). The attachment of a strain gauge on the implant module is indicated on Figure 5-18.

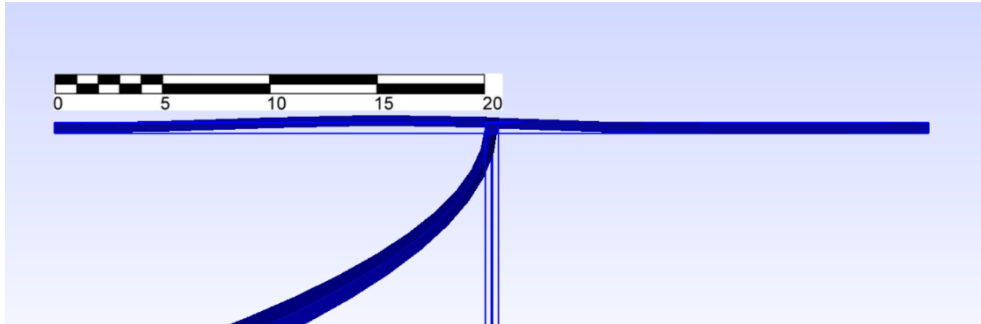


Figure 5-17: Displacement of the sensitive beams in the FEM model



Figure 5-18 Close-up of an attached strain gauge

Because of the fragility of the implant module and the strain gauges, a protecting enclosure is designed containing the implant module, strain gauges with associated wiring and balancing resistors. The enclosure consists of a bottom part, which holds the implant module, and a top part acting as a lid for the bottom part. The enclosure is shown in Figure 5-19. Figure 5-20 shows a close-up of the implant module in the enclosure.

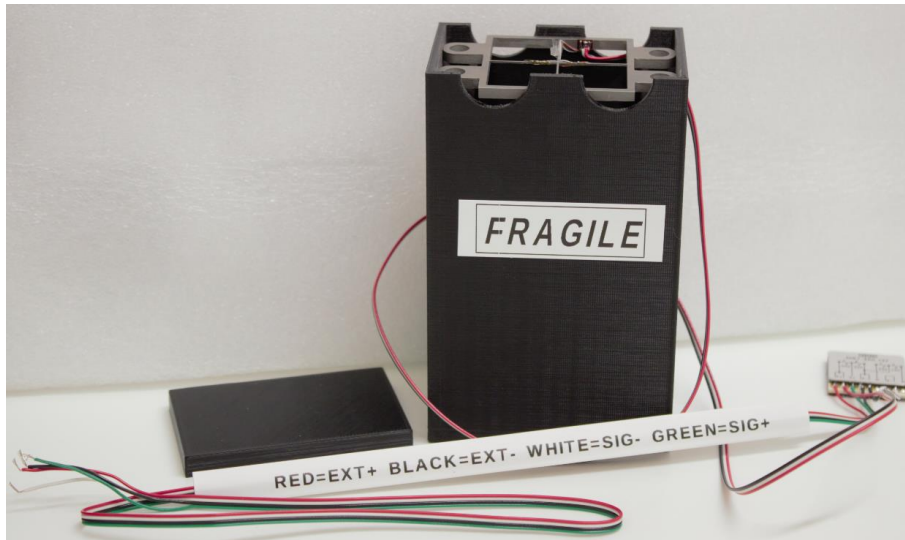


Figure 5-19 Enclosure of the implant module

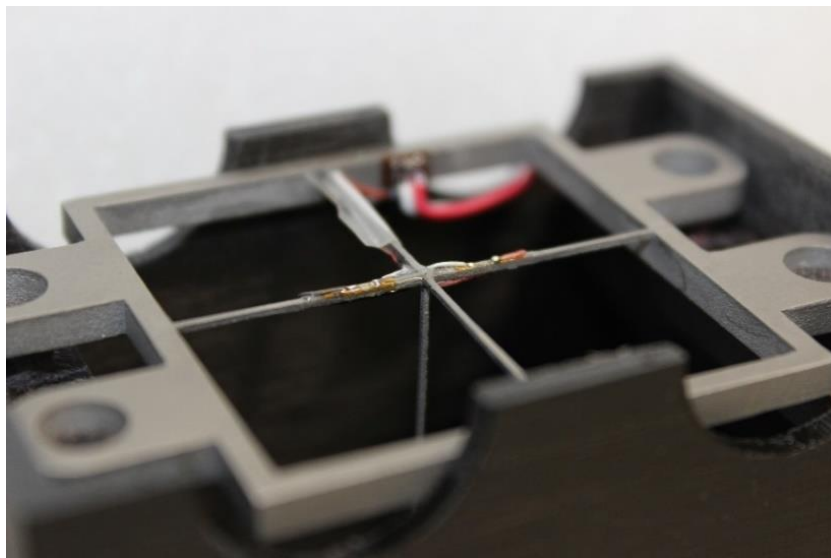


Figure 5-20 Close-up of the implant module in the enclosure, the frame has outer dimensions equal to 70 mm on 45 mm

5.2 Structural components

The micromotion sensor is sensitive to the motion of the implant, but is also influenced by external movements. Therefore, a rigid attachment to the environment has to be ensured. In addition, a mould for the tissue is included to represent the skull, such as in the FEM model. An anti-vibration table is used to eliminate the vibrations from the environment.

5.2.1 Anti-vibration table

The micromotion sensor is influenced by motion and vibrations in the environment as well. An anti-vibration table avoids the influence of vibrations in the environment and is thus useful to eliminate undesirable movements. The linear actuator is also placed on the same anti-vibration table because of spatial limitations. This means that vibrations from the motor itself are also

included in the motion of the implant module, although they are minimal and can thus be neglected.

5.2.2 Frame

The attachment of the implant module to the environment has to be rigid in order to minimise frame deformations. In this way the deformation of the frame can be neglected with respect to the deformation of the implant module. Figure 5-21 shows the design of the frame. Practical notes for the design include leeway for the wires of the sensors, workable space for setting up the frame and visual apertures to keep direct visual contact with the moving parts. In addition, the implant has to be lowered in a controllable way, as also established in a hyperdrive on a rodent's head. The controllable insertion of the implant ensures low risk of damage to the implant while inserting. Moreover, it enables the insertion depth to be measured easily.

Figure 5-21 shows a CAD drawing of the anti-vibration table with the frame attached to it. The assembly consists mainly of the following components:

- A. The anti-vibration table in order to minimise motion exerted by the environment. Tapped holes in the table make it possible to attach other components.
- B. The implant module that is attached with bolts and T-slot nuts to the frame.
- C. Four vertical struts, which are placed on the anti-vibration table. These four vertical struts with angle brackets at the bottom are the only connection to the anti-vibration table and are therefore twice as thick as the other struts. They have a square section with a width of 40 mm.
- D. Horizontal struts to connect the four vertical struts. The square section has a width of 20 mm.
- E. Angle brackets that make sure every strut is connected and does not move.
- F. Angle brackets that ensure the four vertical struts are rigidly attached to the anti-vibration table.
- G. A subframe consisting of horizontal struts with a square section of 20 mm by 20 mm. The subframe is movable in a controlled way by using threaded rods.
- H. Two threaded rods that are held in place by two interlocked bolts at each rod on top, so that the threaded rods cannot move down and the attached subframe cannot fall downwards. The angle brackets are loosened in order to move the subframe and are tightened afterwards to ensure a rigid assembly.
- I. Bolts to attach the implant module to the frame. Washers provide a larger contact surface between the bolts and the implant module.

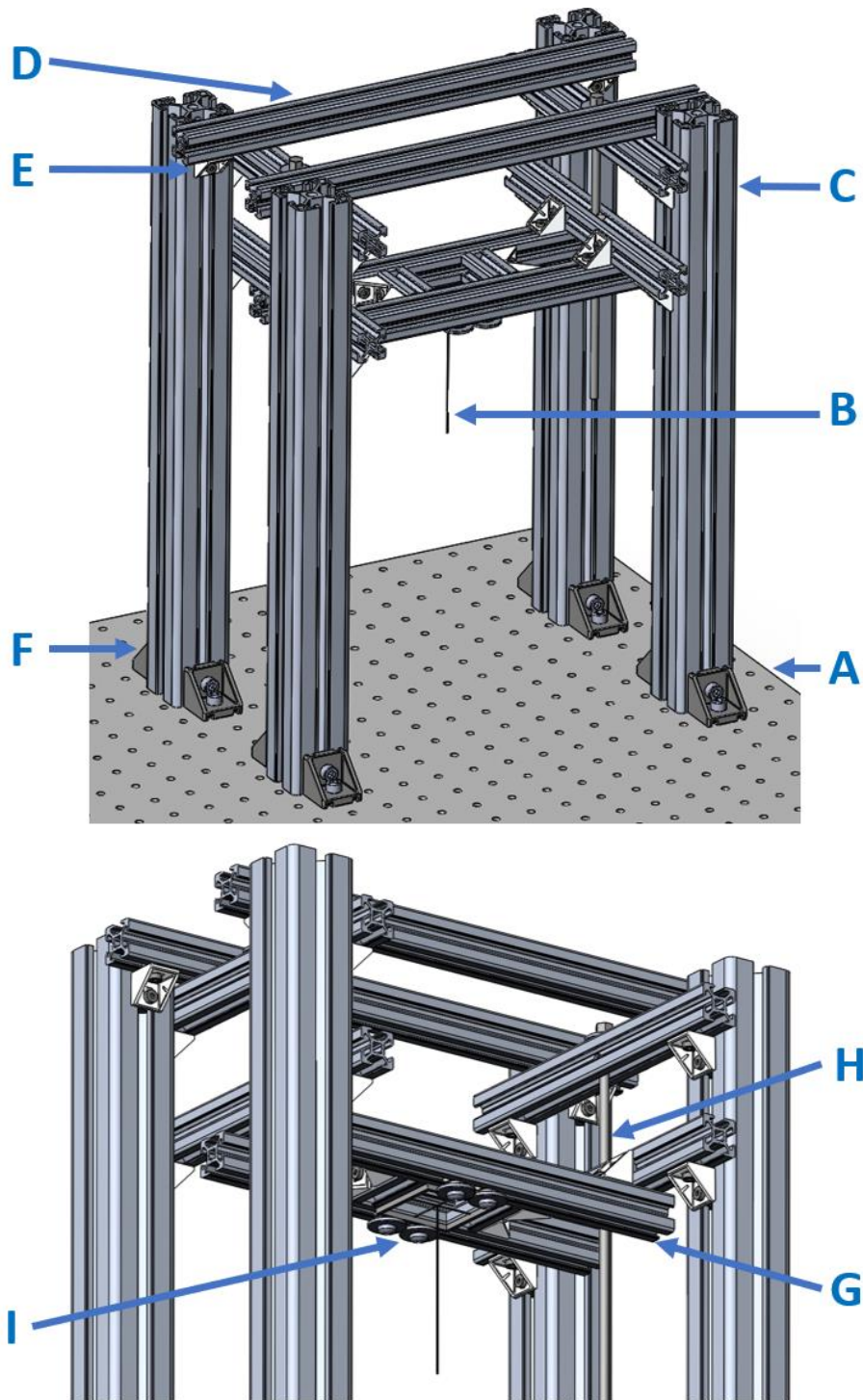


Figure 5-21 CAD drawing of the frame for the implant module

Figure 5-22 shows two pictures of the actual frame, attached to the anti-vibration table. The picture at the left shows the entire assembly of the frame with the implant module put in place. The picture at the right shows a close-up of a bottom view of the implant module.

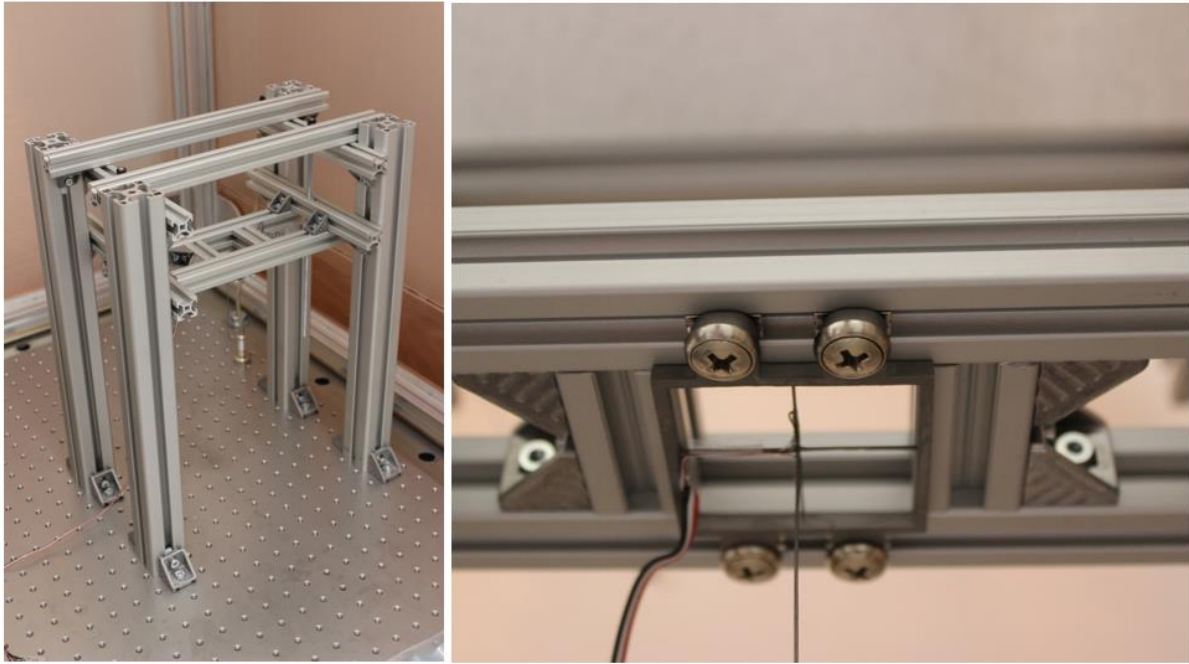


Figure 5-22 Frame with the implant module attached to the anti-vibration table

5.2.3 Mould

The mould contains the tissue phantom and serves as the rat's skull. Dimensions of the up-scaled brain are 150 mm x 150 mm x 200 mm, which are also the dimensions of the mould cavity. On top of that, the material must resist a temperature of 90 °C because tissue phantoms are mostly made of hydrogels, which are often heated until that temperature. The simplest way is to produce the mould out of different plexiglass parts, also known as polymethylmethacrylate. These parts are produced by a laser cutter, after which they are glued together with super glue and silicone glue. Figure 5-23 is a CAD drawing of the mould. The following parts are important and are therefore described:

- A. Plate that is positioned at the caudal or back side of the brain tissue. It is used to apply the respiration pressure, which explains why it must be able to move linearly in the rostral and caudal direction.
- B. Four screw thread rods are added to the mould. By screwing on nuts at the two ends of one rod the front and back plate are stronger clamped between the left and right plate. Notice that the rods are removed at the caudal side after the tissue phantom has stiffened.
- C. 3D printed connector between back plate and hinge connection. The used printing technique is stereolithography, also known as resin printing, executed by using a Formlabs Form3 SLA printer.
- D. Through one half of the hinge connection, combined with the other half, connected with the motor, a full hinge connection can be made.
- E. Two plates that can be removed after pouring and stiffening of the tissue phantom, which allows the caudal plate to move backwards.
- F. Cap on top of the skull that is applied after the last pouring of the tissue phantom. It has a hole of 10 mm in the middle of the skull, which mimics the craniotomy.

- G. Holes through which the connectors of the pressure sensors reach the outside of the mould. These holes also serve as vent holes.
- H. Bolts to press the plates together as well as to attach the mould onto the anti-vibration table.

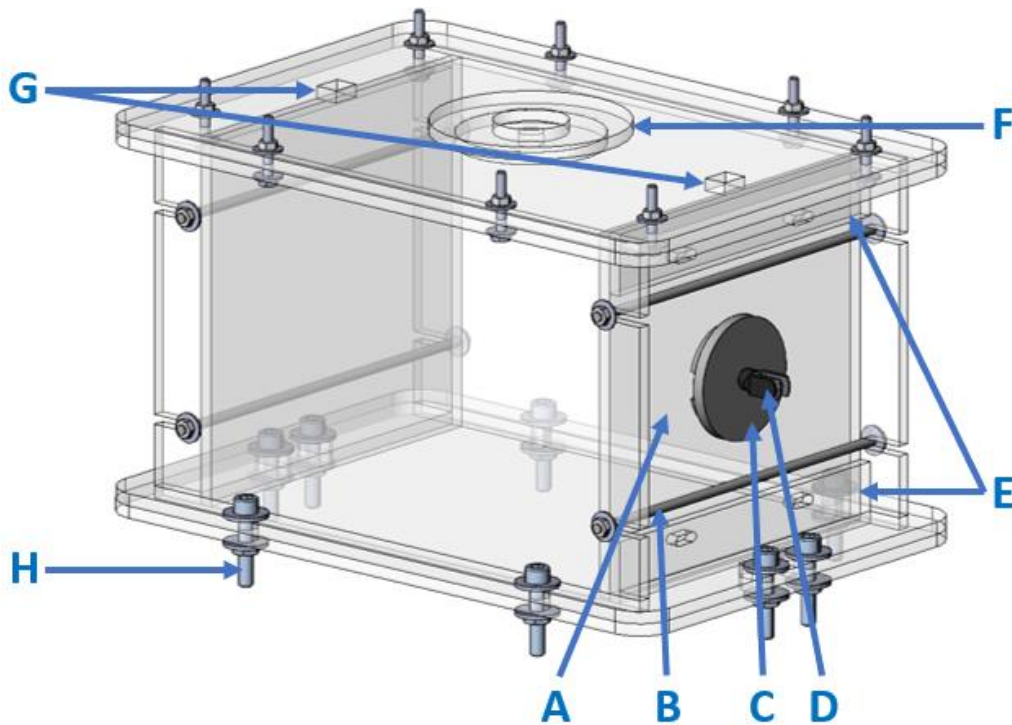


Figure 5-23 CAD drawing of the mould

Figure 5-24 shows the assembled mould. The pressure sensors are already attached to the front and back plate of the mould. Their connectors are black and are located outside of the mould. To test the mould for leaks it is filled with water. In case of leak holes silicone glue is used to close them. Figure 5-24 also shows the application of silicone glue at all edges.

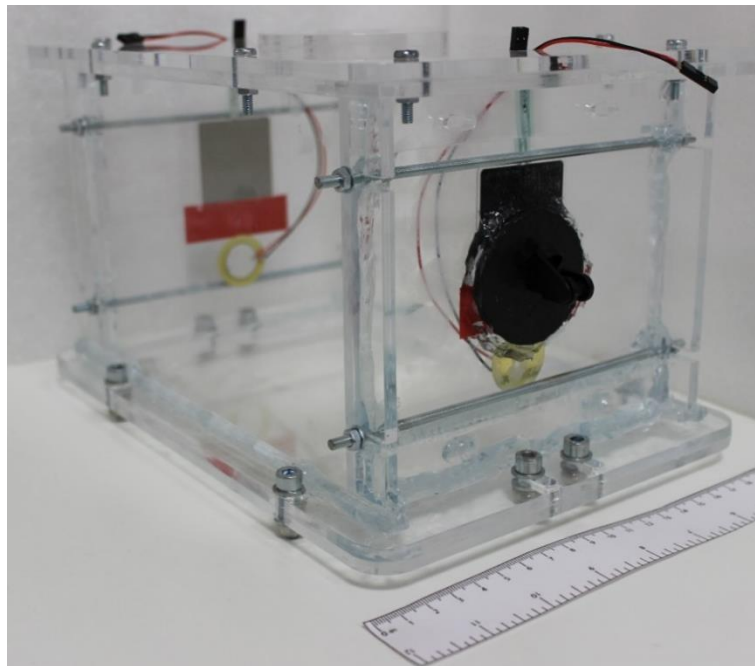


Figure 5-24 Mould

5.3 Actuator

The representation of the actuation of the FEM model in the experiment set-up consists of a sinusoidal pressure wave applied at the caudal side of the tissue phantom. This pressure can be applied by using an actuator. However, a pressure sensor needs to be included to monitor the applied pressure.

5.3.1 Selection

The actuation at the caudal side of the tissue consists of a triangular wave motion. Multiple designs can achieve this kind of motion, although some have a better performance than others. Pneumatic or hydraulic systems with a compressor or pump can create a cyclic compression and expansion, and can achieve quite accurate trajectories between two positions. However, compressed air implies volume work and thus causes a delay in motion. Hydraulic systems, like pneumatic systems, are less affected by this phenomenon, but require cumbersome in-flows and outflows of fluids.

Another suitable candidate for the actuation is an electric motor with a mechanical transmission to convert the rotation into a translation. Nanotec is a supplier of linear actuators with microscale accuracy. The rotational motion of a stepper motor is transferred to a translation through a captive leadscrew. This means that the leadscrew itself does not rotate together with the rotor. The second column of Table 5-3 lists all demands and wishes concerning the linear actuator. The calculations of the required linear stroke, speed and force are attached in Appendix D. It is desirable that a software program controls the motor. Furthermore, the motor has to be positioned very accurately. Finally, the hinge connection with the caudal plate must be attached to the motor. The following motor and controller are selected at Nanotec: LGA421S14-A-TJBA-019 – captive linear actuator – NEMA 17 and CL3-E-2-0F (Nanotec, 2021). Table 5-3 lists the technical data of the actuator, which meet all quantitative demands. Nanotec also provides a free software package for motor control. Additionally, the step size is 5 $\mu\text{m}/\text{step}$ and a hinge connection can be screwed on the linear actuator.

Table 5-3 Demands/wishes and technical data actuator

Criterion	Demands/wishes	Technical data actuator
Stroke (mm)	2	19,05
Speed (mm/s)	≈ 25	26
Force amplitude (N)	≈ 25	469,8
Motor control	Ability to control the motor with a software program	✓
Positioning motor	Possibility to slowly move lead screw for correct positioning	✓ (5 $\mu\text{m}/\text{step}$)
Hinge connection	Possibility to connect a hinge to motor	✓

Figure 5-25 shows the captive linear actuator attached to the environment through a base frame. The assembly is built up with the following components:

- A. The linear actuator with the electrical terminals on top.
- B. One half of the hinge connection. The full hinge connection is made by combining this half with the other half attached to the mould.
- C. A metal plate to constraint the linear actuator with bolts. This plate connects the actuator with an angle bracket.
- D. An angle bracket to connect the top surface of the actuator perpendicular to the anti-vibration table.
- E. A spacer with a thickness of 5 mm to position the actuator at the required height.

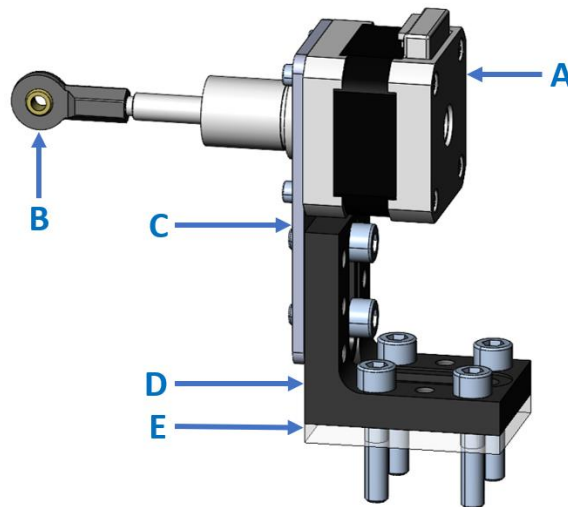


Figure 5-25 CAD drawing motor

Figure 5-26 shows the actual assembly of the linear actuator, attached to the anti-vibration table by the angle bracket. The terminals on top are connected to the controller.

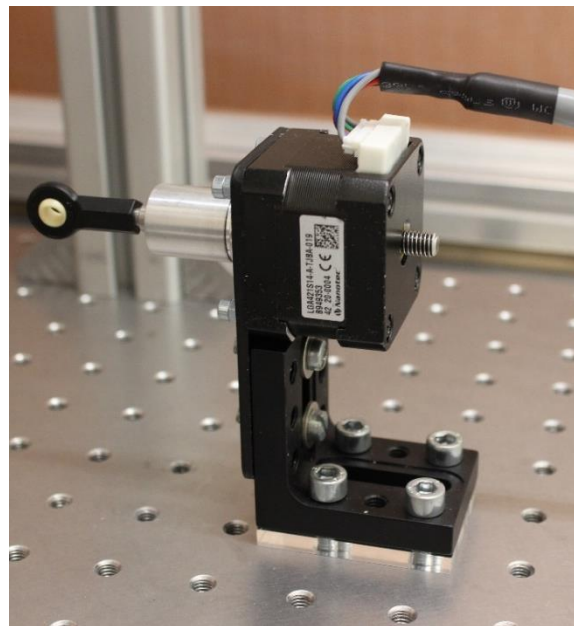


Figure 5-26 Linear actuator on base frame

5.3.2 Control

Along with the linear actuator and the corresponding controller, Nanotec also provides software packages to drive the linear actuator. Plug & Drive Studio is a software package with a built-in graphical user interface and a command-line interface for testing, operating and debugging the behaviour of the linear actuator. Figure 5-27 shows the graphical user interface with options to choose the desired trajectory of the motor.

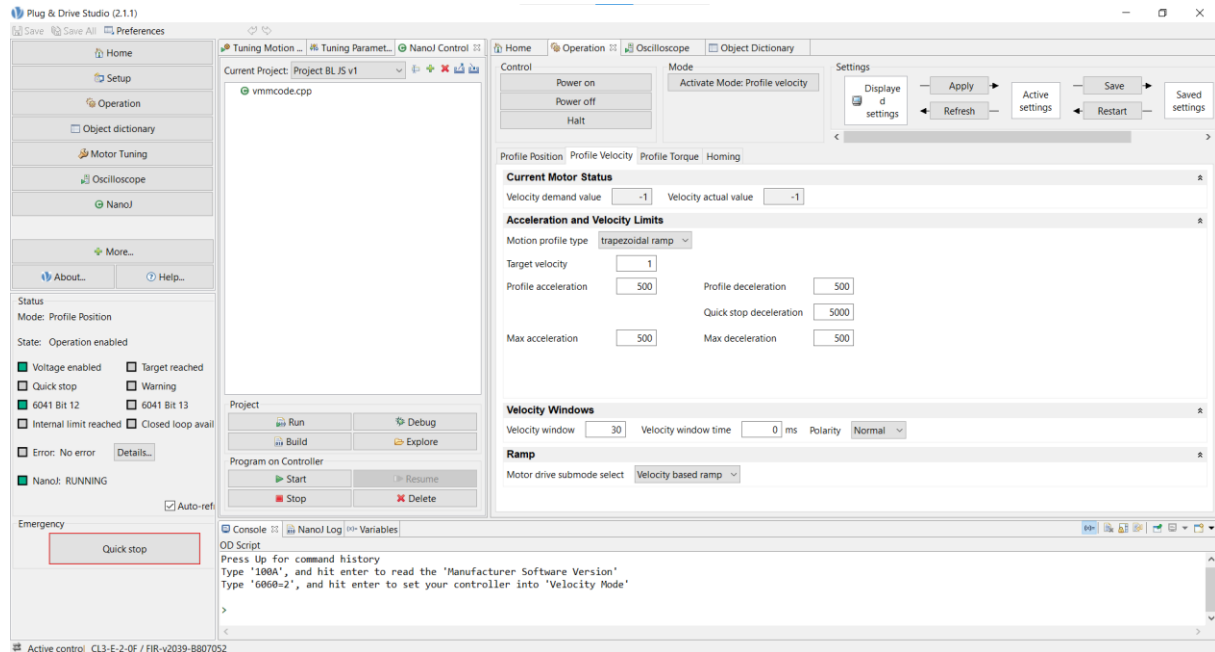


Figure 5-27 GUI of Plug & Drive studio (Nanotec, 2021)

A built-in oscilloscope provides real-time data read in by the controller. The operator can choose to follow a position defined trajectory, a velocity defined trajectory or a torque defined trajectory. Moreover, complex trajectories with intermediate values and states are possible to implement using a code-based interface with predefined parameters and object dictionaries. Scripts written in C++ are readable by the controller and a built-in feedback loop is available in order to base the motion and behaviour of the motor on the received feedback.

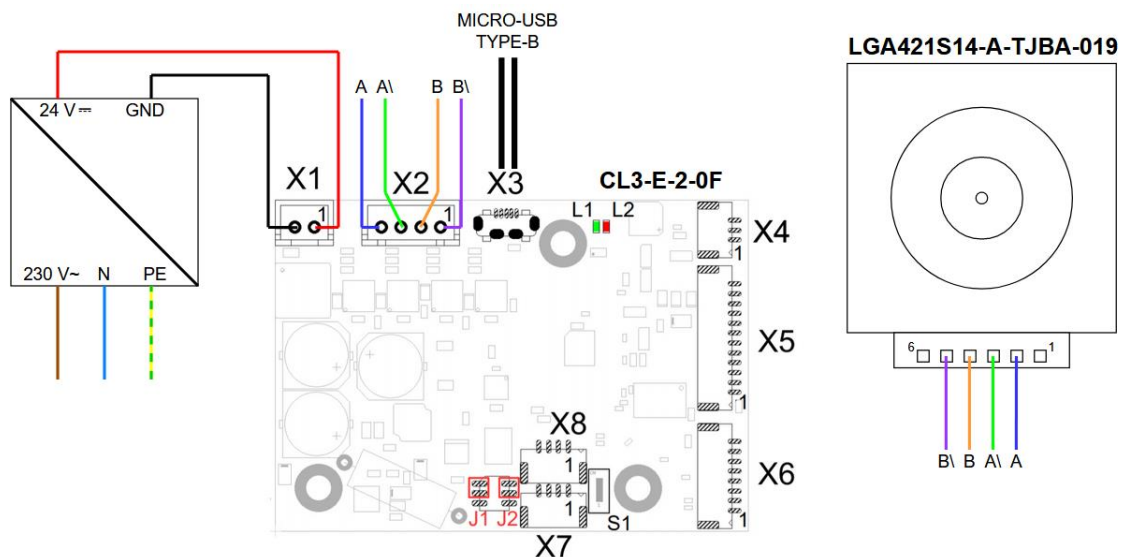


Figure 5-28 Motor circuit diagram (Nanotec, 2021)

Figure 5-28 shows the motor circuit diagram. A power supply transforms 230 VAC out of the grid to 24 VDC, which is the input voltage of the controller. The power supply and its connections are drawn on the left. The controller is located in the middle of the diagram. At X1 the input voltage arrives, at X2 the motor driver outputs depart. These outputs are A, A\, B and B\.. The first two outputs drive a first set of four coils in the motor, whereas the second two outputs drive another set of four coils. At X3 the micro-USB cable departs to a PC from which the controller is operated. On the right the motor is drawn with its inputs A, A\, B and B\.. Figure 5-29 shows all the components of the motor circuit put together with on the left the controller on top of the power supply and in the middle the motor. A parts list on required components is added in Appendix I.

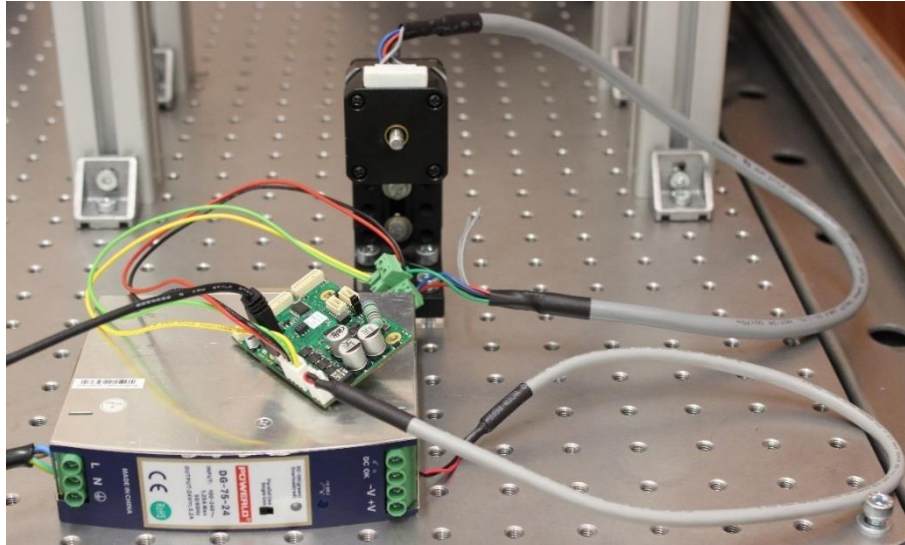


Figure 5-29 Motor circuit

5.3.3 Pressure sensors

Because the motor cannot measure the pressure it applies on the tissue, a pressure sensor needs to be included in the set-up. Two types of pressure sensors are placed inside the mould: piezo electric pressure sensors (piezo) and force sensitive resistors (FSR). The properties of the piezo and the FSR are explained in Table 5-4. The most obvious difference is that strain results in a charge in a piezo whereas in an FSR it results in a changing resistance. Moreover, a piezo is passive, which means that it does not need excitation whereas an FSR is active and does need excitation. Therefore, a piezo seems the best option, due to the fact that steady voltage supply is not necessary. However, because a piezo only measures pressure changes it is difficult to calibrate, which questions the measurements of magnitudes of pressures. Yet, they can be used to qualitatively measure the trend of the pressure waves.

An FSR can measure static pressures and will therefore be used as the preferred sensor. It is important to mention that this sensor's accuracy is around 10% in the full dynamic range. Only a small range is used in the experiment due to the fact that approximately 1000 Pa is applied, which corresponds with a mass of 156 grams. Finally, hysteresis in the FSR results in the fact that it takes time to reach the correct resistance value. Therefore, the hysteresis curves must be drawn up by means of calibration.

Table 5-4 Property table piezo and FSR

Property	Piezo	FSR
Working principle	Strain associated with the deformation of a sensing element is converted to a charge. Resistance decreases when strain changes.	Encapsulates a pressure-sensitive ink, the resistance is a function of the strain. Resistance decreases with force.
Excitation	Passive, no excitation needed.	Active, excitation needed.
Measurement	Pressure changes, dynamic pressures.	Static pressures.
Interface	Arduino	Arduino
Cost (€)	~2	~10
Dynamic range	Measures how fast force changes, not the static force amplitude.	5 kg
Accuracy	Cannot measure static pressure.	$\pm 10\%$ (when full range is used)
Hysteresis	-	$\pm 5\%$

One sample of each sensor type is attached to both the rostral and the caudal plate. The sensors are placed on the inside of the mould, which makes it possible to measure the pressure between the tissue phantom and respectively the rostral and the caudal plate. Figure 5-30 shows the piezo placed below the FSR. Notice that the connectors reach the outside of the mould through the vent hole in the mould.

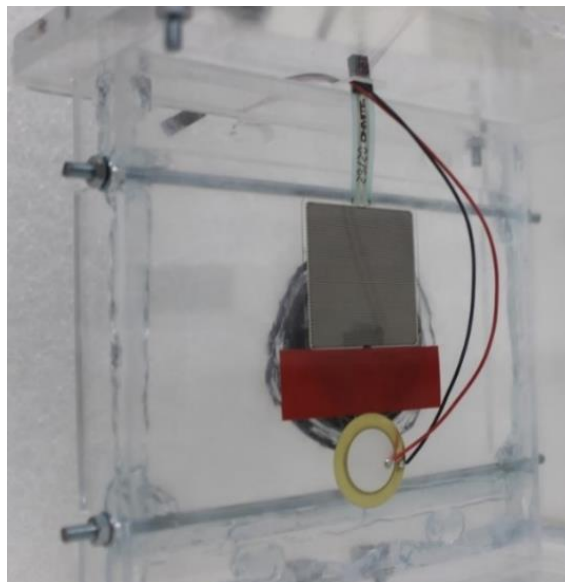


Figure 5-30 FSR and piezo attached to the caudal plate

In addition to the sensors being mechanically constrained, the electrical connection must also be executed. Both sensors can be interfaced by an Arduino. Real-time analog values can thus be read and displayed by the Arduino software or by Excel, Python or Matlab. Figure 5-31 shows the entire Arduino circuit diagram, with the amplifier circuit of the strain gauges con-

connected between the ground and A1. The piezos at the rostral and the caudal side are connected between the ground and respectively A2 and A3. A resistance of 2 M Ω is placed in parallel with the piezo, limiting the voltage and the current, which the piezo produces. A parts list of required components is added in Appendix I.

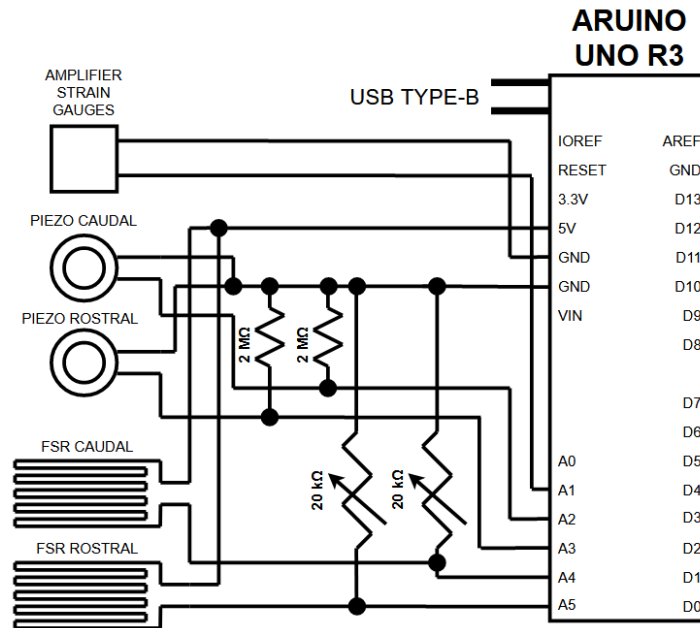


Figure 5-31 Arduino circuit diagram

The FSRs are variable resistors and therefore need to be connected in series with another resistor. The highest sensitivity can be obtained when a resistor is chosen with a value equal to the estimated maximal resistance of the FSR. This maximal resistance is definitely larger than the resistance corresponding with a pressure of 980 Pa, which is the applied pressure, because the hydrogel also applies a hydrostatic pressure to the caudal plate. Figure 5-32 shows the resistance versus force graph of an FSR. A potentiometer with a maximum resistance of 20 k Ω is connected in series with the FSR between 5 V and 0 V, as shown in Figure 5-31. It can be adjusted while calibrating until the desired sensitivity range has been reached. For example, for a total force of 200 grams a resistance of 8 k Ω is needed.

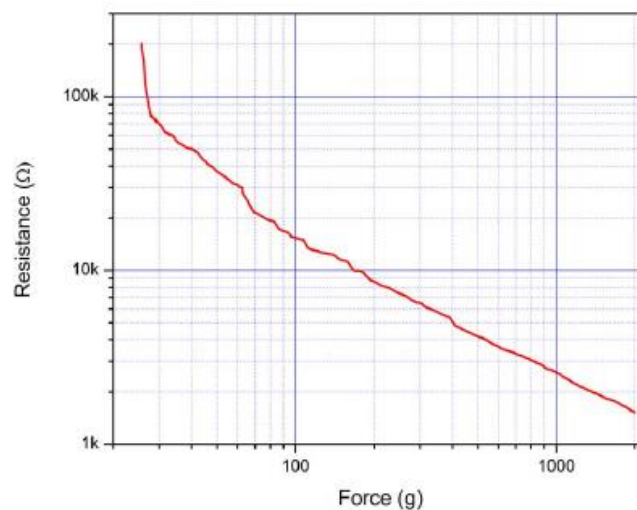


Figure 5-32 Resistance versus force graph (Interlink Electronics, 2021)

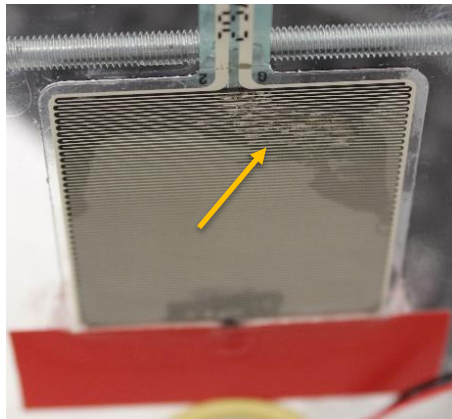


Figure 5-33 Burned rostral FSR

As mentioned in the previous paragraph, the potentiometer can be adjusted during calibration. However, this must be done with due attention. The voltage across the FSR is high when the resistance of the potentiometer is set to a small value. The resistance of the FSR is low when a high force is applied on it. When the conditions above occur at the same time, the current through the resistor becomes high. This can cause the FSR to burn, what eventually happened with the FSR at the rostral side. Figure 5-33 shows the burned rostral FSR, which would actually only be used to measure pressure drops in the tissue. The burnt part is indicated with an orange arrow. Due to the fact that the sensor is burnt, the pressure drop cannot be measured during the experiments. The caudal FSR on the other hand functions as required. It is therefore possible to measure the pressure at the caudal side.

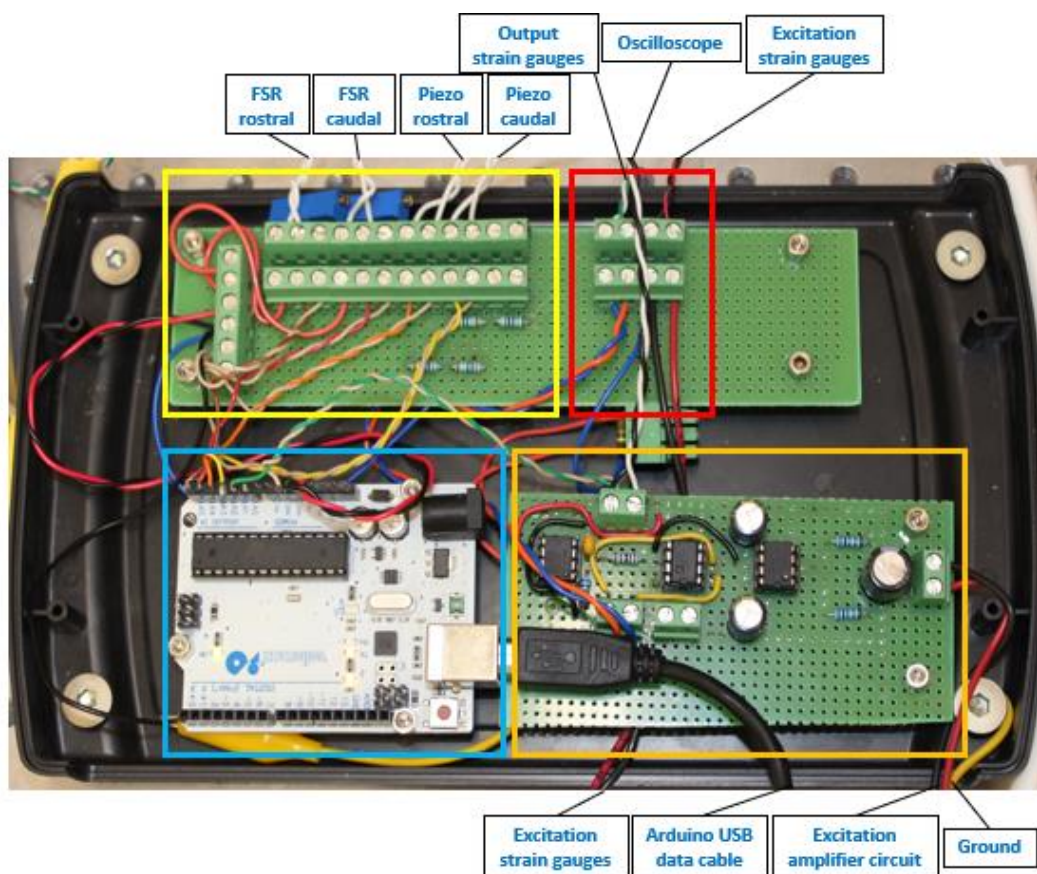


Figure 5-34 Case with electric circuits

When all electric circuits are defined, an enclosure is built in which the circuits of all sensors are placed. Figure 5-34 shows this case consisting of four main parts and is mechanically constrained by four bolts attached to the anti-vibration table. The first yellow rectangle indicates the circuitry of the pressure sensors. Inputs arrive over here by twisted wires connected to the piezos and FSRs at both the rostral and the caudal side. Both the excitation of the strain gauges and the test wires to the oscilloscope for visualisation leave the case at the red rectangle, while the output of the strain gauges enters this rectangle. Furthermore, the blue rectangle indicates the Arduino by which all sensor signals are processed. Finally, the amplifier circuit is located in the orange rectangle, where its excitation also enters.

5.4 Tissue phantom

A hydrogel makes it possible to mimic mechanical properties of organic tissue like materials. Possible options are based on polyvinyl alcohol, agarose, agar etc. The preparation procedures to make these hydrogels are not entirely equivalent, but they follow the same method. A specific amount of powder is dissolved in a solvent at an elevated temperature. This ensures all particles to be dissolved and the solution to have the correct concentration. Afterwards the solution can be poured into the mould and can cool down in order to stiffen.

The provided datasheet of VWR shows the characteristics of the agarose powder and indicates which concentration is needed when a certain gel strength is required (VWR, 2015). The elastic modulus of 50 kPa from the FEM model has to be the same as the elastic modulus of the actual hydrogel. The hydrogel can thus represent the tissue from the FEM model accurately.

Agarose I of VWR is a generally used agarose powder and is a suitable candidate to prepare the tissue phantom. No additional buffer solvent or visualisation dye is required. A solvent of distilled water suffices, because only the mechanical properties of the gel are of interest.

The stiffness of the tissue depends on the concentration of the solution, and thus the mass fraction of the agarose powder in the solvent is expressed in weight percentage. A value of 1200 grams/cm² is obtained from the datasheet for a concentration of 1,5 w% gel. The elastic modulus can be calculated according these values:

$$E = 1200 \frac{g}{cm^2} = 117,7 \text{ kPa} \quad (5-17)$$

Relating this value to the concentration of 1,5 w% gives a value for an elastic modulus of 50 kPa:

$$c = \frac{50 \text{ kPa}}{117,7 \text{ kPa}} \cdot 1,5 \text{ w\%} = 0,637 \text{ w\%} \quad (5-18)$$

Thus, the mass fraction of agarose powder with respect to water equals 0,637 w% according to (5-18). Rounding off this value gives a mass fraction of 0,6 w% and corresponds with an elastic modulus of around 47 kPa, which is still suitable for the experiment.

The volume of the hydrogel is determined by the internal volume of the mould. The dimensions are 150 mm x 150 mm x 200 mm and thus the volume equals 4,5 L. During the heating, some water will evaporate and therefore an additional volume is recommended.

5.5 Conclusion

A micromotion sensor, consisting of an implant attached to four sensitive beams with two attached strain gauges, is selected. The geometry of the tissue and the implant has to be scaled up by a factor of 10:1 as a result of geometrical constraints of the 3D printed implant module. In addition, the FEM model has to be modified by including the sensitive beams and scaling up the geometry. The sensitive beam model shows similar results to the toggle point model, meaning that the sensitive beams correctly replace the toggle point. In addition, the strain gauges are placed in a Wheatstone bridge and an analog circuit is designed to amplify the output voltage signal and to filter high frequency noise.

To eliminate vibrations of the environment, an anti-vibration table is used. An aluminium frame is attached to this anti-vibration table. The implant module is connected to a moveable sub-frame of the aluminium frame in order to lower it into a hydrogel, emulating the brain tissue. The hydrogel is poured into a plexiglass mould, emulating the skull. The mould is also attached to the anti-vibration table. Linear motions can be applied at the caudal surface of the tissue in order to simulate the respiration as input.

A captive linear actuator is found to be a suitable candidate to apply the linear motion. Similar to the aluminium frame, an attachment is designed to connect the actuator to the anti-vibration table. The actuator can be operated via the corresponding software package in order to simulate the respiration input. To determine the applied pressure, an FSR sensor and two piezo electric sensors are included. The sensors with corresponding electric components are connected to a data acquisition system based on an Arduino Uno.

The hydrogel, emulating the brain tissue, consists of a solution of agarose powder and distilled water. The elastic modulus of 50 kPa is obtained by making an hydrogel with a concentration of 0,6 w%.

6 EXPERIMENT

First, a protocol is set up for both the tissue phantom preparation as well as for the experiment itself. The tissue phantom is prepared before testing. Calibrating the micromotion sensor and the pressure sensors is also prior to testing. Next, the components need to be assembled, the implant is inserted in the tissue, the electrical connections are made and the motor control is set up. Finally, measurements are taken during the experiment.

6.1 Protocol

The experiment protocol is composed of consecutive steps in which different prerequisites need to be completed. The preparation protocol and the experiment protocol are spread over two days in order to allow the cooling and solidification process of the hydrogel overnight. An overview of the preparation protocol and the experiment protocol can be found in Appendix E.

First, the hydrogel has to be prepared according to a prescribed procedure, after which it is poured into the mould in different stages. When the mould is filled, it can be positioned and tightened on the anti-vibration table. Subsequently, the implant module is positioned in place after being inserted into the hydrogel. The linear actuator is then positioned and connected to the mould.

The sensors and actuator are connected to the respective interfaces after the hydrogel has been allowed to cool and solidify overnight. The motor is tuned afterwards, according to the desired settings. Finally, the measurements are conducted after the required preparations have been made. Four continuous measurements are carried out during a minimum time frame of five minutes. The frequency of the displacement of the linear actuator is altered for these four measurements from 2 Hz to 1 Hz, 0,5 Hz and 0,25 Hz.

6.2 Gel preparation

A gel concentration of 0,6 w% agarose, as obtained in 5.4, is small enough to use a microwave oven to heat the solution and to use a stirrer to mix the powder in the solvent. Concentrations of 5 w% or higher require special equipment such as an autoclave, according to the recommendations of the supplier (VWR, 2015).

As mentioned in 5.4, Agarose I is a suitable candidate to prepare the tissue phantom. A concentration of 0,6 w% agarose can be obtained by dissolving a mass of 6 grams agarose I powder in 1 kg of solvent, which corresponds with a volume of 1 L distilled water. The mass of the agarose powder is measured by a precision scale.

In total, a volume of 4,5 L has to be casted into the mould. This implies that the casting of the gel is done in several stages. Five stages of approximately 1 L each enhance the agility with which the gel is made and poured. To limit the time between the castings, two stages are processed at the same time. This means that the first two litres of gel solution are made at the same time, followed by the second two litres and finally the fifth and last litre of solution.

First, distilled water is heated during approximately five minutes to easier dissolve the powder in the solvent. The powder is then added and the solution is stirred gently with a metal stirrer for about five to ten seconds. Subsequently, the beakers are heated until approximately 90 °C in order to completely dissolve the powder into the solvent. Figure 6-1 shows a picture of the stirring of the gel solution and a picture of the temperature measurement.

Additional remarks on the preparation protocol are described in Appendix F, as well as the obtained measurements and calculated results regarding the concentration of the hydrogel.

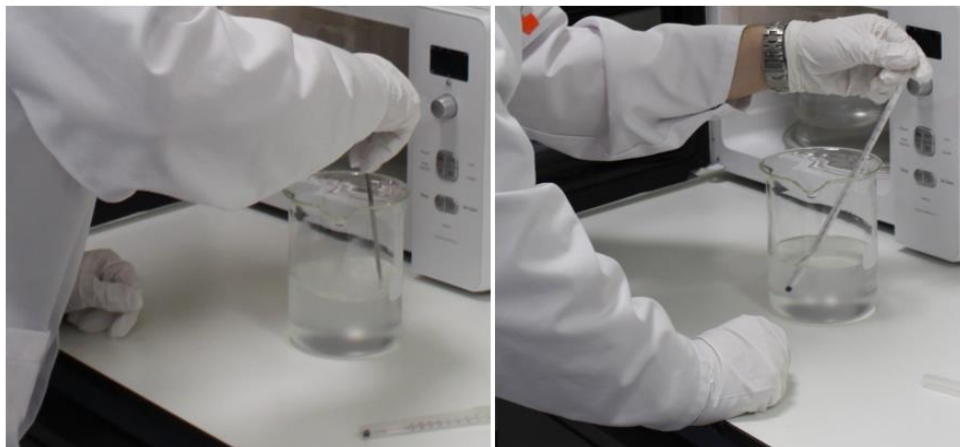


Figure 6-1 Stirring of the gel solution and measuring of the temperature

When bubbles appear at a temperature of approximately 90 °C, the powder is completely dissolved in the solvent, after which the solution has to cool down at room temperature, which equals 22 °C, until approximately 50 °C to 60 °C in order to pour it into the mould (VWR, 2015). This means that when the second two litres, followed by the fifth litre, are poured, the first two litres are already partly cooled down. Note that all solutions have to be poured slowly and carefully into the mould in order to avoid air bubbles and inhomogeneities. Remaining bubbles can be popped to obtain a homogeneous cast. However, a boundary line between the consecutive castings is inevitable because of the rapid solidification and the preparation time between the consecutive castings. Figure 6-2 shows a picture of the pouring process, accomplished under a fume hood, and a picture of the casted gel solution in the mould.

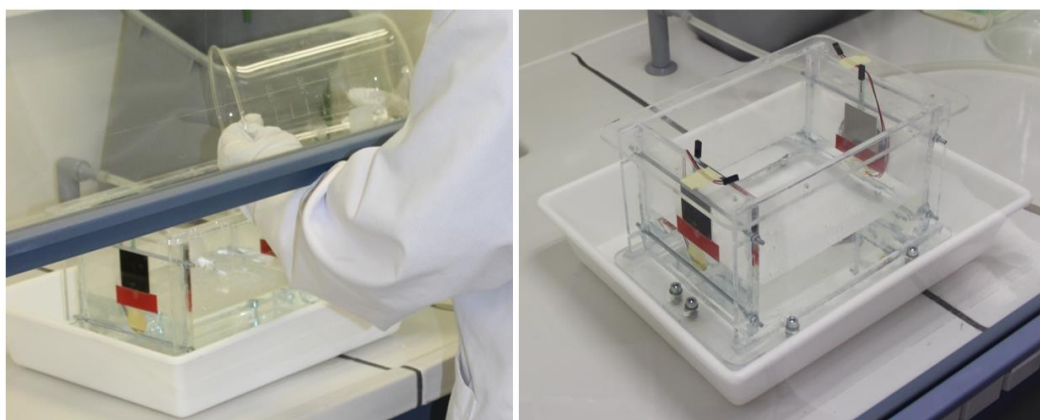


Figure 6-2 The pouring of the gel solution at the left and the gel solution in the mould at the right

6.3 Sensor calibration

A calibration of the sensors is required in order to obtain a repeatable experiment. The micro-motion sensor is calibrated by applying known displacements at a certain height of the implant shank and by measuring the corresponding differential voltage. The calibration of the pressure sensors is done by placing known masses on the sensor and measuring the corresponding analog value from the data-acquisition. The calibration data are attached in Appendix M, provided on an electronic medium.

6.3.1 Micromotion sensor

A certain displacement at a known height of the shank of the implant module makes it possible to calibrate the sensor. The output voltage of the circuit is fed into an oscilloscope and afterwards used to draw up the calibration curve of the displacement in function of the differential output voltage. Figure 6-3 shows the calibration set-up with a motorised microdisplacement actuator and the implant module. The top picture shows the entire calibration set-up with at the left the controller of the motorised microdisplacement actuator, on top of the power supply of the circuit. The implant module is attached underneath the frame. The microdisplacement actuator can be seen in front of the implant module at a distance of 20 mm from the top of the sensor. The top surface of the tissue is situated at this height and therefore the implant has a quasilinear deformation below this height, according to the FEM models as shown in Figure 4-25. The picture on the bottom left side shows a close-up of the motorised microdisplacement actuator and the picture on the bottom right side shows a close-up of the scale of the microdisplacement actuator.

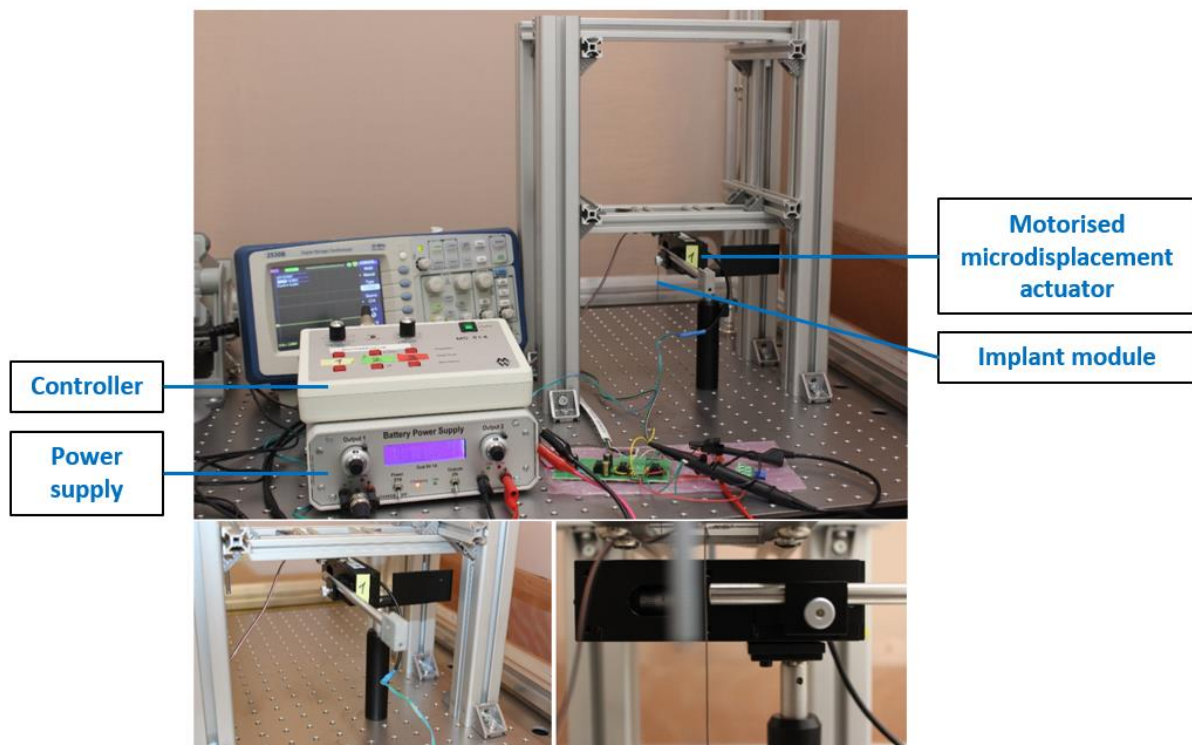


Figure 6-3 Calibration set-up of the implant module

During the calibration process, displacements of 25 μm up to 250 μm with intervals of 25 μm were exerted onto the shank of the implant module at a distance of 20 mm from the top. This represents the height at which the top surface of the tissue is situated and is thus representable for the results in 4.4, which are also obtained from measurements at the top surface of the rat brain. The output voltage of the implant without displacement is subtracted from the output voltage of the maximum displacement. This differential voltage represents the output voltage fed into the data acquisition in the actual experiment. The amplitude of the wave in the experiment is directly related to this differential voltage.

The calibration at each displacement interval is done three times, which means that the differential voltage of the calibration curve is determined by three measurements at each displacement. Figure 6-4 shows the three measurements at a displacement of 75 μm . The vertical black lines represent the boundaries at which the measurement data is split for further selection. The first area, between the first and second vertical black line, represents the output voltage at which the displacement is applied. The third area, between the third and fourth vertical black line, represents the output voltage when no displacement is applied. The difference of these output voltages then represents the direct correlation between the applied displacement and the measured output voltage. A Savitzky-Golay filter is applied in order to achieve a valuable visualisation of the measurements. The filter is of the second order and its frame length includes 101 data points, which corresponds with a time span that approximately equals 20 ms. Appendix G includes the measurement data of the calibrations at displacements ranging from 25 μm to 250 μm .

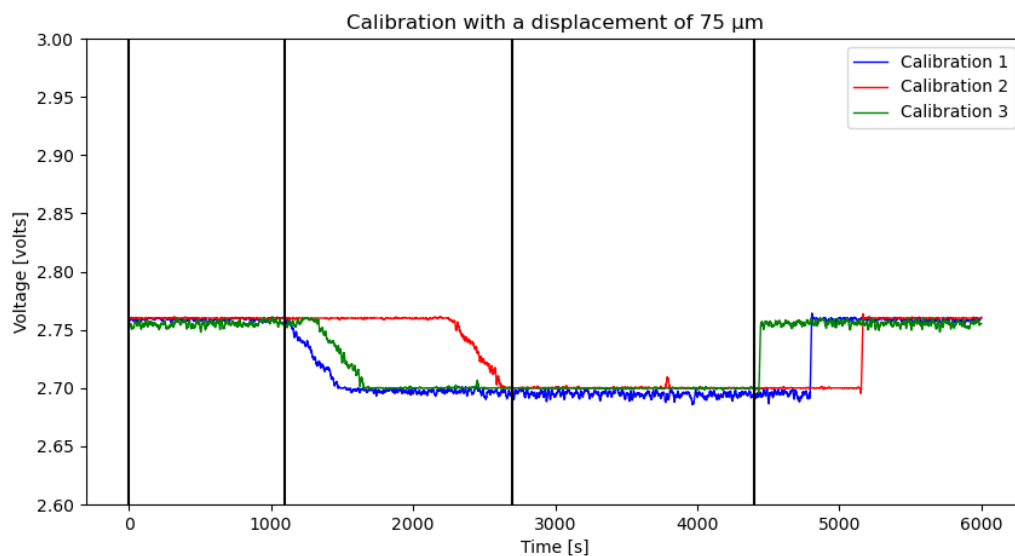


Figure 6-4 Calibration of the implant module with a displacement of 75 μm

The calibration curve is now drawn up from the average of each of the three measurements for every displacement. Figure 6-5 displays the calibration curve for displacements of 25 μm up to 250 μm . The horizontal and vertical lines represent the error bars of the measurements. An error of 20 mV is obtained from the readings of the oscilloscope and an error of 2,5 μm is obtained from the readings of the displacement actuator. A curve fit is added to represent the linear calibration curve.

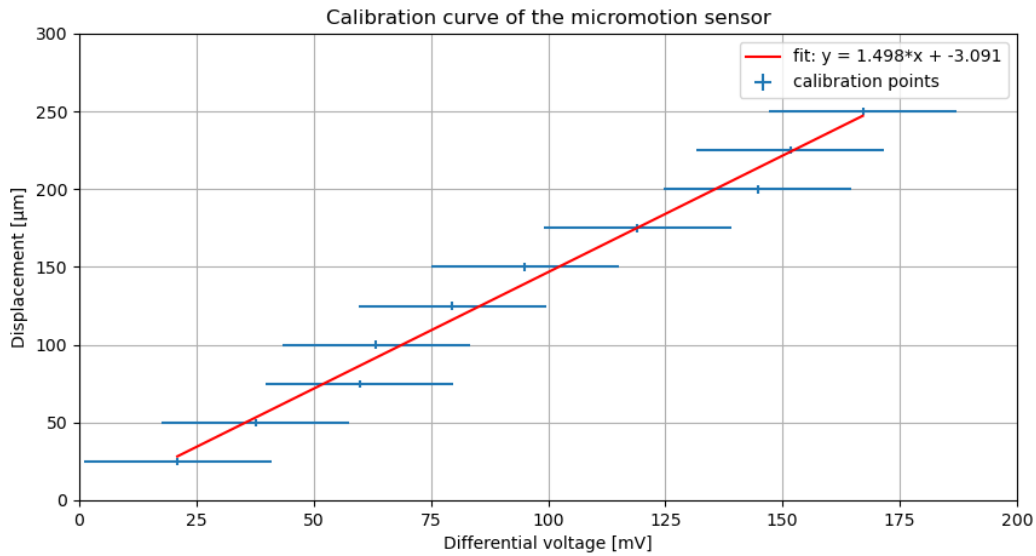


Figure 6-5 Calibration curve of the implant module

6.3.2 Pressure sensors

The caudal FSR sensor can be calibrated by measuring the resistance while known loads are placed on the sensitive area of the sensor. The Arduino assigns an analog value used to draw up the calibration curve of the pressure versus the analog value. Figure 6-6 shows the calibration set-up. A calibration cube is designed in which known masses can be put. The left picture shows that the bottom has the same surface as the sensitive area of the sensors. The right picture shows the cube containing spherical masses.

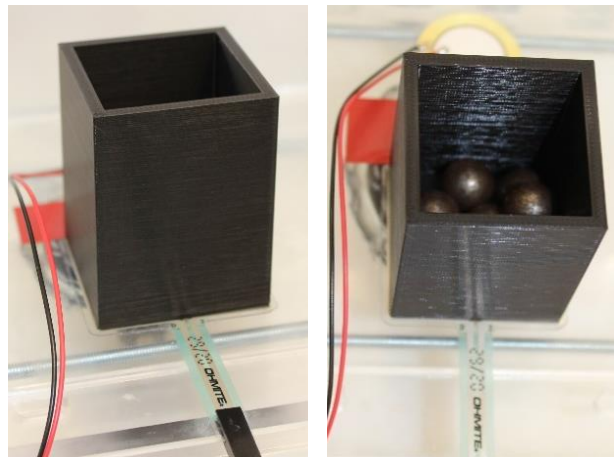


Figure 6-6 Calibration set-up of the caudal FSR

During the calibration process, masses equal 325,9236 gram, 271,6505 gram, 221,4987 gram, 179,0315 gram and 129,9886 gram are placed on the FSR. These masses are measured with a precision scale and are referred to as masses 1, 2, 3, 4 and 5. It is necessary to wait for the analog value to stabilise because the FSR exhibits hysteresis. All calibrations are executed five times, which means that the analog value of the calibration curve is determined by five measurements for each mass.

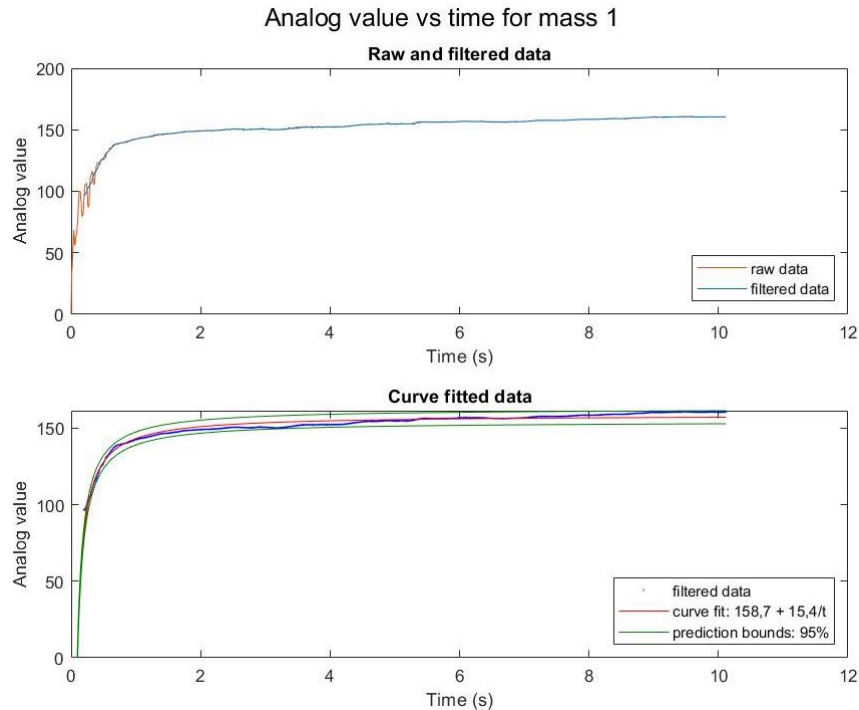


Figure 6-7 Calibration of the caudal FSR with mass 1

Figure 6-7 shows the measurement data of the calibration for mass 1. Note that the offset voltage is already subtracted from the analog value in this curve. The averaged raw data of the five measurements are plotted in orange in the upper graph. A Savitzky-Golay filter is applied in order to achieve a valuable visualisation of the measurements. The filter is of the third order and its frame length includes 51 data points, which corresponds with a time span that approximately equals 0,5 s. The filtered data is plotted in the upper graph in blue. A second graph also shows the filtered data in blue to enable better visualisation. Afterwards, a curve is constructed by curve fitting the filtered data. The fitted curve is of the form: $A + B/t$ with A representing the value to which the signal converges, B is a constant and t is the time. The 95% prediction bounds of this curve fit are plotted in green. The curves for the other four masses can be found in Appendix H. Figure 6-8 shows the calibration curve drawn up based on all known masses and the respective values of their fitted curves. In addition, a curve fit is added to represent the linear calibration curve.

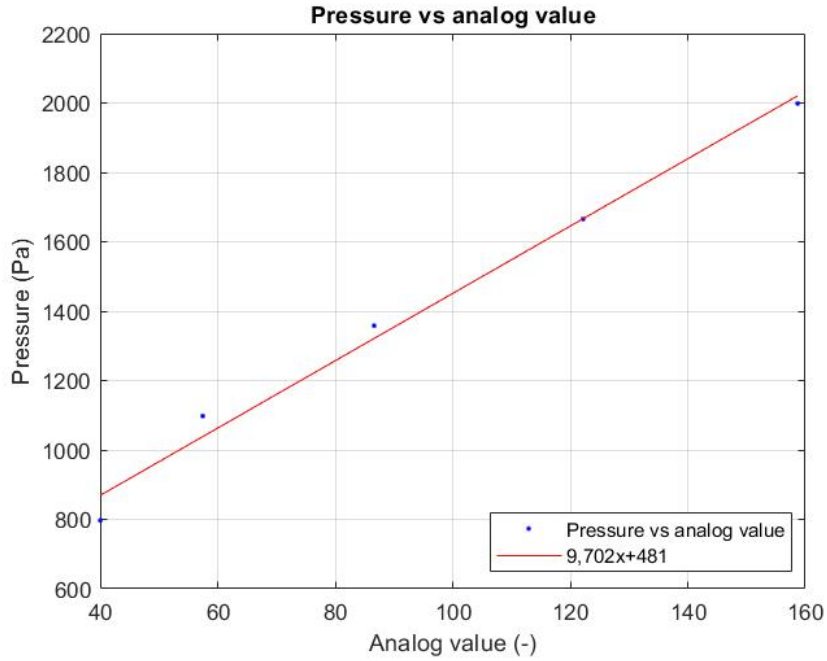


Figure 6-8 Calibration curve of the caudal FSR

Because the FSR cannot measure dynamic pressures, the maximal force applied on the tissue has to be statically calibrated and measured. This is executed 18 hours after the pouring of the gel into the mould. The linear actuator motions, equal to 1,98 mm, 1,90 mm, 1,58 mm and 2,58 mm, are applied on the caudal tissue surface. These linear strokes are measured with a calliper and are referred to as strokes 1, 2, 3, and 4. Figure 6-9 shows the measurement data of the calibration for stroke 1. Note that the plotted data are similar to the data in Figure 6-7. A Savitzky-Golay filter is applied in order to achieve a valuable visualisation of the measurements. The filter is of the third order and its frame length includes 501 data points, which corresponds with a time span of 5 s. The fitted curve is of the form: $A + B/t$ where A represents the value to which the signal converges, B is a constant and t is the time. Value A filled out in the curve fit of the calibration curve results in the applied pressure. Based on the four measurements, the applied pressure is 1337 Pa with minimum and maximum values, which equal 1280 Pa and 1405 Pa.

The piezo sensors are not calibrated because they are only used for a qualitative visualisation of the pressure change.

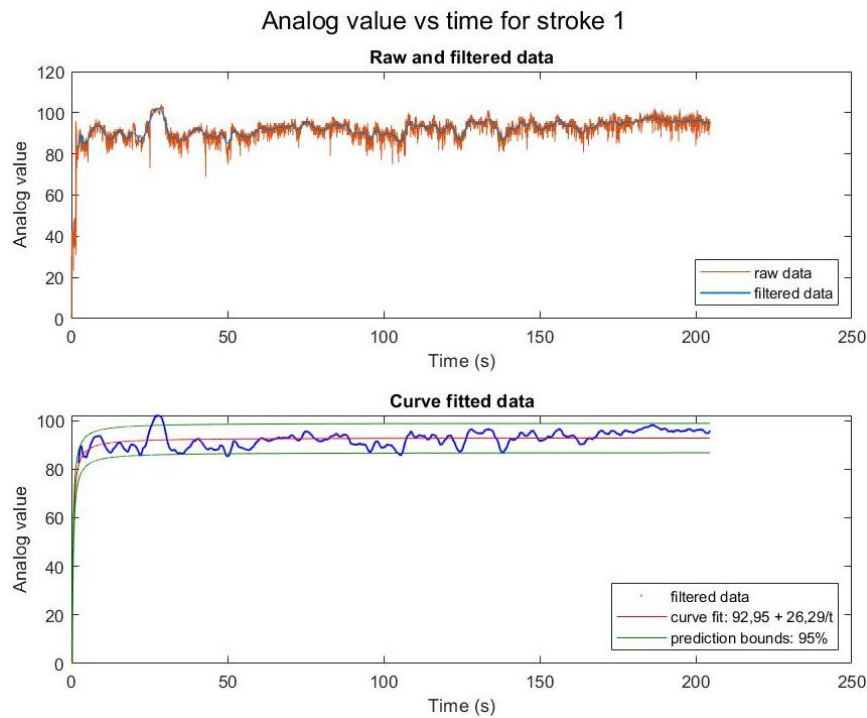


Figure 6-9 Calibration of the caudal FSR at stroke 1

6.4 Assembly and implant insertion

Before starting the experiment, the frame is mounted onto the anti-vibration table based on the technical drawings attached in Appendix J. Afterwards, the implant module is attached to this frame with bolts. The movable part of the frame is placed in the highest possible position using the two threaded rods. This prevents the mould touching the implant and deforming it. The mould is placed in its final position and attached to the anti-vibration table with bolts, after which the implant is lowered just in the centre above the hole. Alignments are done by unscrewing and tightening the bolts, connecting the movable part of the frame with the rigid part.

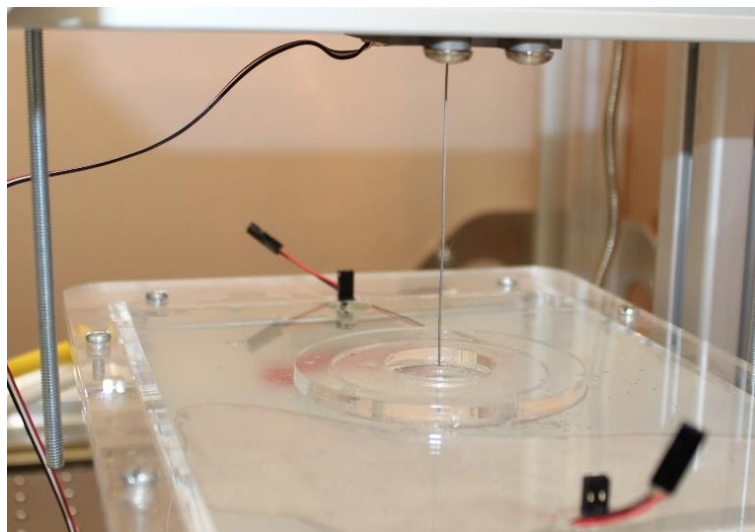


Figure 6-10 Implant positioned in the centre, above the hole

Figure 6-10 shows the implant in the start position of the insertion. Note that the gel is not yet solidified when the implant is inserted. The time between pouring and implant insertion is 25 minutes. The implant is slowly inserted in the gel by unscrewing the threaded rods. The operator monitors the position of the implant at all times during the insertion. Small adjustments of its horizontal position can be made based on visual observations. This ensures the implant enters the tissue through the centre of the hole. The implant is lowered until the distance between the upper surface of the mould and the movable frame equals approximately 15,5 mm. This is done because the thickness of the mould is 5 mm and the thickness of the beams is 0,5 mm. Taking these values into account means that part of the implant with a length of 20 mm is not inserted in the tissue. The final distance between the mould and the movable frame is measured with a calliper at the left and the right side of the mould, these distances equalling 15,44 and 15,59 mm. Figure 6-11 shows the implant in its final position. Finally, all bolts are tightened, the total insertion takes 25 minutes.



Figure 6-11 Top view of inserted implant module

As mentioned before, the implant is lowered into the gel when it is not yet completely solidified. Figure 6-12 shows a picture of the sensitive beams and the gel five minutes after insertion on the left. The right picture is taken the day after, when the gel was completely solidified. The gel turns opaque when it solidifies. Note that the hole with the small diameter, indicated with orange arrows on Figure 6-12, mimics the craniotomy.

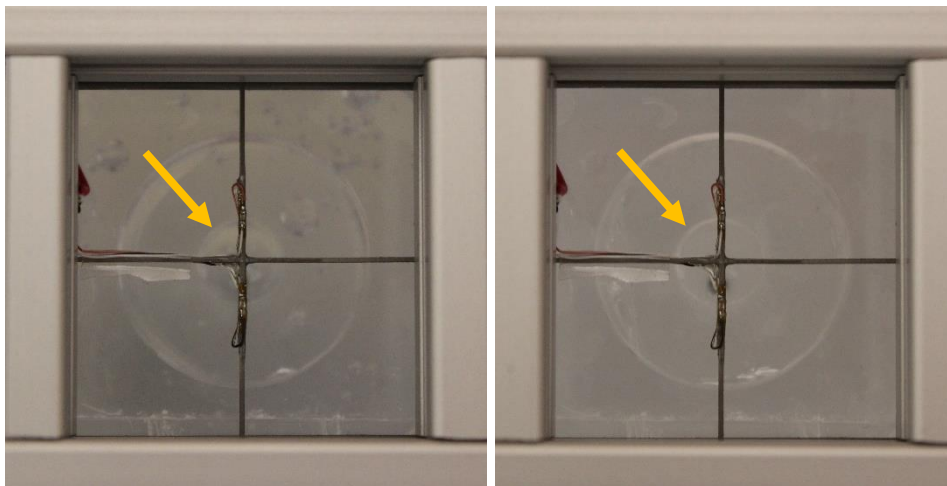


Figure 6-12 Close-up of sensitive beams when gel is not solidified at the left and when the gel has solidified at the right

Finally, the motor is attached onto the anti-vibration table with four bolts, as shown in Figure 6-13. One half of a hinge connection is connected to the mould, the other half to the stepper motor. The start position of the motor is aligned by actuating it forward until the holes of both half hinge connections are aligned. Afterwards, a pin is inserted in both holes, which ensures the hinge connection is established. Finally, the two plates indicated by 'E' in 5.2.3 are removed. This ensures a backward movement of the caudal plate.

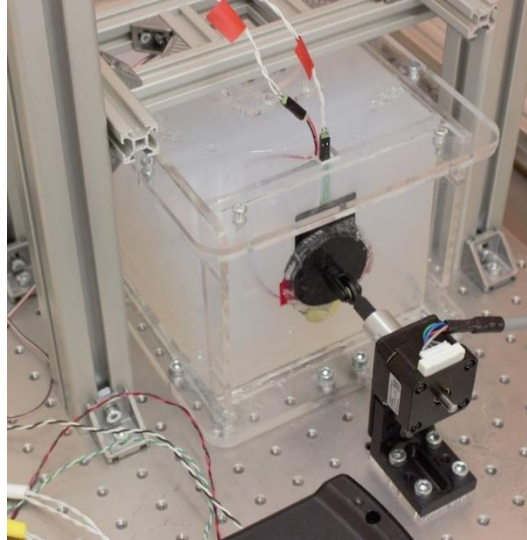


Figure 6-13 Connection of mould and motor to the anti-vibration table

6.5 Electrical connections and motor control

The pressure sensors and amplifier circuit of the strain gauges are connected to the Arduino according to the circuit diagram in Figure 5-31. All wires are twisted in pairs in order to avoid electromagnetic interference and crosstalk. Figure 6-14 shows the connected pressure sensor data cables. The Arduino is connected to a PC and sends the data through a script, written in the integrated development environment (IDE), over a USB connection to an Excel spreadsheet. This spreadsheet reads the value from the analog Arduino ports to which the sensors are connected. The data streamer add-in of Excel is used to read the serial data over the USB connection.

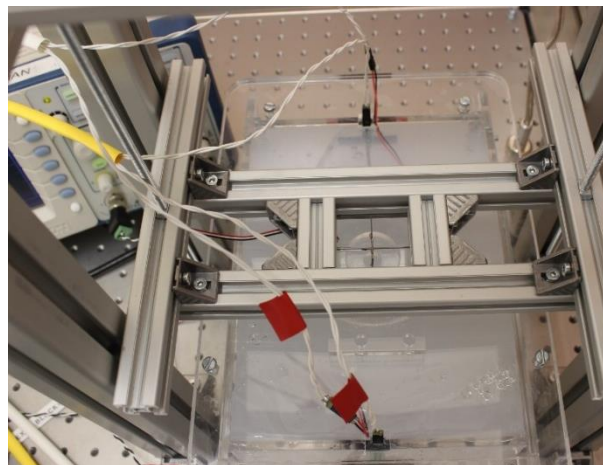


Figure 6-14 Connected pressure sensor data cables

In addition, the amplifier circuit of the strain gauges is connected to an oscilloscope by a BNC connector, a coaxial connector for quick connection and disconnection. The output of the strain gauges is read by the Arduino in order to obtain synchronised signals of the strain gauges and pressure sensors. The oscilloscope is merely used to visualise the output of the strain gauges.

The linear actuator and its corresponding controller are connected according to Figure 5-28. The USB connection connects the controller to the Plug & Drive Studio interface. The initial position of the linear actuator with respect to the mould can be regulated by the interface. The operator can precisely position the motor at a specified position with a small predefined velocity or with a predefined relative position with respect to its current position. When the linear actuator is positioned in the correct place, the operator runs a C++ script, which can be written in the embedded NanoJ editor. Appendix K provided on an electronic medium, contains a C++ script in which the motor moves continuously with an imposed velocity between two points.

6.6 Measurements

The measurements can take place when all mechanical and electrical components are attached and connected. Figure 6-15 shows the total experiment set-up with on the left the rechargeable battery power supply, supplying power to the strain gages circuit. An oscilloscope is placed in the back with the measured strain gauges output voltage presented on the screen. This set-up results in real-time representation, which is important to monitor so that nothing goes wrong during testing. The data acquisition case is placed in the middle. Excitation signals and the ground potential as well as a USB cable are connected to the circuits inside the case. The measurement data are read with the USB cable connection. The tissue phantom inside the mould is located to the right. The motor applies a pressure to the caudal plate of the mould. Both the applied inputs and the measured outputs must be known to relate the input pressure to the displacement of the implant.

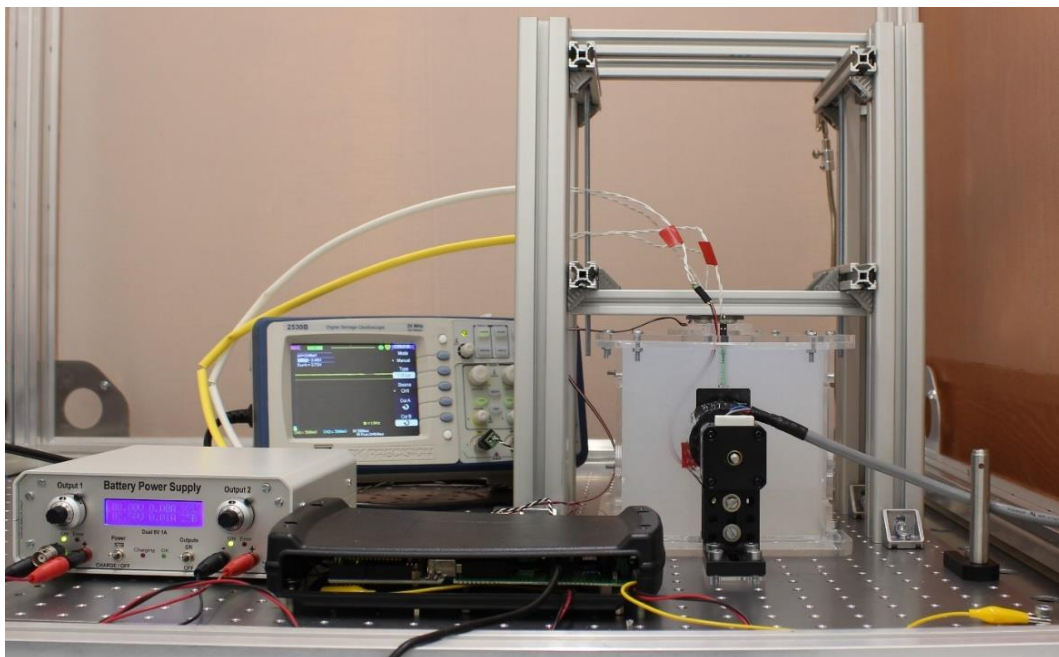


Figure 6-15 Experiment set-up

The applied pressure in the FEM model consists of a sinewave with an amplitude of 980 Pa and a frequency of 2 Hz. The actuated motion in the experiment set-up however consists of a cyclic change of a constant velocity and is thus a triangular wave. Figure 6-16 shows the built-in oscilloscope with the actual values of the position, velocity and torque of the motor. The consideration of this deviant motion regarding the sinewave in the FEM model is due to the fact that linear patterns in the motion are easier to recognise when processing the signals read by the sensors. Furthermore, the sinewave has no significant influence on the maximal obtained displacement of the implant. The viscoelastic behaviour of the tissue is easier to recognise as nonlinearities of the signals obtained.

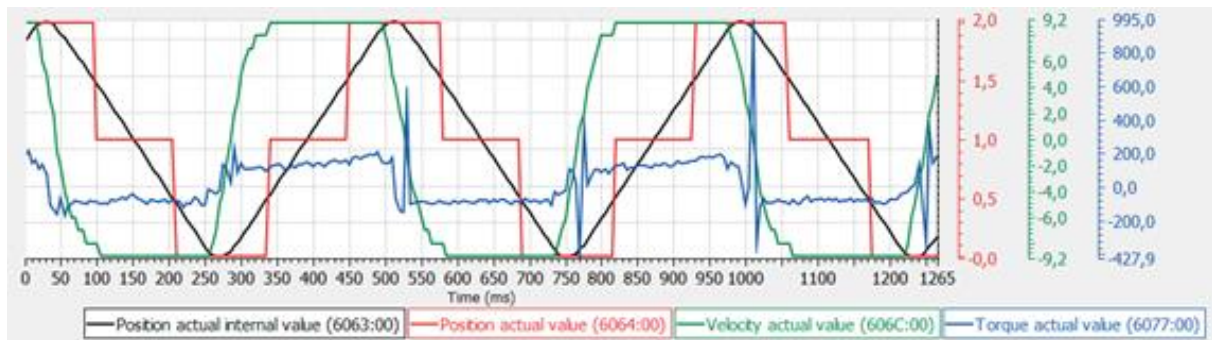


Figure 6-16 Built-in oscilloscope of Plug & Drive Studio (Nanotec, 2021)

The actuator can measure the torque and can display the value within the built-in oscilloscope. However, its use is limited because of the complex interpretation of the torque translated to an applied linear pressure to the tissue. The torque is plotted as the percentage of the rated torque of the motor multiplied by ten. The rated torque indicates the maximum torque at a certain speed without overheating. The position and velocity can be interpreted more accurately because they can be related directly to the linear position and velocity of the motor. The actual positions are plotted in black and red, their scale is the red one in mm. The black graph represents the real displacements of the linear actuator while the red graph is an average signal with integer values as possible values. However, the red graph is merely used as a diagnostic tool and is not of importance in this context. The actuator moves between 0 mm and 2 mm. Finally, the velocity is represented in green with the unit of mm per seconds. The velocity ranges between -9,2 mm and 9,2 mm per seconds. A variation in value of the constant velocity slope changes the applied frequency whereas a variation in the linear stroke of the leadscrew changes the applied pressure. Due to the fact that the latter is not directly controllable, an additional pressure sensor is included in the set-up.

As mentioned in 6.3.2, the caudal side displacement is estimated to be 2 mm. The measurements start ten minutes after the calibration of the FSR. Eight measurements are taken with approximately ten minutes between the start times of the measurements. During one measurement, the motor is actuated in such a way that it moves according to a triangular wave with 2 mm as peak-to-peak value. The frequency is varied from 2 Hz to 1 Hz, 0,5 Hz and 0,25 Hz for the first four measurements to investigate the viscoelastic effects on the displacement of the implant.

During these first four measurements, an unwanted influence is perceived. It concerns an undesirable contact of the sensor connector with the mould. This can be explained by the fact that the caudal plate tilts too much to the rostral side. To prevent this the motor is slightly moved backwards during positioning. Positioning is done by placing the removable plates of the mould back in their places, after which the motor is moved backwards until the caudal plate

touches these plates, which are then removed again. Again a series of four measurements is taken at the four different input frequencies.

Five output signals are read by the Arduino: two FSR signals, two piezo signals and one of the strain gages circuit. The Excel spreadsheet is saved and is easily accessible using Matlab or Python. Hence, later calculations such as filtering and representation of the results can be done by both programs. The measurement data are attached in Appendix N. A movie of the experiment is attached in Appendix O. Both are provided on an electronic medium.

6.7 Conclusion

The hydrogel preparation and the experiment are conducted according to a predefined protocol. Since the volume of the hydrogel is rather large, the gel has to be prepared in five steps. The solution of every consecutive step is first heated to approximately 90 °C and later cooled to approximately 50 °C before pouring it into the mould. Attention has to be paid during the casting to avoid air bubbles and inhomogeneities in the hydrogel.

Furthermore, the micromotion sensor and the FSR sensor need to be calibrated. The micromotion sensor is calibrated by applying a displacement ranging from 25 µm to 250 µm to the implant shank at the height of the top surface of the hydrogel. The FSR sensor is calibrated by applying a pressure ranging from 800 Pa to 2000 Pa in order to measure the steady state analog value that the sensor reaches. A calibration curve is built up to correlate the measurement data to the corresponding input.

When the mould is attached to the anti-vibration table, the implant can be inserted and positioned in place so that the insertion depth is equal to 70 mm. When the implant is inserted, the hydrogel has to cool down in order to solidify and to obtain its final state. The implant is inserted while the gel is not yet solidified in order to improve the attachment of the hydrogel to the implant.

Afterwards, the linear actuator is connected and the measurements are conducted. Four different measurements are taken for a timespan of five minutes, each in order to simulate different frequencies of 0,25 Hz, 0,5 Hz, 1 Hz and 2 Hz. The displacement of the linear actuator is estimated to be 2 mm, corresponding to a desired pressure of approximately 980 Pa.

7 VALIDATION OF FINITE ELEMENT MODEL

To validate the finite element respiration model the data obtained during the experiment need to be analysed. These data are represented for all sensors at the four frequencies. Afterwards the observed physical differences between the respiration model and the experiment are discussed. Based on these differences a new FEM model, the experiment model, is set up. It mimics the experiment with its deviating preconditions. Finally, an overview and discussion of obtained values is given, starting from the respiration model and ending with the experiment model.

7.1 Data analysis

The results of the continuous measurement in the time domain at an applied frequency of 2 Hz are displayed in Figure 7-1. The first graph shows the displacement of the implant module. The second graph shows the signal of the FSR at the caudal side. The third and fourth graph show the signals of the piezo sensors respectively at the caudal and at the rostral side. Note that the results are plotted for a time span of ten seconds from the data of five minutes for better visualisation.

The data of the strain gauge measurement are filtered by a hardware filter included in the amplifier circuit. Hence, no further filtering is required. The FSR and piezo sensors, on the other hand, are not hardware but software filtered by a Savitzky-Golay filter. The filter is of the fifth order and its frame length includes 25 data points, which corresponds with a time span of approximately 250 ms.

The displacement shown on the first graph is obtained by converting the analog value from the data-acquisition into a differential voltage and later on by including the calibration curve, shown in Figure 6-5. As seen on the graph, the implant module reaches a value of approximately 400 μm at the height of the top surface of the tissue when a displacement of 2 mm is applied at the caudal side of the hydrogel. The shape remains triangular, although the edges are not entirely linear.

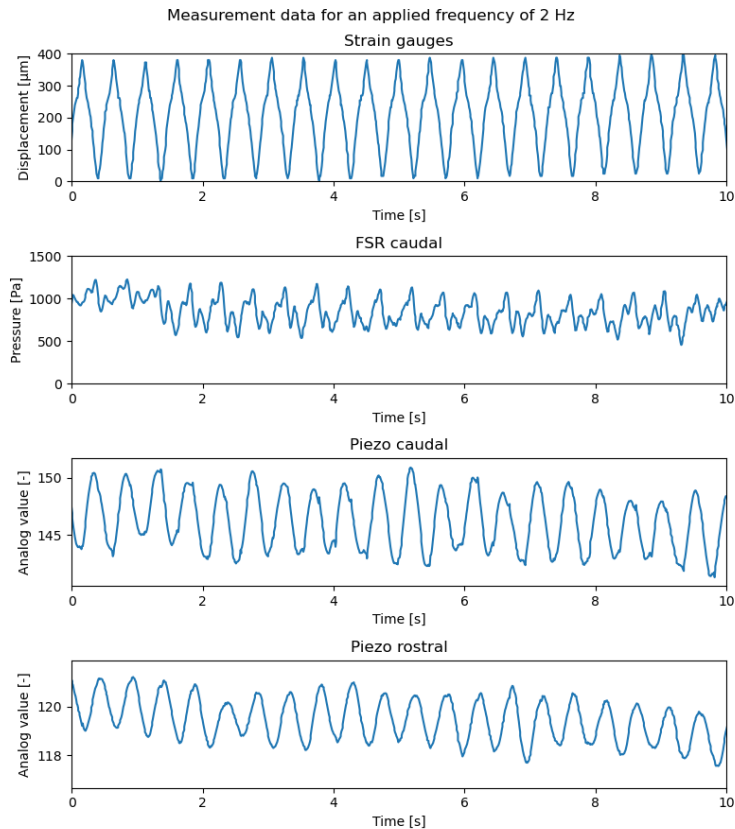


Figure 7-1 Measurement data of the strain gauges, FSR sensor and piezo sensors for a frequency of 2 Hz

In contrast with the measurement of the strain gauges, the measurement of the FSR is obtained by correlating the measurement data to the calibration curve, shown in Figure 6-8. The magnitude of the pressure difference reached values of roughly 600 Pa. However, this value does not correspond with the real applied pressure, which is calibrated in 6.3.2. Figure 6-7 shows that it takes some time for the FSR to reach its final value and thus the magnitude of the pressure in Figure 7-1 is meaningless without the relation to the calibration in 6.3.2. The curve consists of multiple deviating shapes, whereas the peaks of the FSR readings match with the peaks of the strain gauges measurement. An explanation of the deviating shapes can be found in the behaviour of the FSR sensor, interacting with the tissue. The displacement of the tissue is not entirely synchronised with the displacement of the actuator, because of the viscoelasticity of the tissue. Figure 4-20 shows the difference in elastic displacement and viscoelastic displacement in the respiration model. The pressure on the FSR is thus not synchronised with displacement of the actuator because of both the hysteresis of the FSR and the viscoelasticity of the hydrogel.

The magnitude of the measurement of the piezo sensors is not of any consequence in the scope of this measurement because the piezo sensors only measure instantaneous differential pressure. However, the shape and frequency are meaningful. The shape should be similar to a block wave, representing the derivative of the triangular pressure wave. This means that the value of the piezo sensor should be high at a rising edge of the pressure wave and the value should be low at a falling edge of the pressure wave. In addition, the frequency is directly related to the applied frequency of approximately 2 Hz.

Figure 7-2 displays the results of the measurements for an applied frequency of 1 Hz. The same remarks as explained for Figure 7-1 are still applicable.

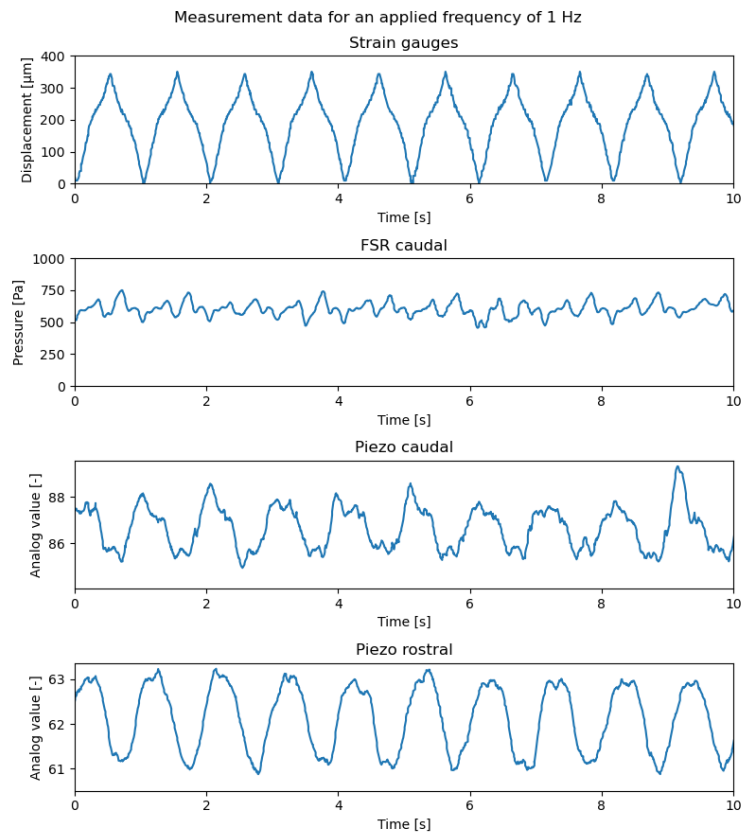


Figure 7-2 Measurement data of the strain gauges, FSR sensor and piezo sensors for a frequency of 1 Hz

The deviations in the shape of the triangular pressure wave are more clearly visible in Figure 7-2. The nonlinear edges can be explained by the hysteresis of the loading and unloading curve of the viscoelastic tissue. The micromotion sensor reaches measurement values of approximately 350 μm . The FSR on the other hand does not display meaningful results, although the repetitive pattern according to the triangular wave is still noticeable. The value of the difference pressure reaches values of around 300 Pa. However, this pressure is not the real applied pressure as mentioned before and the calibration of the FSR should be taken into account again.

The piezo sensors performed like in the first measurement. The superposed peaks at higher frequencies are possibly the result of vibrations of the caudal plate since the caudal plate is directly connected to the actuator and is not fixed to the other plates of the mould. Therefore, the caudal plate is not mechanically isolated from the actuator and is affected by the vibrations of the actuator. Figure 7-2 also shows more visible peaks at high frequencies at the caudal side than at the rostral side.

Figure 7-3 displays the results of the measurements for an applied frequency of 0,5 Hz. The micromotion sensor measures values of around 300 μm and deviating lines are clearly present. The FSR measurements result in a difference pressure of approximately 500 Pa, although these results are again of no consequence since the real applied pressure is determined by the static calibration of the FSR. The piezo sensors at a frequency of 1 Hz behave similarly to the piezo sensors at a frequency of 0,5 Hz. A block wave can be seen in the measurements with small peaks at high frequencies, probably due to vibrations of the actuator.

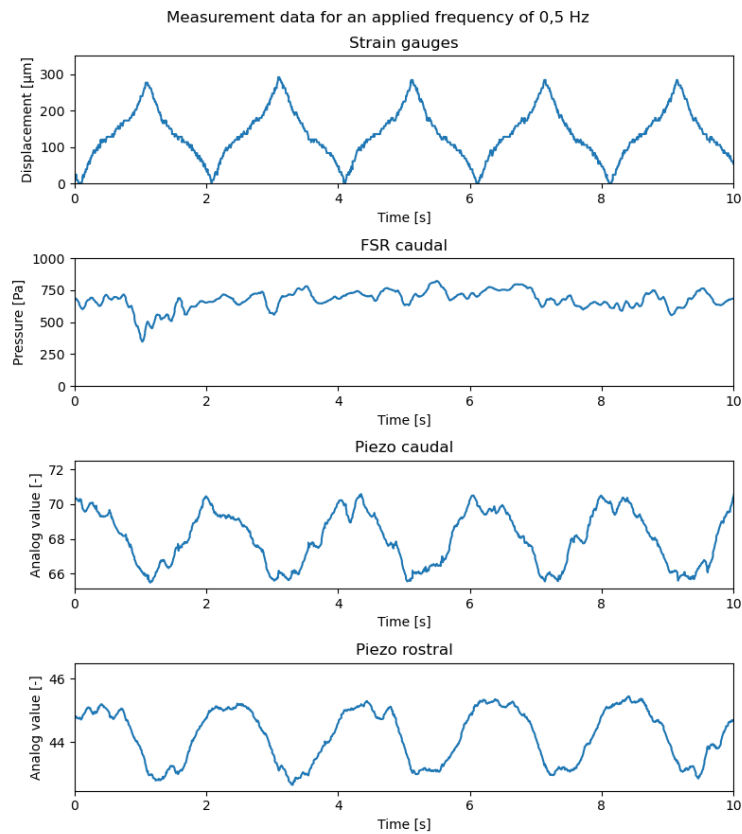


Figure 7-3 Measurement data of the strain gauges, FSR sensor and piezo sensors for a frequency of 0,5 Hz

Figure 7-4 displays the results for the measurement at a frequency of 0,25 Hz. The deviations on the straight lines in the measurements of the micromotion sensor indicate the viscoelastic behaviour of the tissue. The loading and unloading curves are clearly visible on Figure 7-4. A maximal displacement of approximately 400 μm is measured, which is still consistent according to the other values measured.

The FSR shows a remarkably different behaviour according to the previous measurements. However, the pressure magnitude is again of no consequence, since the calibration of the FSR results in the applied pressure. In addition, the shape is different from the other results, proving that the FSR is not suitable for dynamic pressure measurements.

The piezo sensor measurements display a similar shape as the previous results. A block wave can be deduced from the graph. The deviations of the rising and falling edge can be explained by the viscoelastic behaviour of the tissue.

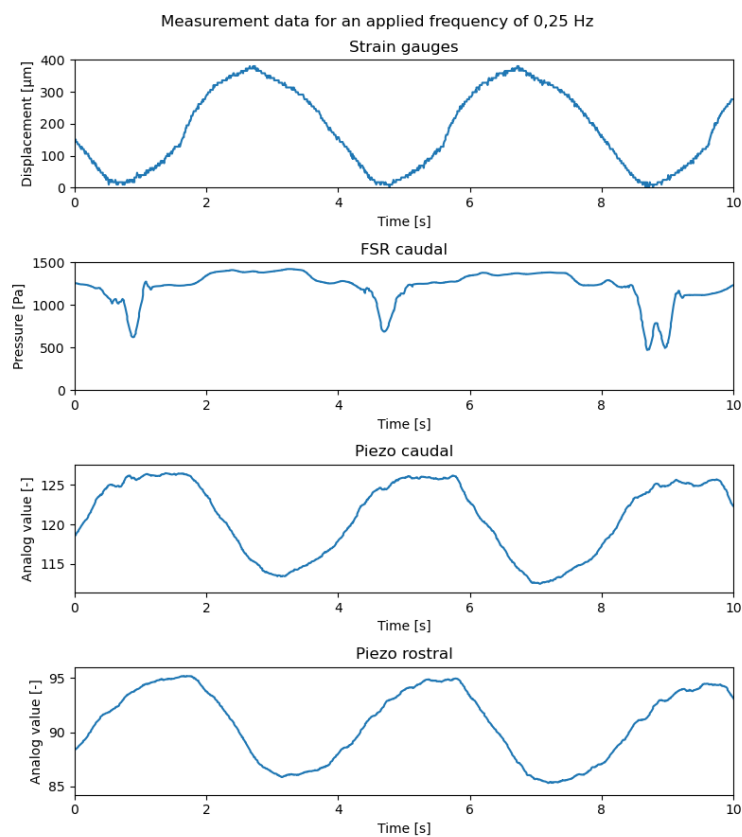


Figure 7-4 Measurement data of the strain gauges, FSR sensor and piezo sensors for a frequency of 0,25 Hz

Figure 7-5 shows the measurement data of the strain gauges for the different frequencies. Four periods are displayed for each frequency. Nonlinear edges can be deduced from all four graphs due to the viscoelastic behaviour of the tissue. However, the curve shape is not the same for all measurements. The shapes at 2 Hz and 1 Hz are more similar than to the other frequencies. This can be explained by two influencing factors: time and applied pressure. For low frequencies, the loading takes longer. Furthermore, the viscoelastic displacement is time dependent. Therefore, the shapes are more triangular at high frequencies. This effect becomes visible when the displacement curves at 0,25 Hz and 2 Hz with the same amplitude, are compared. The amplitude of the displacement is smaller if the applied pressure is lower than demanded. Therefore, the full hysteresis curve of the maximal applied pressure is not covered during the experiment. This is why the displacement trend at 0,5 Hz is totally different for all the other trends.

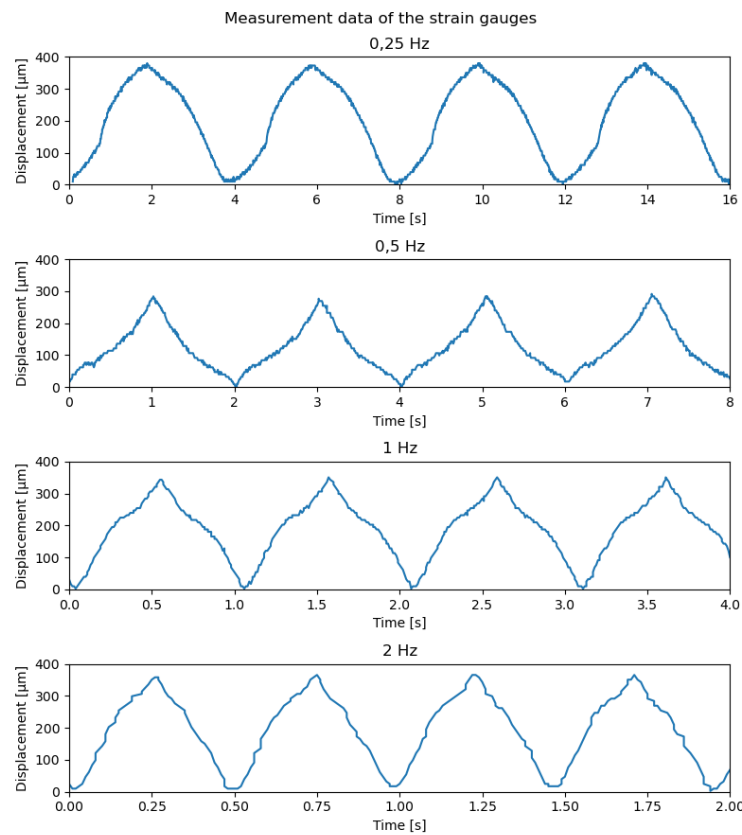


Figure 7-5 Measurement data of the strain gauges for different frequencies

In addition, the power spectra in the frequency domain are represented for the raw measurement data of ten seconds for an applied frequency of 2 Hz, 1 Hz, 0,5 Hz and 0,25 Hz as shown in respectively Figure 7-6, Figure 7-7, Figure 7-8 and Figure 7-9. The four spectra on the figure display the scaled power spectrum of the measurement of respectively the strain gauges, the FSR at the caudal side, the piezo sensor at the caudal side and the piezo sensor at the rostral side. The power spectra are obtained by first subtracting the mean of the signal from the data, subsequently applying a Hann window function on the measurement data to avoid smearing in the power spectrum and later applying a fast Fourier transform. The scaled power is then obtained by taking the square of the absolute value of the measurement data and by scaling the result with respect to the peak at the applied frequency.

Figure 7-6 shows that the applied frequency is not exactly 2 Hz but rather 1,7 Hz, showing that the velocity parameters of the linear actuator are slightly different from the required parameters. However, this does not influence the maximal displacement of the implant module. In addition, the strain gauges and piezo sensors only display a prominent peak at the applied frequency. Peaks at other frequencies are negligible. The FSR, on the other hand, displays measurements with peaks at harmonic frequencies.

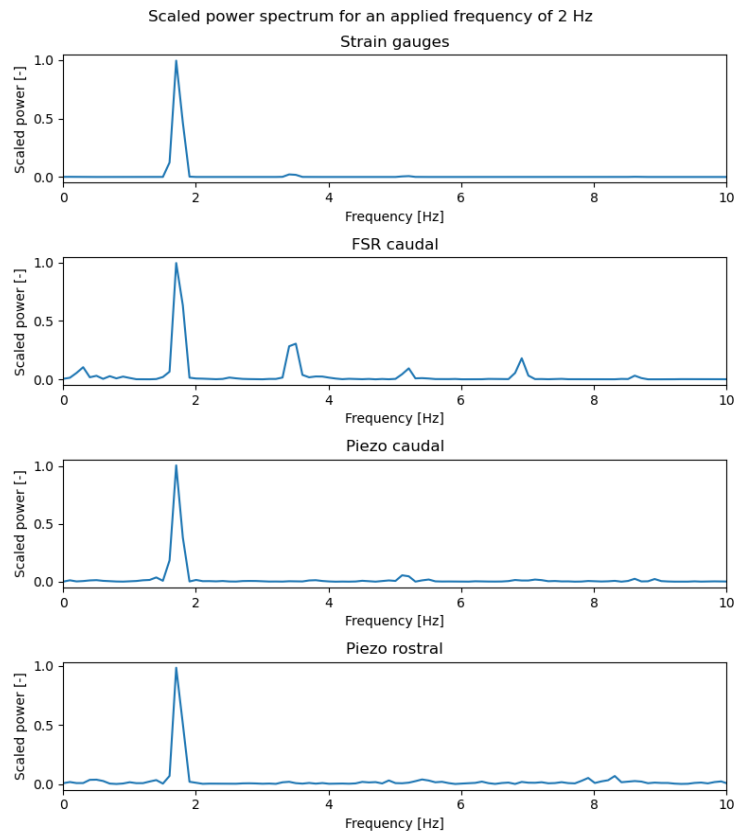


Figure 7-6 Scaled power spectrum of the strain gauges, FSR sensor and piezo sensors for a frequency of 2 Hz

The same behaviour is present in the measurement results at 1 Hz in Figure 7-7. The actual applied frequency is closer to 0,85 Hz. The strain gauges and the piezo sensors show prominent peaks only at the applied frequencies. The FSR again displays peaks at harmonic frequencies and even at very low frequencies. The peak at low frequencies can be explained by the small deviations of the FSR signal over time, resulting in a wave with low frequency superposed with the applied frequency.

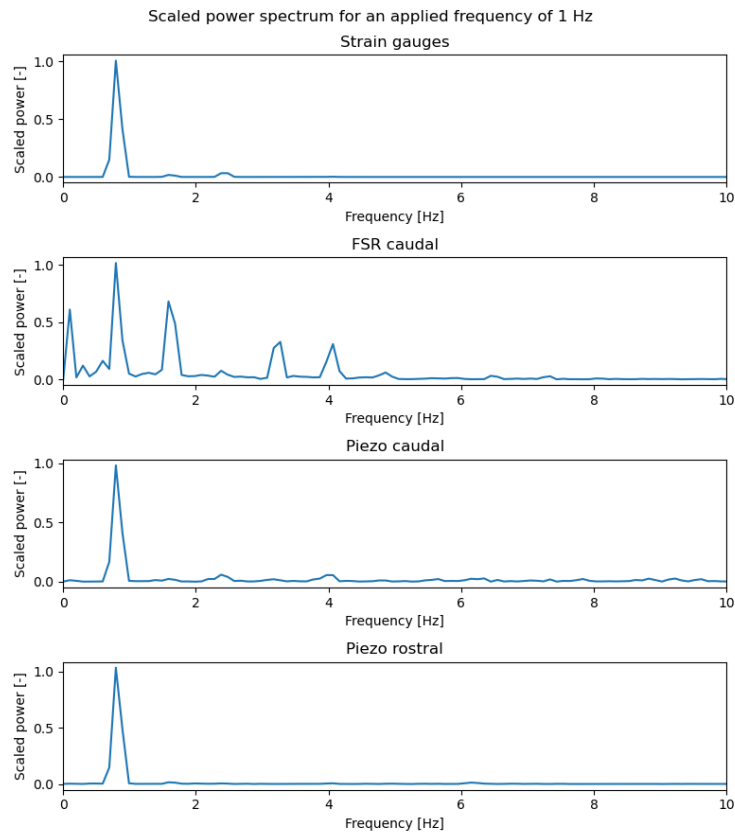


Figure 7-7 Scaled power spectrum of the strain gauges, FSR sensor and piezo sensors for a frequency of 1 Hz

Figure 7-8 displays the power spectra for an applied frequency of 0,5 Hz. The actual frequency applied is again slightly different and is close to 0,4 Hz. The FSR measurement again shows multiple peaks at elevated frequencies and also shows a prominent peak close to the zero frequency region. The magnitude of the peak at the zero frequency region is even larger than the peak at the applied frequency, which means that deviations in the FSR signal are strongly present. Figure 7-3 also shows a deviant behaviour.

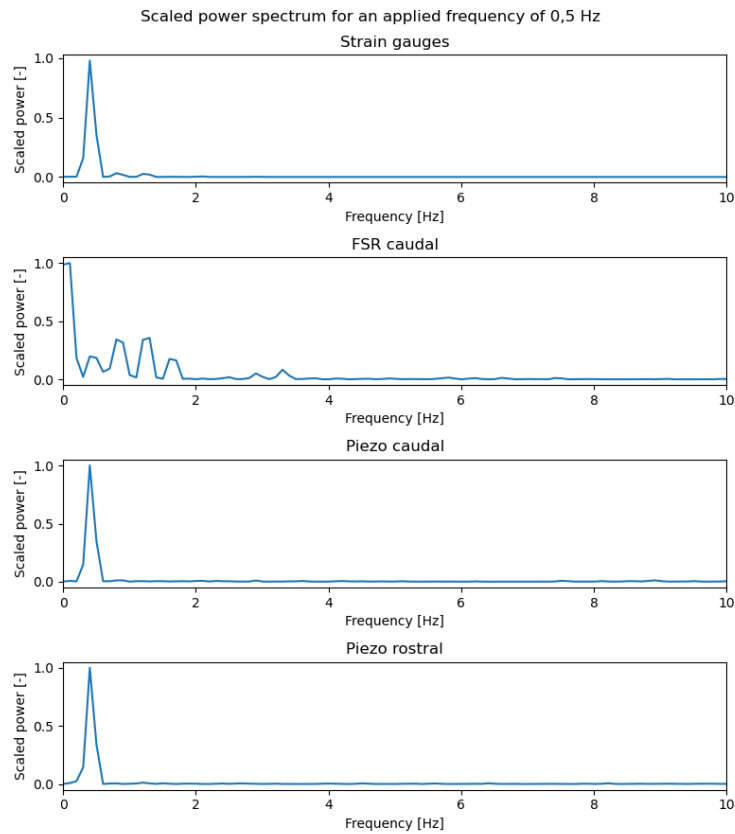


Figure 7-8 Scaled power spectrum of the strain gauges, FSR sensor and piezo sensors for a frequency of 0,5 Hz

The power spectrum for an applied frequency of 0,25 Hz is shown in Figure 7-9. The actual applied frequency is approximately 0,2 Hz. The strain gauges and the piezo sensors display a prominent peak at the applied frequency. The FSR, on the other hand, again displays measurements with harmonic frequencies. Although there is still a peak present at the zero frequency region, the magnitude of the peak is less than the peak at the applied frequency.

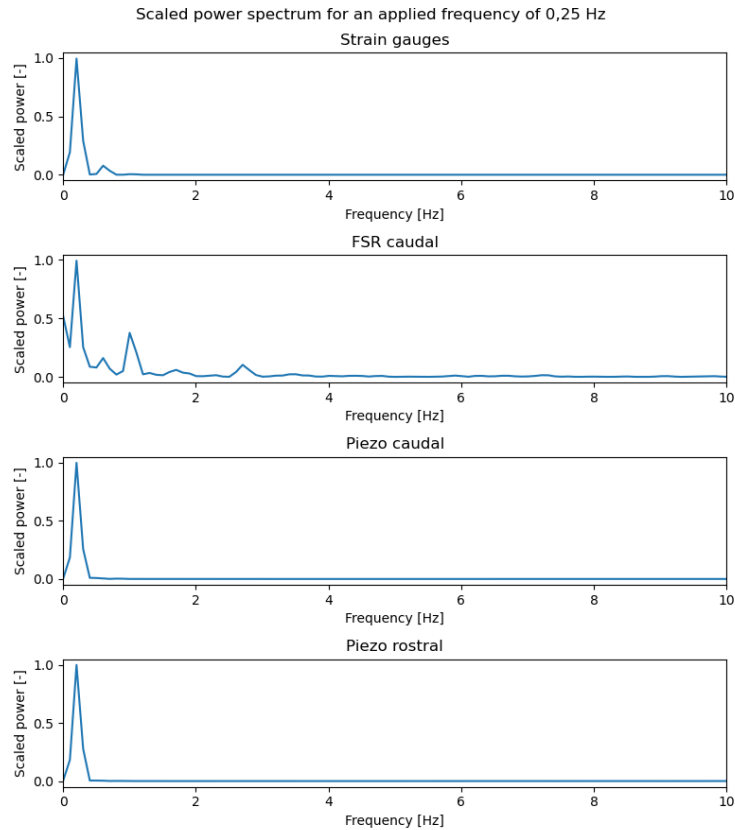


Figure 7-9 Scaled power spectrum of the strain gauges, FSR sensor and piezo sensors for a frequency of 0,25 Hz

7.2 Differences between respiration model and experiment

The experiment is conducted in order to validate the respiration model. Hence, the experiment set-up should approach the FEM model as closely as possible. The same loads must be applied while the boundary conditions have to be identical. However, the set-up will never simulate the model exactly and vice versa. During the experiment a number of notable deviations from the respiration model are observed. The first deviation is the presence of an air gap between the gel and the top plate, as shown in Figure 7-10. The gap is located towards the caudal side, also called the actuation side. The formation of the gap can be explained by overnight shrinkage of the gel. Another cause is the fact that some gel was slipping out of the mould via the vent holes during the positioning of the mould.

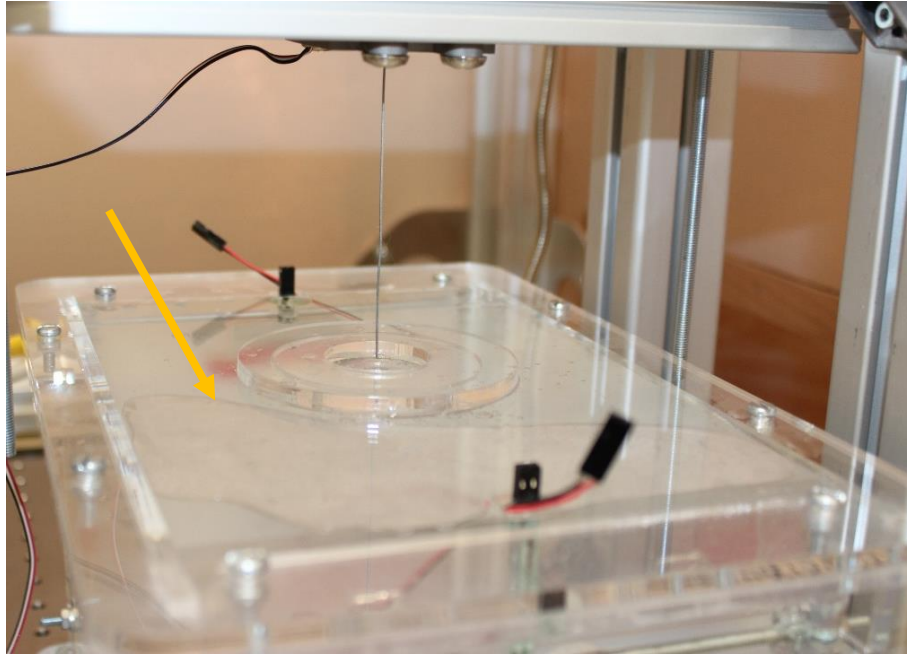


Figure 7-10 Air gap between tissue and top plate, indicated by the arrow

The second important deviation is the inclination of the caudal plate in its two most extreme positions. Figure 7-11 shows the start position on the left and the end position on the right. The caudal plate is at the start position perpendicular to the bottom plate of the mould. However, the caudal plate inclines during the actuation. More specifically, the plate rotates around its baseline with the bottom plate. Therefore, the bottom of the caudal plate does not move in the rostral direction while the top of the caudal plate does move in the rostral direction. Whereas the input displacement in the middle of the plate is 2 mm, the top displacement is 4 mm. In the left picture in Figure 7-11 an inclination line is added, which is the end position that the caudal plate reaches, as shown in the right picture.

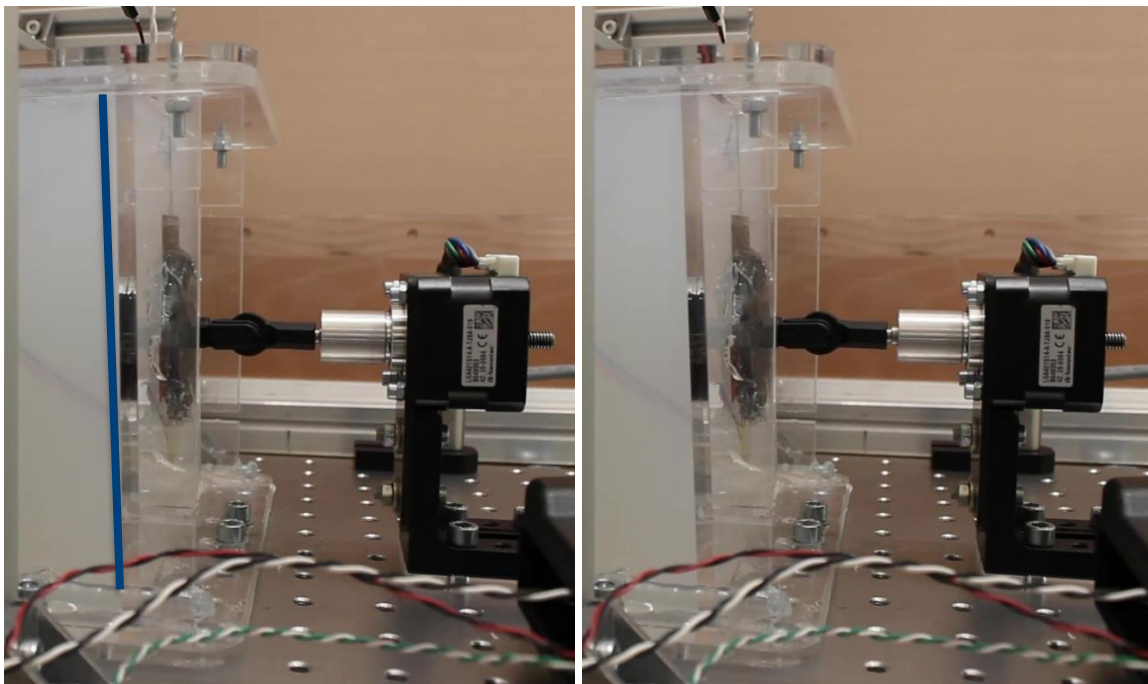


Figure 7-11 Start and end position inclination difference

A result of the rotation of the caudal plate is a different pressure distribution. In the respiration model, an equally distributed load is considered. However, the pressure increases towards the top when the caudal plate is skewed. This is because the gel is pressed harder towards the top. Note that the hydrogel itself applies a hydrostatic pressure at the caudal plate. However, the hydrostatic pressure at the moment when the actuator is in standstill is assumed to be equal to the hydrostatic pressure when the actuator applies full pressure. The pressure distribution Q is determined as the pressure difference with respect to standstill. Therefore, the hydrostatic pressure is not taken into account. This pressure distribution Q is distributed linearly in the experiment towards the top of the caudal plate. Figure 7-12 is a pressure diagram of the caudal plate taking into account only the total pressure P_{Tot} applied by the actuator and the pressure distribution applied to the tissue. Note that the largest inclination angle of the caudal plate is only $1,5^\circ$ and is therefore neglected. The pressure distribution measured by the FSR is indicated in green. Using the measured pressure, Q and P_{Tot} can be calculated. A first relation between Q and P_{Tot} is:

$$P_{Tot} = \frac{QH}{2} \quad (7-1)$$

with:

- H , the height of the caudal plate equal to 150 mm

The measured pressure P_{meas} equals:

$$P_{meas} = Q(D_{FSR} + L_{FSR}/2) \quad (7-2)$$

with:

- D_{FSR} , the distance between the bottom of the caudal plate and the FSR equal to 68,75 mm
- L_{FSR} , the FSR side length equal to 40 mm

P_{meas} is determined as explained in 6.3.2 and equals 1337 Pa. This value is inserted in (7-2), Q equals 15,06 Pa/mm. This results in a total pressure in (7-1), which equals 1130 Pa. The calculations are also performed for the minimum and maximum of the possible pressure range, resulting in pressures of respectively 1073 Pa and 1198 Pa.

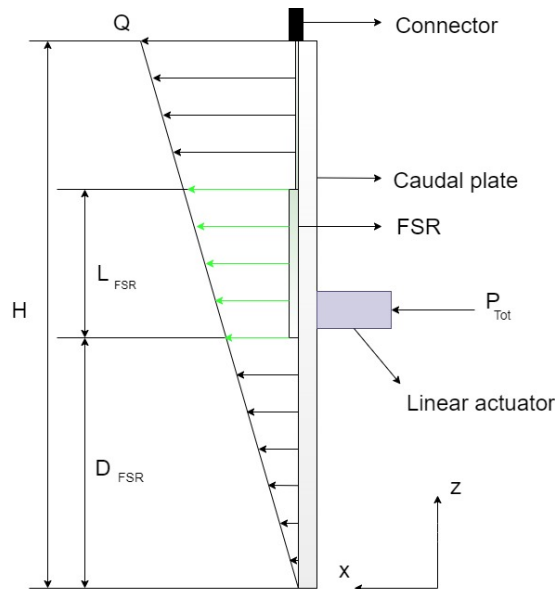


Figure 7-12 Pressure diagram caudal plate with FSR connected to the linear actuator

7.3 Experiment model

The respiration model is adapted based on the observations during the experiments as described in 7.2. The new model simulates the behaviour of the tissue and the implant during the physical experiment. All modifications in the experiment model relate to boundary conditions or the applied load. First, the boundary constraints at the left, right and top surface are changed. These surfaces are totally clamped in the respiration model, which is not the case during the experiment. Because of the air gap and the fact that the gel does not stick to the mould, the left, right and top surface may move in the rostral or caudal direction. Movements towards other directions are constrained as in the respiration model.

Second, the maximal displacement of the caudal surface x_{caud} is defined as a linear function depending on the z-position:

$$x_{caud} = \frac{z}{H} \cdot 4 \text{ mm} \quad (7-3)$$

This ensures that the middle of the plate translates with a maximal stroke, which equals 2 mm. Next to this extra boundary condition, the applied load is also changed. The respiration pressure needs to be modelled as a distributed pressure as mentioned in 7.2. On top of that the function also varies in time. The motor does not follow a sinusoidal trajectory but a triangular trajectory. Hence, in this model a triangular pressure wave is applied. Finally, the applied pressure P_{app} in the experiment model depends on the z-position, time and applied frequency f_{app} :

$$P_{app} = \frac{Qz}{2} + \frac{Qz}{\pi} \arcsin(\sin(\pi f_{app} t)) \quad (7-4)$$

After all these boundary and load conditions have been set, the simulation of the experiment model results in a colour plot of the displacement field of both the implant and the tissue. Figure 7-13 shows the displacement of the tissue and the implant when the largest pressure is applied. Note that the tissue and the implant are intersected in the sagittal plane in order to make the inserted part of the implant visible. Remember that all displacements are scaled, in this case by a factor 10. The ONELAB files are attached in Appendix L, provided on an electronic medium.

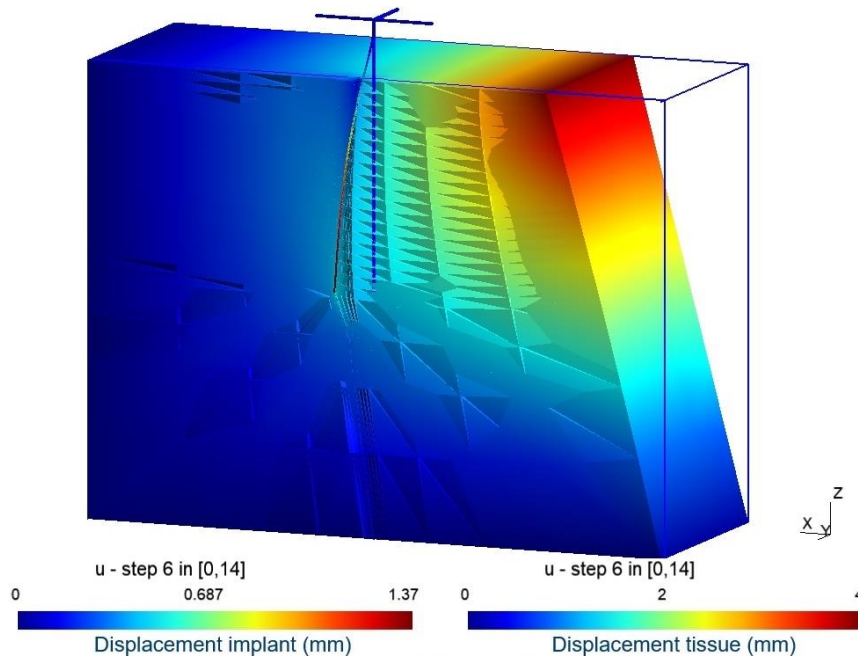


Figure 7-13 Colour plot displacement experiment model (intersection in sagittal plane)

The inclination of the caudal surface towards the top is clearly observable in the colour plot. The maximal rostral displacement of the caudal surface is 4 mm. This is as expected: the higher on the caudal surface, the larger the applied pressure is. Hence, the displacement is also larger at the top. Note that the colour of the colour plotted caudal surface changes linearly towards the top. Furthermore, the linear increase of pressure towards the top results in a different behaviour of the implant in comparison with the respiration model. Figure 7-14 shows the scaled implant displacements in the respiration model and in the experiment model. Both are intersections in the sagittal plane. While the rostral displacement of the implant in the respiration model increases linearly towards its tip in the tissue, this is not the case in the experiment model. Indeed, the pressure is not equally distributed but increases towards the top of the caudal surface and as a result also towards the top of the implant. Thus, the implant is not linearly displaced, which results in the displacement profile plotted in Figure 7-14.

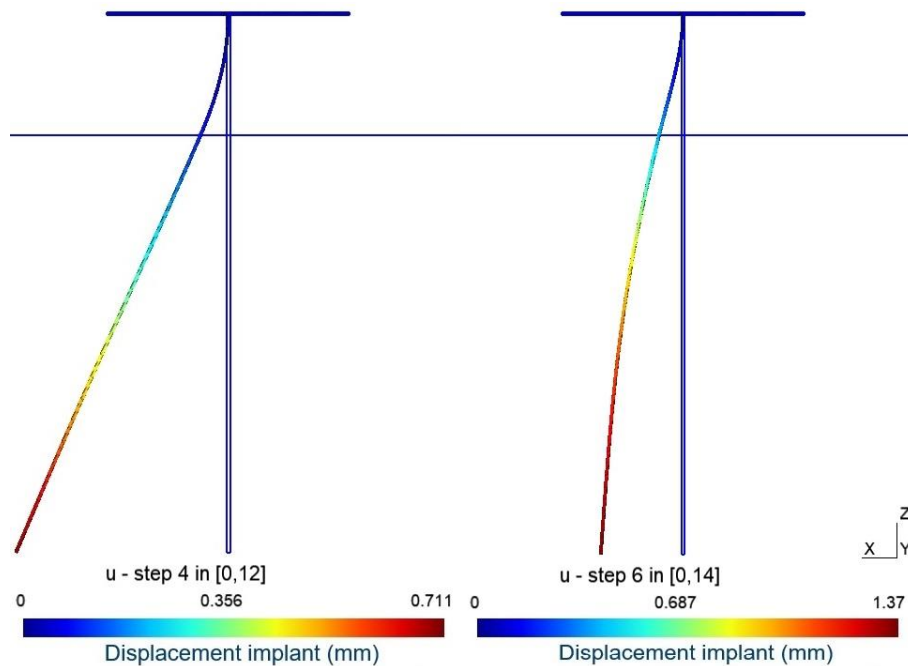


Figure 7-14 Implant displacement in the rostral direction in respiration model at the left and in experiment model at the right (section in sagittal plane)

Additionally, the rostral implant displacement at the gel surface level can be plotted for the four different applied frequencies: 2 Hz, 1 Hz, 0,5 Hz and 0,25 Hz. This is done because of the fact that this displacement is measured throughout the experiment. Figure 7-15 shows four plots, each case plotting one period. Note that the displacement is lagging more and more over time due to the fact that data before the start time of 0 seconds are not available. Hence, the viscoelastic displacement during the first steps is calculated less accurately than during the later time steps. In fact, the lagging is actually quite limited to a phase shift of 0,15, 0,35, 0,6 and 1 seconds. However, the viscoelastic behaviour of the tissue influences the implant displacement. For example, during linear loading the displacement increases more at larger loads. The reverse is true for the linear unloading, the larger the load the smaller the displacement change in a certain time step is.

The displacement curves of the different applied frequencies can be compared. A similarity between the curves is the amplitude of the displacement, which equals 400 μm at all frequencies in the model. To compare the rostral displacement in the experiment model with the rostral displacement according to the measurement data, the first period of Figure 7-5 is plotted for

the four different applied frequencies in Figure 7-16. The modified experiment model results in maximal implant displacements at the gel surface in the same order of magnitude as the maximal displacements during the experiment, which range between 300 μm and 400 μm . In addition, the rostral tip displacement in the model equals 1,37 mm.

The slopes of the loading and unloading curves are steeper for lower frequencies. Indeed, the period at a lower frequency is longer, which results in slower loading and unloading. The main difference between the model and the experiment is the trend of the loading and unloading curves. The unloading trend at 0,25 Hz is the same in both cases. However, this is not the case for the loading trend at 0,5 Hz.

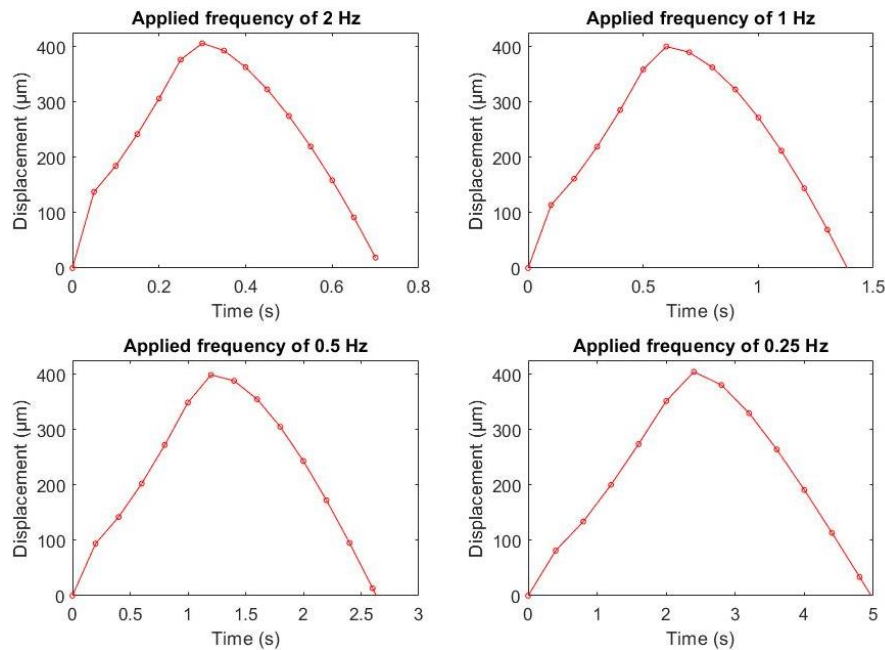


Figure 7-15 Implant rostral displacement vs time at the gel surface level in the experiment FEM model

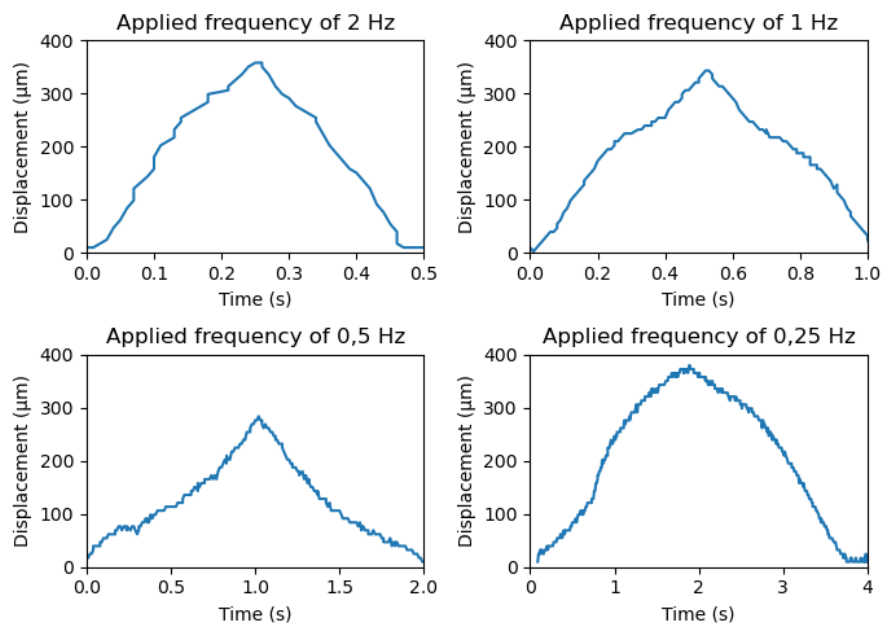


Figure 7-16 Implant rostral displacement vs time at the gel surface level according to the measurement data

Additionally, the curve trends at other frequencies do not correspond with the measurements, as shown in Figure 7-15 and Figure 7-16. This can be explained by the fact that the reduced relaxation function of rat brain tissue in the model is not the same as the reduced relaxation function of agarose gel. Figure 7-17 is a qualitative hysteresis curve of agarose gel based on the measured displacement. Notice the curve differences with the hysteresis curve of rat brain tissue in the model shown in Figure 4-5. The implant displacement rate is larger during testing when the load is low or high, in between the displacement rate is smaller. This behaviour can also be observed in Figure 7-1, Figure 7-2, Figure 7-3 and Figure 7-4.

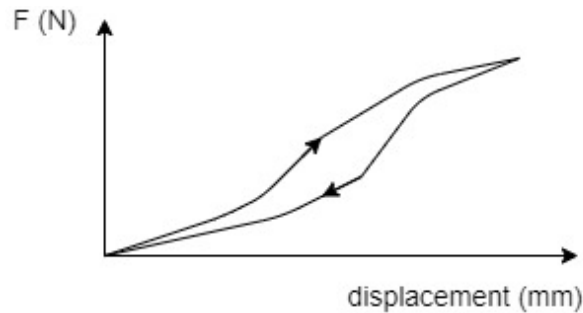


Figure 7-17 Qualitative hysteresis curve

7.4 Discussion and conclusion

In 4.4, a rostral implant displacement at the brain surface of $11,4\ \mu\text{m}$ is reported. This value is based on the respiration model simulation. The estimation corresponds with the normal displacement data due to respiration at the centre of a small craniotomy when the dura is removed. The normal displacement for a small craniotomy with diameter of $2,35\ \text{mm}$ ranges between $6\ \mu\text{m}$ and $20\ \mu\text{m}$. Because the craniotomy in the respiration model has a diameter, which equals $1\ \text{mm}$, the expected displacement is smaller than $20\ \mu\text{m}$ (Gilletti & Muthuswamy, 2006).

The experiment is set up based on the influence of respiration on the implant displacement. Maximal rostral implant displacements at the gel surface between 300 and $400\ \mu\text{m}$ are reported. This is an upscaled value corresponding with a displacement of $40\ \mu\text{m}$ in real brain tissue. This is more than three times the expected value of $11,4\ \mu\text{m}$ in the respiration model, although it is still situated in the same order of magnitude. Non-similarities between the respiration model and the experiment set-up cause this difference.

These non-similarities include the boundary conditions between gel and mould. The gel can move with respect to the left, right and top plate of the mould during the experiment. Real brain tissue is modelled as glued to the skull in the respiration model. This is done to approximate the rigid environment around the tissue, including the meninges. A second difference between experiment and model is the applied pressure. It is equally distributed over the caudal surface in the model while during the experiment the caudal surface rotates due to a linear pressure distribution.

The maximal rostral implant displacement equals $400\ \mu\text{m}$ at the gel surface in the experiment model. This value corresponds with the measured values ranging between 300 and $400\ \mu\text{m}$.

Hence, the experiment model succeeds in mimicking the physical interactions during the experiment. It can be concluded that the measured values equal two times the maximal normal displacement after a small craniotomy measured by Gilletti and Muthuswamy.

However, when an exact simulation of the respiration model is desired, it is proposed to correctly mimic the boundary conditions during a second experiment set-up iteration. It is necessary to replace the hinge connection, which allows flexible movement and rotation of the caudal plate, by a rigid connection. In this way, the plate will not rotate. Additionally, air gaps must be avoided by placing risers. The gel in the risers can flow into air gaps when they occur.

8 CONCLUSION

The main goal of this thesis was the development and validation of an estimation technique for the displacement of an implanted electrode in rat brain. A mathematical model was developed in which the brain tissue is represented as a viscoelastic material, based on the second order Kelvin-Voigt model and existing data of the reduced relaxation function of real rat brain. The geometries of the brain tissue and the implant are simplified, based on the anatomy of the real rat brain. Furthermore, three FEM models were constructed in which different loads are applied to the brain tissue. The multiple loads model includes linear acceleration and head rotation during normal animal behaviour, static intracranial pressure and respiration. The heartbeat model mimics the influence of the blood pressure by mimicking the blood vessels in the tissue. Finally, the respiration model manages to include the skull as well.

Results showed that the largest rostral implant displacement is caused by respiration. It is estimated at 70,6 μm at the tip of the implant and at 11,4 μm at the top surface of the brain tissue. The order of magnitude corresponds with existing data on the implant displacement perpendicular to the brain surface due to respiration, ranging from 5 μm to 30 μm . The rostral implant displacement caused by the heartbeat is estimated at 4,3 μm at the tip of the implant and at 1,4 μm at the top surface of the brain tissue. Real implant displacement perpendicular to the brain surface due to heartbeat ranges between 2 and 4 μm .

Based on the intermediate results, it is clear that the respiration has the largest influence on the implant displacement. An experiment set-up was designed and built to validate the respiration model, using a scale factor of 10:1. This scale factor was used due to production constraints concerning the implant, produced by a 3D-printing technique. The implant is connected to four sensitive beams on which two strain gauges are attached. The beams bended while displacing the implant, the bending was measured by the strain gauges. This customised sensor with corresponding signal conditioning made it possible to measure the implant displacement although the strain gauges were placed outside the tissue. Furthermore, the brain tissue was mimicked by an agarose hydrogel with an elastic modulus of 50 kPa. Pressure waves with an amplitude of 1130 Pa were applied at the caudal surface of the tissue by a cyclic translation of 2 mm at frequencies of 2 Hz, 1 Hz, 0,5 Hz and 0,25 Hz.

The rostral displacement of the implant at the gel surface was measured during the experiment. Viscoelastic behaviour was observed in the measurement data. The results showed an implant displacement of approximately 400 μm at 0,25 Hz, 300 μm at 0,5 Hz, 350 μm at 1 Hz and 400 μm at 2 Hz. Converting this value to real brain tissue dimensions results in a rostral displacement at the brain surface ranging from 30 μm to 40 μm . This value is more than three times the calculated value of 11,4 μm by the FEM model. This can be explained by the formation of an air gap between the tissue and the skull. Additionally, the pressure waves were not equally distributed over the caudal surface because an inclination of that surface was observed. Based on these two observations, a new FEM model was set up by adapting the previous respiration model. Results showed a rostral displacement at the gel surface of 400 μm , which corresponds with the acquired measurement data. It can be concluded that both the FEM model and the set-up succeeded in the context of a proof of concept to estimate the displacement of an implant. However, further research should pay attention to both the development of a more efficient hydrogel-mould connection and the application of an equally distributed pressure.

References

- Andersen, M. L., & Tufik, S. (2016). *Rodent model as tools in ethical biomedical research*. Switzerland: Springer.
- Antona-Makoshi, J., Eliasson, E., Davidsson, J., Ejima, S., & Ono, K. (2015). Effect of Aging on Brain Injury Prediction in Rotational Head Trauma—A Parameter Study with a Rat Finite Element Model. *Traffic Injury Prevention* 16, 91-99.
- Battaglia, F. P., Kalenscher, T., Cabral, H., Winkel, J., Bos, J., Manuputy, R., . . . Pennartz, C. (2009). The lantern: an ultra-light micro-drive for multi-tetrode recordings in mice and other small animals. *Journal of Neuroscience Methods*, 291-300.
- Baumgartner, D., Lamy, M., & Willinger, R. (2009). Finite element analysis of traumatic brain injuries mechanisms in the rat. *IRCOBI Conference*, (pp. 97-108). York (UK).
- Betten, J. (2008). *Creep Mechanics*. Berlin Heidelberg: Springer-Verlag .
- Camilo, L. M., Motta-Ribeiro, G. C., de Ávila, M. B., Paula, L. F., de Abreu, M. B., Carvalho, A. R., & Zin, W. A. (2018). Variable Ventilation Associated With Recruitment Maneuver Minimizes Tissue Damage and Pulmonary Inflammation in Anesthetized Lung-Healthy Rats. *Anesthesia & Analgesia*, 784-791.
- Cook, R. D. (1995). *Finite element modeling for stress analysis*. New York: John Wiley & sons, inc.
- Cops, J., Mullens, W., Verbrugge, F. H., Swennen, Q., Reynders, C., Penders, J., . . . Hansen, D. (2018). Selective abdominal venous congestion to investigate cardiorenal interactions in a rat model. *PLOS One*.
- De Roeck, W. (2020). Finite element based desing: pre-processing. KU Leuven.
- Delbeke, J., Haesler, S., & Prodanov, D. (2020). Failure Modes of Implanted Neural. In L. Guo, *Neural Interface Engineering: Linking the Physical World and the Nervous System* (pp. 123-172). Switzerland: Springer.
- Eftekhari, S., Westgate, C. S., Johansen, K. P., Bruun, S. R., & Jensen, R. H. (2012). Long-term monitoring of intracranial pressure in freely-moving rats; impact of different physiological states. *Fluids and Barriers of the CNS*, 17-39.
- Fung, Y. (1981). *Biomechanics, Mechanical Properties of Living Tissues*. New York: Springer.
- Gefen, A., Gefen, N., Zhu, Q., Raghupathi, R., & Margulies, S. S. (2003). Age-Dependent Changes in Material Properties of the Brain and Braincase of the Rat. *Journal of neurotrauma*, Vol. 20, No. 11, 1163-1177.
- Gilletti, A., & Muthuswamy, J. (2006). Brain micromotion around implants in the rodent somatosensory cortex. *Journal of Neural Engineering*, 189-195.
- Guillaume, A., Osmont, D., Gaffie, D., Sarron, J., & Quandieu, P. (1997). Effects of perfusion on the mechanical behavior of the brain exposed to hypergravity. *Journal of Biomechanics*, Vol. 30, No. 4, 383-389.

- Hamilton, W. J. (1982). *Textbook of human anatomy*. London and Basingstoke: The Macmillan Press LTD.
- Holzapfel, G. A., & Ogden, R. W. (2006). *Mechanics of Biological Tissue*. Berlin Heidelberg: Springer-Verlag.
- Hopcroft, M. A., Nix, W. D., & Kenny, T. W. (2010). What is the Young's modulus of silicon? . *Journal of microelectromechanical systems*, Vol. 19, No. 2, 229-238.
- Interlink Electronics. (2021). Interlink Electronics FSR Force Sensing Resistors. *FSR Integration Guide*, 1-32.
- Karimi, A., & Navidbakhsh, M. (2014). An experimental study on the mechanical properties of rat brain tissue using different stress-strain definitions. *Journal of Materials Science: Materials in Medicine*, 1623-1630.
- Kobayashi, S., Yano, M., Kohno, M., Obayashi, M., Hisamatsu, Y., Ryoke, T., . . . Matsuzaki, M. (1996). Influence of aortic impedance on the development of pressure-overload left ventricular hypertrophy in rats. *American Heart Association*, Vol. 94, No. 12, 3362-3368.
- Krenk, S., & Høgsberg, J. (2013). *Statics and mechanics of structures*. Dordrecht: Springer.
- Ledberg, A., & Robbe, D. (2011). Locomotion-Related Oscillatory Body Movements at 6–12 Hz Modulate the Hippocampal Theta Rhythm. *PLoS ONE*, 1-10.
- Mangelschots, J. (2021, February 24). *Home*. Retrieved from Strain2Data: <https://www.strain2data.eu/>
- Mao, H., Zhang, L., Yang, K. H., & King, A. I. (2006). Application of a finite element model of the brain to study traumatic brain injury mechanisms in the rat. *Stapp Car Crash Journal* , Vol. 50, 583-600.
- Martin, R. B., Burr, D. B., Sharkey, N. A., & Fyhrie, D. P. (2015). *Skeletal Tissue Mechanics*. New York: Springer .
- Materialise. (2020, November 2). *Metal 3D Printing*. Retrieved from Materialise: <https://www.materialise.com/en/manufacturing/3d-printing-technology/metal-3d-printing>
- Mautz, W. J., & Bufalino, C. (1989). Breathing pattern and metabolic rate responses of rats exposed to ozone . *Respiration Physiology*, 69-78.
- Naessens, D. M., Vos, J. d., VanBavel, E., & Bakker, E. N. (2018). Blood-brain and blood-cerebrospinal fluid barrier permeability in spontaneously hypertensive rats. *Fluids and Barriers of the CNS*, 15-26.
- Nanotec. (2021, February 16). *Home*. Retrieved from Nanotec: <https://en.nanotec.com/>
- NERF. (2021, April 12). *Responsible research*. Retrieved from nerf.be: <https://www.nerf.be/responsible-research-1>
- Nickson, C. (2020, November 3). *Lung Recruitment Manoeuvres in ARDS*. Retrieved from Life in the fastlane: <https://litfl.com/lung-recruitment-manoevres/>
- Nowak, K., Mix, E., Gimsa, J., Strauss, U., Sriperumbudur, K. K., Benecke, R., & Gimsa, U. (2011). Optimizing a Rodent Model of Parkinson's Disease for Exploring the Effects and Mechanisms of Deep Brain Stimulation. *Parkinson's Disease*, 1-19.

- ONELAB. (2021, April 8). *Open Numerical Engineering LABoratory*. Retrieved from ONELAB: <https://onelab.info/>
- Pasquet, M. O., Tihy, M., Gourgeon, A., Pompili, M. N., Godsil, B. P., Léna, C., & Dugué, G. P. (2016). Wireless inertial measurement of head kinematics in freely-moving rats. *Scientific Reports*, 1-13.
- Polanco, M., Bawab, S., & Yoon, H. (2016). Computational Assessment of Neural Probe and Brain Tissue Interface under Transient Motion. *Biosensors* 6, 27, 1-13.
- Princeton University. (2020, October 30). *Composite materials*. Retrieved from Princeton University: https://www.princeton.edu/~humcomp/bikes/design/desi_30.htm#:~:text=Composite%20Materials&text=The%20Young's%20modulus%20of%20the,volume%20fraction%20of%20the%20fibers.
- Prodanov, D., & Delbeke, J. (2016). Mechanical and biological interactions of implants with the brain and their impact on implant design. *Frontiers in Neuroscience*, 10:11.
- Rashid, B., Destrade, M., & Gilchrist, M. (2012). Mechanical characterization of brain tissue in compression at dynamic strain rates. *Journal of the mechanical behavior of biomedical materials*, Vol. 10, 23-28.
- Schulz, H., & Muhle, H. (2000). Chapter 16 - Respiration. In G. J. Krinke, *The Laboratory Rat* (pp. 323-344). Stein: Academic Press.
- Sengupta, P. (2013). The laboratory rat: relating its age with human's. *International Journal of Preventive Medicine*, 624-630.
- Shafieian, M., Darvish, K. K., & Stone, J. R. (2009). Changes to the viscoelastic properties of brain tissue after traumatic axonal injury. *Journal of Biomechanics*, 2136-2142.
- Sharp, P. E., Tinkelman, A., & Cho, J. (2001). Angular Velocity and Head Direction Signals Recorded From the Dorsal Tegmental Nucleus of Gudden in the Rat: Implications for Path Integration in the Head Direction Cell Circuit. *Behavioral Neuroscience*, 571-588.
- Shulyakov, A. V., Fernando, F., Cenkowski, S. S., & Bigio, M. R. (2009). Simultaneous determination of mechanical properties and physiologic parameters in living rat brain. *Biomechanics and Modeling in Mechanobiology, Springer-Verlag*, 415-425.
- Subbaroyan, J., Martin, D. C., & Kipke, D. R. (2005). A finite-element model of the mechanical effects of implantable microelectrodes in the cerebral cortex. *Journal of Neural Engineering* 2, 103-113.
- University of Washington. (2021, April 12). *Interaural line*. Retrieved from BrainInfo: <http://braininfo.rprc.washington.edu/CentralDirectoryDefinition.aspx?ID=3469&questID=2>
- van Daal, R. J., Sun, J.-J., Ceyssens, F., Michon, F., Kraft, M., Puers, R., & Kloosterman, F. (2020). System for recording from multiple flexible polyimide neural probes in freely behaving animals. *Journal of Neural Engineering*, 1-13.
- Vincent, J. (2012). *Structural Biomaterials*. Princeton: Princeton University Press.
- Vishay Precision Group, Inc. (2021, March 19). *Premier Solutions for Stress Analysis and Sensor Design*. Retrieved from micro-measurements: <https://micro-measurements.com/>

- VWR. (2015, March). Agaroses. Retrieved from https://at.vwr.com/assetsvc/asset/de_AT/id/15973021/contents
- Wu, J., Lei, L., Chen, X., Cai, X., Li, Y., & Han, T. (2014). A Three-Dimensional Microdisplacement Sensing System Based. *Sensors*, 20533-20542.
- Yang, P., Wang, Z., Zhang, Z., Liu, D., Manolios, E. N., Chen, C., . . . Chen, N. (2018). The extended application of the rat brain in stereotaxic coordinates in rats of various body weight. *Journal of Neuroscience Methods*, 60-69.
- Zhou, R., Li, Y., Cavanaugh, J. M., & Zhang, L. (2020). Investigate the Variations of the Head and Brain Response in a Rodent Head Impact Acceleration Model by Finite Element Modeling. *Frontiers in Bioengineering and Biotechnology*, 1-16.

Appendices

Appendix A	Elastic modulus calculation
Appendix B	Creep function calculation
Appendix C	Convergence graphs
Appendix D	Motor selection calculation
Appendix E	Preparation protocol and experiment protocol
Appendix F	Preparation of hydrogel
Appendix G	Micromotion sensor calibration curves
Appendix H	FSR calibration curves
Appendix I	Electronic components
Appendix J	Technical drawings

Provided on an electronic medium

Appendix K	NanoJ script for motor control
Appendix L	FEM models
	Model 1: Multiple loads model
	Model 2: Heartbeat model
	Model 3: Respiration model
	Model 4: Upscaled heartbeat model
	Model 5: Upscaled respiration model
	Model 6: Experiment model
Appendix M	Calibration data
Appendix N	Measurement data
Appendix O	Movie experiment

Appendix A ELASTIC MODULUS CALCULATION

Based on Table 2-3 the value for the elastic modulus of the brain E_b is estimated at 50 kPa. The elastic modulus of the meninges E_m is estimated at 20 MPa, a value which has been used in FEM models to model the brain-skull boundary (Mao, Zhang, Yang, & King, 2006). One overall modulus can be calculated by these elastic moduli. It is important to mention that the calculations followed are based on equations for composite materials. These composite materials consist of a matrix of fibres. When the material is loaded in the direction of the fibres these equations for composite materials are valid. Although the brain and the meninges are not a composite material, it is assumed that the equations for composite materials can be followed (Princeton University, 2020):

$$E(V_b + V_m) = E_b V_b + E_m V_m \quad (A-1)$$

with:

- E , the overall elastic modulus
- E_b , the elastic modulus of the brain equal to 50 kPa
- E_m , the elastic modulus of the meninges equal to 20 MPa
- V_b , the volume of brain
- V_m , the volume of meninges

The volumes of the brain and the meninges can be calculated based on the assumptions on the geometry in 3.3.1 and the thickness of the meninges tissue t_m , which equals 0,45 mm. Note that the thickness of the subarachnoid space filled with CSF is not taken into account. The total volume can be calculated as:

$$V_b + V_m = l_t \cdot w_t \cdot t_t \quad (A-2)$$

with:

- l_t , the length of the tissue equal to 20 mm
- w_t , the width of the tissue equal to 15 mm
- t_t , the thickness of the tissue equal to 15 mm

The volumes of the brain and the meninges can be calculated as:

$$V_b = (l_t - 2t_m) \cdot (w_t - 2t_m) \cdot (t_t - 2t_m) \quad (A-3)$$

$$V_m = l_t \cdot w_t \cdot t_t - (l_t - 2t_m) \cdot (w_t - 2t_m) \cdot (t_t - 2t_m) \quad (A-4)$$

V_b and V_m equal respectively 3797,3 mm³ and 702,7 mm³, with a total volume of 4500 mm³. When all the known parameters are filled out in (A-1), the overall elastic modulus results in 3,17 MPa, rounded off to 3 MPa.

Appendix B CREEP FUNCTION CALCULATION

The values in Table 2-4 can be filled out in (2-3) to construct the reduced relaxation function for PDx. This results in:

$$g(t) = g_{\infty} + g_1 e^{-\beta_1 t} + g_2 e^{-\beta_2 t} + g_3 e^{-\beta_3 t} \quad g(0) = 1$$

$$g(t) = 0,141 + 0,145 e^{-0,386t} + 0,243 e^{-4,483t} + 0,471 e^{-57,875t} \quad g(0) = 1 \quad (\text{B-1})$$

As explained in 3.2.2 not the reduced relaxation function but the reduced creep function is advised to obtain the viscoelastic displacements. The relationship in Laplace domain between the two functions is given by (3-7). Although (B-1) is a third order model, a second order model is simpler to convert into the Laplace domain and to calculate the creep function. Therefore, the reduced relaxation function in (B-1) is calculated by eliminating the exponential multiplied by the smallest factor and by the lowest decay rate. Indeed, the first exponential term is of least importance. The other two decay rates are still the same but the factors changed, the subscript 'o' corresponds with the values used in (B-1):

$$g_{\infty} = \frac{g_{\infty,o}}{g_{\infty,o} + g_{2,o} + g_{3,o}} = 0,1649 \quad (\text{B-2})$$

$$g_1 = \frac{g_{3,o}}{g_{\infty,o} + g_{2,o} + g_{3,o}} = 0,5509 \quad (\text{B-3})$$

$$g_2 = \frac{g_{2,o}}{g_{\infty,o} + g_{2,o} + g_{3,o}} = 0,2842 \quad (\text{B-4})$$

This results in an approximately reduced relaxation function:

$$g(t) = 0,1649 + 0,5509 e^{-57,875t} + 0,2842 e^{-4,483t} \quad g(0) = 1 \quad (\text{B-5})$$

Figure B-1 shows the original relaxation function (B-1) in blue and the approximately reduced relaxation function (B-5) in orange. (B-5) is converted to the Laplace domain with wxMaxima, afterwards the creep function is calculated based on (3-7). Finally, the reduced creep function is converted back into time domain, which results in (B-6). Note that this is the creep function for the second order model, because the creep function for the third model would be more complex.

$$k(t) = \exp \left(\frac{\left(\frac{(g_1 + g_2)((\beta_1 + \beta_2)g_{\infty} + \beta_1 g_2 + \beta_2 g_1)}{g_{\infty}} - \frac{2(\beta_1 g_2 + \beta_2 g_1)}{g_{\infty}} \right) \sinh\left(\frac{At}{2}\right)}{A} - \frac{(g_2 + g_1) \cosh\left(\frac{At}{2}\right)}{g_{\infty}} \right) + \frac{1}{g_{\infty}} \quad (\text{B-6})$$

with A:

$$A = \sqrt{(\beta_2^2 - 2\beta_1\beta_2 + \beta_1^2)g_{\infty}^2 + ((2\beta_1^2 - 2\beta_1\beta_2)g_2 + (2\beta_2^2 - 2\beta_1\beta_2)g_1)g_{\infty} + \beta_1^2 g_2^2 + 2\beta_1\beta_2 g_1 g_2 + \beta_2^2 g_1^2}$$

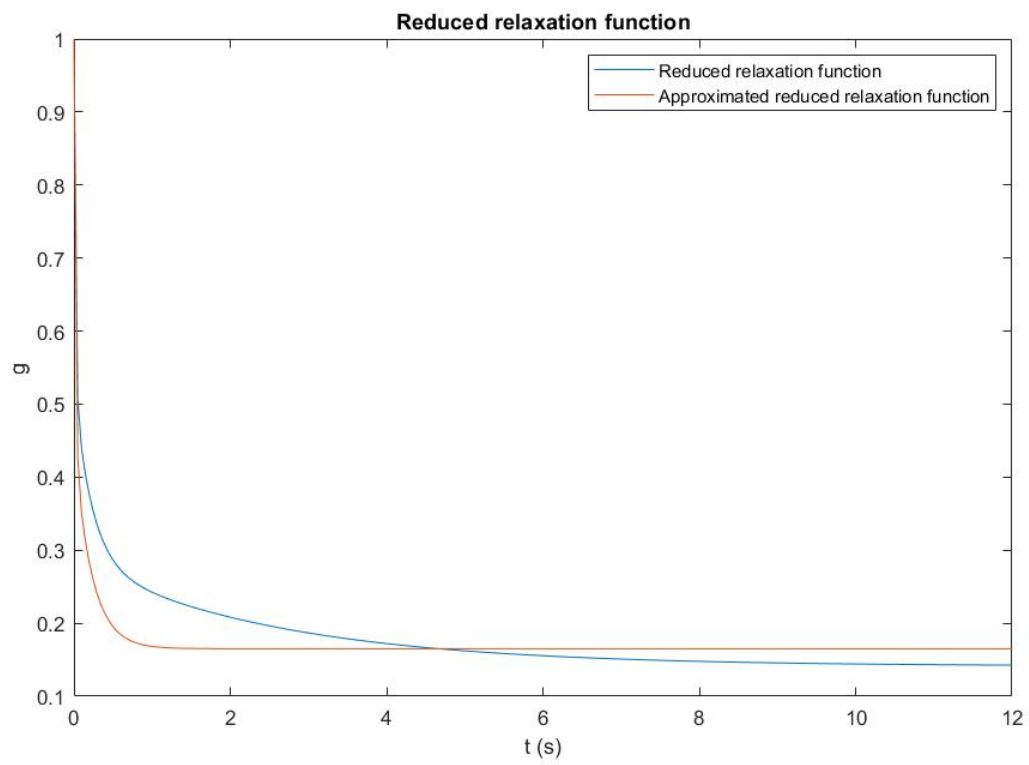


Figure B-1 Reduced relaxation function

Appendix C CONVERGENCE GRAPHS

To determine the total displacement of the implant tip in the multiple loads model, all displacements due to the four loads are calculated and added. A separate convergence analysis can be performed for each of these loads. The procedure is identical to the one followed in 4.1.1. The maximal implant tip displacement ranges for linear acceleration from 4,37 to 4,72 μm ; for rotation from 0,0119 to 0,0128 μm ; for static intracranial pressure 0,010 to 0,005 μm and for respiration from 10,8 to 11,6 μm . Figure C-1, Figure C-2, Figure C-3, Figure C-4 are the convergence graphs for linear acceleration, rotation, intracranial pressure and respiration.

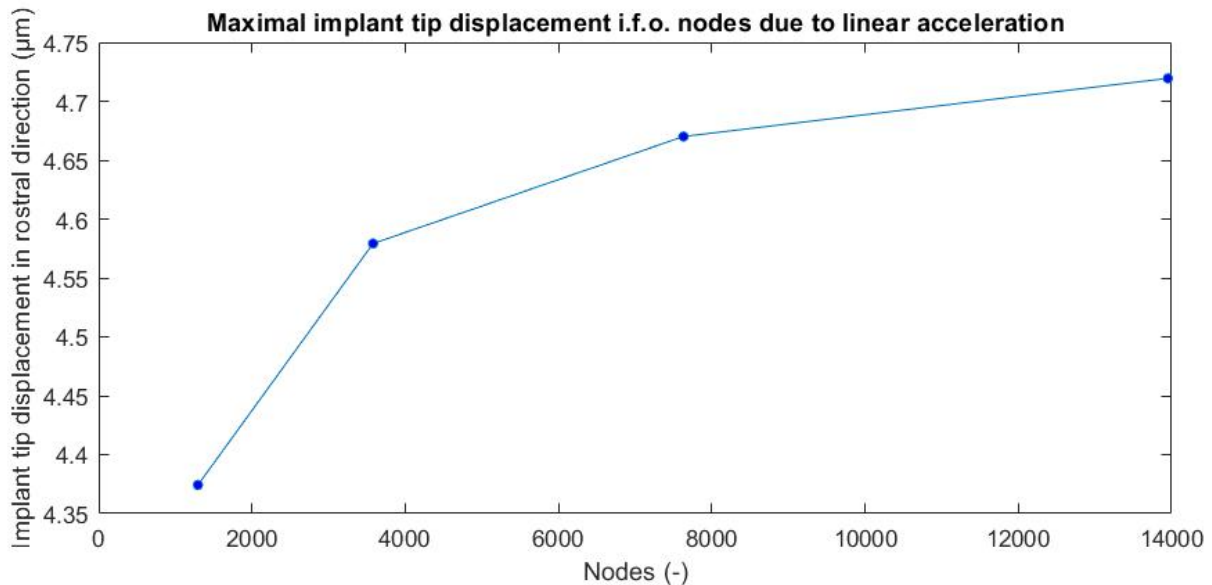


Figure C-1 Convergence graph multiple loads model, linear acceleration

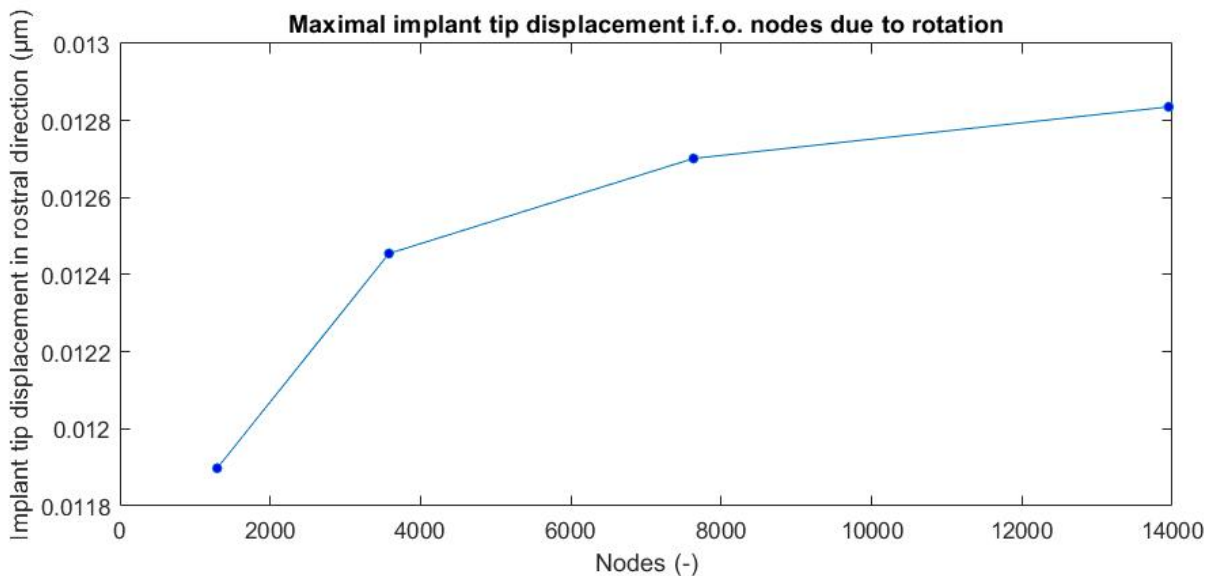


Figure C-2 Convergence graph multiple loads model, rotation

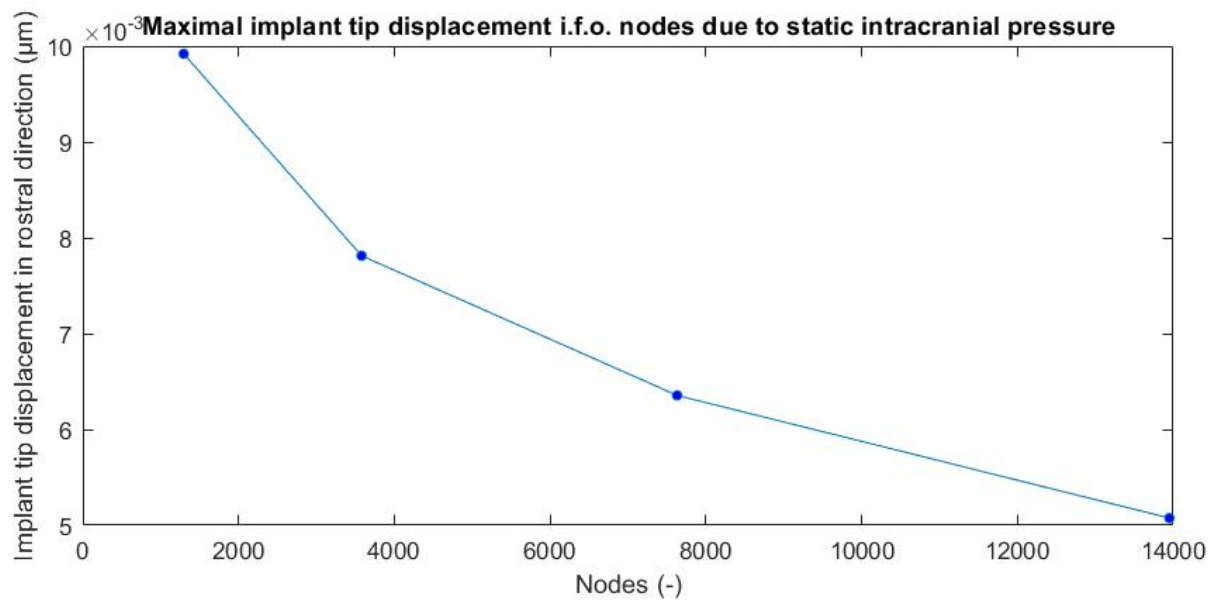


Figure C-3 Convergence graph multiple loads model, static intracranial pressure

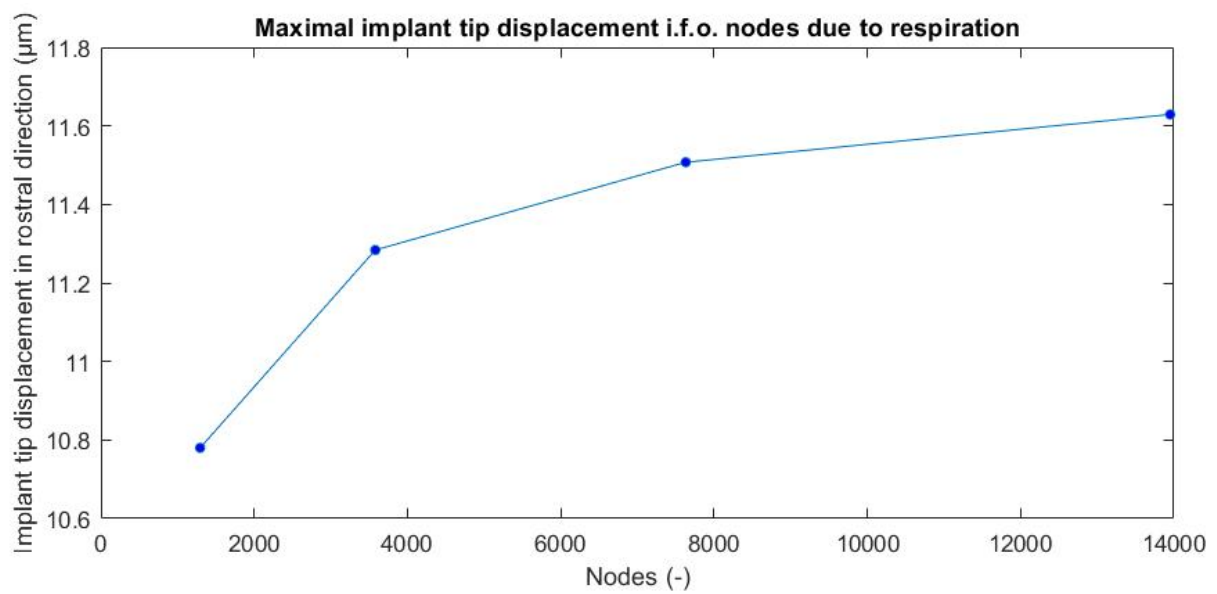


Figure C-4 Convergence graph multiple loads model, respiration

Appendix D MOTOR SELECTION CALCULATION

The linear force amplitude the motor needs to deliver, can be calculated by multiplying the respiration pressure, applied by the motor on the tissue block, by the area of the caudal plate. This results in:

$$F_{mot} = P_{c,resp} \cdot w_h \cdot t_h \quad (D-1)$$

$$F_{mot} = 980 \text{ Pa} \cdot 0,15 \text{ m} \cdot 0,15 \text{ m} = 22,05 \text{ N} \quad (D-2)$$

with:

- $P_{c,resp}$, the respiration pressure = 980 Pa
- w_h , the width of the hydrogel = 0,15 m
- t_h , the thickness of the hydrogel = 0,15 m

To calculate the linear stroke of the motor, the mean displacement of the caudal surface is determined based on the respiration model. This mean displacement is estimated to be 2 mm. Figure D-1 shows the position of the caudal surface, it is a sine wave $x(t)$ with magnitude 2 mm and frequency 2 Hz:

$$x(t) = 0,002 \sin(2 \cdot \pi \cdot 2 \text{ Hz} \cdot t) \text{ m} \quad (D-3)$$

Figure D-2 shows the velocity function $v(t)$, which can be determined by deriving (D-3), this results in:

$$v(t) = 0,025 \cos(2 \cdot \pi \cdot 2 \text{ Hz} \cdot t) \text{ m/s} \quad (D-4)$$

Finally, Figure D-3 shows the acceleration function $a(t)$, which can be determined by deriving (D-4), this results in:

$$a(t) = 0,316 \sin(2 \cdot \pi \cdot 2 \text{ Hz} \cdot t) \text{ m/s}^2 \quad (D-5)$$

The amplitude of (D-3), (D-4) and (D-5) are respectively the linear stroke, the linear velocity and the linear acceleration, which must be in range of the motor.

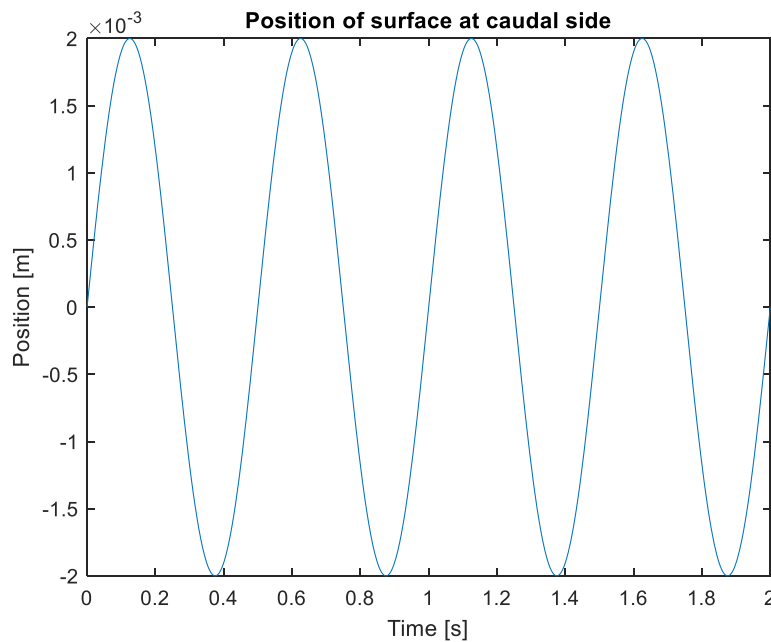


Figure D-1 Position of surface at caudal side

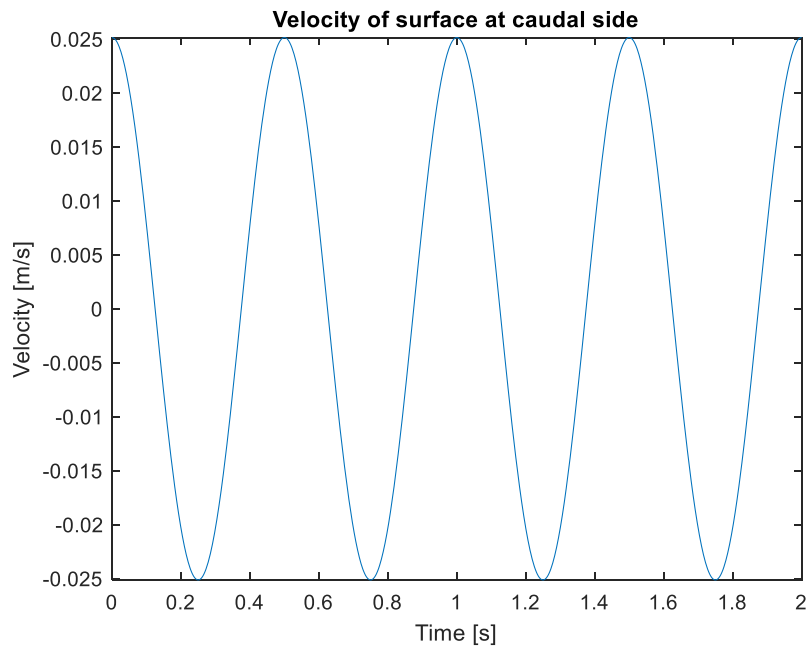


Figure D-2 Velocity of surface at caudal side

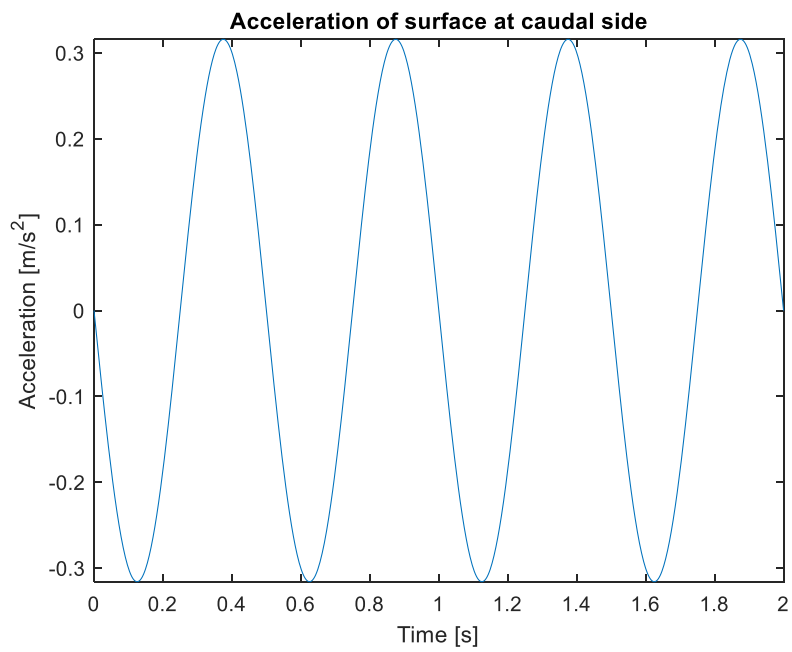


Figure D-3 Acceleration of surface at caudal side

Appendix E PREPARATION PROTOCOL AND EXPERIMENT PROTOCOL

Table E-1 shows the preparation steps of the experiment protocol the day before the experiment. Table E-2 shows the experiment protocol.

Table E-1 Preparation protocol on the day before the measurements

Step	Time	Task
1	14h00-17h00	Agarose gel preparation
	15h00-17h00	Agarose gel pouring
2	17h00-17h30	Attaching mould to anti-vibration table <ul style="list-style-type: none"> a. Placing the mould in the right place b. Tighten the mould with bolts to the anti-vibration table with Allen key
3	17h30-18h00	Inserting implant in gel <ul style="list-style-type: none"> a. Slightly lowering subframe with threaded rods b. Checking final distance with calliper/ruler c. Tightening subframe to frame in the final position
4	18h00-18h45	Attaching linear actuator to plate and anti-vibration table <ul style="list-style-type: none"> a. Attaching motor to anti-vibration table b. Wiring motor to power source and PC c. Aligning hinge with motor and connecting hinge components

Table E-2 Experiment protocol on the day of the measurements

Step	Time	Task
5	9h00-9h45	Connecting interfaces <ul style="list-style-type: none"> a. Connecting FSR and piezo sensors to Arduino and PC b. Testing Excel interface c. Connecting wires strain gauges, power sources and oscilloscope to electric circuit d. Testing Excel interface and oscilloscope
5'	9h45-10h30	Motor tuning
6	10h30-12h45	Calibration and measurements <ul style="list-style-type: none"> a. Calibration 2 mm (30') b. Measurement 2 mm 2 Hz (5' continuous measurement) c. Measurement 2 mm 1 Hz (5' continuous measurement) d. Measurement 2 mm 0,5 Hz (5' continuous measurement) e. Measurement 2 mm 0,25 Hz (5' continuous measurement)

Appendix F PREPARATION OF HYDROGEL

Table F-1 gives an overview of the measured masses of each of the five stages. Each stage is indicated by the letter 'L', followed by an ascending number. A solution of 1 L, corresponding to one stage, is divided over two beakers in order to avoid spillage while the solution is being heated in the microwave, which means that each stage is heated by using two beakers. Hence, the heating process of 2 L at the same time is achieved by heating four beakers simultaneously in the microwave oven. Therefore, the sub-indices in Table F-1 represent the two half litres of each stage.

Table F-1 Overview of the measured masses before mixing and heating

Stage	Stage with sub-index	Mass agarose powder (grams)	Mass empty beaker 1 L (grams)	Mass beaker 1 L + distilled water (grams)	Mass distilled water (grams)
L1	L1.1	5,9959	259,7	734,1	474,4
	L1.2		261,2	785,7	524,5
L2	L2.1	5,9961	265,7	753,9	488,2
	L2.2		256,4	769,3	512,9
L3	L3.1	6,0012	262,3	757,8	495,5
	L3.2		267,5	779,1	511,6
L4	L4.1	5,9988	261,1	756,2	495,1
	L4.2		257,1	766,6	509,5
L5	L5.1	6,0073	261,3	763,0	501,7
	L5.2		266,2	768,8	502,6
Total		29,9993	2618,5	7634,5	5016,0

After a first preheating, half of the agarose powder of each stage is mixed in a beaker. Table F-2 shows the measured masses when the solutions were fully heated and poured into a larger beaker of 1,8 L for every stage. Two beakers of 1,8 L contain the volume of the first two stages and are afterwards poured simultaneously into the mould.

Table F-2 Overview of the measured masses after mixing and heating

Stage	Mass empty beaker 1,8 L (grams)	Mass beaker 1,8 L + solution (grams)	Mass solution (grams)
L1	441,4	1427,4	986,0
L2	435,5	1340,2	904,7
L3	443,0	1385,5	942,5
L4	437,2	1376,2	939,0
L5	442,6	1404,4	961,8
Total	2199,7	6933,7	4734,0

According to the measurements, the initial total mass of distilled water is 5016,0 g and the total mass of the distilled water and agarose powder after heating is 4734,0 g, which means that a

mass of 282 g is lost. This is largely explained by the evaporation of the distilled water. Therefore, the actual concentration c of the obtained solution may not be calculated with the initial mass of 5016,0 g of the distilled water, but with the mass of the solution $m_{solution}$ of 4734,0 g after heating. Losses due to the transfer of the solution into the other beakers are small compared to the losses of evaporation and are hence neglected.

$$c = \frac{m_{agarose}}{m_{solution} - m_{agarose}} = \frac{29,9993 \text{ g}}{4734,0 \text{ g} - 29,9993 \text{ g}} = 0,638 \text{ w\%} \quad (\text{F-1})$$

The value of the obtained concentration is very close to the value corresponding to an elastic modulus of 50 kPa.

Table F-3 shows the heating process of the solutions during the five stages. The shaded time periods indicate how long the beakers with distilled water and agarose powder are heated. The minor differences in temperature can be explained because of the slightly different volumes in each beaker, resulting in one beaker heating up faster than another one and the beakers are being measured randomly. Between the casting of $L1$ and $L2$ and the casting of $L3$ and $L4$ there was a timespan of approximately hour. Between the casting of $L3$ and $L4$ and the casting of $L5$ there was a timespan approximately 40 minutes.

Table F-3 Heating process of the solutions during the five stages

Heating of L1 and L2	Heating of L3 and L4	Heating of L5
5'	5'	2'
32 °C	42 °C	34 °C
Adding agarose	Adding agarose	Adding agarose
5'	5'	5'
47 °C	55 °C	57 °C
5'	5'	5'
59 °C	53 °C	75 °C
5'	5'	5'
70 °C	62 °C	91 °C
5'	5'	
89 °C	72 °C	
	5'	
	68 °C	
	5'	
	88 °C	
Cooling	Cooling	Cooling
52 °C	51 °C	50 °C

The hydrogel had been casted the day before the experiment in order to let it cool down overnight to room temperature of 22 °C, and to let it solidify. Between the last pour of $L5$ and the first measurement there was a timespan of approximately eighteen hours.

Appendix G MICROMOTION SENSOR CALIBRATION CURVES

Figure G-1 to Figure G-10 show the filtered measurement data of the calibration of the micromotion sensor with displacements ranging from 25 μm to 250 μm . The vertical black lines represent the boundaries at which the measurement data is split for further selection. The first area, between the first and second vertical black line, represents the output voltage at which the displacement is applied. The third area, between the third and fourth vertical black line, represents the output voltage when no displacement is applied. A Savitzky-Golay filter of the second order is used with a frame length of 101 data points.

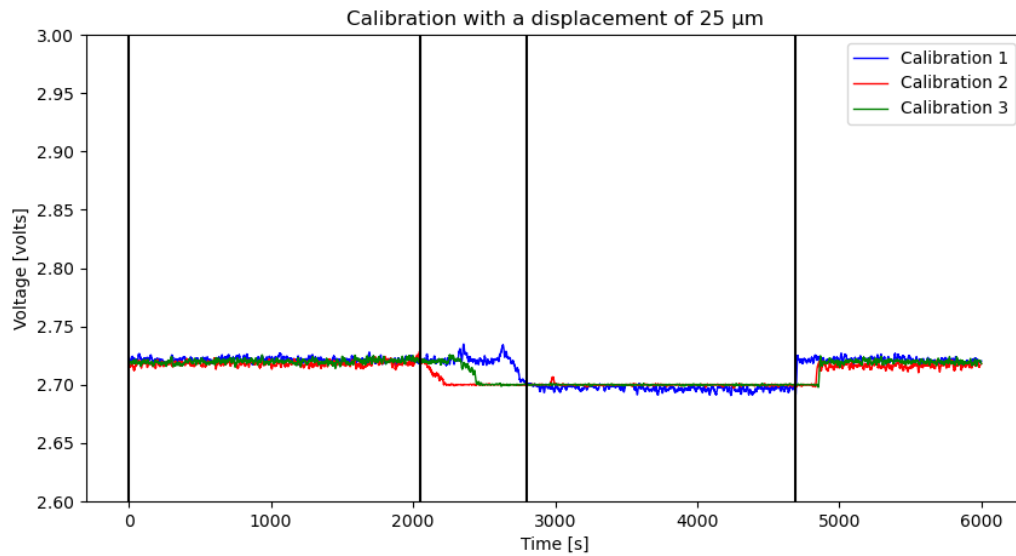


Figure G-1 Measurement of the micromotion sensor calibration with a displacement of 25 μm

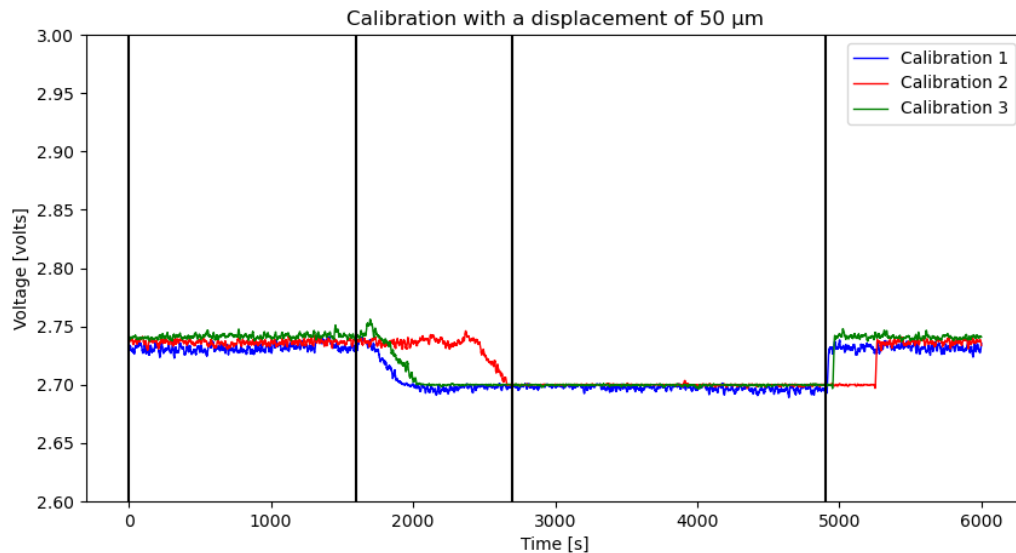


Figure G-2 Measurement of the micromotion sensor calibration with a displacement of 50 μm

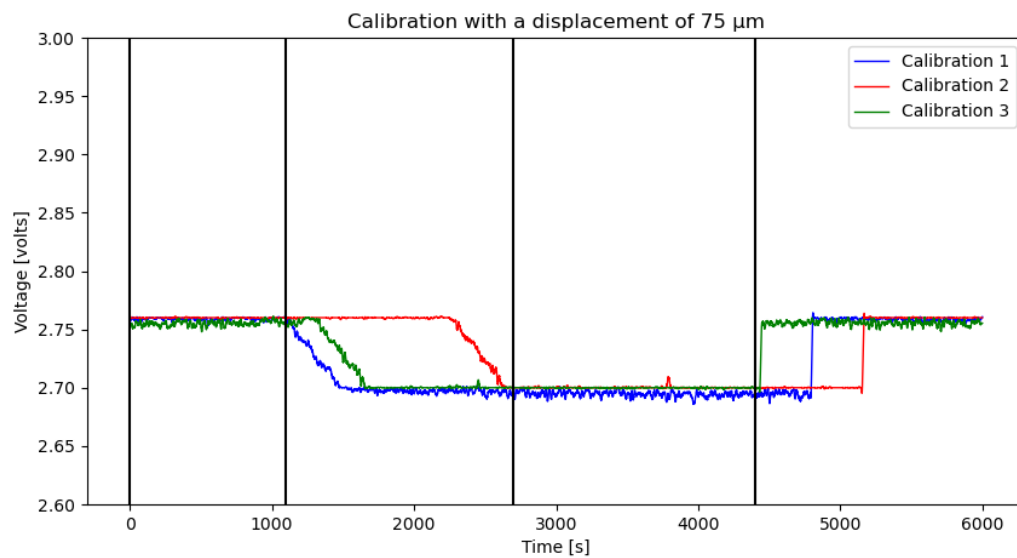


Figure G-3 Measurement of the micromotion sensor calibration with a displacement of 75 μm

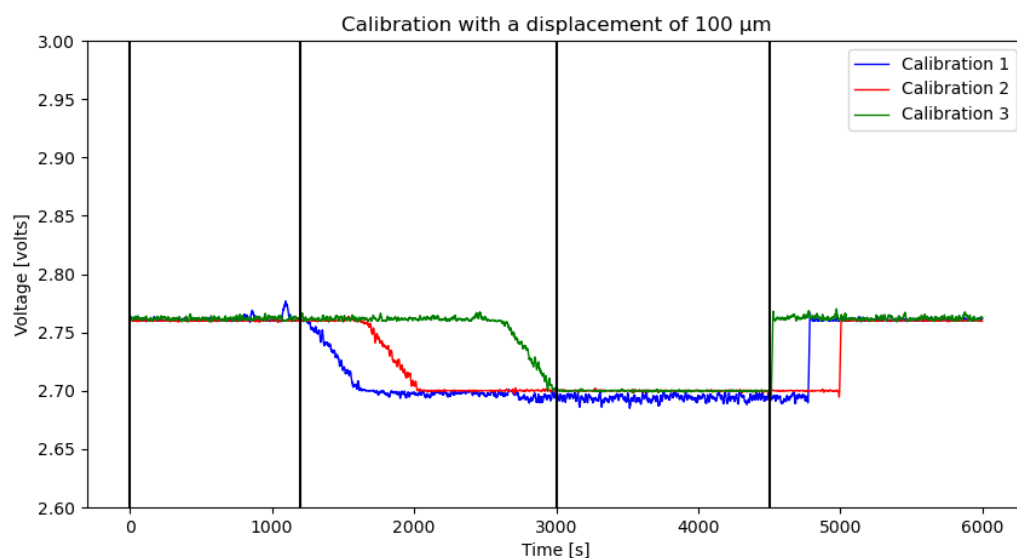


Figure G-4 Measurement of the micromotion sensor calibration with a displacement of 100 μm

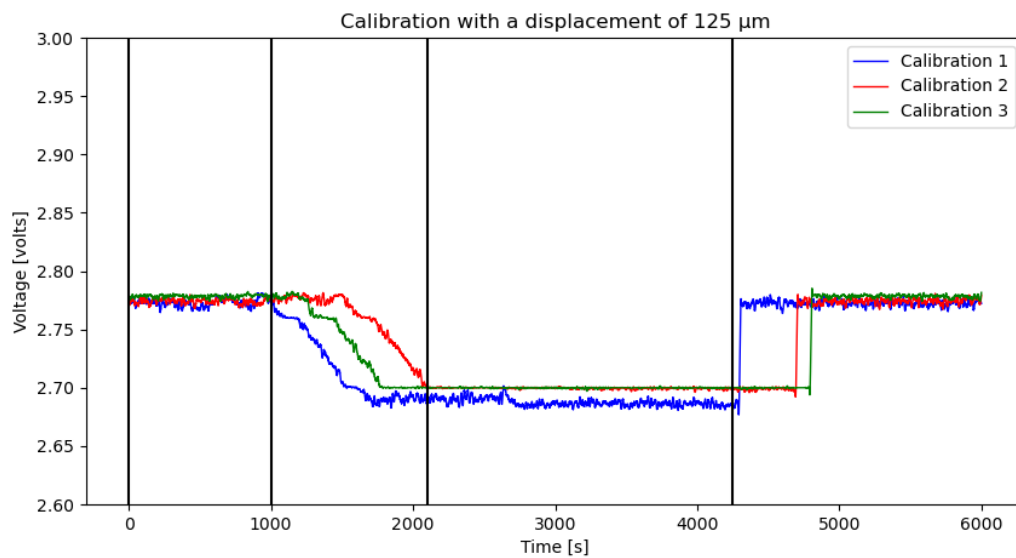


Figure G-5 Measurement of the micromotion sensor calibration with a displacement of 125 μm

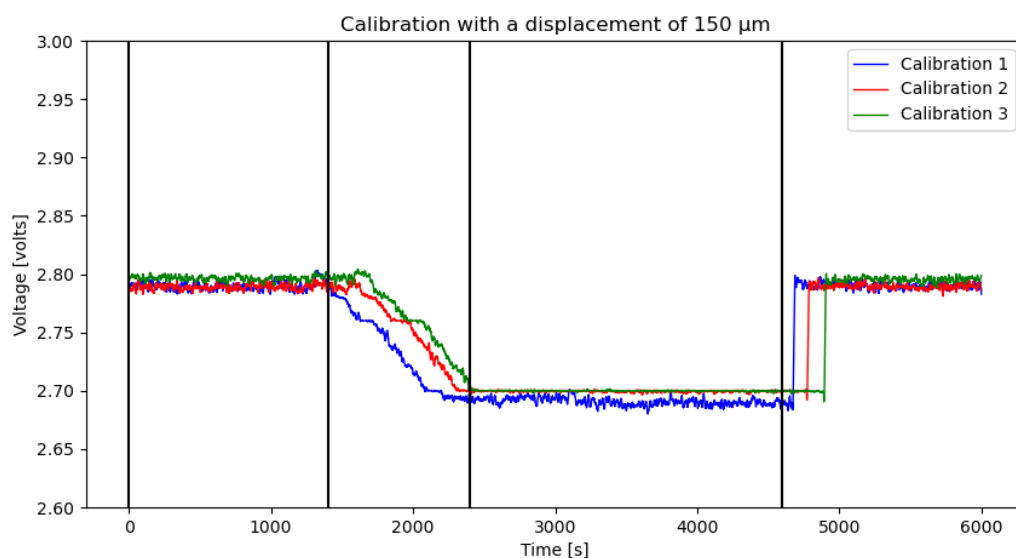


Figure G-6 Measurement of the micromotion sensor calibration with a displacement of 150 μm

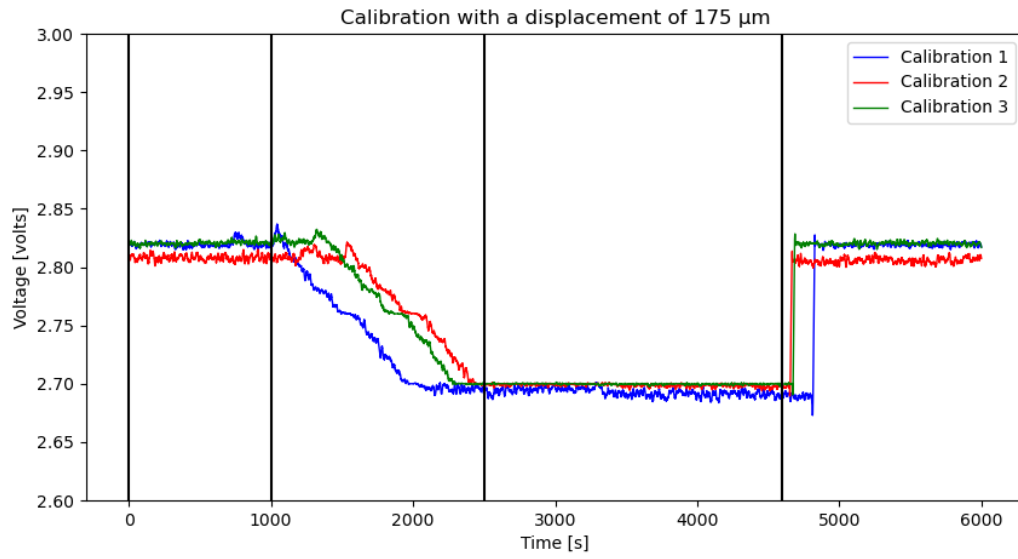


Figure G-7 Measurement of the micromotion sensor calibration with a displacement of 175 μm

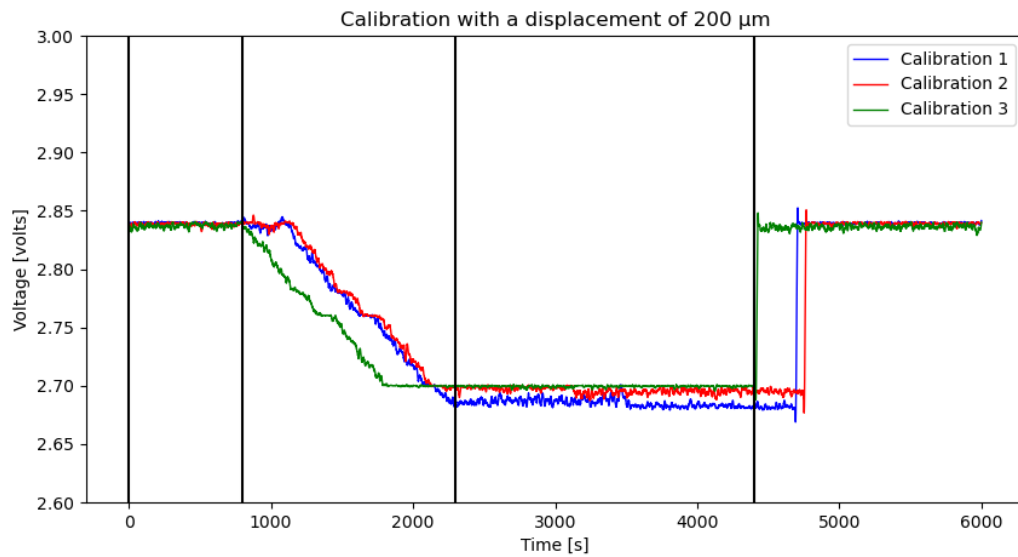


Figure G-8 Measurement of the micromotion sensor calibration with a displacement of 200 μm

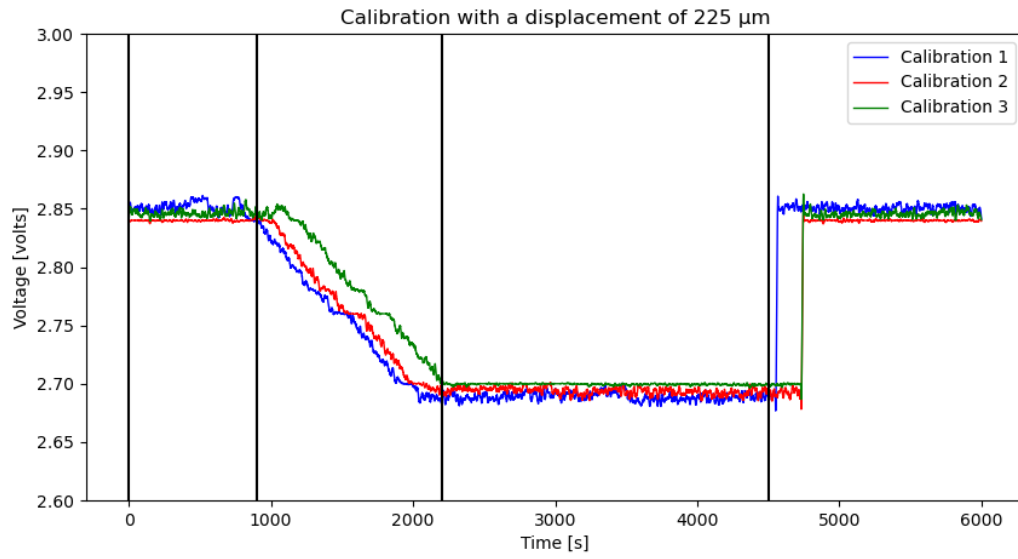


Figure G-9 Measurement of the micromotion sensor calibration with a displacement of 225 μm

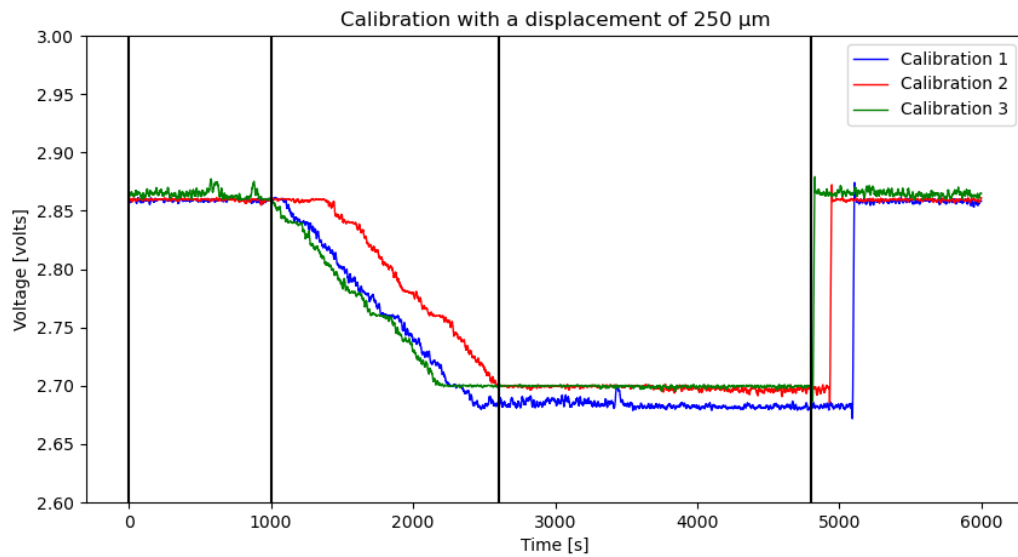


Figure G-10 Measurement of the micromotion sensor calibration with a displacement of 250 μm

Appendix H FSR CALIBRATION CURVES

During the calibration process, masses equal to 325,9236 gram, 271,6505 gram, 221,4987 gram, 179,0315 gram and 129,9886 gram are placed on the FSR. These masses are referred to as masses 1, 2, 3, 4 and 5. Figure H-1, Figure H-2, Figure H-3 and Figure H-4 show the calibration curves for respectively mass 2, mass3, mass 4 and mass 5.

The linear actuator motions, equal to 1,98 mm, 1,90 mm, 1,58 mm and 2,58 mm, are applied on the caudal tissue surface. These linear strokes are referred to as strokes 1, 2, 3, and 4. Figure H-5, Figure H-6 and Figure H-7 show the calibration curves for respectively stroke 2, stroke 3 and stroke 4.

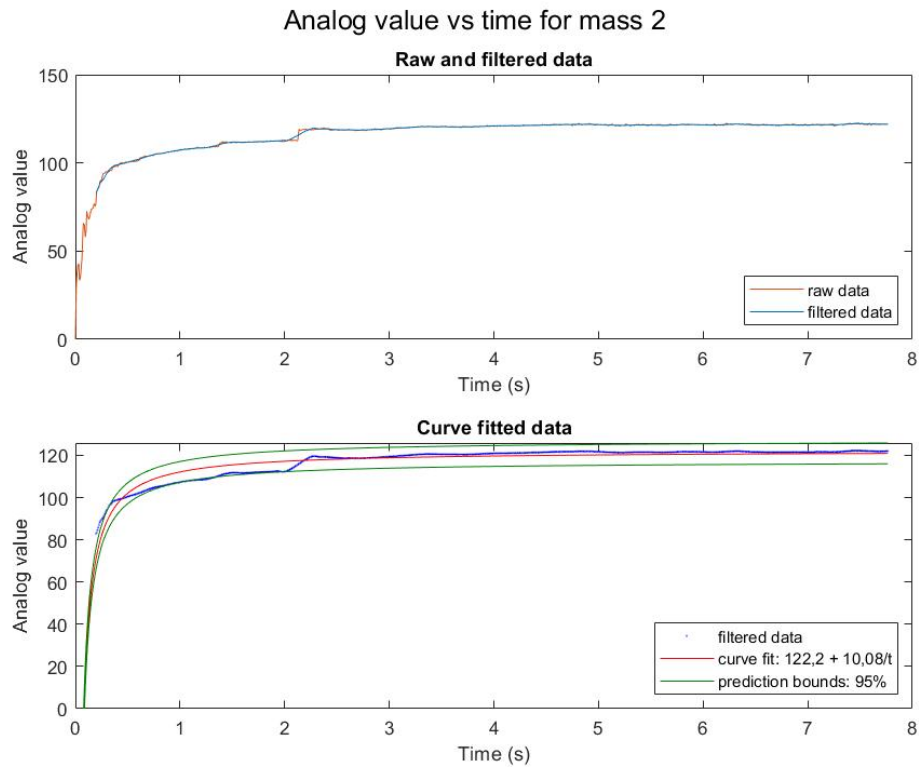


Figure H-1 Calibration of the caudal FSR with mass 2

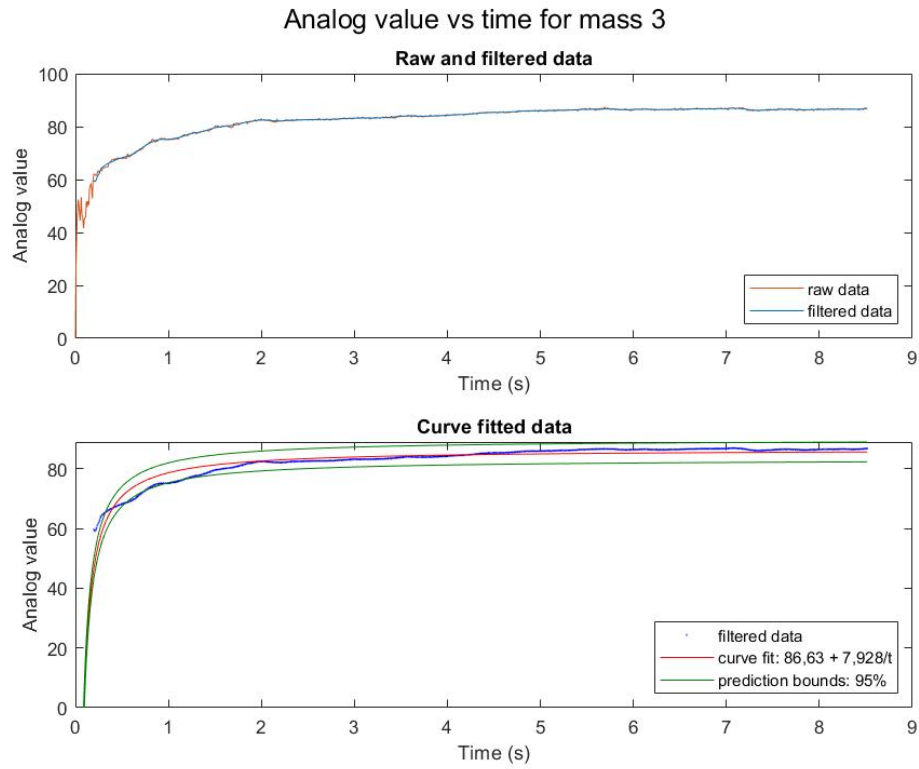


Figure H-2 Calibration of the caudal FSR with mass 3

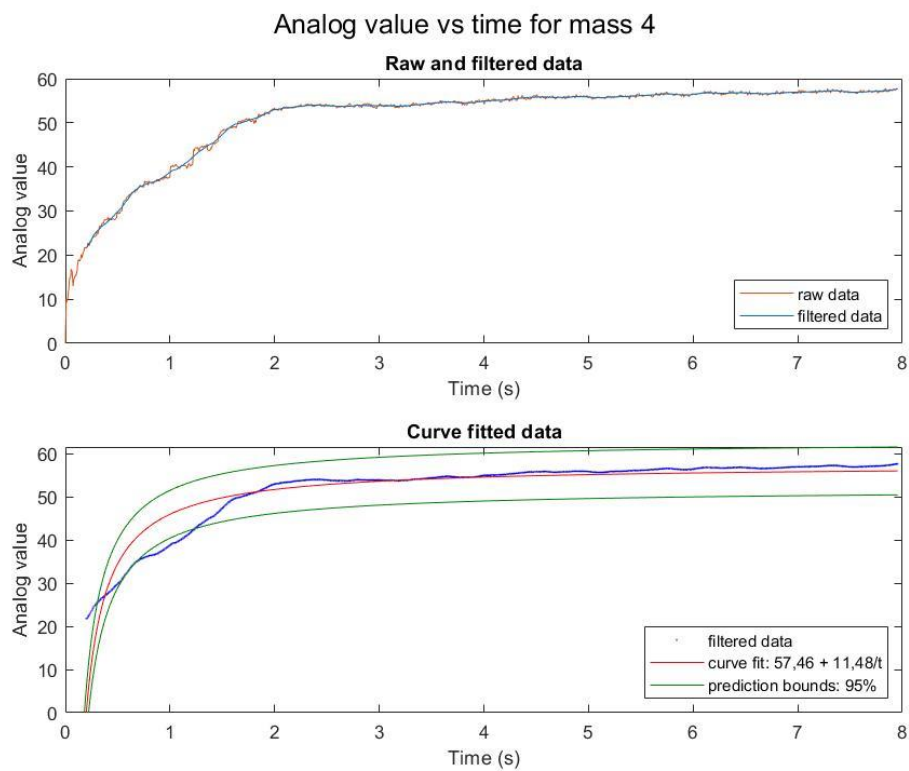


Figure H-3 Calibration of the caudal FSR with mass 4

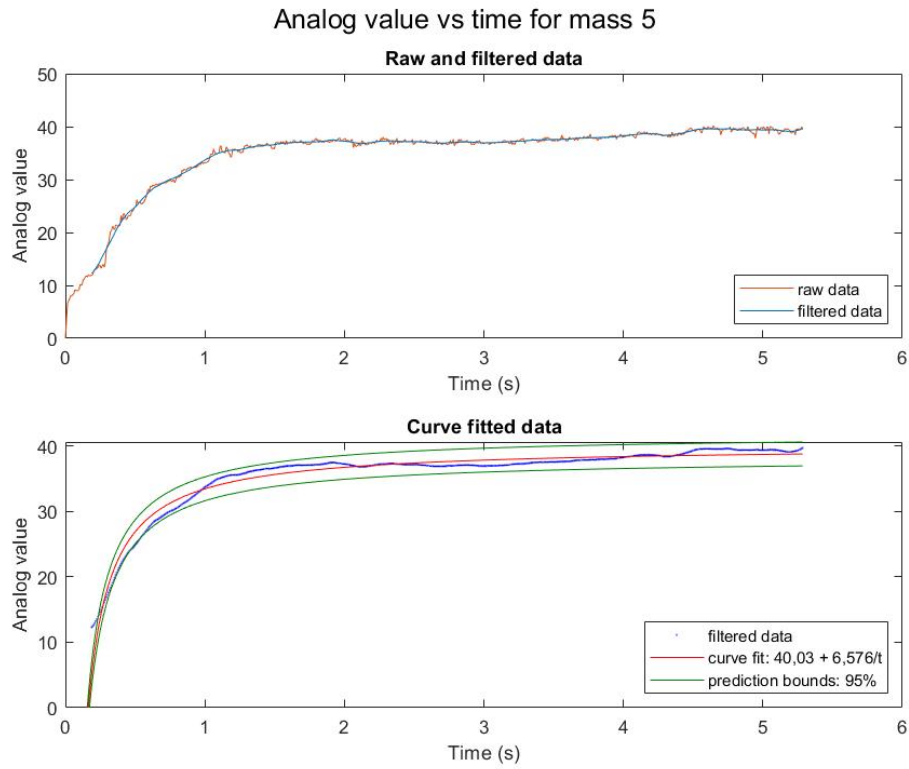


Figure H-4 Calibration of the caudal FSR with mass 5

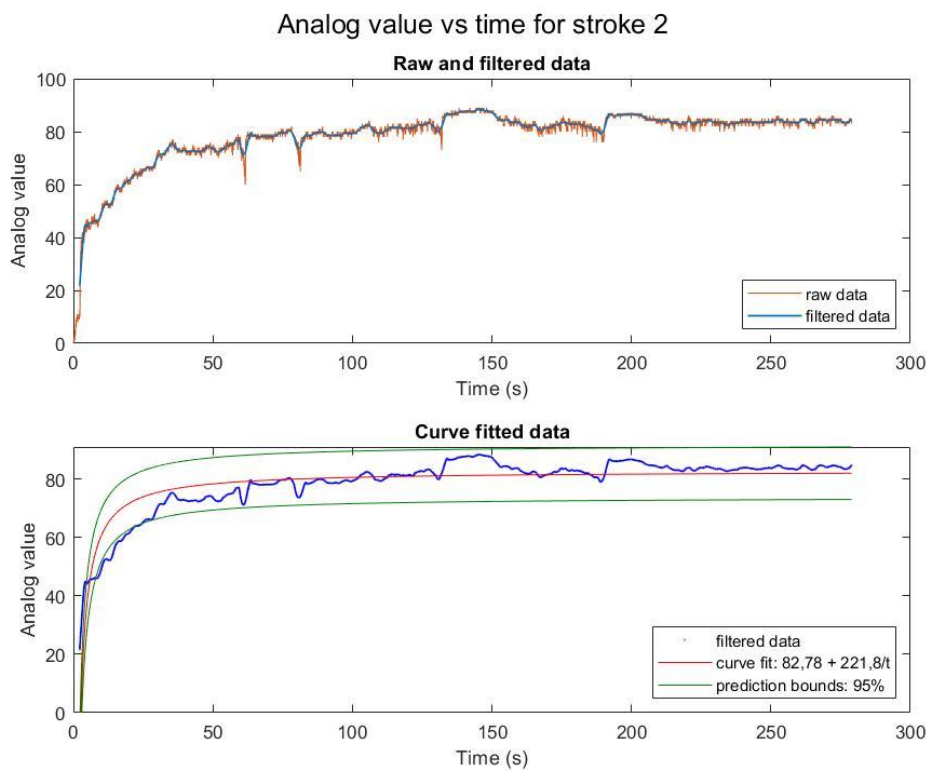


Figure H-5 Calibration of the caudal FSR at stroke 2

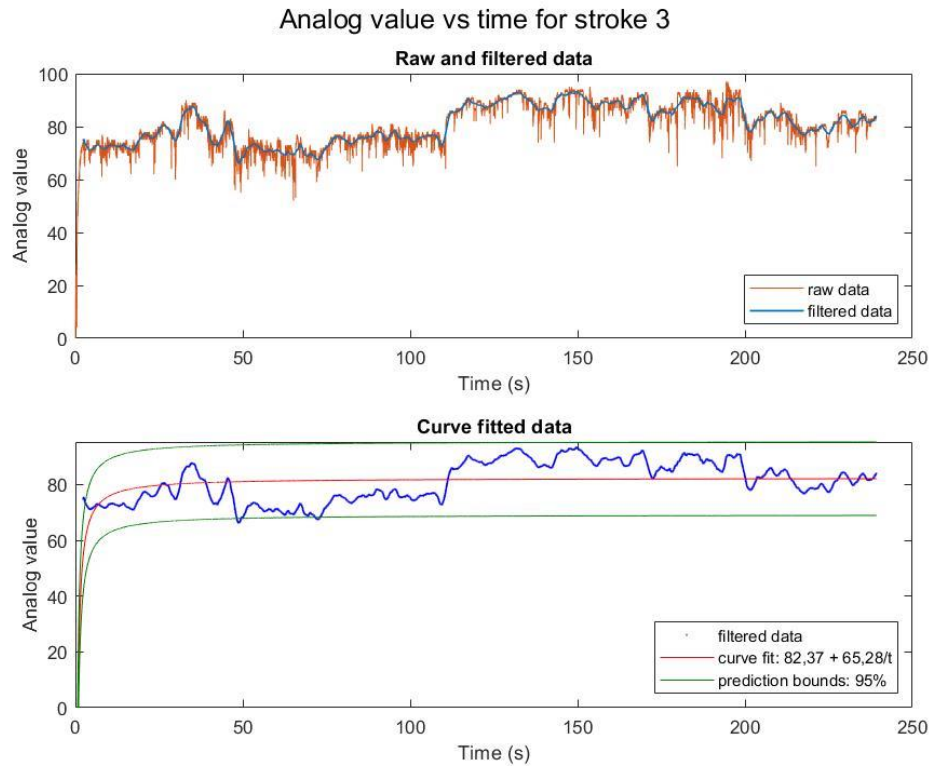


Figure H-6 Calibration of the caudal FSR at stroke 3

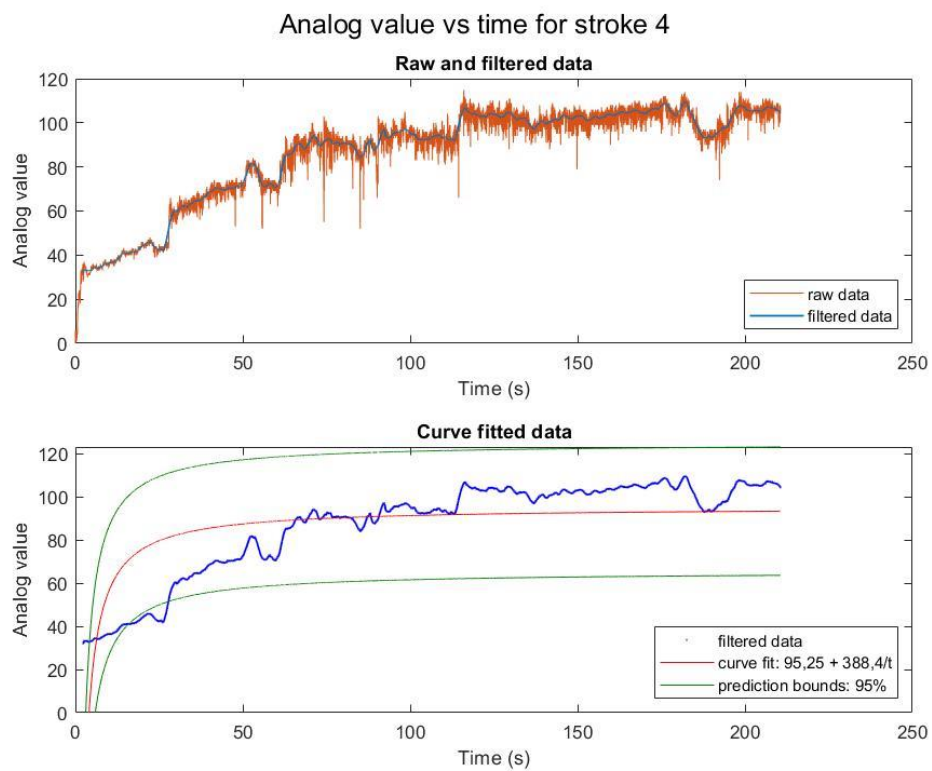


Figure H-7 Calibration of the caudal FSR at stroke

Appendix I ELECTRONIC COMPONENTS

Table I-1 shows the parts list with the required components in order to build the electronic circuits of the strain gauge amplifier and pressure sensors.

Table I-1 Parts list of the electronic components

Quantity	Part name
<i>Amplifier circuit and strain gauges</i>	
1	Dual battery power supply 2 x 8 V 1 A
3	Electrolytic capacitor 200 μ F 16 V
1	Ceramic capacitor 1 μ F 50 V
3	Resistor 1 k Ω
1	Resistor 22 k Ω
1	Resistor 240 k Ω
1	Buffer BUF634
1	Instrumentation amplifier AD627
1	Operational amplifier OPA227
2	Micro-Measurements strain gauges 015DJ
<i>Motor (Nanotec)</i>	
1	LGA421S14-A-TJBA-019 – Captive linear actuator – NEMA 17
1	CL3-E-2-0F – Motor controller for CANopen, Modbus RTU or USB
1	ZK-JST-EHR-6-0.5M-S – Motor cable, 0.5M
1	ZK-XHP2-500-S – Power cable, 0.5M
1	ZK-XHP4-300 – Motor cable, 0.3M
1	Micro-USB cable
1	TT Electronics DG-75-24 DIN Rail Power Supply 24V DC 3.2A 75W, 1 Phase
<i>Pressure sensors</i>	
2	FSR01CE, Force sensing resistor, square, 5Kg
2	RS PRO, SMD Diaphragm External Piezo Buzzer
2	Resistor 2 M Ω
2	Potentiometer 20 k Ω
<i>Arduino</i>	
1	ATmega328 uno development board
1	USB cable

Appendix J TECHNICAL DRAWINGS

0 Assembly experiment set-up

A Subassembly frame

AA Subsubassembly outer frame

AA1 Drilled profile

AB Subsubassembly subframe

AB1 Implant module

B Subassembly mould

BA Subsubassembly mould set-up

BA1 Top plate

BA2 Top edge

BA3 Bottom plate

BA4 Bottom edge

BA5 Side plate

BA6 Rostral plate

BA7 Caudal plate

BA8 Outer part lid

BA9 Inner part lid

BA10 Connector

B1 Removable spacing plate

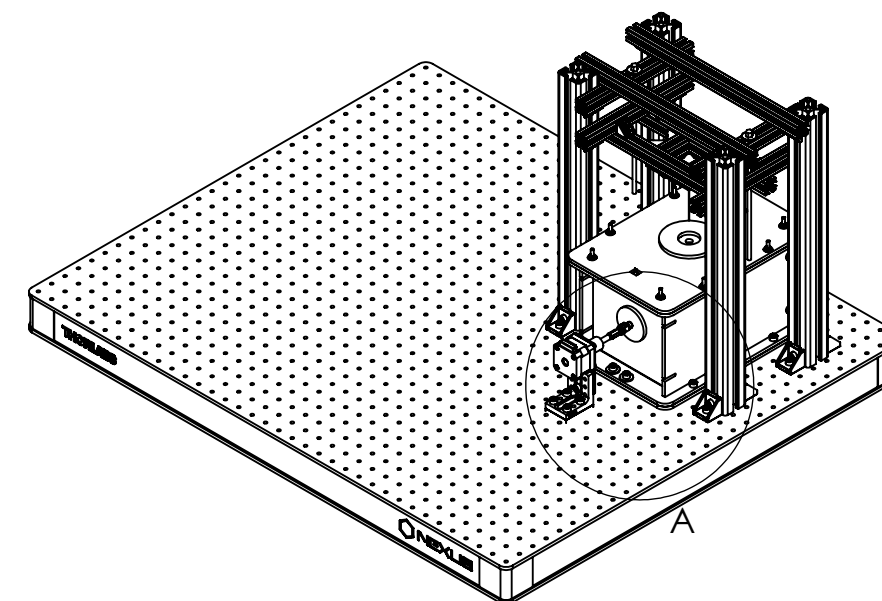
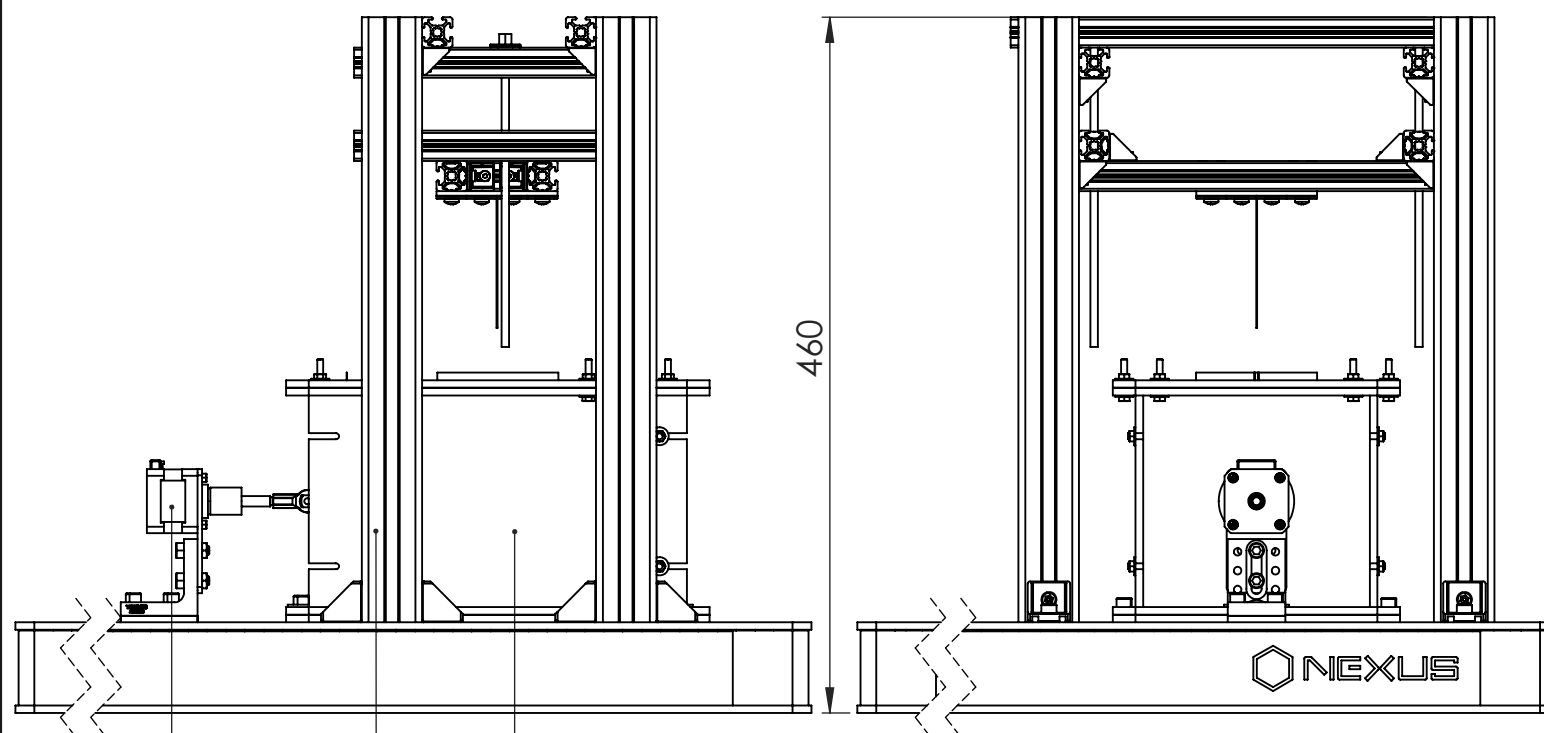
C Subassembly linear actuator

C1 Spacer plate

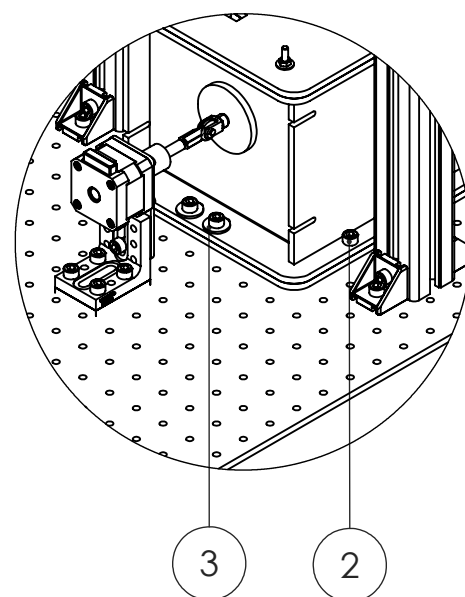
1 Implant module case

2 Implant module case lid

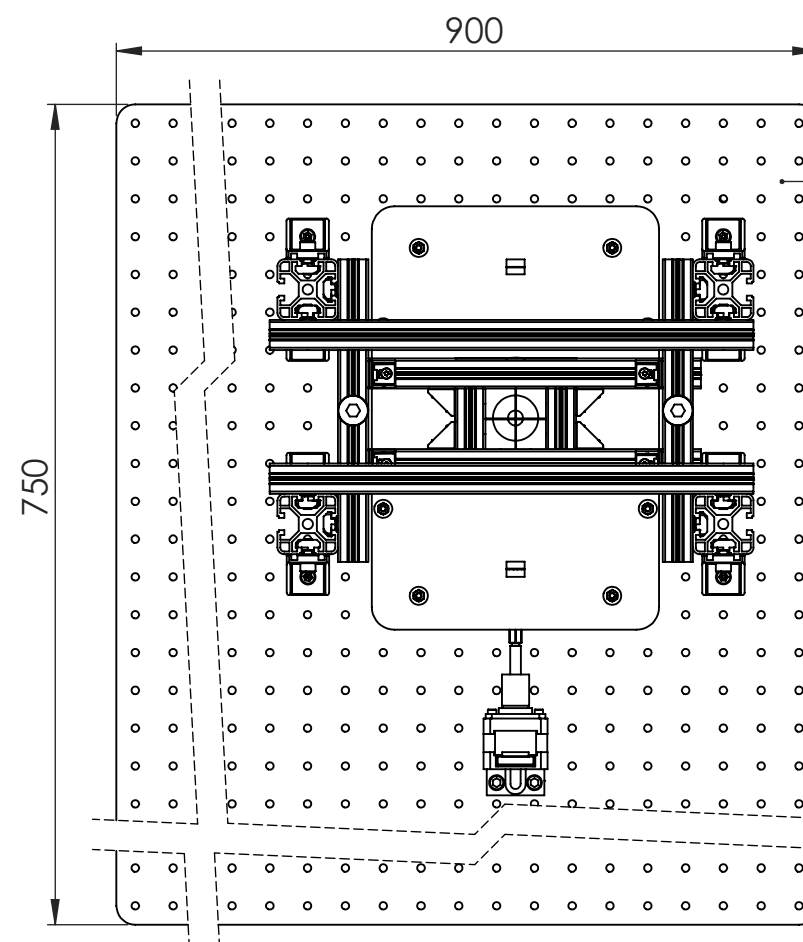
3 Calibration cube



SCALE 1:10

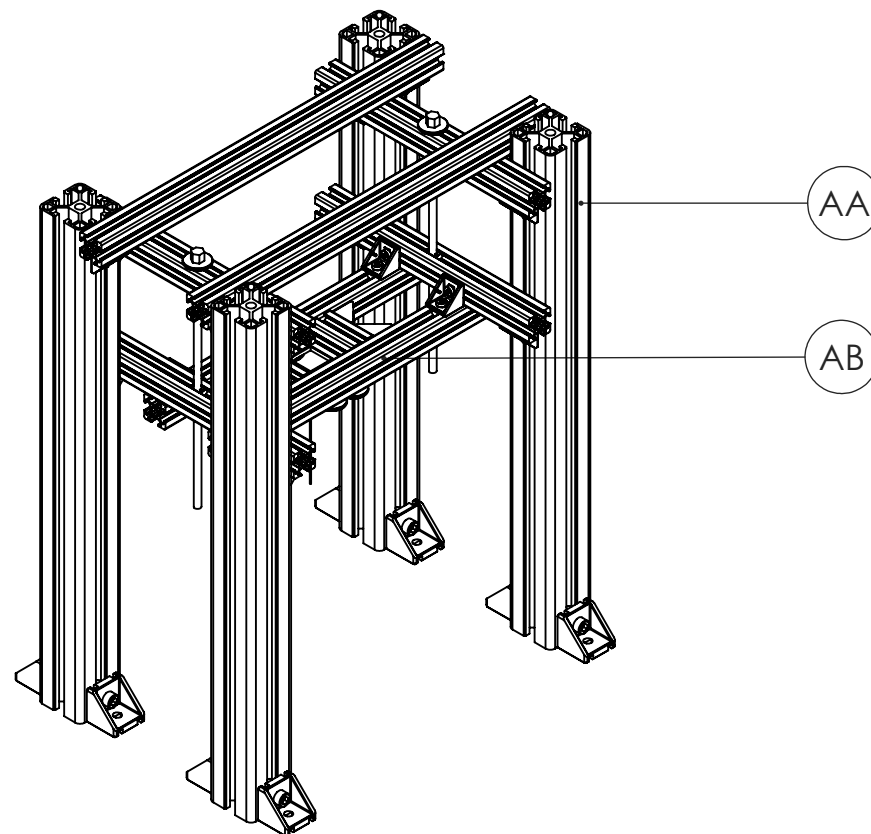
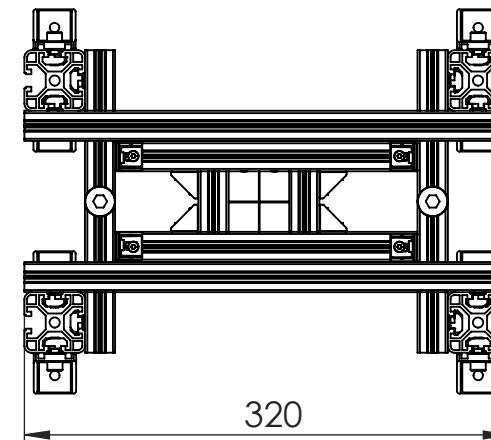
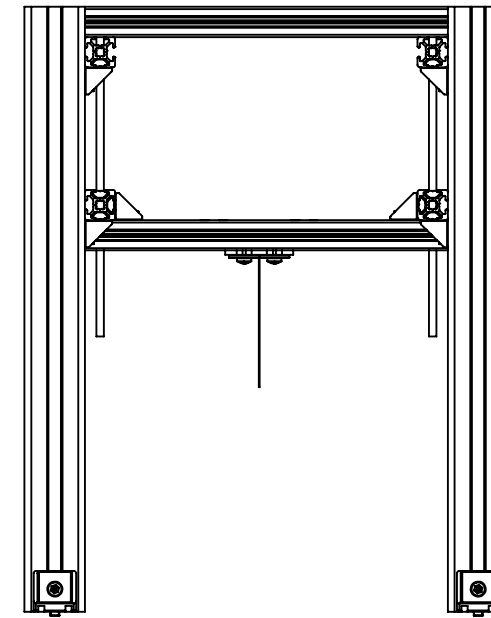
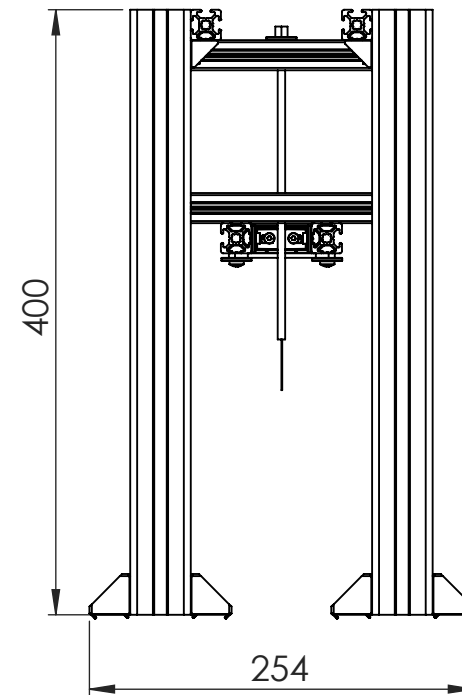


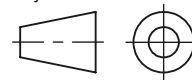
DETAIL A

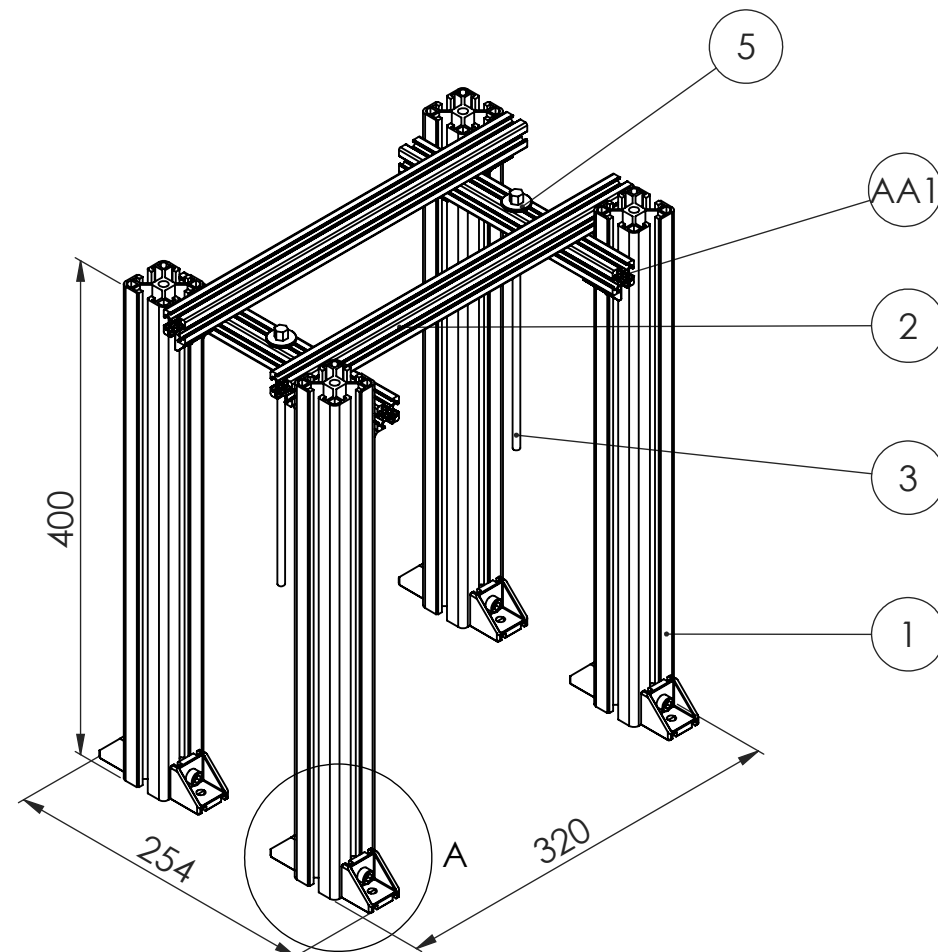
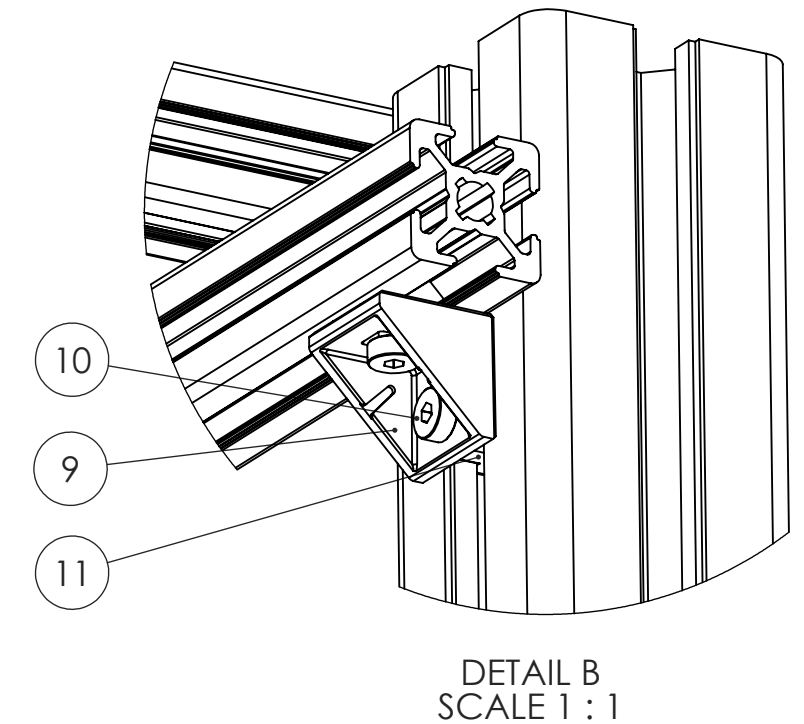
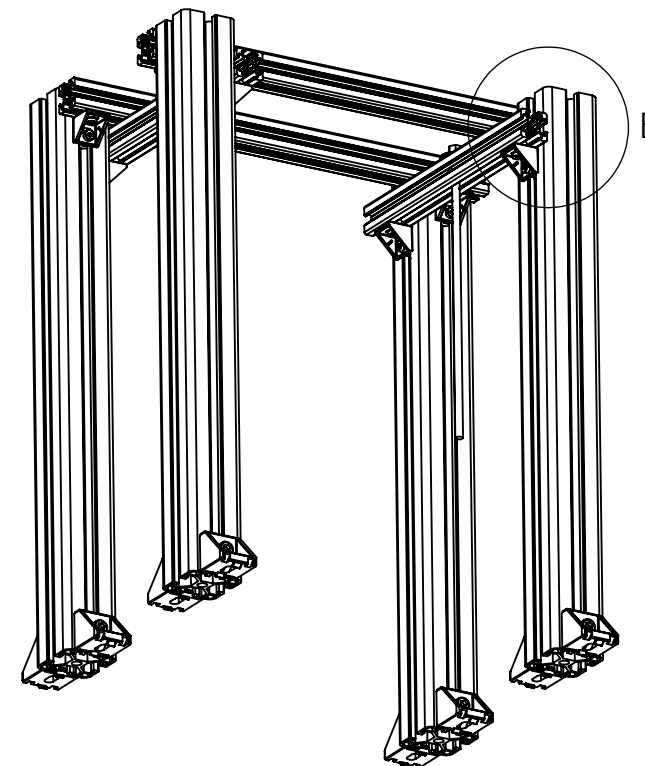
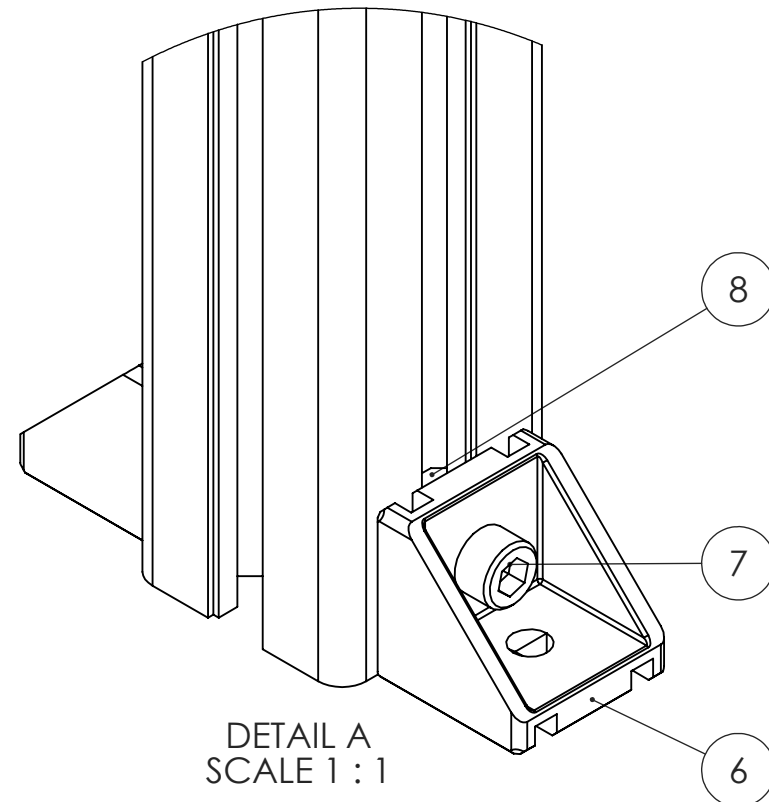


ITEM NO.	Description	Material, comments	QTY.
A	Subassembly frame		1
BA	Subsubassembly mould set-up		1
C	Subassembly linear actuator		1
1	Nexus breadboard	Thorlabs (Stock No. B7590A)	1
2	Hexagon socket head cap screw M6x30	DIN912-M6-30	20
3	Washer M6	DIN6902-M6 200HV	8

Roughness	Dimensional Tolerances according ISO 2768-m	Material	Geometric and position Tolerances according ISO 2768-K
Projection method	Scale 1:5	Drawn by Brecht Lenaerts	Comments
	Unit mm	Teamleader /	
	Date 18/05/2021	Checked by Jeroen Samoeys	
ASSOCIATIE KU LEUVEN	Assembly experiment set-up		Number 0
			A3



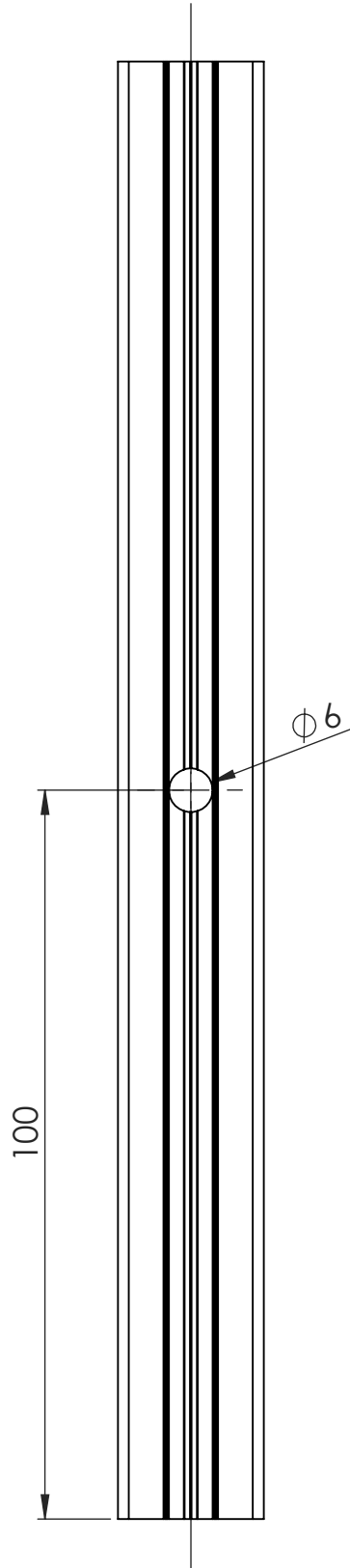
ITEM NO.	Description		Material, comments	QTY.
AA	Subsubassembly outer frame			1
AB	Subsubassembly subframe			1
Roughness	Dimensional Tolerances according ISO 2768-m		Material	Geometric and position Tolerances according ISO 2768-K
Projection method 	Scale	1:5	Drawn by Jeroen Samoeey	Comments
	Unit	mm	Teamleader /	
	Date	10/05/2021	Checked by Brecht Lenaerts	
ASSOCIATIE KU LEUVEN	Subassembly frame		Number A	A3



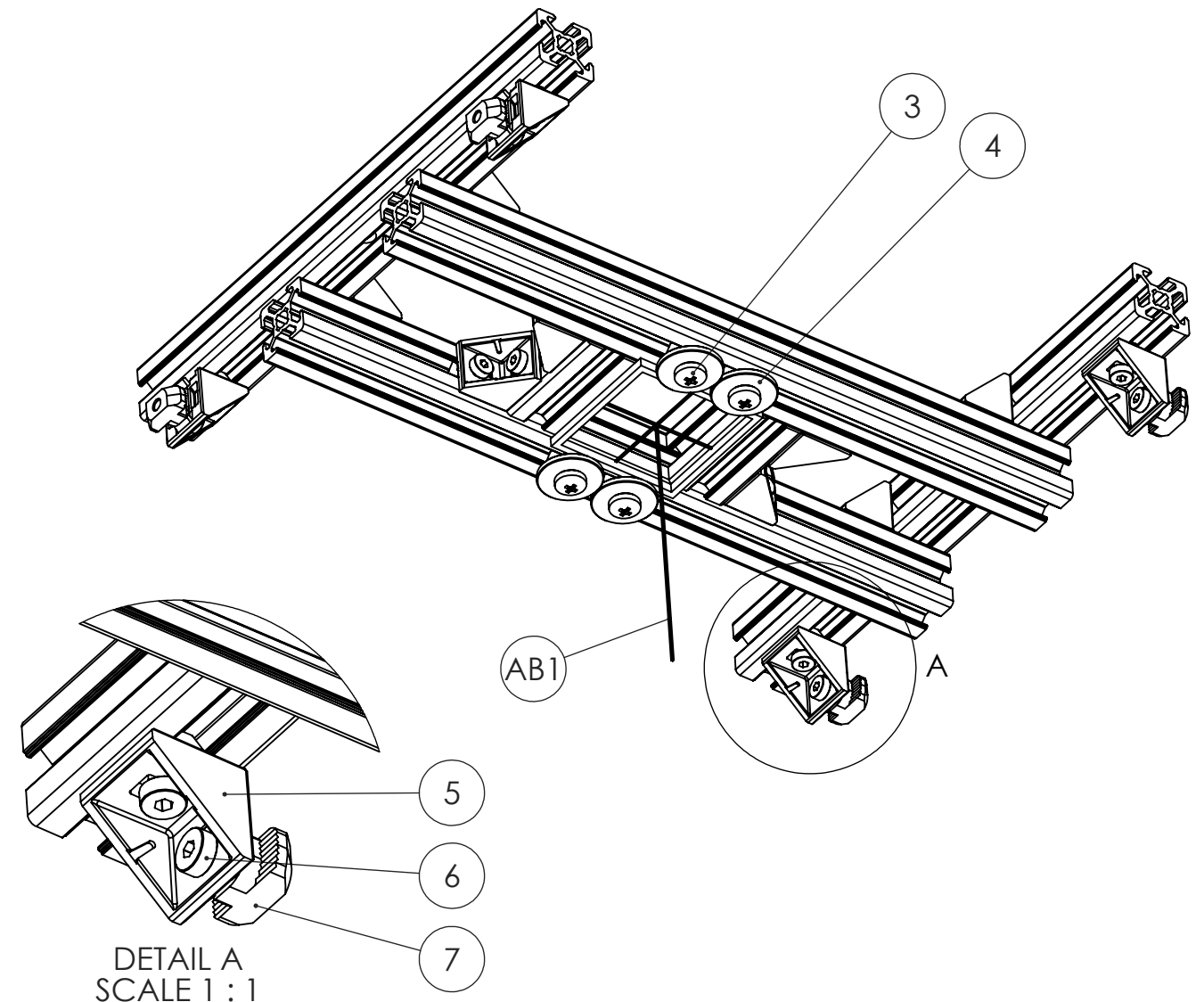
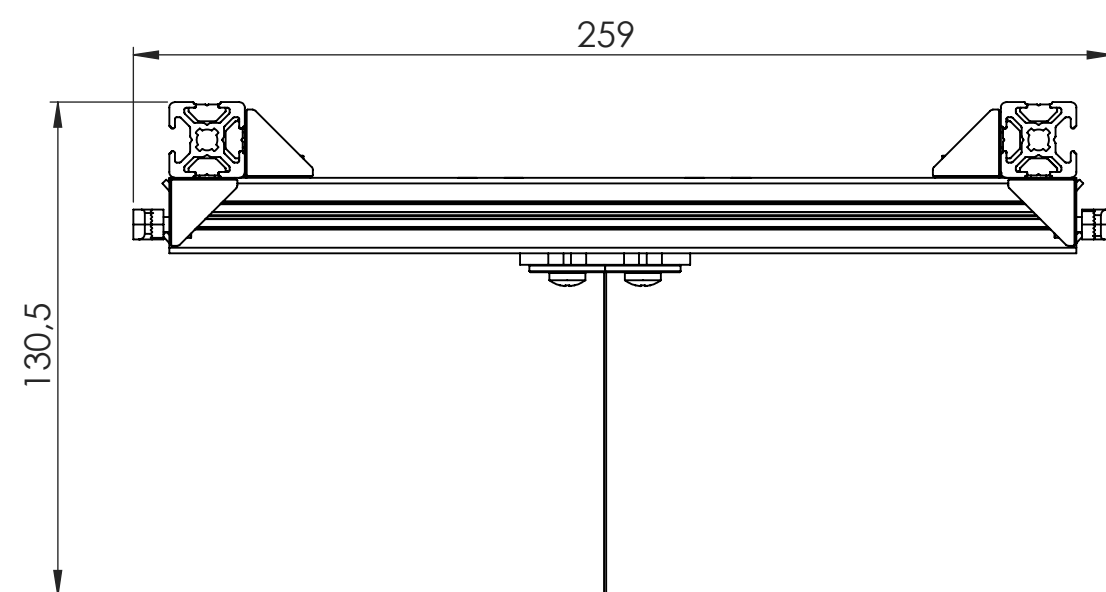
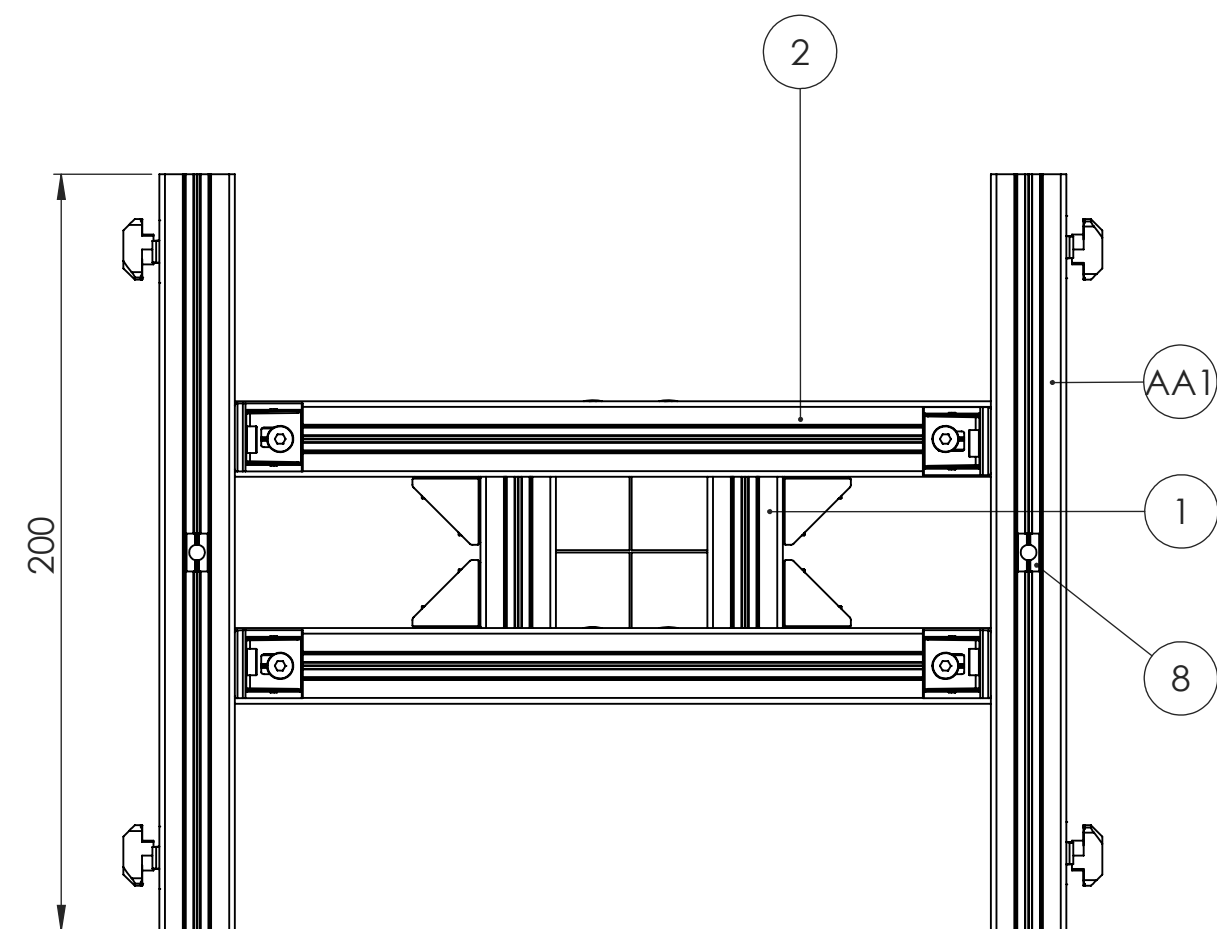
ITEM NO.	Description	Material, comments	QTY.
AA1	Drilled profile		2
1	Profile 8 40x40 L=400 mm	RS (Stock No. 761-3319)	4
2	Profile 6 20x20 L=320 mm	RS (Stock No. 212-3293)	2
3	Threaded rod M5x0.8 L=400 mm	123-3D.nl	2
4	Hexagon nut M5x0.8	ISO4033-M5x0.8	4
5	Washer M5	DIN7091-M5 100HV	2
6	Angle bracket 8 30 mm	RS (Stock No. 390-1798)	8
7	Hexagon socket head cap bolt M6x14	DIN912-M6x14	8
8	T-slot nut M6	RS (Stock No. 390-1798)	8
9	Angle bracket 6 20 mm	RS (Stock No. 466-7354)	8
10	Hexagon socket head cap bolt M4x8	DIN912-M4x8	16
11	T-slot nut M4	RS (Stock No. 466-7354)	16

Roughness	Dimensional Tolerances according ISO 2768-m	Material	Geometric and position Tolerances according ISO 2768-K
Projection method	Scale 1:5	Drawn by Jeroen Samoeys	Comments
	Unit mm	Teamleader /	
	Date 10/05/2021	Checked by Brecht Lenaerts	
ASSOCIATIE KU LEUVEN			Number AA A3

Subsubassembly outer frame

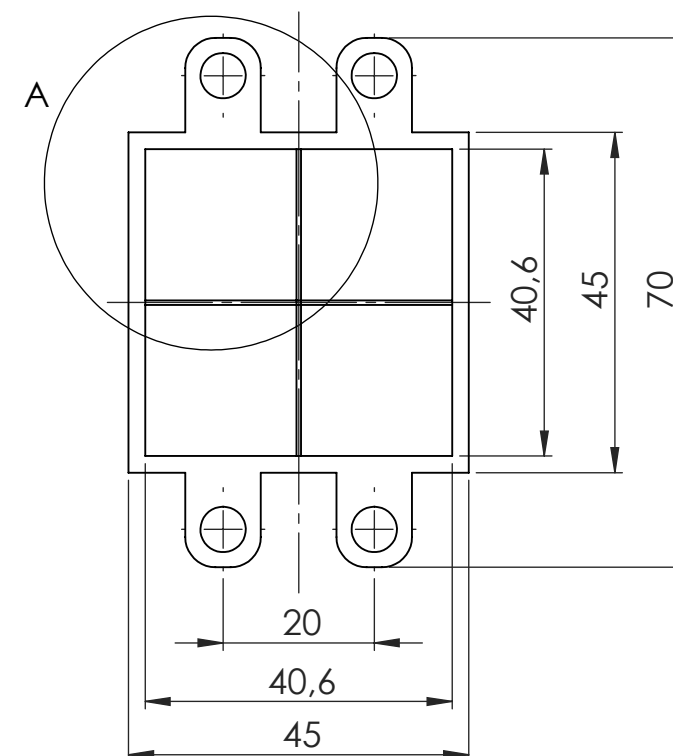
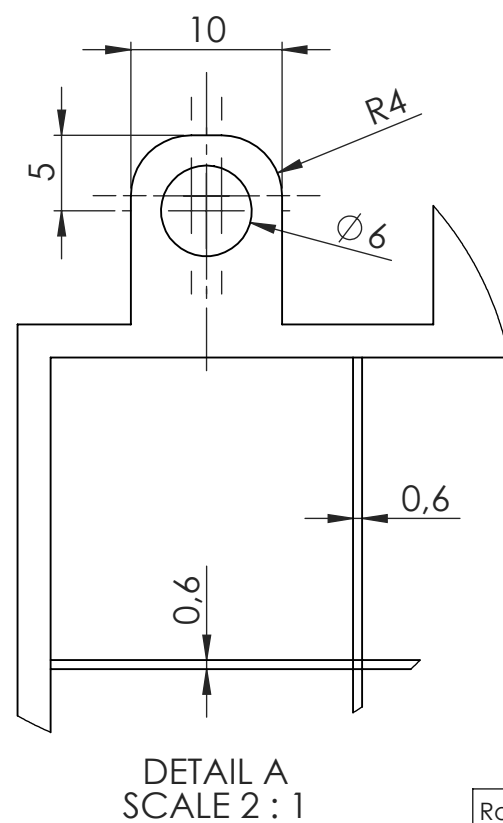
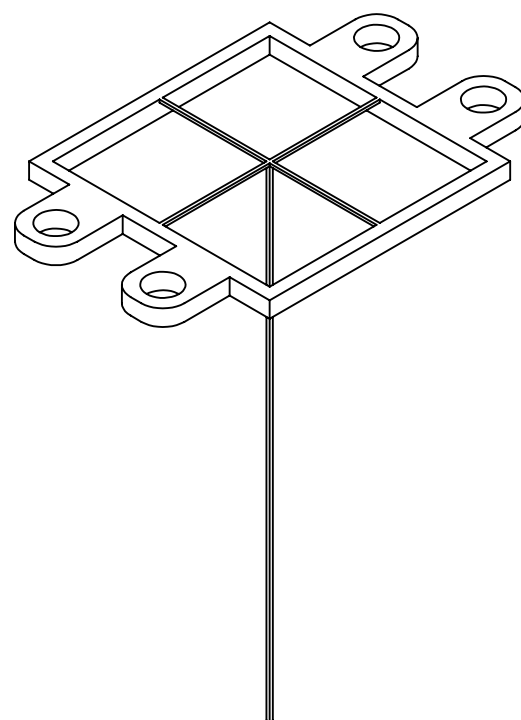
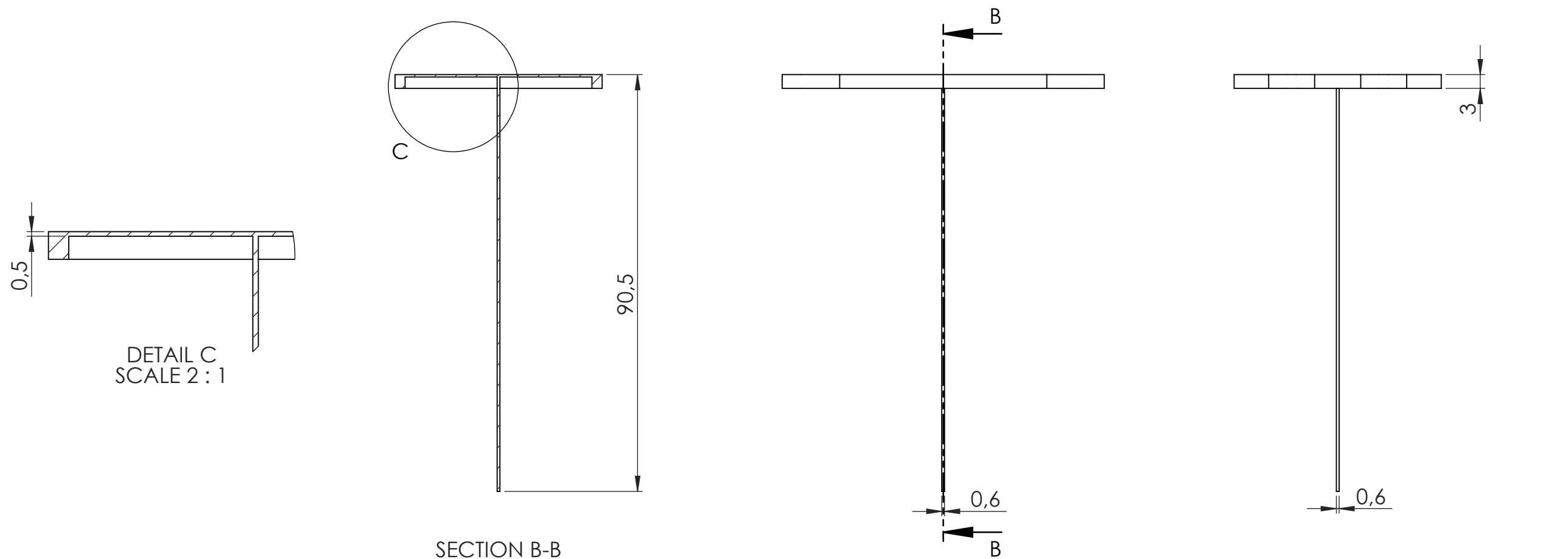


Roughness $\sqrt{3}$	Dimensional Tolerances according ISO 2768-m	Material AlMgSi0,5	Geometric and position Tolerances according ISO 2768-K	
Projection method 	Scale 1:1	Drawn by Jeroen Samoeey	Comments Strut profile 20x20x200	
	Unit mm	Teamleader /		
	Date 3/05/2021	Checked by Brecht Lenaerts		
ASSOCIATIE KU LEUVEN	Drilled profile		Number AA1	A4

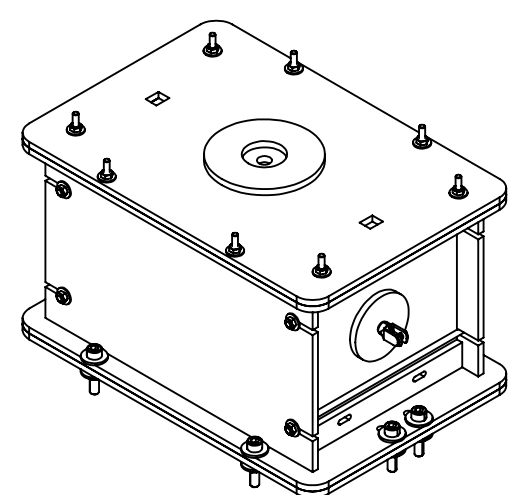
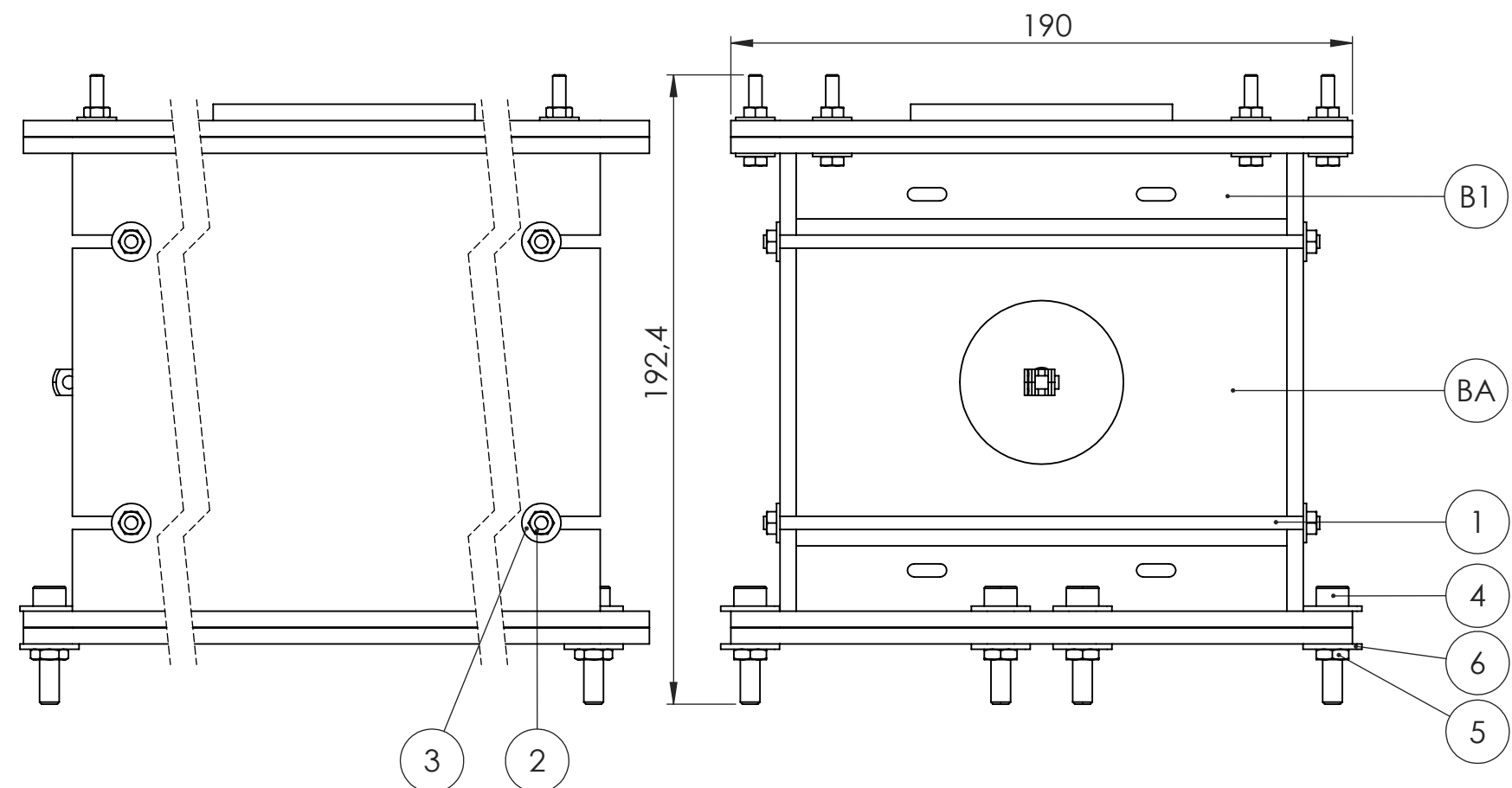


ITEM NO.	Description	Material, comments	QTY.
AA1	Drilled profile		2
AB1	Implant module		1
1	Profile 6 20x20 L=40 mm	RS (Stock No. 212-3293)	2
2	Profile 6 20x20 L=240 mm	RS (Stock No. 212-3293)	2
3	Cross head cap bolt M5x10	DIN1207-M5x10	4
4	Washer M5	DIN7091-M5 100HV	4
5	Angle bracket 6 20 mm	RS (Stock No. 466-7354)	12
6	Hexagon socket head cap bolt M4x8	DIN912-M4x8	24
7	T-slot nut M4	RS (Stock No. 466-7354)	24
8	Sliding element M5	RS (Stock No. 466-7297)	6

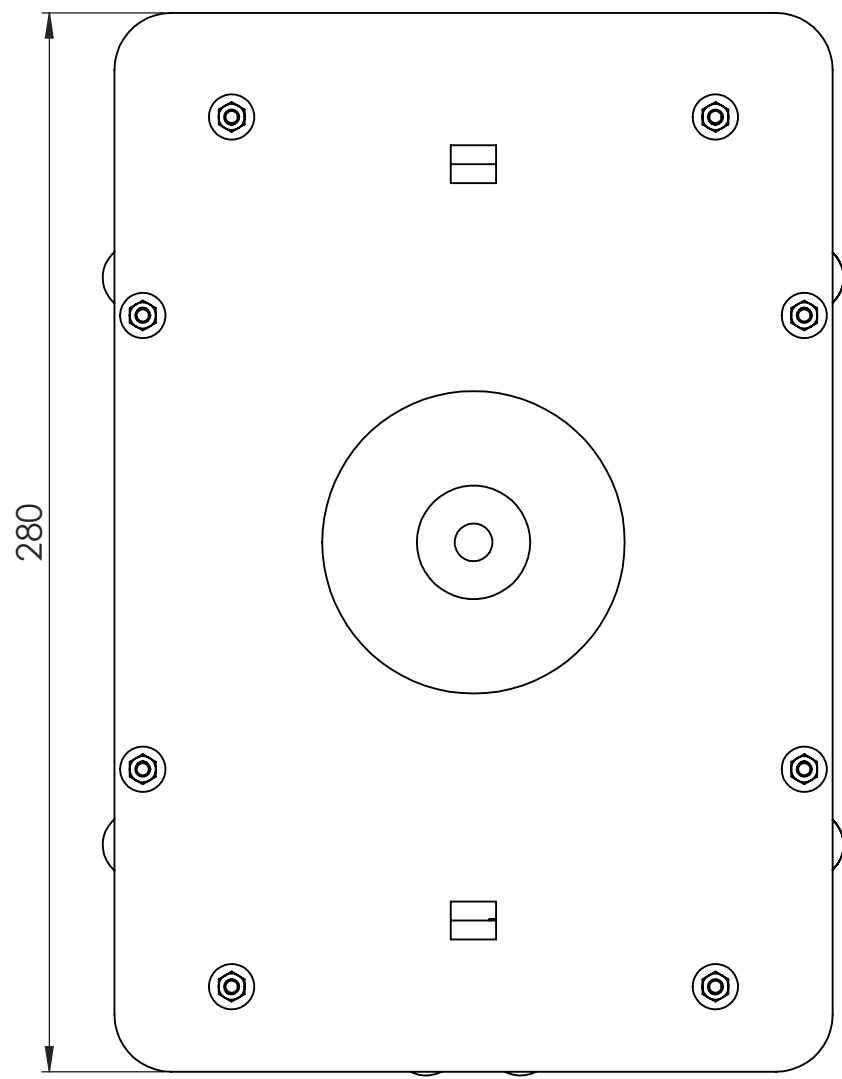
Roughness	Dimensional Tolerances according ISO 2768-m	Material	Geometric and position Tolerances according ISO 2768-K
Projection method	Scale 1:2	Drawn by Jeroen Samoeys	Comments
	Unit mm	Teamleader /	
	Date 18/05/2021	Checked by Brecht Lenaerts	
ASSOCIATIE KU LEUVEN	Subsubassembly subframe		Number AB A3

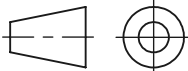


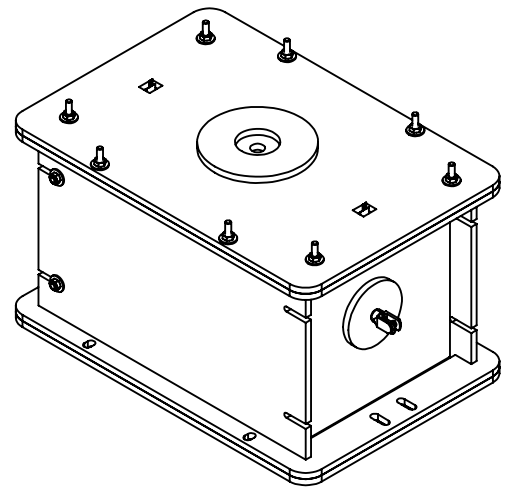
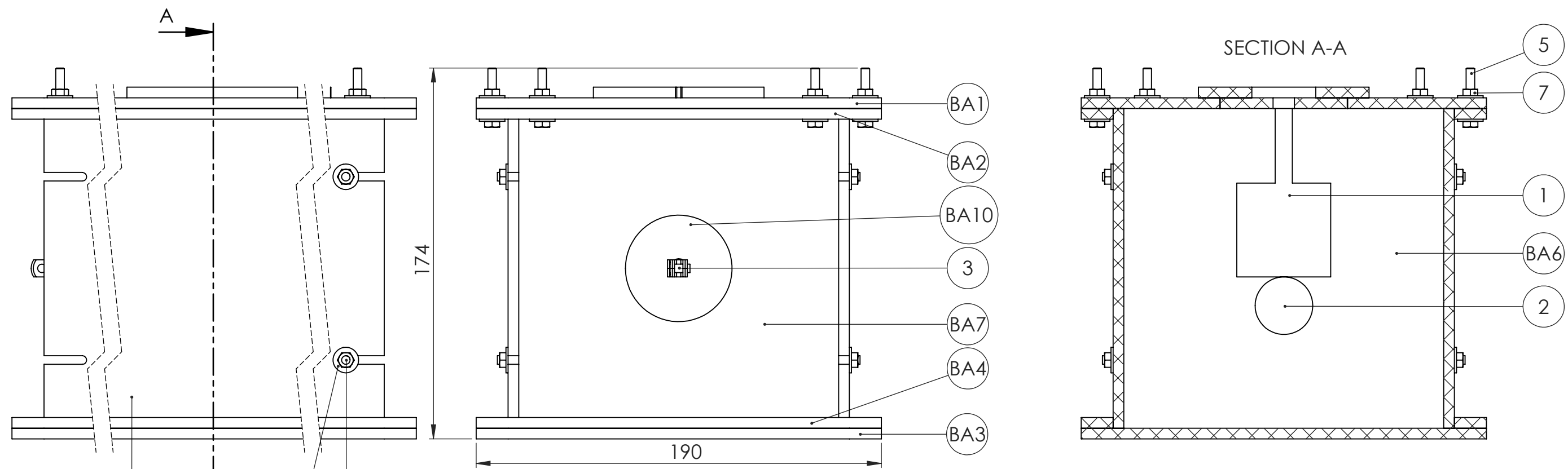
Roughness $\sqrt{15}$	Dimensional Tolerances according ISO 2768-m	Material SS316L	Geometric and position Tolerances according ISO 2768-K	
Projection method 	Scale 1:1	Drawn by Jeroen Samoeys	Comments	
	Unit mm	Teamleader /		
	Date 18/05/2021	Checked by Brecht Lenaerts		
ASSOCIATIE KU LEUVEN	Implant module		Number AB1	A3



SCALE 1:5



ITEM NO.	Description	Material, comments	QTY.		
BA	Subsubassembly mould set-up		1		
B1	Removable spacing plate		1		
1	Lead screw M4x160	L=160	2		
2	Hexagon nut M4x1	ISO4035-M4x1	4		
3	Washer M4	DIN6902-M4 200HV	4		
4	Hexagon head screw M6x30	DIN912-M6x30	8		
5	Hexagon nut M6x1	ISO4035-M6x1	8		
6	Washer M6	DIN6902-M6 200HV	16		
Roughness		Dimensional Tolerances according ISO 2768-m	Material	Geometric and position Tolerances according ISO 2768-K	
Projection method		Scale 1:2	Drawn by Brecht Lenaerts	Comments	
		Unit mm	Teamleader /		
		Date 19/05/2021	Checked by Jeroen Samoeey		
ASSOCIATIE KU LEUVEN		Subassembly mould		Number B	A3



SCALE 1:5

ITEM NO.	Description	Material, comments	QTY.
BA1	Top plate	Plexiglass (PMMA)	1
BA2	Top edge	Plexiglass (PMMA)	1
BA3	Bottom plate	Plexiglass (PMMA)	1
BA4	Bottom edge	Plexiglass (PMMA)	1
BA5	Side plate	Plexiglass (PMMA)	2
BA6	Rostral plate	Plexiglass (PMMA)	1
BA7	Caudal plate	Plexiglass (PMMA)	1
BA8	Outer part lid	Plexiglass (PMMA)	1
BA9	Inner part lid	Plexiglass (PMMA)	1
BA10	Connector	FLGPBK01 Photopolymer resin	1
1	Force sensing resistor	Ohmite (Stock No. FSR01CE)	2
2	Piezo electric transducer 15Vpp	RS (Stock No. 724-3162)	2
3	Clevis joint with spring-loaded fixing clip and rod end bearing	Igus (Stock No. GERMFE-04)	1
4	Hexagon socket head cap screw M4x12	DIN912-M4x12	1
5	Hexagon head screw M4x25	DIN912-M4x25	8
6	Lead screw M4x160	L=160	2
7	Hexagon nut M4x1	ISO4035-M6x1	12
8	Washer M4	DIN6902-M4 200HV	20

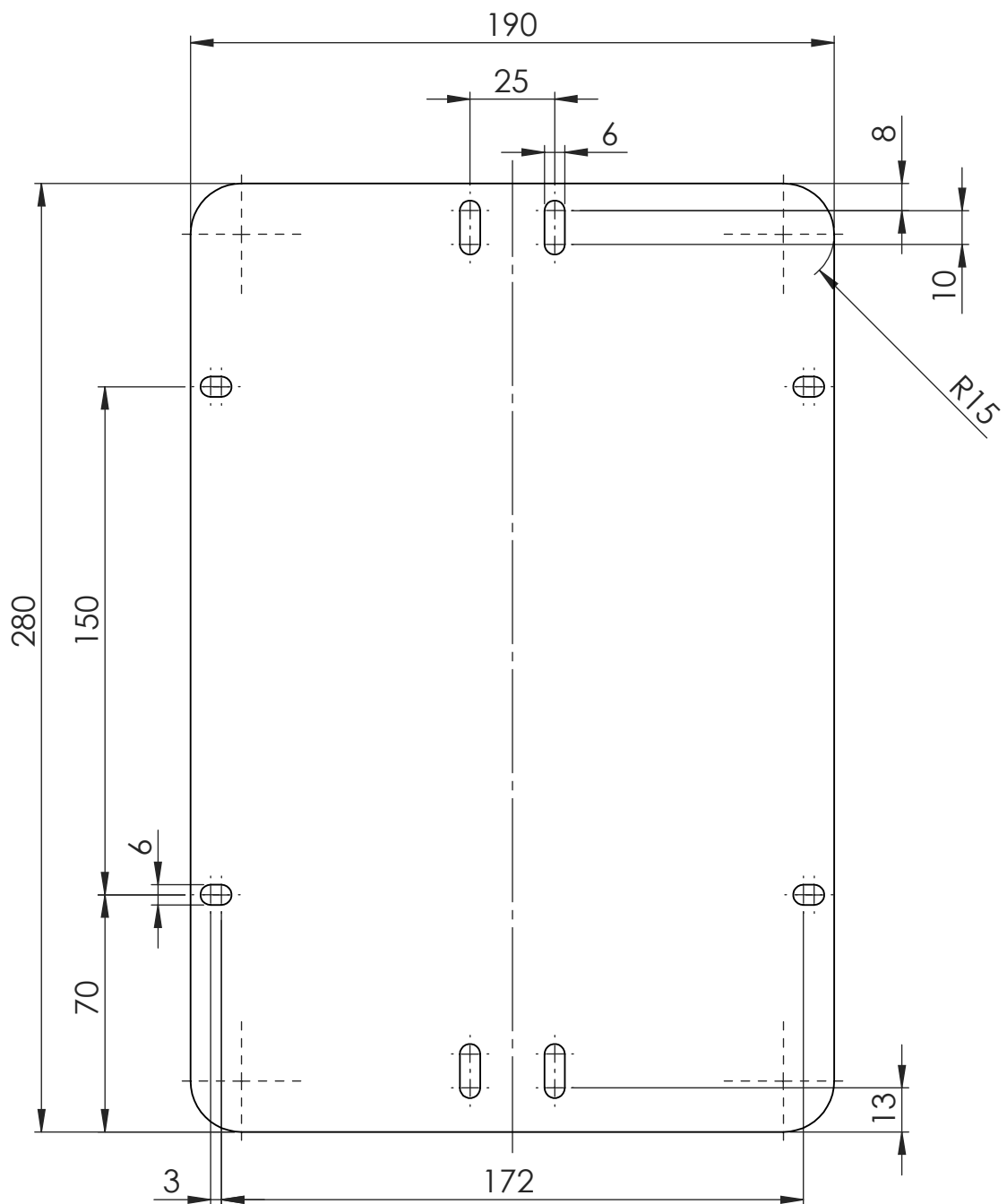
Roughness	Dimensional Tolerances according ISO 2768-m	Material	Geometric and position Tolerances according ISO 2768-K
Projection method	Scale 1:2	Drawn by Brecht Lenaerts	Comments
	Unit mm	Teamleader /	
	Date 19/05/2021	Checked by Jeroen Samoeey	
ASSOCIATIE KU LEUVEN	Subsubassembly mould set-up		Number BA A3



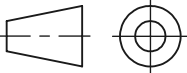
SOLIDWORKS Educational Product. For Instructional Use Only.

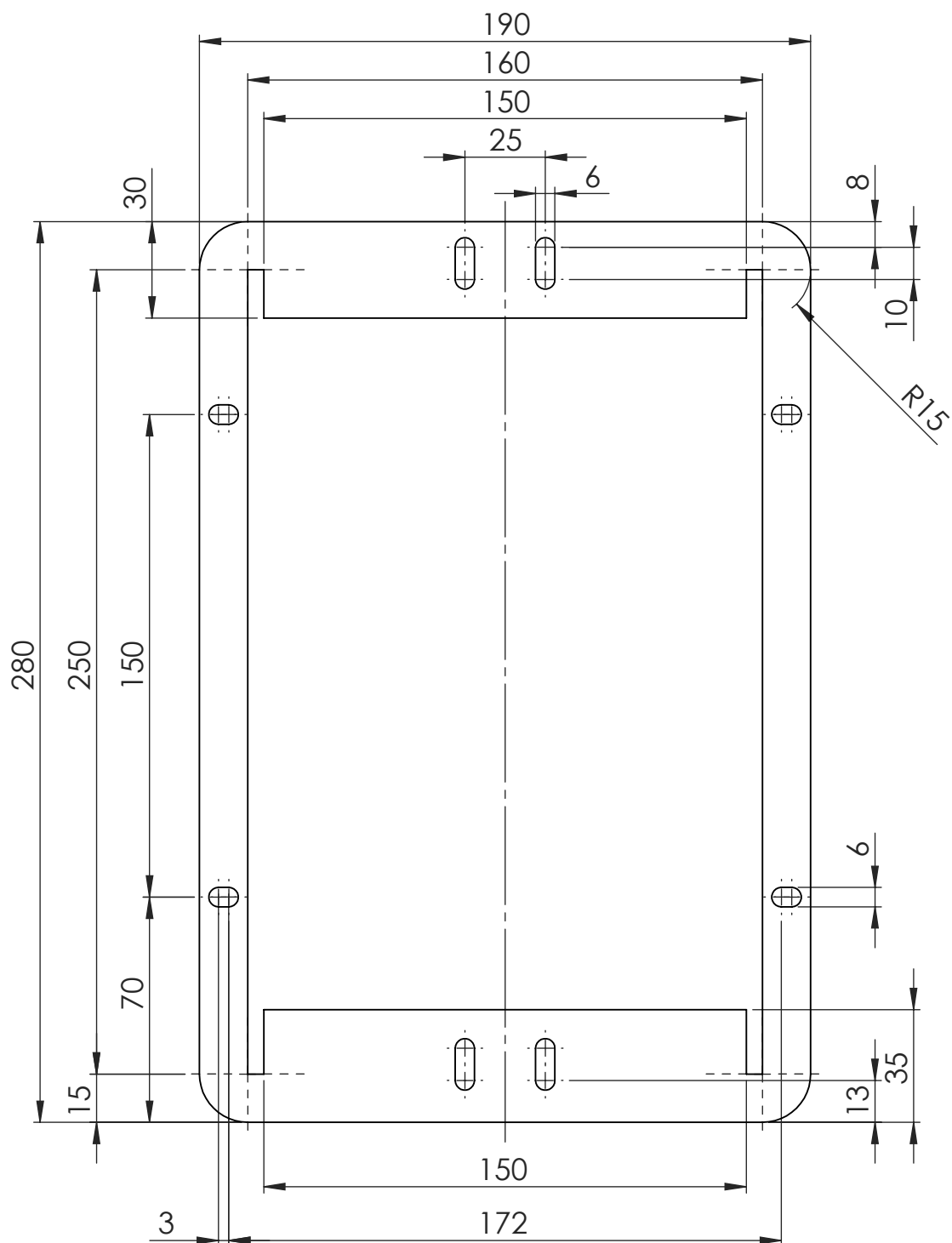


SOLIDWORKS Educational Product. For Instructional Use Only.

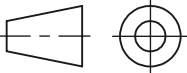


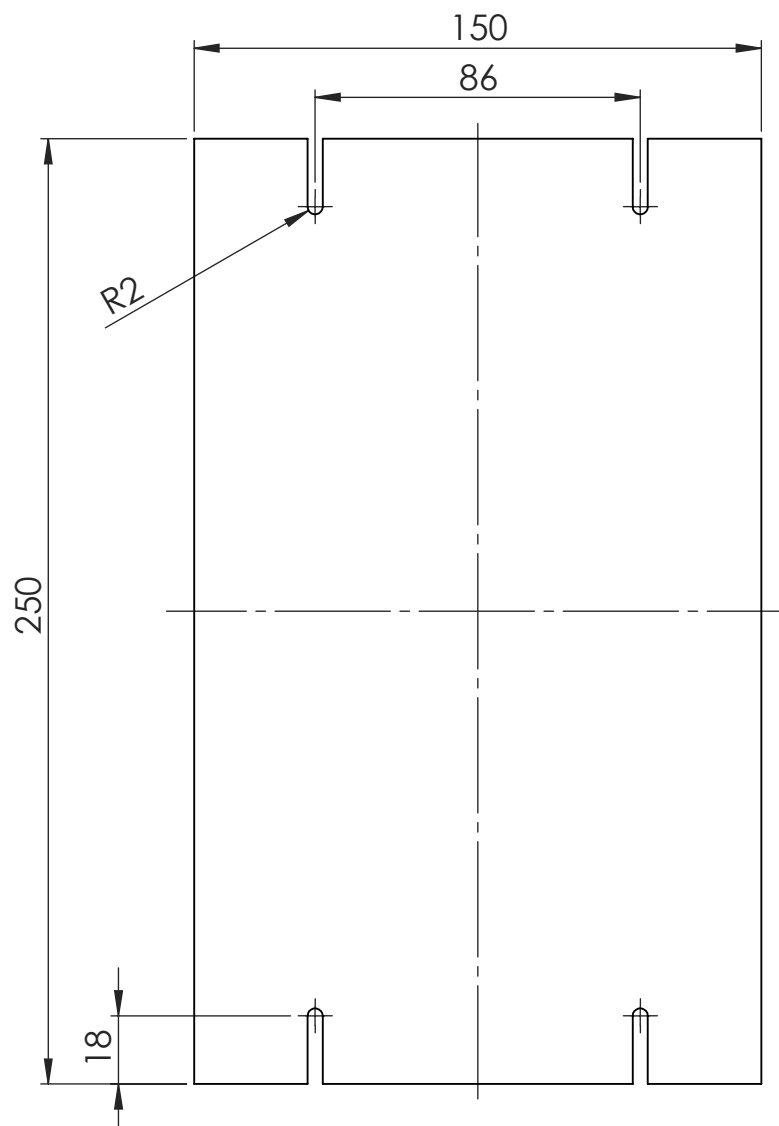
Note: thickness is 5.

Roughness	Dimensional Tolerances according ISO 2768-m	Material Plexiglass (PMMA)	Geometric and position Tolerances according ISO 2768-K	
Projection method 	Scale 1:2	Drawn by Brecht Lenaerts	Comments	
	Unit mm	Teamleader /		
	Date 3/05/2021	Checked by Jeroen Samoeey		
ASSOCIATIE KU LEUVEN	Bottom plate		Number BA3	A4

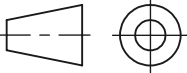


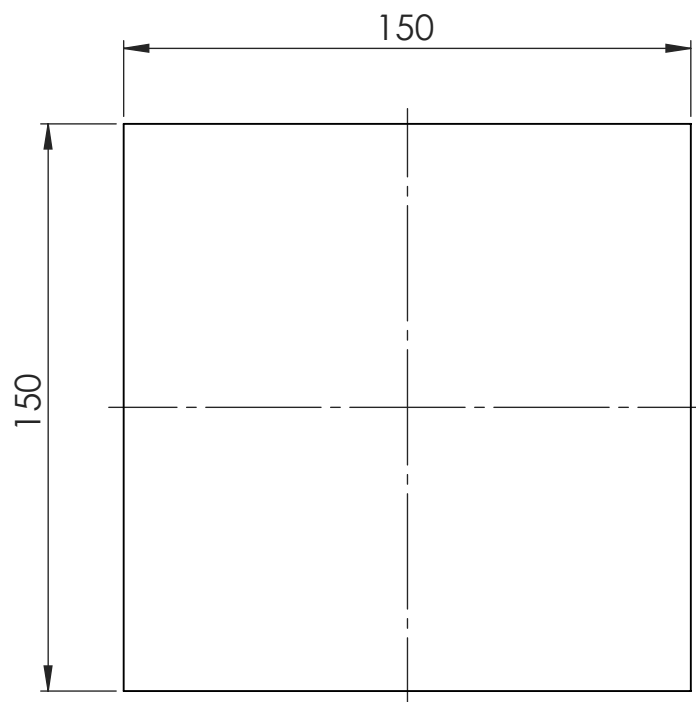
Note: thickness is 5.

Roughness	Dimensional Tolerances according ISO 2768-m	Material Plexiglass (PMMA)	Geometric and position Tolerances according ISO 2768-K
Projection method	Scale 1:2	Drawn by Brecht Lenaerts	Comments
	Unit mm	Teamleader /	
	Date 11/05/2021	Checked by Jeroen Samoeey	
ASSOCIATIE KU LEUVEN	Bottom edge		Number BA4
			A4

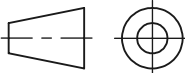


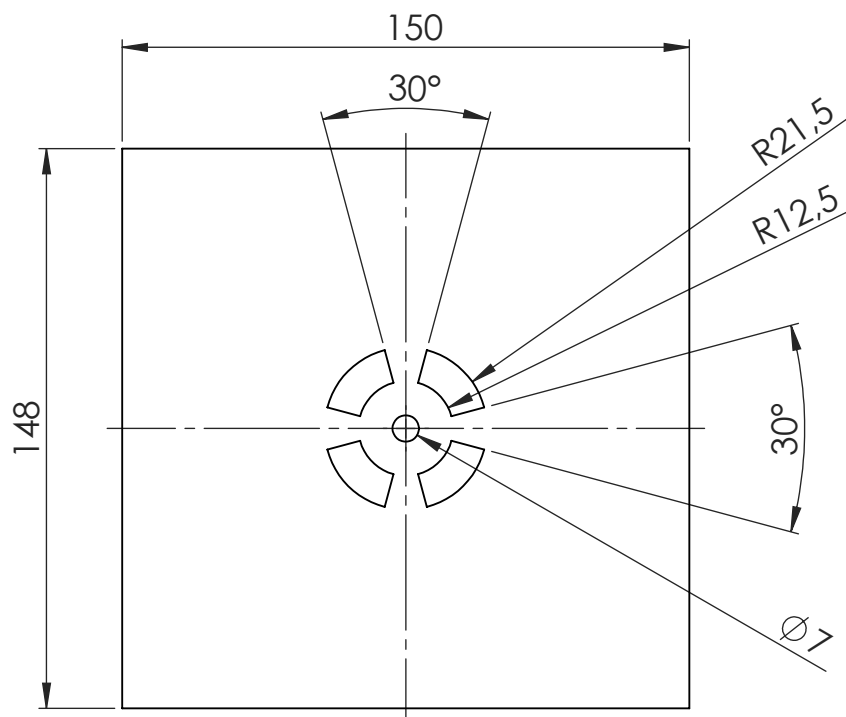
Note: thickness is 5.

Roughness	Dimensional Tolerances according ISO 2768-m	Material Plexiglass (PMMA)	Geometric and position Tolerances according ISO 2768-K	
Projection method 	Scale 1:2	Drawn by Brecht Lenaerts	Comments	
	Unit mm	Teamleader /		
	Date 8/05/2021	Checked by Jeroen Samoeey		
ASSOCIATIE KU LEUVEN	Side plate		Number BA5	A4

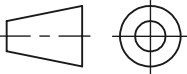


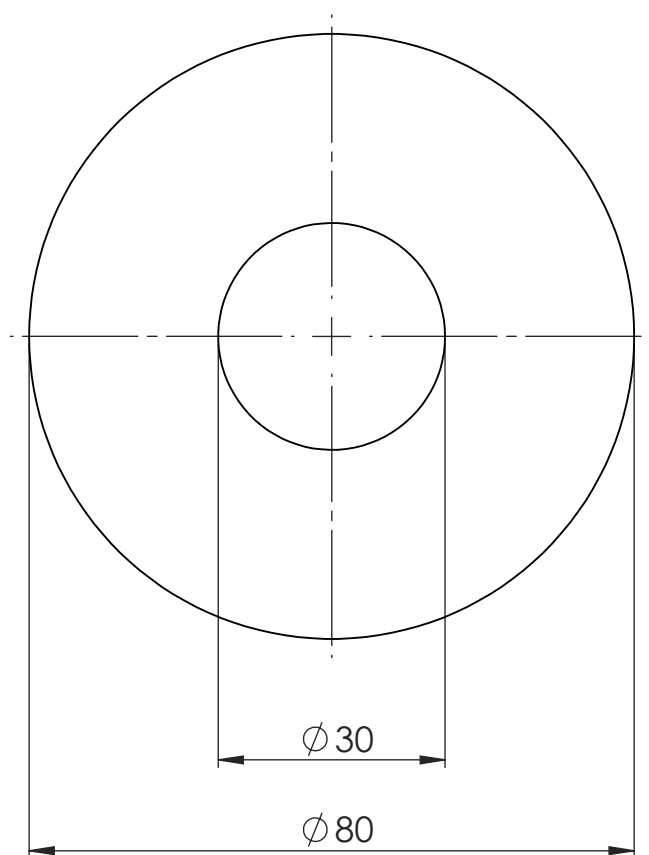
Note: thickness is 5.

Roughness	Dimensional Tolerances according ISO 2768-m	Material Plexiglass (PMMA)	Geometric and position Tolerances according ISO 2768-K		
	Scale 1:2	Drawn by Brecht Lenaerts	Comments		
	Unit mm	Teamleader /			
	Date 8/05/2021	Checked by Jeroen Samoeey			
ASSOCIATIE KU LEUVEN	Rostral plate			Number BA6	A4

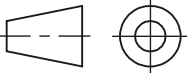


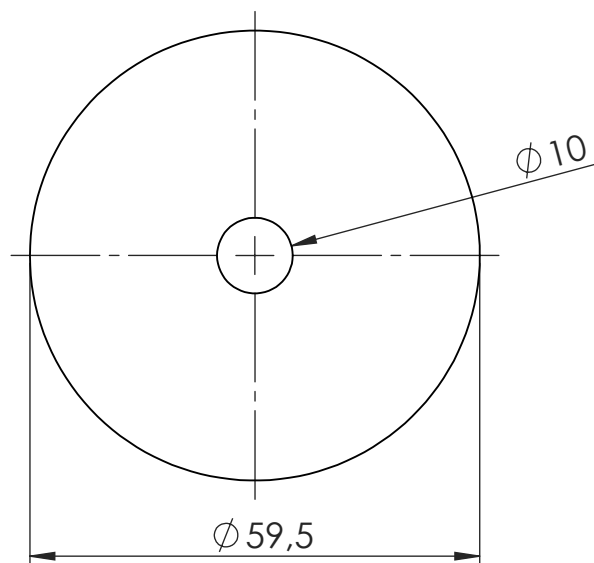
Note: thickness is 5.

Roughness	Dimensional Tolerances according ISO 2768-m	Material Plexiglass (PMMA)	Geometric and position Tolerances according ISO 2768-K	
Projection method 	Scale 1:2	Drawn by Brecht Lenaerts	Comments	
	Unit mm	Teamleader /		
	Date 8/05/2021	Checked by Jeroen Samoeey		
ASSOCIATIE KU LEUVEN	Caudal plate		Number BA7	A4

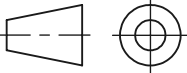


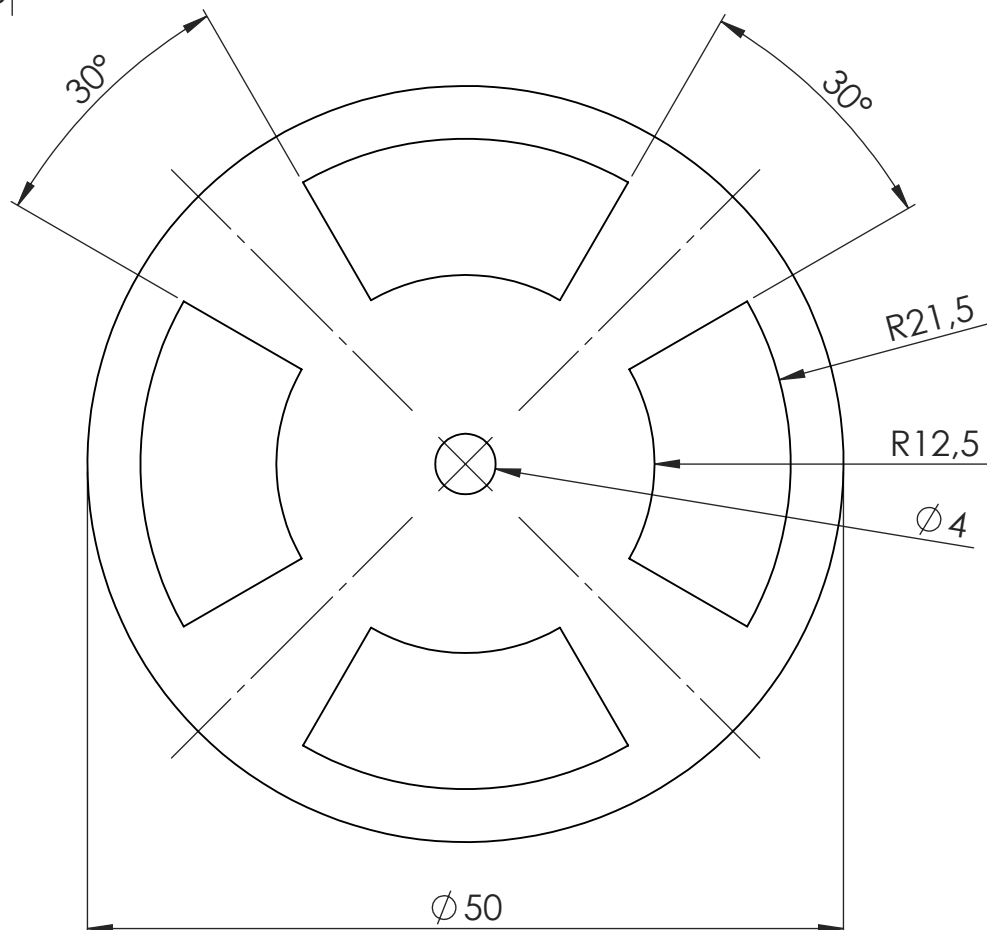
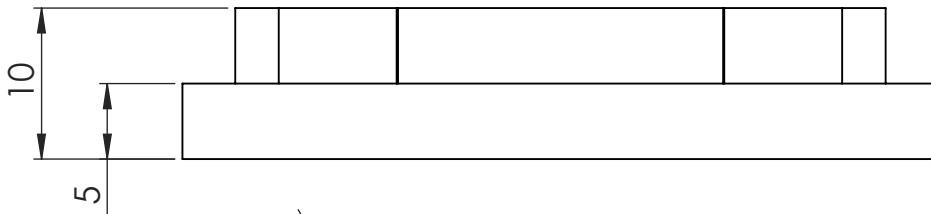
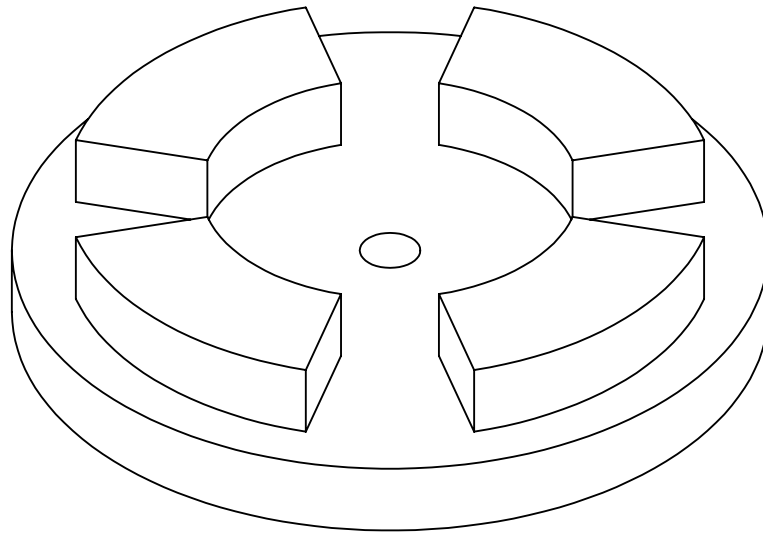
Note: thickness is 5.

Roughness	Dimensional Tolerances according ISO 2768-m	Material Plexiglass (PMMA)	Geometric and position Tolerances according ISO 2768-K	
Projection method 	Scale 1:1	Drawn by Brecht Lenaerts	Comments	
	Unit mm	Teamleader /		
	Date 8/05/2021	Checked by Jeroen Samoeey		
ASSOCIATIE KU LEUVEN	Outer part lid		Number BA8	A4

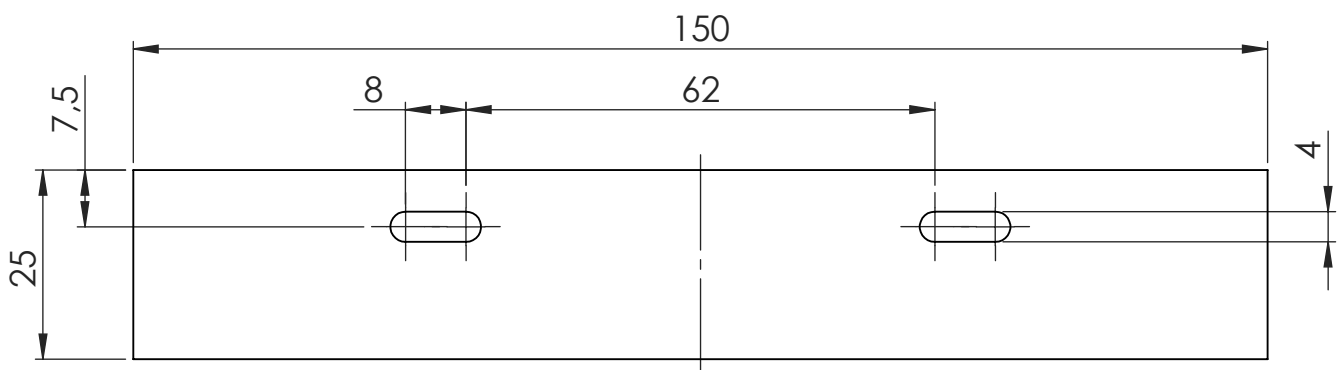


Note: thickness is 5.

Roughness	Dimensional Tolerances according ISO 2768-m	Material Plexiglass (PMMA)	Geometric and position Tolerances according ISO 2768-K	
Projection method 	Scale 1:1	Drawn by Brecht Lenaerts	Comments	
	Unit mm	Teamleader /		
	Date 8/05/2021	Checked by Jeroen Samoeey		
ASSOCIATIE KU LEUVEN	Inner part lid		Number BA9	A4

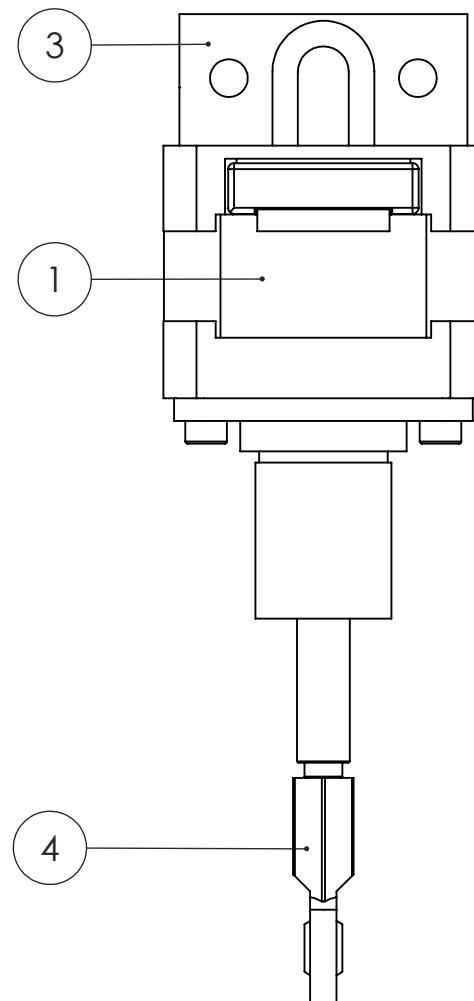
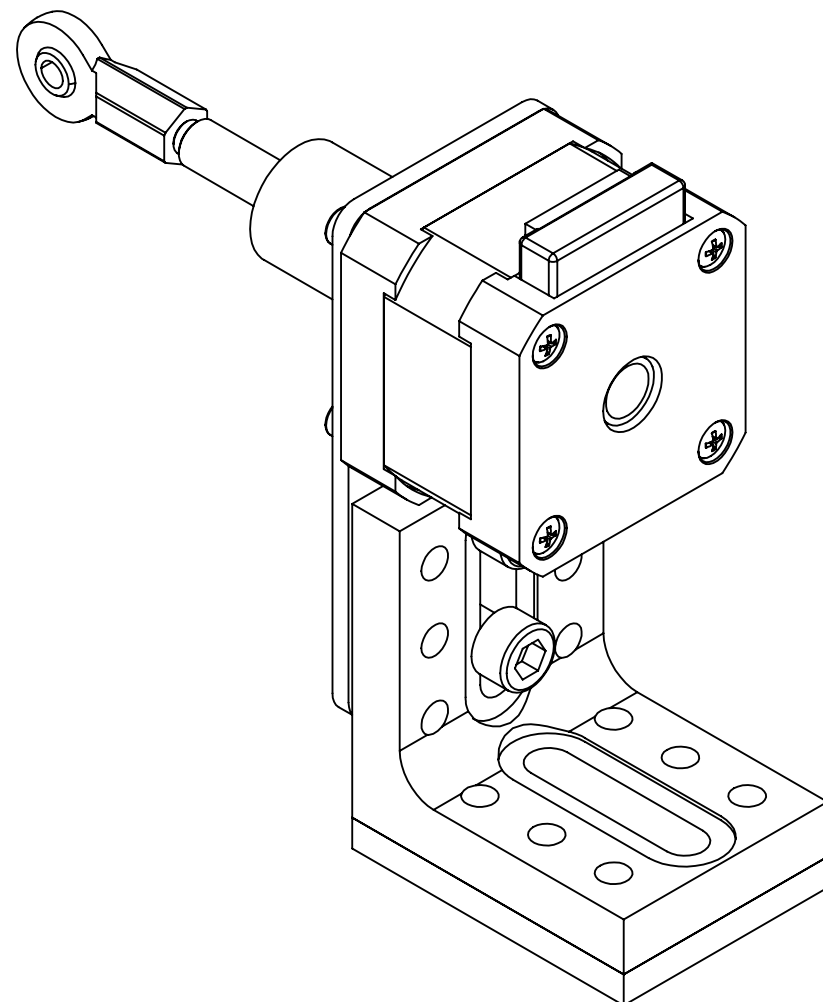
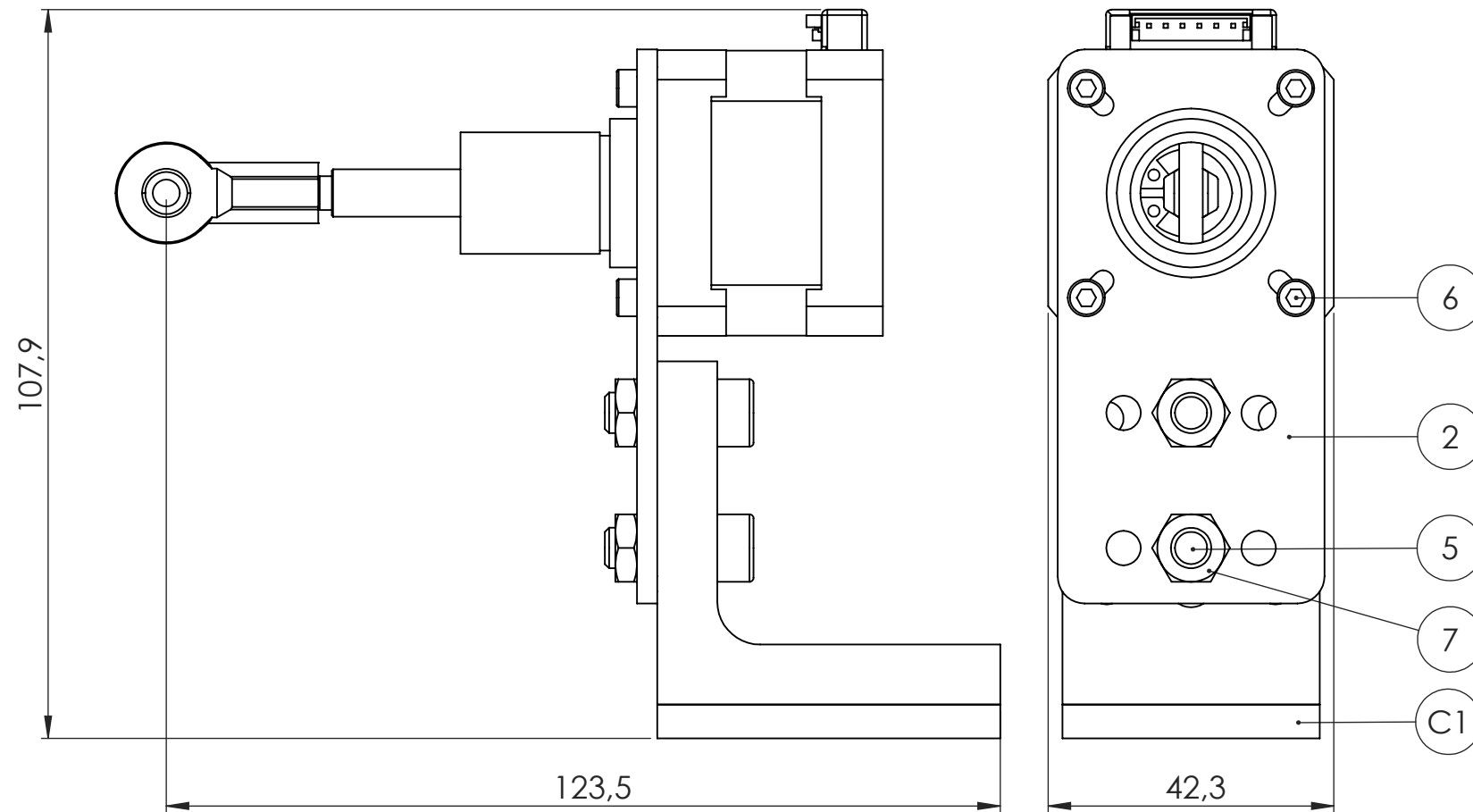


Roughness	Dimensional Tolerances according ISO 2768-m	Material FLGPBK01 Photopolymer resin	Geometric and position Tolerances according ISO 2768-K	
Projection method 	Scale	2:1	Drawn by	Brecht Lenaerts
	Unit	mm	Teamleader	/
	Date	11/05/2021	Checked by	Jeroen Samoeey
ASSOCIATIE KU LEUVEN			Connector	
			Number BA10	A4



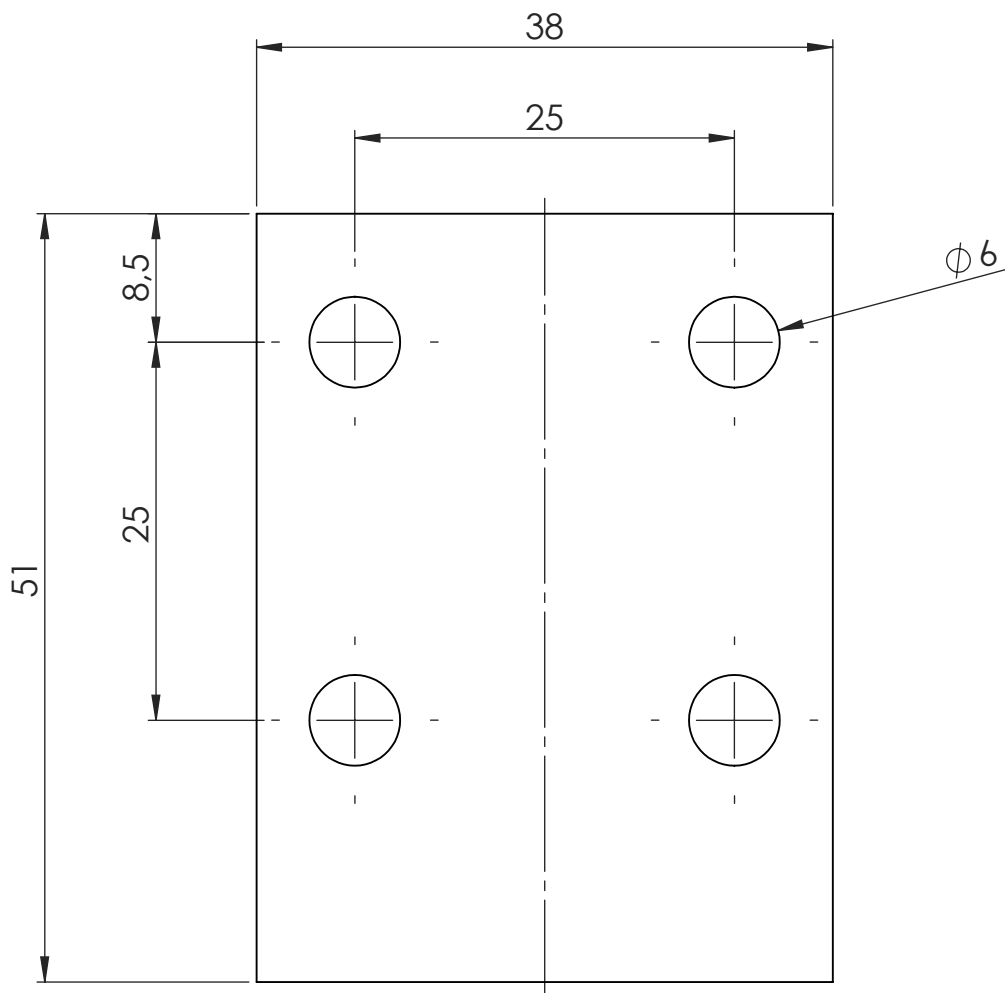
Note: thickness is 5.

Roughness	Dimensional Tolerances according ISO 2768-m	Material Plexiglass (PMMA)	Geometric and position Tolerances according ISO 2768-K	
Projection method 	Scale 1:1	Drawn by Brecht Lenaerts	Comments	
	Unit mm	Teamleader /		
	Date 8/05/2021	Checked by Jeroen Samoeey		
ASSOCIATIE KU LEUVEN	Removable spacing plate		Number B1	A4

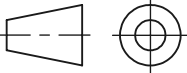


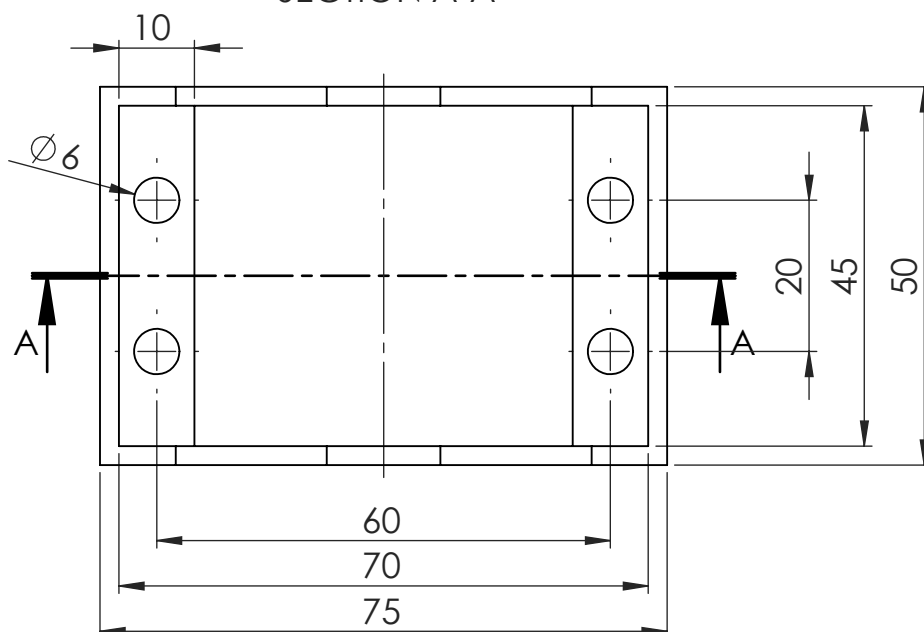
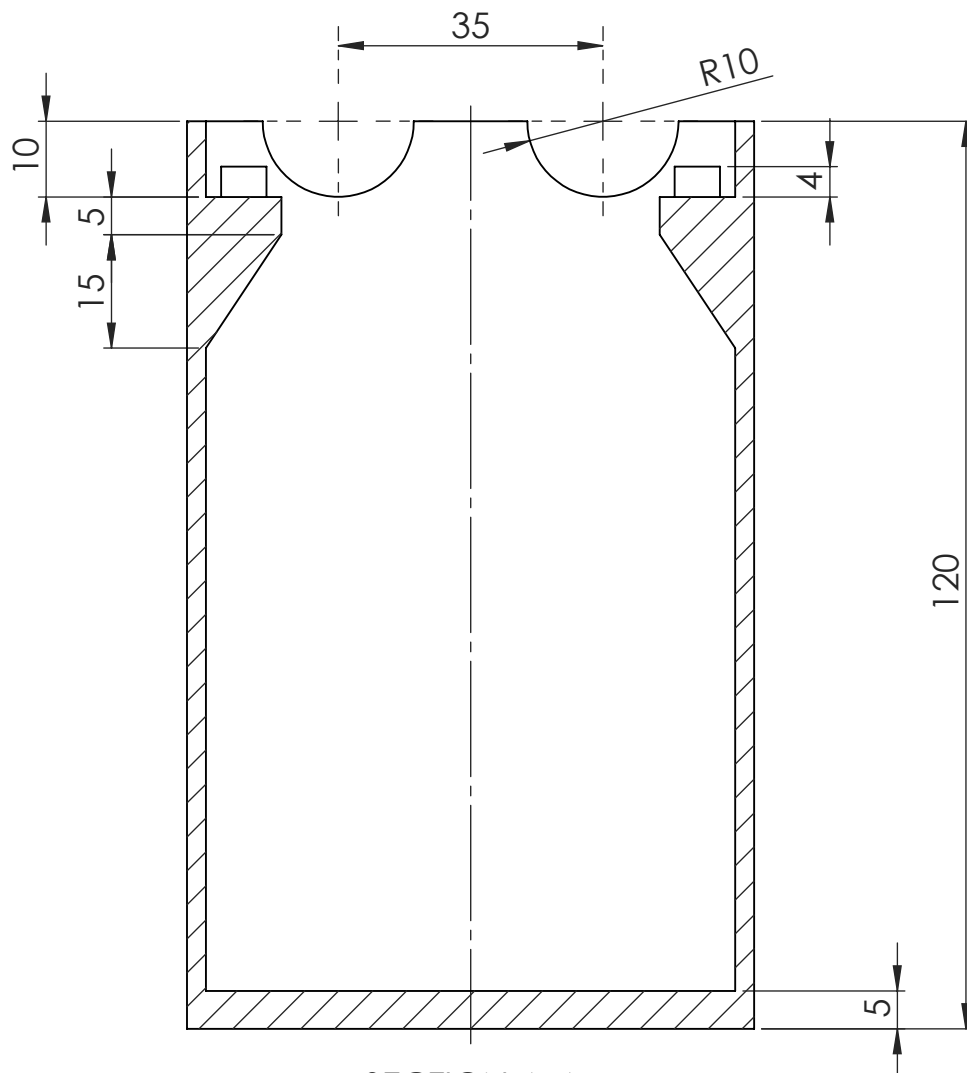
ITEM NO.	Description	Material, comments	QTY.
C1	Spacer plate	Plexiglass (PMMA)	1
1	Captive linear actuator - NEMA 17	Nanotec (Stock No. LGA421S14-A-TJBA-019)	1
2	NEMA17 Motor Mounting Plate	123-3D.nl	1
3	Angle Bracket with M6 x 1.0 Tapped holes	Thorlabs (Stock No. AB90A/M)	1
4	Rod end with female thread	Igus (Stock No. EBRM-04-J4)	1
5	Hexagon head screw M6x30	DIN912-M6x30	2
6	Hexagon socket head cap screw M3x8	DIN912-M3x18	4
7	Hexagon nut M6x1	ISO4035-M6x1	2


Roughness	Dimensional Tolerances according ISO 2768-m	Material	Geometric and position Tolerances according ISO 2768-K
Projection method	Scale 1:1	Drawn by Brecht Lenaerts	Comments
	Unit mm	Teamleader /	
	Date 11/05/2021	Checked by Jeroen Samoeey	
Subassembly linear actuator			Number C
			A3



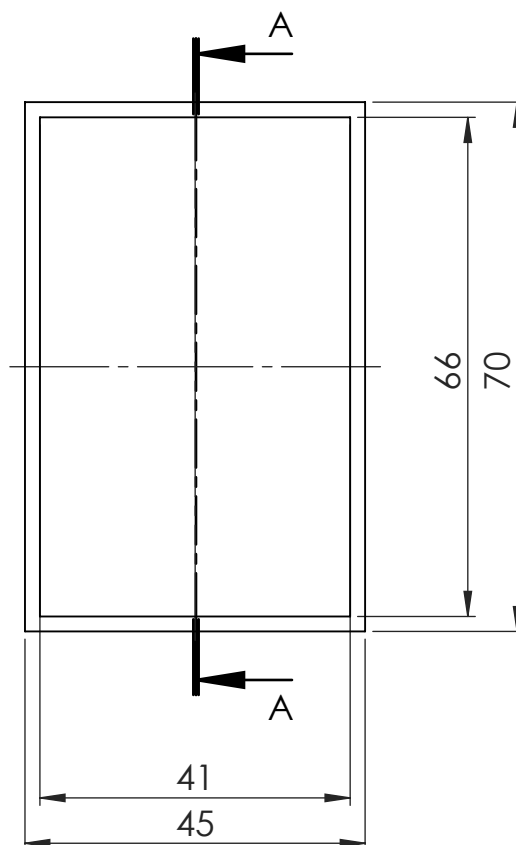
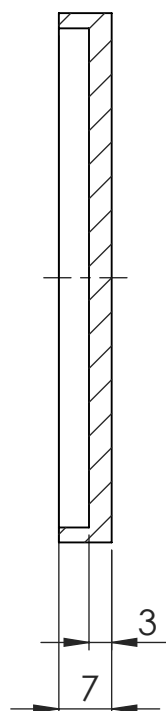
Note: thickness is 5.

Roughness	Dimensional Tolerances according ISO 2768-m	Material Plexiglass (PMMA)	Geometric and position Tolerances according ISO 2768-K	
Projection method 	Scale 2:1	Drawn by Brecht Lenaerts	Comments	
	Unit mm	Teamleader /		
	Date 8/05/2021	Checked by Jeroen Samoeey		
ASSOCIATIE KU LEUVEN	Spacer plate		Number C1	A4

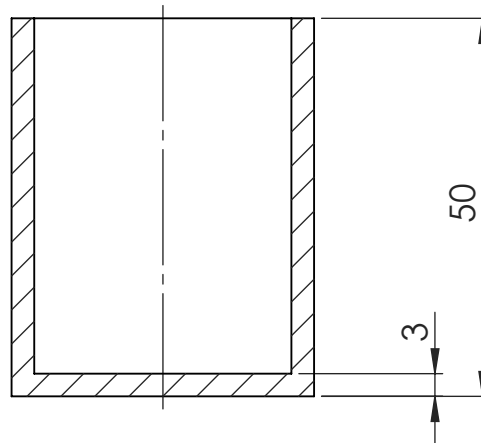


Roughness	Dimensional Tolerances according ISO 2768-m	Material	PLA	Geometric and position Tolerances according ISO 2768-K		
	Scale	1:1	Drawn by	Jeroen Samoeey	Comments	
	Unit	mm	Teamleader	/		
	Date	10/05/2021	Checked by	Brecht Lenaerts		
ASSOCIATIE KU LEUVEN	Implant module case			Number	1	A4

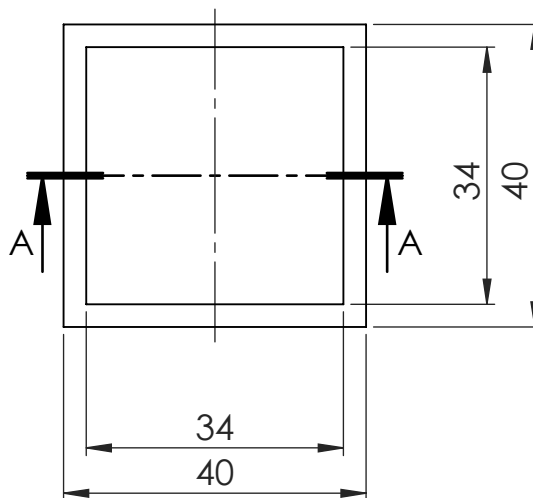
SECTION A-A

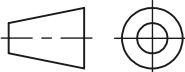


Roughness	Dimensional Tolerances according ISO 2768-m	Material PLA	Geometric and position Tolerances according ISO 2768-K	
	Scale 1:1	Drawn by Jeroen Samoeys	Comments	
	Unit mm	Teamleader /		
	Date 8/05/2021	Checked by Brecht Lendaerts		
ASSOCIATIE KU LEUVEN	Implant module case lid		Number 2	A4



SECTION A-A



Roughness	Dimensional Tolerances according ISO 2768-m	Material PLA	Geometric and position Tolerances according ISO 2768-K	
	Scale 1:1	Drawn by Jeroen Samoey	Comments	
	Unit mm	Teamleader /		
	Date 8/05/2021	Checked by Brecht Lenaerts		
ASSOCIATIE KU LEUVEN	Calibration cube		Number 3	A4

FACULTEIT INDUSTRIËLE INGENIEURSWETENSCHAPPEN
CAMPUS GROEP T LEUVEN
Andreas Vesaliusstraat 13
3000 LEUVEN, België
tel. + 32 16 30 10 30
iiw.groep@kuleuven.be
www.iw.kuleuven.be

